$K_S\Lambda$ Photoproduction on the Neutron within the Resonance Region

by

Charles Edward Taylor

A dissertation

submitted in partial fulfillment

of the requirements for the degree of

Doctor of Philosophy in the Department of Physics

Idaho State University

December 2012

Abstract

QCD-based models predict many N* states that decay through modes that have yet to be measured or precisely identified. These decay mechanisms give insight into the underlying symmetries of the excited-baryon states. There are competing models for the quark symmetries and dynamics ranging from preferentially paired-quark distributions to hybrid gluonic excitations. Measurement of the differential cross section and single- and double-polarization observables provide strong constraints on identifying the N* excitation spectrum. In this paper, we report preliminary differential cross-section measurements of the $\gamma D \rightarrow K_S \Lambda(p)$ reaction employing a circularly-polarized photon beam onto unpolarized LD_2. The energy of the photon beam ranged from 1.3 to 2.65 GeV, which spans from threshold to the resonance regimes. The final-state particles were used to reconstruct the missing mass of the spectator proton. The yield of this missing mass was then used for the determination of the differential cross section. We observe an increase of cross section in the central cms region for photon energies of 1.9 to 2.2 GeV. We regard this work on the $K_S \Lambda$ energy-dependent differential cross section as the first necessary step in identifying the underlying physics in the resonance regime. The work will form the foundation for further studies in extracting the polarization observables for circularly- and linearly-polarized photons from our analyzed dataset, which was taken by the CLAS detector in Hall B of Jefferson Lab in 2006 and 2007.

Acknowledgments

I would like to express my profound gratitude for Phil Cole taking me on has his grad student. I had been working in industry for 7 years when I went back to school for my doctorate. Much of the math and physics I was not using was gone. My first semester was very intimidating, but Cole's strong teaching abilities allowed me to quickly catch back up. He has been key in the completion of my thesis. I will always appreciate the significant effort he put into my work and thesis. Phil should also be recognized for his keen ability to find the funding for his and other grad students in our ISU group.

I also would like to thank Pawel Nadel-Turonski for being my co-advisor at Jefferson Lab. He guided me through the analytic process as well as taught me much of the physics of the CLAS system. I have always been impressed by Pawel's knowledge and great patience. He significantly advanced my understanding of how data should be analyzed.

I must also express my gratitude to Franz Klein, Eugene Pasyuk, and Ken Livingston for teaching me the finer details of how the CLAS system is run, while they were acting as the run coordinators. These gentlemen's knowledge on the CLAS system and software is profound. Eugene and Ken were essential in my learning of how the calibration code functions and how to cook the g13a data set. Similarly, Franz was always willing to share is expertise on the code architecture.

Paul Mattione and Nick Zachariou have been instrumental in helping me learn the jlab coding environment. Without them this analysis would have been remarkably more difficult. Both were also very helpful in getting me around Newport News while I

was temporarily staying at Jefferson Lab. They will forever have my respect and I will think of them as friends.

Finally I would like to thank my family for always being supportive. Whenever I had doubts, they did not. My father always knows how to make me feel special, and my older sister and brother could always make me laugh. I am most thankful for my twin brother. Without him, my life would have been completely different.

Table of Contents

List of Figures

List of Tables

Chapter 1

Introduction

From the earliest experiments, excited nucleons (baryons) have been observed to have significantly varying masses and charges, hinting at a large complex theory to catalogue them. Fortunately using the quantum numbers offered by the *standard model,* it is possible to treat all the varying nucleons as the *same* particle but in different resonant states (see Fig. 1.1). Similar to the theories detailing atomic and nuclear excited states, the individual nucleons themselves can be treated as excited particles (implying that the particles which make them up are energized into higher 'orbits' and 'spins'). Figure 1.2 shows the classification of particles (or baryon states) as the baryon octet (left) and decuplet (right). The quantum numbers charge, spin, and isospin of the nucleon can be derived from the charge, spin, and isospin of its constituent quarks.

The baryon positions in these triangular grids emphasize the symmetry of states using the quantum numbers I, Q and S along the different axes. Nucleons with nearly like mass (like the proton and neutron) can be treated as an underlying state having isospin ($I = 1/2$), but with opposite isospin projections ($I_3 = +1/2$ and $-1/2$ respectively). Similarly, the top row of decuplet can be treated as a family of particles, Δ, with different charges ($Q = -1, 0, +1, +2$). The strangeness of a particle determines which row the baryon falls into. The Δ resonances do not have any strangeness, while the rest (called hyperons) have at least one strange quark. Each baryon has a similar mass to the other baryons within the same row. The two diagrams in Fig. 1.2 differ by their total angular momentum, which is the sum of the particle's spin and orbital angular momentum. Meaning that while the neutron the Δ^0 are both made of up and down quarks and have no charge, they differ by their total angular momentum and isospin, I = 1/2 and 3/2, respectively.

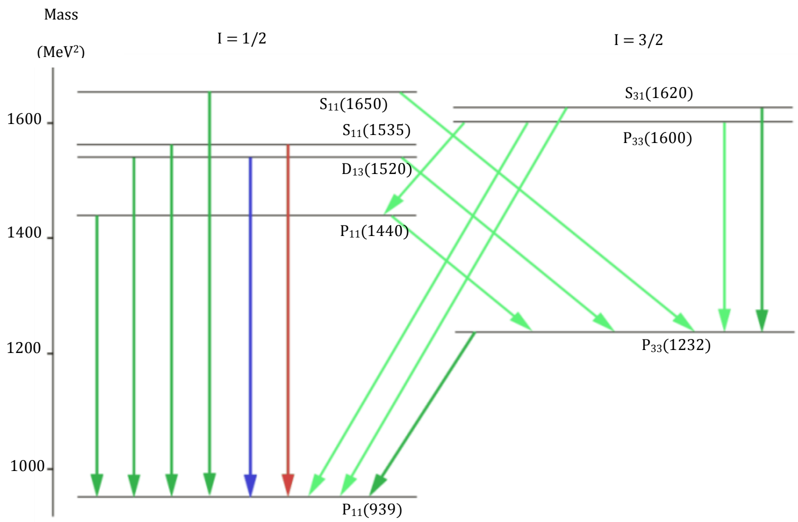

Figure 1.1: A diagram similar to nuclear excited states. This cartoon illustrates the first few levels of the excited states of a nucleon. The left side represents the 1/2-isospin, while the right is the 3/2–isospin. The green lines represent the emission of a pion, while the blue and red are the η and ρ mesons, respectively.

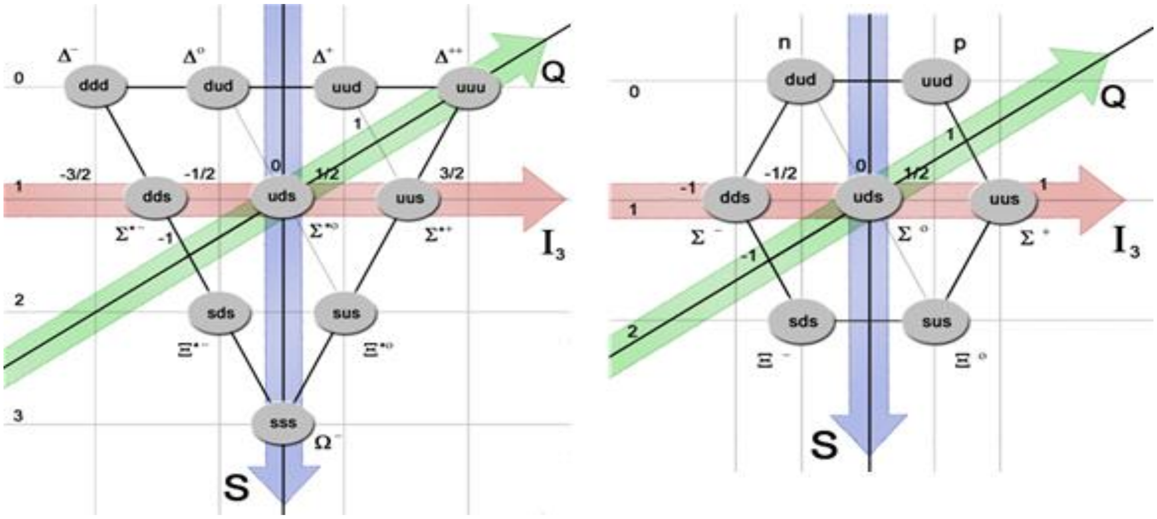

Figure 1.2: Diagram of the baryon (a)Decuplet and (b)Octet, illustrating the three different quantum values that can be used to define the symmetry the elementary particles are both made of up and down quarks and have no charge, they differ by their angular momentum and isospin, I = $^{1}/_{2}$ and $^{3}/_{2}$, respectively.

1.1 The Standard Model

Initially it was believed that neutrons and protons were the most elementary particles within the nucleus and the π mesons (pions) were the exchange particles of the strong nuclear force between them. But each new experiment revealed more new baryons and mesons (collectively called hadrons). By the 1950s several dozen hadrons were experimentally found. Adding to the confusion, some of these new particles had lifetimes many orders of magnitude longer than what was predicted by the strong interaction for the particle's mass. It seemed evident that these nucleons where more complex than initially perceived and a new model was needed. From this need, the *standard model* was developed.

In the standard model, the baryon is defined as being made up of three quarks (qqq) and the meson is a quark and antiquark pair ($q\bar{q}$). The combined quantum numbers of the quarks define the quantum numbers of the hadrons they make. Quarks are categorized first by their charge and then by their generation (relating to their mass), collectively referred to as a quark's *flavor*. Ordered with respect to increasing generation, the quarks with charge +2/3 are *up*, *charmed*, and *top*; while the −1/3 are *down*, *strange,* and *bottom*. The quarks making up the hadrons must sum to a balanced integer charge. The total charges of some of the possible configurations of quarks are illustrated in Table 1.1.1. Each quark has its corresponding antiquark. Likewise, the mesons have their own antiparticle. The meson of opposite charge is usually the antiparticle of a charged meson, while neutral mesons tend to be their own antiparticle. The quarks of heavier generations will decay to the lower flavors though the process, called the weak decay, which is the generation "switching" mechanism. The much smaller probability for this decay process allows for hadrons with these heavier quarks to live longer than expected with the strong decay process.

Table 1.1: An example of how the quantum values of quarks combine to give hadrons their quantum numbers. This shows the calculation of charge for a hadron given the quarks it is made up of, where Q is the charge and n_{pos} and n_{neg} are the number of positive and negative quarks (pos = {u,c,t} and neg = {d,s,b}). The $\overline{pos}$ and $\overline{neg}$ correspond to the antiquarks.

Particle	Quarks	Charge $Q = 2/3\left(n_{pos} - n_{\overline{pos}}\right) - 1/3\left(n_{neg} - n_{\overline{neg}}\right)$
π^+	$u\bar{d}$	1 = 2/3 (1 – 0) – 1/3 (0 – 1)
π^0	$(u\bar{u} - d\bar{d})/\sqrt{2}$	0 = 2/3 (1 – 1) – 1/3 (1 – 1)
proton	uud	1 = 2/3 (2 – 0) – 1/3 (1 – 0)
Δ^-	ddd	–1 = 2/3 (0 – 0) – 1/3 (3 – 0)
Λ^0	uds	0 = 2/3 (1 – 0) – 1/3 (2 – 0)

1.2 Baryon Spectroscopy

A spectrum can be produced with the assortment of measured baryons, similar in concept to the spectrum produced by atomic resonances. Both in atomic and nuclear physics, the *Heisenberg uncertainty principle* broadens the spectral lines because of the particle's short lifetimes with respect to the energy's measurement. The significantly shorter lifetimes (typically ~10^{-24} s) of the baryons make their energies much broader, significantly complicating their identification. The 'spectral lines' begin to overlap as their peaks broaden, creating a flat distribution. Only the strongest resonances are distinguishable within the summation of energies.

Until recently, the largest majority of baryon spectroscopy measurements were made with pion beams. Figure 1.3 shows the nucleon resonances for well-established baryon resonances for the energetic collision of a pion with a proton. After the strong low-lying resonances, the broad peaks become too overlapping for clear identification. With some difficulty, various partial wave analysis (PWA) techniques can be applied to isolate these resonances. The quantum numbers of each baryon resonance can be used determine the angular distribution of their decay products. The CLAS detector system (detailed in chapter 3) was designed to take advantage of this. Many of the experiments use a polarized beam (and sometimes a polarized target) to enable clear measurement of these preferential angles.

1.3 Missing Baryon Resonances

The theories based on the *standard model* have been very successful in predicting many of the lower-lying baryon resonances, but they also predict resonances at higher energies that have yet to be seen. There are a few possibilities for the "missing" resonances. Until recently, the πN coupling has been the dominant source of the empirical data[1],[2],[3]. Most of the missing resonances exist in higher energy range ($W > 1800$ MeV/c^2), where photon beams onto nucleons (γN) are expected to have a higher coupling (probability of interaction) than that of πN. Another problem is the wide-overlapping peaks of the previous unpolarized photoproduction experiments. The use of single- or double-polarization observables will tighten the coupled-channel partial wave analysis (PWA), making resonances easier to distinguish. The problem could also be due to the models being used. These models may be missing some fundamental factors, such as the tight bonding of two of the three quarks within the baryon (as proposed by the di-quark model[2],[3].

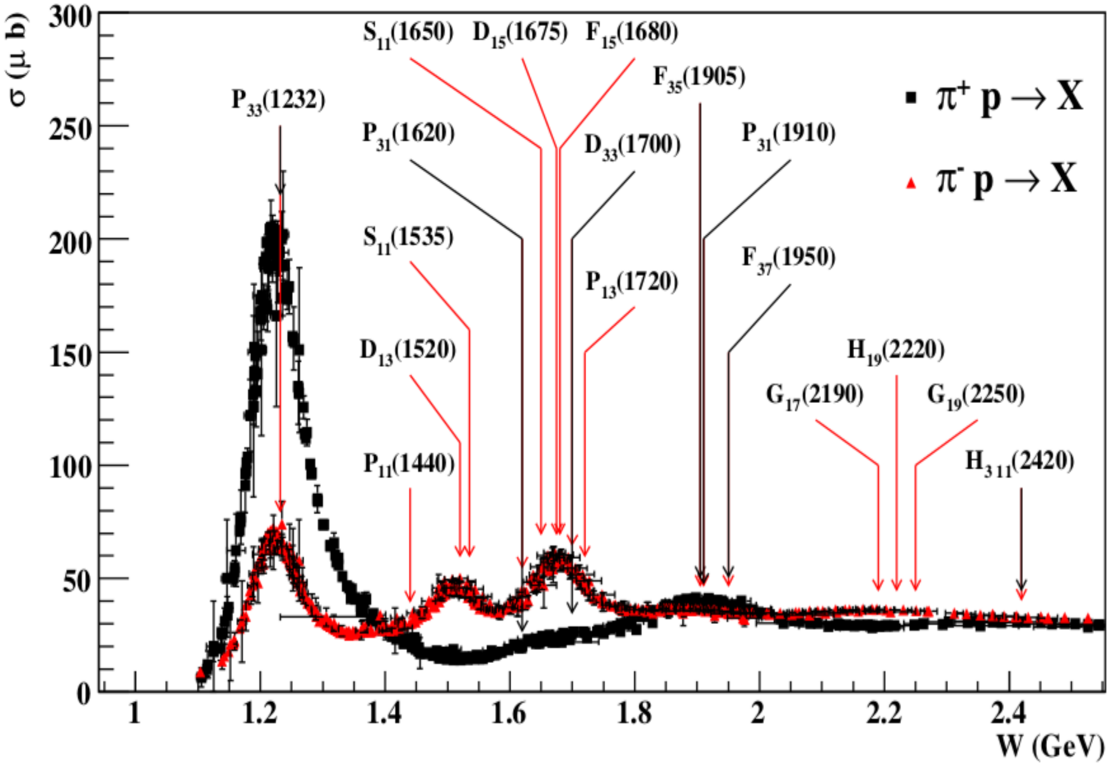

Figure 1.3: The resonances from baryon excitation with at least 3-star PDG rating[4]. The labels first indicate the total angular moment, *L*, with subnumbers indicating 1/2 for the isospin, I and spin, J, of the baryon. The parenthetical values indicate the mass of the particle (in MeV)[5].

As a part of a series of experiments, the work of this thesis is focused on aiding in the exploration and establishing the existence of the "missing" resonances through analyzing the $\gamma n \rightarrow K_S\Lambda$ reaction. While strangeness photo and electroproduction has been studied in the K^+ channel, there has been little research on the neutral kaon channel. The $K_S\Lambda$ channel is predicted to have sensitivity to the $D_{13}(1900)$ resonance[6], whose existence is still contested based on the $K^+\Lambda$ data results[7],[8].

1.4 The Diquark Model and their Decay Widths

Many theories predicted on the *standard model* that baryons have three constituent quarks. However, Koniuk[2], and Capstick and Isgur[3] proposed a different configuration of the quarks where two are tightly bound and orbited by the third. This produces the requirement that the paired quarks be in anti-symmetric, unexcited states to form colorless baryons. Such a requirement reduces the number of degrees of freedom for the excited nucleon states, thereby accounting for some of the missing resonances.

Capstick and Roberts performed calculations for the coupling amplitude of several strangeness channels to the N* and Δ* states[9]. They present their results for the Nγ, Nπ, and ΛK amplitudes in Fig. 2.2. The states with significant amplitudes for both the Nγ and ΛK are expected to have the best likelihood of empirical verification.

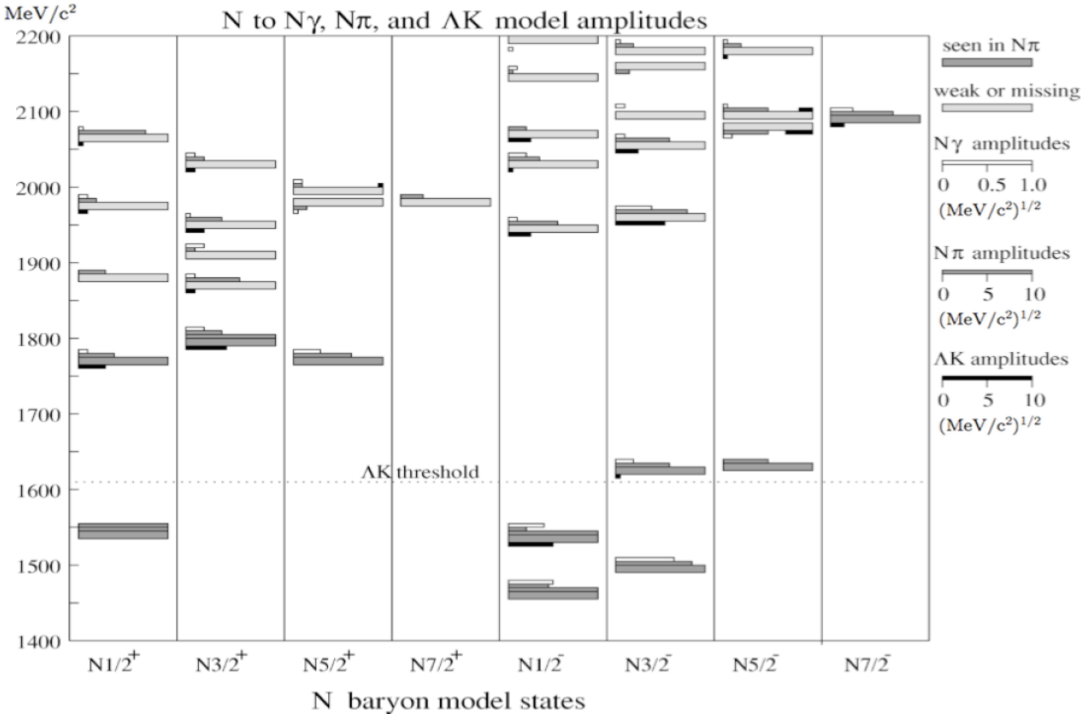

Figure 1.4: The coupling amplitudes as predicted by Capstick and Roberts[9] for the N* model states with mass less than 2.2 GeV/c² into the Nγ, Nπ, and ΛK channels. The amplitudes are represented by the length of the bars at each respective spin-parity designation and mass. This model is based on 3 constituent quarks.

Although the Nπ always has higher amplitudes, it has been shown that the Nγ channel offers a significantly improvement on helicity amplitude of the neutron over the proton interactions[3]. The gluon fields from the pion interactions with the proton prove to be significantly more difficult to model than that of a photon probe as QED is very well understood.

Chapter 2

Theory

In modern physics, there have been traditionally two key theories outside of the realm of classical physics, relativity and quantum mechanics. Special relativity is a theory that describes systems at velocities near the speed of light (where frames of reference that respect that the speed of light is constant are required), while quantum mechanics evaluates the interactions of tiny systems (where measurements become a distribution of probabilities). Relativistic quantum field theory merges the two theories for systems that are both small and fast. Fields are used to describe the forces between the particles, where the force exchange particles (gauge bosons) are the quanta of those fields. In quantum field theory only three of the four fundamental forces are considered: *electromagnetic*, *weak,* and *strong* interactions. The *gravitational* force is far too weak to play a significant role.

Consequently, three related theories are used for each of the interactions of particles. The theory of the electromagnetic interactions is given by *quantum electrodynamics* (QED). The photon, γ, is the only gauge particle in QED, yielding a corresponding U(1) symmetry group. Photons do not interact with each other. Next, the weak interaction is the force by which quarks change from one type to another. Combined with QED, the theory of the weak interactions is called the *electroweak theory* (EWT). Three generators form the symmetry group of SU(2) for the weak interaction. These generators correspond to the three gauge bosons; W^+, W^-, and Z bosons. Therefore, the electroweak theory is defined by the $SU(2)\otimes U(1)$ gauge group.

The strong interaction is the nuclear force that holds nucleons together and the means by which they quickly decay (on the order of magnitude 10^{-24}). Its fields are mediated by eight types of gluons, which relate to the eight generators used with the SU(3) group. These gluons are described by their color and are the primary motive behind the theory of *Quantum Chromodynamics*. QED and QCD are discussed in more detail in the section 2.1, while the electroweak is discussed in section 2.2.

Experimentally quarks have never been observed alone. This leads to the principle of quark confinement. The force between quarks does not weaken with distance; therefore it would not be possible to completely free a quark from its neighboring quarks. However at higher energies, it is possible to separate quarks enough to produce a new quark/antiquark pair between them. The new quarks then create new particles with the original quarks, breaking the initial confinement between them. At high enough energies this process can happen multiple times from the original quark pair. This is most commonly observed when the quarks from projectile hadron interact with that of a target hadron. For example, consider a pion beam incident upon a proton target. A negative pion's anti-up quark can interact with one of the up quarks in the proton, creating a new neutral pion.

2.1 Quantum Electrodynamics and Chromodynamics

All of the models in field theory are based on the oldest of the field theories- the quantum electrodynamics theory. In QED all possible electromagnetic interactions can be expressed by a Feynman diagram (see Fig. 2.1). The vertices represent the coupling of the particle (represented by straight lines) with the photon (represented by a squiggly line). An arrow on particle line that is pointing against the defined direction of time indicates it is the antiparticle. Every way a diagram can be turned or reconfigured

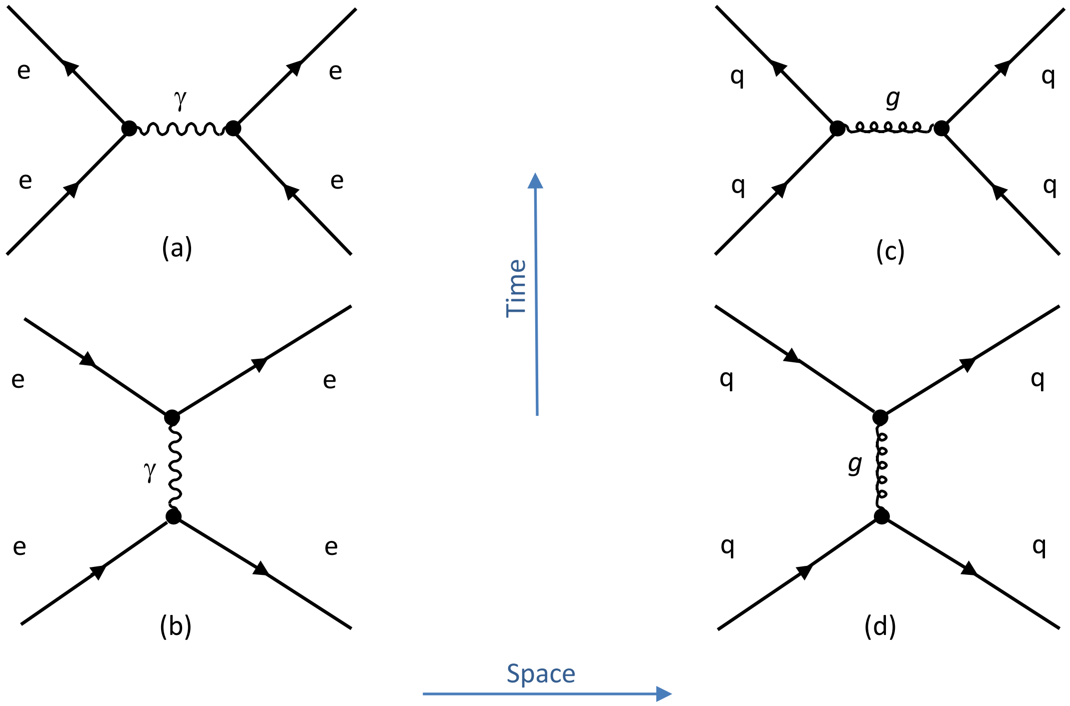

Figure 2.1: Feynman diagram comparing QED and QCD with one rotation of the diagram. (a) two scattering electrons, (b) electron-positron annihilation and pair production, (c) quarks scattering, and (d) quark annihilation and creation.

represents another topology of the original reaction. If you turn the Feynman diagram depicting the scatter of two elections on its side, it then describes an electron-position annihilation and subsequent production. *All* of these reactions can ultimately be reduced to $e \rightarrow e + \gamma$. That is for any vertex, the charge particle (electron) either emits or absorbs a photon, γ.

Here “e“ could be either an electron or a positron. Conceptually, the electron could be replaced with any charge-carrying particle (quark or lepton). QED does not apply with non-charge carrying particles such as the neutrinos. Though photons are the force-carrying particle of charged particles, they themselves have no charge. This is in agreement with the lack of interaction between photons.

Similar to QED, the quantum chromodynamics reactions can be portrayed both by Feynman diagrams and formulas, except the single electric charge carrying γ is replaced by the color-charged gluons g (with the basic reaction $q \rightarrow q + g$). Gluons carry a dual charge of a color and anti-color pair. With SU(3), there are $N^2 - 1 = 3^2 - 1 = 8$ combinations of color charge. Quarks have a single color charge. When a quark undergoes a strong interaction, the gluon carries away the quarks original color with the antiparticle of the quarks new color. Looking at Fig. 2.1 again, we see how the Feynman diagrams of QCD appear to have a similarity to those of QED. However, unlike photons, gluons can interact with each other. So these are the color charge carried by one gluon can influence the color charge of another.

Only partons (quarks and gluons) have color– namely red, green, and blue (r-g-b), which is in agreement with the confinement principle. Since color cannot be observed, all other particles must have no color charge or have neutral color. Hadrons are made up of quarks that sum up to a color neutral charge. With three quarks, a baron's final state after a reaction must remain color neutral, meaning a balance of r-g-b (the color singlet). A prime example of this is the Δ^{++} resonance, which has three *up* quarks. This resonance was the initial motivator for the development of the color degree of freedom. Mesons have just two quarks, so they must have a color paired with its anti-color so their color cancels out. Leptons have no color at all and are not affected by the strong force.

2.1.1 Determining Probability Amplitudes with Feynman Diagrams

The interaction between any given set of particles can be described by probability amplitudes. The calculations of these amplitudes include complicated integrals which often possess many variables. Fortunately these difficult mathematical problems have a strong structure. The formulas can be broken into individual terms for each propagator and interaction, which can be defined by a specific rule set. This allows the particle interaction to be representation by a Feynman diagram (as seen in Fig. 2.1). The structures are defined by the Lagrangian-dependent Feynman's rules:

1. The 4-momenta of the incoming and outgoing particle are represented by a solid line with an arrow to indicate whether it is a particle or antiparticle.
2. Each vertex represents the coupling constant for the interaction
3. The propagators are represented by a solid line (fermion), curvy line (boson) or spiral line (gluon) between two points.

We can therefore define the probability amplitude for the transition of the initial state into the final state by the interaction matrix (S-matrix) as:

$$S_{fi} = \langle \varphi_F | S | \varphi_i \rangle \,. \tag{2.1}$$

The S-matrix is defined by the perturbation series:

$$S = \sum_{n=0}^{\infty} \frac{i^n}{n!} \int \prod_{j=1}^{n} d^4 x_j T \prod_{j=1}^{n} L_v(x_j) \equiv \sum_{n=0}^{\infty} S^{(n)}, \tag{2.2}$$

where T is the time-ordered product of the operators and L_v is the Lagrangian of the interaction. The time-order product is used when the order of two operators in a product depends on their space-time location. The Lagrangian can be rewritten as $-g\bar{\varphi}\gamma^{\mu}\varphi A_{\mu}$, where φ the state of particle, g is the coupling constant, γ^{μ} is gamma matrix, and A_μ is the bosinic field. Using the Feynman diagram and the associate rules. The S-matrix for two body reactions can then be rewritten as[10]:

$$S^{(2)} = \frac{(ie)^2}{2!}\int d^4x_i d^4x_f\, T\bar{\varphi}(x)\gamma^\mu\varphi(x)A_\mu(x)A_\mu\bar{\varphi}(x')\gamma^\nu\varphi(x')A_\nu\,(x')\,, \qquad (2.3)$$

2.1.2 Baryon Resonances in the Standard Model

Experimentally, there are four categories of couplings for the production of excited baryons: meson-baryon, baryon-baryon, lepton-baryon, and photon-baryon interactions. Most of the current measurements of baryon states were made using pion beams[11]. This meson-baryon model has several supporting models[12]. Proton colliders can be used for baryon-baryon coupling, though their energies are orders of magnitude greater than the low-lying baryon resonance region. For this reason, these colliders are not used directly for the measurement of the baryon resonances. The CLAS detector can collect data for both lepton-baryon and photon-baryon interactions within the low-lying states region.

2.2 The Weak Interaction

As mentioned in the introduction, all baryons can be thought of as the same particle in different excited states. From this viewpoint, the proton is considered the ground state. It is well known from beta decay that a neutron can decay into a proton. However despite having similar masses and having the same spin, a *down* quark changes into an *up* quark for the neutron to decay. It was also noticed that parity and conjugation were broken in flavor-changing decays. QCD does not offer a solution to this problem.

Furthermore, many of the baryons being discovered had lifetime orders of magnitude longer than predicted by QCD.

In 1979, Glashow-Weinberg-Salam established a theory to explain this process- the weak interaction. However particles can and will through the mediation of the W and Z bosons. Not everyone chooses to use the term “weak isospin” defined by EWT, yet all particles have whatever property it is that allows for the weak process to occur. Quarks and leptons both can interact and decay by this process. Unlike the photon and gluon, the charged W and neutral Z bosons have large masses (almost two orders of magnitude greater than the proton mass). They are also short lived, with lifetimes below 3x10^{-25} seconds. Because of this, the coupling constant of the weak process is very small. The weak interaction has a short range of influence of 10^{-17} meters. These factors allow heavy quarks to hold the state of their parent particle longer than what is predicted by QCD. These particles have a remarkable range of lifetimes (between 10^{-26} to 10^{3} seconds).

So for the beta decay, the down quark’s transformation into an up quark can be expressed by:

$$\begin{aligned} d &\rightarrow u + W^{-} \\ &\rightarrow u + e^{-} + \bar{\nu}_e, \end{aligned} \tag{2.4}$$

where $\bar{\nu}_e$ is the electron anti-neutrino. The W and Z bosons themselves decay rapidly. It was more recently discovered that the neutral Z bosons decay into a fermion along with its antiparticle.

2.2.1 Weak Isospin and Weak Hypercharge

In EWT (occasionally called quantum flavordynamics– QFD), two new quantum numbers are defined to describe the weak interaction- the weak isospin T_3 and the weak hypercharge Y_W. The weak isospin is defined as the fundamental property of all particles for the weak interaction. Both quark and leptons have a weak isopin of ±½. Combined with the electromagnetic force, the weak hypercharge is also considered a fundamental property of all particles; however its form changes between charged and neutral particles. Without charge, just the weak isospin exists. The weak hypercharge is defined as:

$$Y_W = 2\,(Q - T_3)\,, \tag{2.5}$$

where Q is the electrical charge. The weak hypercharge is the generator of the U(1) group in electroweak theory.

2.2.2 CP Violation

Traditionally the laws of physics do not depend on parity. That is, if all of the spatial axes are reversed within an experiment, the measurement should mirror the original system's measurement. For the most part, parity in nature is observed. However Chen Ning Yang and Tsung-Dao Lee[13] were able to show parity is not invariant in the weak interaction.

To address this problem, Richard Feynman and Murray Gell-Mann developed the left-handed theory. The mirror reflection of a left-handed particle yields a right-handed antiparticle, offering the concept of *charge conjugation*. The term “charge” is misleading since charge conjugation also can be applied to neutral particles. What it really represents is the transformation of a particle into its corresponding antiparticle, which may or may not include a charge. Precisely:

$$C|\phi\rangle = \mp|\phi\rangle = |\bar{\phi}\rangle, \tag{2.6}$$

where the charge conjugation operator C when applied two times on the particle state $|\phi\rangle$ returns the original particle state, or $C^2 = I$. The neutral mesons and the photon have no charge and are their own antiparticles, making them eigenstates of operator C.

It was believed that the symmetry of the charge conjugation and parity combined could bring invariance within all intermediating forces. Though this method did significantly decrease the violations in parity (such as the decay of charge pions to a muon/neutrino pair), there were still some of instances where symmetry was broken. The most notable of these violations was the transitions of the neutral kaons to its antiparticle and back again. In 1964 Gell-Mann and Pais discovered by that the probabilities of the transitions from K^0 (with S= 1) to $\bar{K}^0$ (with S = –1) and from $\bar{K}^0$ to K^0 were not equal.

The unmeasured state $|K_i\rangle$ of a neutral kaon must contain both the kaon and anti-kaon states, however by CP symmetry:

$$CP|K^0\rangle = -|\bar{K}^0\rangle \tag{2.7}$$

$$CP|\bar{K}^0\rangle = -|K^0\rangle. \tag{2.8}$$

So assuming symmetry is conserved, state of a neutral kaon with CP equal to 1 or −1 must remain in the same state after the interaction. From this we get the normalized eigenstates:

$$CP|K_1\rangle = 1/\sqrt{2}\,(|K^0\rangle + |\bar{K}^0\rangle) \tag{2.9}$$

$$CP|K_2\rangle = 1/\sqrt{2}\,(|K^0\rangle - |\bar{K}^0\rangle)\,. \tag{2.10}$$

The linear combination of these two eigenstates can be used to define the state of a neutral kaon. That is:

$$|K^0\rangle = 1/\sqrt{2}\,(|K_1\rangle + |K_2\rangle)\,. \tag{2.11}$$

Since the eigenstates $|K_1\rangle$ is positive and $|K_2\rangle$ is negative, conservation of CP requires that the $|K_1\rangle$ decay into two pions and the $|K_2\rangle$ into three pions. The decay to two pions is a straightforward decay, while the decay to three pions reduces phase space significantly thereby increasing the lifetime of the K_S. For this reason the K_1 is called the short-lived kaon, K_S, and the K_2 the long-lived Kaon, K_L.

At this point, it seems that symmetry has been conserved. However, it has been discovered that the long-lived kaons contain a small mixture of the eigenstates $|K_1\rangle$ and the short-lived with $|K_2\rangle$ [13]. With the measured divergence from the expected CP symmetry, $\epsilon = 2.266 \pm 0.017 \times 10^{-3}$, the state of the kaons can be written as:

$$|K_S\rangle = 1/\sqrt{1-|\epsilon|^2}\,(|K_1\rangle + \epsilon|K_2\rangle)\,, \tag{2.8}$$

$$|K_L\rangle = 1/\sqrt{1-|\epsilon|^2}\,(|K_2\rangle + \epsilon|K_1\rangle)\,. \tag{2.9}$$

This leads to the violation of CP invariance, since this would imply that the long-lived kaon could be in the positive CP state and the short-lived in a negative.

The neutral kaon can transition in out of its anti-particle state. That is, each quark is replaced with the other's antiparticle. However, the probability of this transition is not equal in both directions. This is called *indirect* CP violation and was believed to be isolated to the kaons. Recently experiments at Fermilab and CERN have shown evidence of a *direct* CP violation, by studying the decay instead of the mixing of neutral kaons[41].

2.3 The Strangeness of K_S, Λ, and Σ^0

Everyday matter is made up of only up and down quarks. High-energy interactions are required to create matter with heavier quarks. The most easily observed of these are the *strange* quarks produced with kaon production. A cursory glance at Fig. 1.2 will show all but the top rows of baryons in the decuplet and octet have at least one strange quark, collectively called hyperons. Similar diagrams can be found for the strangeness of the mesons. At the center of the octet, we can see the neutral hyperons, Λ and Σ^0. Both have the quark configuration up, down, and strange (uds). The up and down quarks in the Λ both are in a spin-singlet state, while they are in the spin triplet state for the Σ^0. The Λ has an isospin of 0 restricting this channel to the $\frac{1}{2}^+$ N* resonances, while the Σ^0 has isospin 1 allowing both N* and Δ states. The neutral kaon has a down and strange antiquark ($d\bar{s}$).

The study of how the strange hadrons couple with non-strange hadrons will help illuminate the processes involved in the baryon resonances. The photoproduction of the K_S is of particular interest in the study of missing resonances. Previously, most strangeness studies have been on the $K^+\Lambda$ and $K^+\Sigma^0$ channels since the charged kaons are easier to detect than the neutral kaon. However, K^+ mesons found in the *t* channel will tend to be forwardly diffracted, which will complicate the measurement of the angular distributions from the resonance contribution. Due to the lack of interaction between the incident photons and the neutral mesons, the *t*-channel K_S intermediate states are small. This allows for the enhancement of the nucleon resonance contribution and creates a clear delineation of the angular distribution of the predicted observables.

Since a pure neutron target does not exist in nature, fewer studies have been made of strangeness photoproduction from the neutron. With the use of a deuterium target (a nucleus with a proton-neutron pair), the K_S decay channels was the clear choice for the cross section for quasi-free neutrons- specifically for the $\gamma D \rightarrow K_S\Lambda(p)$ and the $\gamma D \rightarrow K_S\Sigma^0(p)$ reactions. These two channels offer clear separation from most of background phase space. The total cross section of the $K_S\Lambda$ is predicted to be twice that of the $K^+\Lambda$ channel[14].

2.4 Decay Processes for the $n(\gamma,K_S)Y$ Reactions

In the two-body process different invariant kinematic quantities can be well described by the Mandelstam variables, which are kinematic invariants. These variables carry the information of the energy, momentum, and angles that is preserved regardless of the reference frame. In a system with two incoming momenta of p_1 and p_2 and an outgoing of p_3 and p_4, these variables are defined as:

$$s = (p_1 + p_2)^2 = (p_3 + p_4)^2 \,,$$

$$t = (p_1 - p_3)^2 = (p_2 + p_4)^2 \,,$$

$$u = (p_1 - p_4)^2 = (p_2 + p_3)^2 \,, \tag{2.10}$$

were *s*, *t*, and *u* are constrained by the property:

$$s + t + u = m_1^2 + m_2^2 + m_3^2 + m_4^2 \, . \tag{2.11}$$

The *s* channel gives the squared center of mass energy. In the CLAS system, it closely relates to the resonant states of nucleons generated. These states then rapidly decay. The *t* channel is from the 4-momentum transfer squared and represents the non-resonant scattering of the photon off the nucleon. The *u* channel has no simple physical description. There is no Lorentz frame where it reduces to anything straightforward. However, at times it can be thought of as a scattering-like process similar to the *t* channel, except with the exchange of virtual particles.

From this we can examine channels that contribute the $\gamma n \rightarrow K_S\Lambda$ total cross section, as can be seen in Fig. 2.2. The first Feynman diagram illustrates the excitation of the neutron by the photon and subsequent decay. Both the *u* channel and *t*-channel seen in b and c, respectively, show the scatter of the photon off the neutron. The *u* channel has an exchange of a virtual photon, while the *t*-channel exchanges kaons. The final Feynman diagram shows one of the top competing background channels for the $K_S\Lambda$ total cross section, $\gamma n \rightarrow K_S\Sigma^0$. Though the *s*-channel is predicted to be dominate and is the only process of interested for baryon resonance, all channels need to be considered for measuring the differential and total cross sections.

In section 4.1 the treatment of the competing reactions is discussed. As will be shown, most of the competing channels can be reduced from the $K_S\Lambda$ signal with mass and momentum cuts. However, the $K_S\Sigma^0$ (shown in Fig. 2.2 (d)) overlaps with the missing mass peak corresponding to the $K_S\Lambda$ reaction. Fits to both peaks can be used to extract the yields for either reaction.

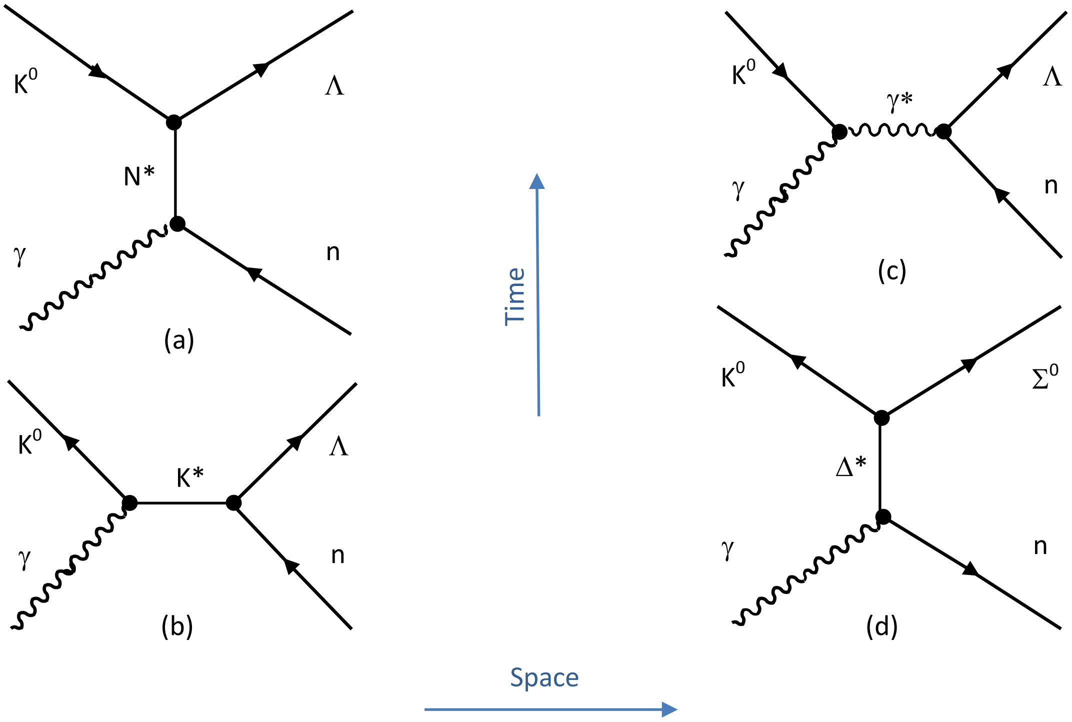

Figure 2.2: The Feynman diagrams for the possible n(γ,K^0)Y reactions found in this analysis where time passes vertically. (a) corresponds to the s channel with the baryon resonance, (b) the scatter u channel with a gamma exchanged, (c) the t channel with an exchange K*, and (d) the main competing channel in this analysis, $\gamma D \rightarrow K^0\Sigma^0(p) \rightarrow K^0\Lambda\gamma(p)$

2.5 Differential Cross Sections

The cross section σ is the measure of a specific event happening with the interaction of particles and is measured in units of cm^2. Some of these possible interactions were discussed in the previous section. These interactions can be represented by a particle's absorption and subsequent decay. Others are described as scattering by the exchange of different force carrying particles or mesons. Therefore, by definition the total cross section is defined as the probability of any interaction happening, properly normalized by the beam flux. For a photon beam this can be written as:

$$\sigma = \frac{Probability\ of\ interaction}{number\ of\ photons\ per\ unit\ Area} = \frac{N_S}{N_i}\frac{A_{target}}{\rho \ell N_A}, \tag{2.12}$$

where N_s is the number of scattered particles and N_i is the number of incident particles for the given interaction area within the target. The area is given by the target density ρ, length ℓ, atomic weight A_{target}, and Avogadro's number.

With an isotropic phi distribution $d\Omega = 2\pi\ d(cos\theta)$, where the 2π comes from the isotropic phi angle. The scattered events were reduced to just the kaon's track by taking the derivative with respect to the K_S's theta (or polar angle). We can therefore write the differential cross section as:

$$\frac{d\sigma}{dcos\theta_{CM}^{K_S}} = \frac{A_{target}}{\rho \ell N_A}\frac{1}{N_i(\sqrt{s})}\frac{d}{d(cos\theta_{CM}^{K_S})}N_S\left(\sqrt{s}, \theta_{CM}^{K_S}\right), \tag{2.13}$$

where the number of scattered events is taken as a function of the center-of-mass event energy $\sqrt{s}$ and the angle $\theta_{CM}^{K^0}$with respect to the kaon angle.

Due to the limitations of measurement, we can approximate the differential cross section by binning by discrete energy $\sqrt{s}$ and angle ranges. Each of these bins has an associated acceptance, $\mathcal{F}\left(\sqrt{s}, \theta_{CM}^{K^0}\right)$. The channels used for the reconstruction limit each measurement. In the case of this study only the decay of the K_S to π^+ and π^- and the Λ to the proton and π^- are used, though other decay modes are possible. Using their associated branching ratios (the ratio of decay rates for each channel, Γ_i/Γ_{tot}) to correct the scattering values, we can write the differential cross section as:

$$\frac{d\sigma}{dcos\theta_{CM}^{K_S}} = \frac{A_{target}}{\rho\ell N_A} \frac{1}{\Delta cos\theta_{CM}^{K_S}} \quad \frac{N_S\left(\sqrt{s},\theta_{CM}^{K_S}\right)}{N_i\left(\sqrt{s}\right)} \frac{N_{corr}}{\mathcal{F}\left(\sqrt{s},\theta_{CM}^{K^0}\right)} \frac{\Gamma_{K_S}}{\Gamma_{K_S\rightarrow\pi^+\pi^-}} \frac{\Gamma_\Lambda}{\Gamma_{\Lambda\rightarrow p\pi^-}}. \tag{2.3}$$

Since the Σ^0 always decays to $\Lambda\gamma$, a close variation to equation 2.3 will be used to model and extract the differential cross section of the $\gamma n \rightarrow K^0\Sigma$ reaction. The branching ratio of the Σ^0 will replace that of Λ.

Chapter 3

Experimental Design and Method

The dataset for this study was collected at the Thomas Jefferson National Accelerator Facility (TJNAF or JLab) in Newport News, Virginia. This is primarily a research center which focuses on investigating the internal structure of the nucleon. The lab has a unique racetrack-type accelerator which provides up to 6 GeV polarized electrons to three different user halls. The analysis for this dissertation was made on the g13a dataset, which was taken within Hall B using the CLAS detector system. The target for these experiments was a deuterium target. This allows the use of neutrons (in addition to the protons) for the study of the interactions of circularly- and linearly-polarized photons with nucleons.

3.1 Continuous Electron Beam Accelerator Facility (CEBAF)

Jefferson Lab's accelerator has a unique design, departing from the more commonly used colliders rings of CERN and Fermilab. It was designed to produce a nearly continuous stream of electrons which can be distributed among three user halls. The accelerator beam line is primarily made up of four regions: two resonant frequency linear accelerators sections and two magnetic recirculation arcs. After the 67 MeV electrons are injected into the beam line, they are accelerated by the first LINAC accelerator for approximately 1400 meters. Magnets then steer the electrons through one of the five recirculation arcs into the next linear accelerator. Each accelerator boosts the energy by 600 MeV for every pass. Finally the electron beam is steered through one of the final four recirculation arcs back to its starting point. On the final

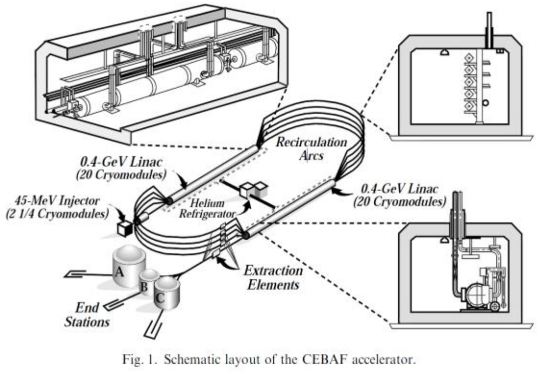

Figure 3.1: Diagram of the Continuous Electron Beam Accelerator Facility (CEBAF)

Figure 3.2: Arial photo of CEBAF- the center grassy mound at the bottom of the picture is Hall B

pass, the beam only travels the first set of recirculation arcs and is delivered to the halls as seen Fig. 3.1.

Electrons are accelerated through this circuit up to five times until it may reach a top energy of 6 GeV. Lower- and higher-energy electrons continue through the loop sharing the same beam lines through the accelerators. However, each discrete energy group is curved through its own recirculation arc, where the higher energy electrons are channeled through the lower loops. During any of the cycles, the electrons can be diverted into one or more of the Halls at the desired current and energy.

Each of the LINAC accelerator consists of 168 superconducting RF Niobium cavities. The cavities are cooled to -271^{o} with liquid Helium. The standing waves in the cavities are kept in phase with the electron bunches. This enables the use of a nearly continuous beam, with a full bunch length of 1 picosecond, separated by 2 ns.

3.2 CEBAF Large Acceptance Spectrometer (CLAS)

Each of the user halls for the Continuous Electron Beam Accelerator Facility (CEBAF) has their own detector configurations depending on the focus of their studies. The research in Hall B is interested in a broad range of experiments that require a full profile of the angular distributions of particle decay. These experiments include comprehensive studies of missing baryon resonances, form factors of the resonances as well as the spin structure of nucleons and nucleon correlations inside nuclei. With this in mind, the CEBAF Large Acceptance Spectrometer (CLAS) in Hall B was designed to have approximately 4π detector acceptance. It was later enhanced to have a highly polarized photon beam[15][16]. Its design can be grouped into two sections- the photon production section and the detector section (see Fig. 3.3).

The photon production section produces polarized photons using variations in the configuration of diamond radiators through rotations in a goniometer. It can make linearly-polarized photons in both the parallel and perpendicular directions. After the photon beam is produced, a magnetic field within the tagger deflects the post bremsstrahlung electrons off the beam axis and measures them to determine the photon bremsstrahlung energies. The photon then passes through the collimator and pair spectrometer before it enters the detector section.

The detector section consists of the target, start counter, drift-chambers, Cerenkov counters, time-of-flight (TOF) paddles, and electromagnetic calorimeter. Once the nucleon is excited within the target, it rapidly decays and the decay products strike and pass through the start counter. The charged daughter particles' paths are curved as they pass through the toroidal magnetic field. The trajectories are recorded as they pass through the drift-chamber contained between the coils. When the particle hits the outside TOF paddles, the time of flight can be calculated with a comparison to the start counter. Further, data are collected from the particles as they interact with Cerenkov counters, and electromagnetic calorimeter.

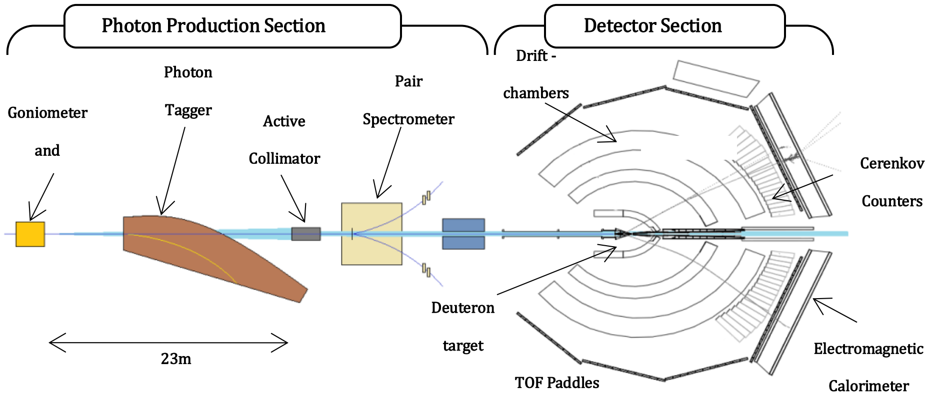

Figure 3.3: An illustration of a simplification of two different sections of the CLAS system, separated into a polarized photon production beamline and the detector section

3.3 Polarized Photon Production

There are two methods of polarization for the photons used in Hall B, circular and linear. When polarized electrons are incident upon an amorphous radiator, bremsstrahlung radiation is produced in the form of *circularly*-polarized photons. If an unpolarized electron beam is incident upon a thin diamond radiator, then *linearly*-polarized photons are produced through coherent bremsstrahlung (CB). Tight collimation will further eliminate unpolarized photons from the coherently-produced photons. The g13a used circularly-polarized photons and g13b used linearly polarized photons.

Photons (bremsstrahlung radiation) are produced when electrons are decelerated by the positive charge of a nucleus it is passing. Only an insignificant proportion of energy is transferred to the nucleon, making the determination of photon energy simple. With known incident electron energy, E_o, it is only necessary to measure the remaining electron energy after the scattering event, $E_{e,}$ to determine the photon energy, E_γ.

$$E_\gamma = E_e - E_{e'} \tag{3.1}$$

Each recorded event can be then associated with up to 63 photons recorded by the electron energy in the tagger databanks.

3.3.1 Circular Polarization

Circularly polarized photons are produced when the longitudinally polarized electron beam interacts with thin metal radiator foils. The foils are held in a long tray assembly, ordered by material type and thickness. The tray can be shifted to adjust the radiator foil used for photon production. Gold is the most common metal used, because it can be made very thin for minimizing multiple scattering. The amorphous structure of the gold allows the polarization of the electron to be translated as it produces bremsstrahlung radiation. A more detailed description of g13 specific settings is given in section 3.5.

3.3.2 Diamond Radiators and Goniometer

A linearly-polarized photon beam can be produced from an unpolarized electron beam incident upon a diamond radiator. The lattice structure of the diamond allows for the electrons to scatter off a periodic array of aligned scattering centers, created a preferred direction of bremsstrahlung. A goniometer controls the alignment of the diamond (see Fig. 3.4)[17]. A more detailed description of g13 specific settings is given in section 3.5.

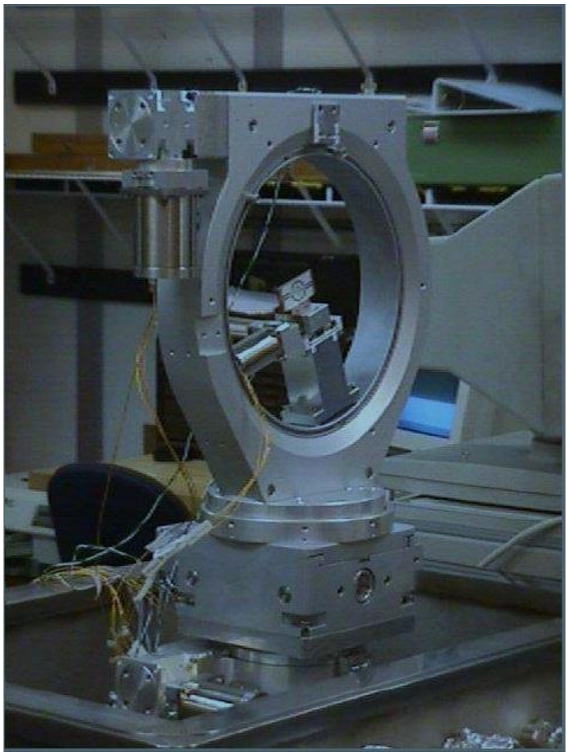

Figure 3.4: Image of the Goniometer use to align the diamond radiator

3.3.3 Photon Tagger

As previously discussed, in determining the energy of the photon, it is sufficient to take the difference between the measured electron energy and the known incident energy. With this in mind, the photon tagger was designed with dual purpose; it removes the electrons from the beam axis of incidence and measures their energy. The concept of photon tagging is well understood[17]. The JLab photon tagger was uniquely engineered to operate within the GeV range and has a tagging range between 20 to 95% of the incident energy[18].

Figures 3.5 and 3.6 illustrate the internal structure and function of the photon tagger. After the electron beam strikes the radiator, the photons and electrons enter the magnetic field of the two poles within the tagger. Only the charged electrons are affected by the field as photons pass through unscattered. The post-bremsstrahlung electrons are deflected into the hodoscope plane (where the energy and timing measurements are made), while the full energy electrons are guided into the beam dump.

The hodoscope has the key role in the determination of the photon energy being produced. The system measures the energy of the deflected electron, which is in turn used for the calculation of the photon energy. It must be able to accurately measure both the electron energy and the time of the event. To gather reliable electron energy resolution, it was necessary to use many small scintillators across the focal plane. Due to the large size of the focal plane (9 meters), the energy plane is made up of 384 overlapping E-counters. However for reliable timing, the scintillators must be thicker to allow for sufficient light for the output pulse.

The timing plane is made up of 61 T-counters. The scintillators detectors are laid out in a venetian-blind-style configuration; that is, within each plane the detectors have a 10% overlap between them. This produces 121 timing bins for the electrons/photons. All of the detectors within the two separate focal planes are aligned so that their active region is facing in the direction of the incident electrons. This significantly reduces the number of events from scattered electrons. The background is further cut down with the use of geometric constraints derived from the events between the two different detector planes.

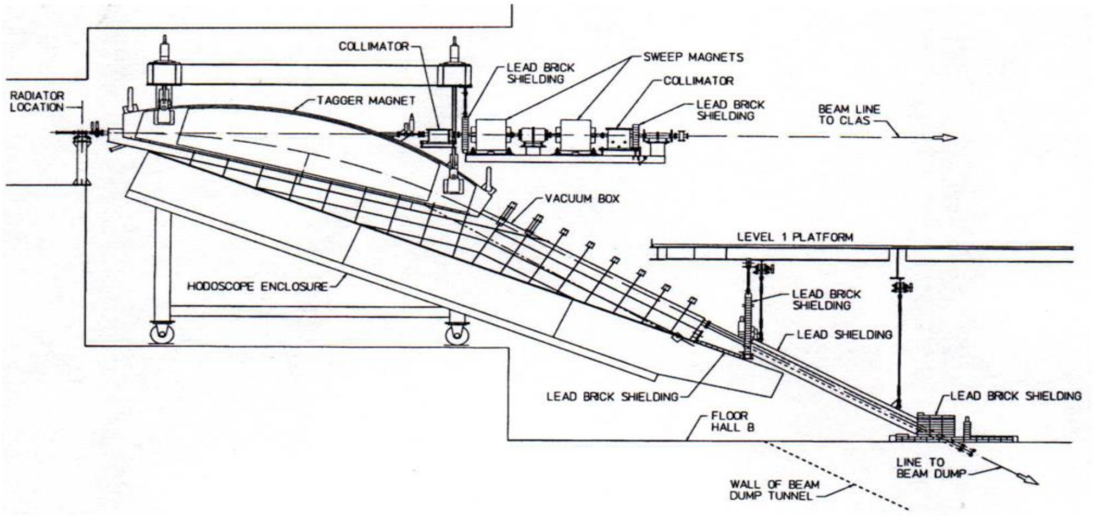

Figure 3.5: Design of the photon tagger[18]. The electron and photon beams enter from the left side, where a magnetic field bends the electrons down into the counters, and the photon beam continues along the beam line

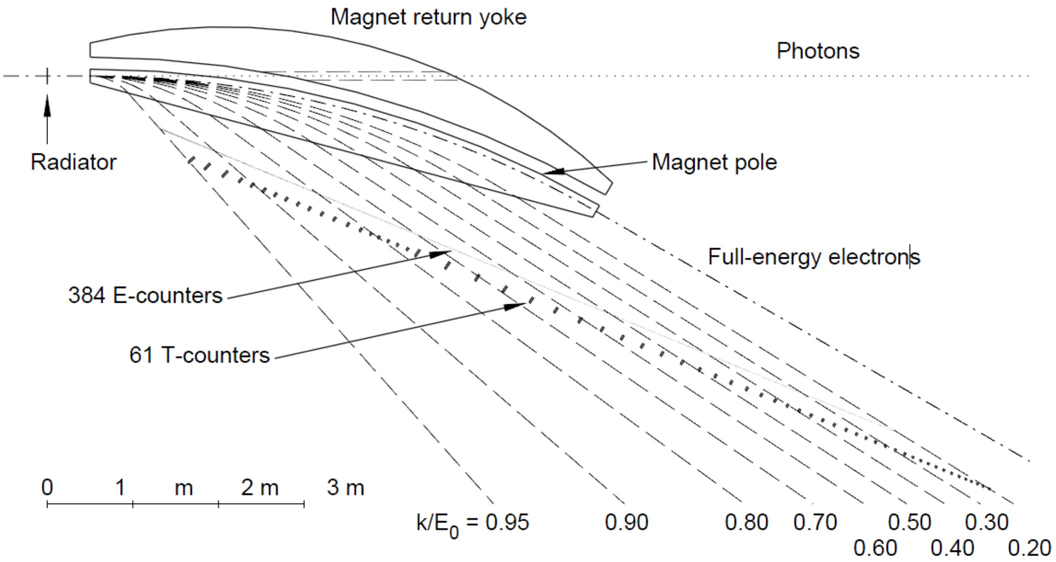

Figure 3.6: Illustration of how the elections are bent into different counters depending on their energy[18]. There are two rows of counters: one row for determining the energy of the electrons, and a second row for the time the electron arrives.

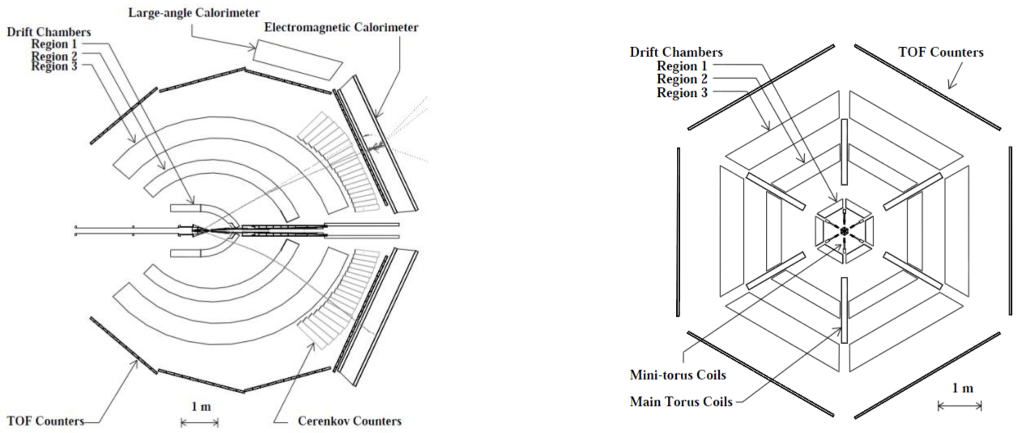

Figure 3.7: Illustration of the CEBAF large acceptance spectrometer (CLAS) from the side and front

3.4 CLAS Detector Assembly

The CLAS detector assembly is composed of multiple layers of detection systems, with six toroidal magnets segmenting the body into six separate sectors[18]. The large toroidal magnets bend the trajectories of the charged decay particles so that it is possible to determine their momentum. The outer detectors enable further classification of the particle detected.

3.4.1 Target

A liquid deuterium target was used for in the g13 experiment. It was contained within a 40 cm cylindrical cell, see Fig. 3.8. The cell was made from Kapton because it has high structural and thermal stability while having low impedance to particles passing through it. Kapton is reasonably resistant to radiation damage. This allows the experiment to yield a high rate of events with an adequate rate of photons in the tagger. To maximize acceptance, the deuterium target was positioned 20 cm upstream from the center of CLAS. The liquid-deuterium in the target had a density of approximately 0.1625 g/cm^3 [19].

Figure 3.8: Kapton container for the liquid deuterium target[21]

3.4.2 Start Counter

The start counter surrounds the deuterium target chamber and is used to measure the start time of the decay particles flight through the following drift chambers. It was built to accommodate the full acceptance design of the CLAS detector and the high intensity photon runs[20]. The body has six sectors; each composed of four EJ-200 scintillators paddles with acrylic light guides. The paddle for each scintillator has a “leg” length of 502 mm and a “nose” region of 93 mm. They were 2.15 mm thick and 29 mm wide. The start counter can contain a target up to 40 cm long and spans the entire azimuth. The timing resolution of 260 ps on the start counter is sufficiently accurate to synchronize information with the tagger.

For calibration, the time recorded is compared with the time recorded by the tagger upstream of the target and with the RF time from the accelerator. The time-delay correction for each paddle is made from several different factors. The time of event is given by:

$$t = c_0 + c_1 T + t_w - t_{pos},$$

where t_w is the time-walk parameter, t_{pos}, is the correction for the time it takes the pulse to hit the photomultiplier from this incident point along the paddle, and c_o and c_1 are fitting parameters. The time-walk parameter corrections for the variation of time in leading-edge discriminators due to differing pulse heights.

The start time of the particle event in is calculated by taking the difference of the times from the two beam bunches in the accelerator and the time the particle is first detected by the start counter. After the event start time is discovered, the photon can be matched to the detected event by taking the difference of the time of the photons measured in the tagger and the particle times measured in CLAS.

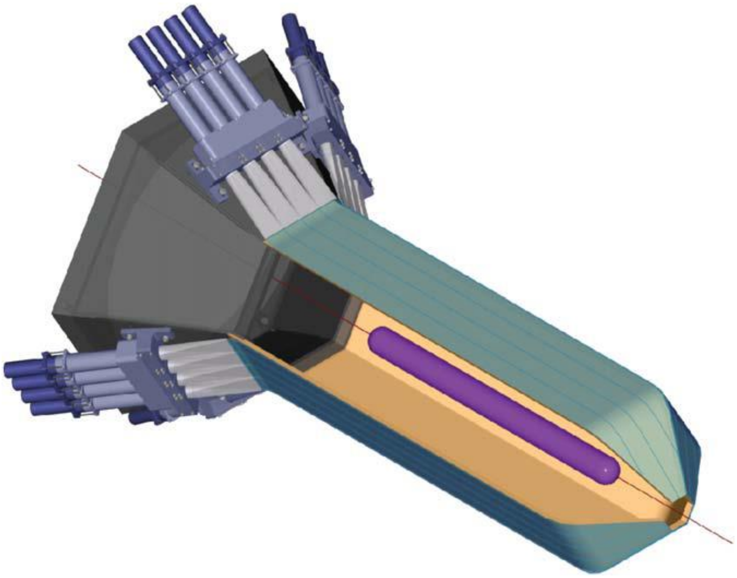

Figure 3.9: Design of the start counter used in the g13 runs, 3-D rendering of detector design, which illustrates the 6 separate sectors of the CLAS design

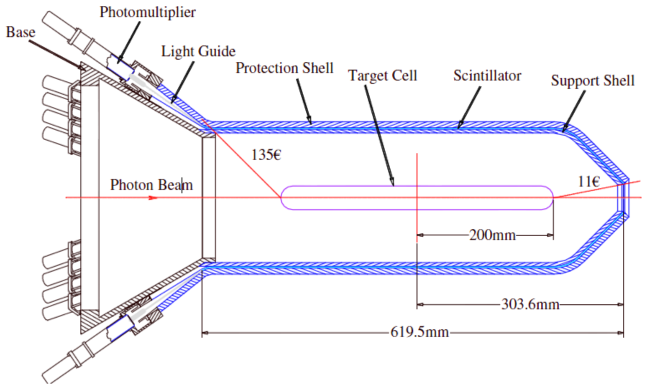

Figure 3.10: the start counter used in the g13 runs, cross-sectional view of the start counter[22].

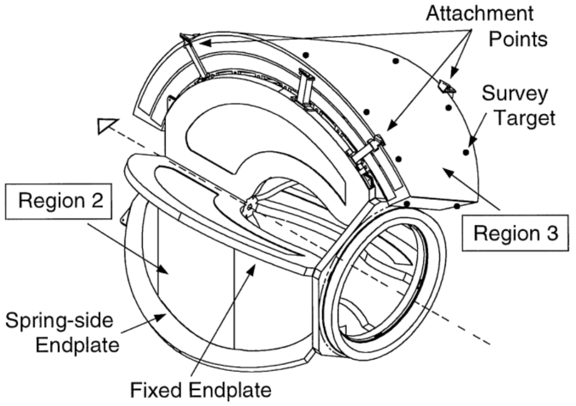

Figure 3.12: Diagram of the assembly of the drift chambers on the torus cryostat[18],

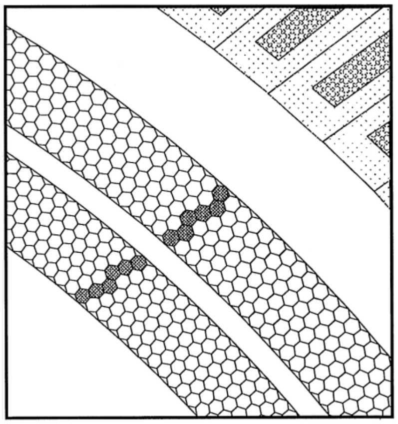

Figure 3.11: Illustration of a particle trajectory through a segment of the drift chamber. Each hexagon has field wires at its vertices and the sense wire at its center[18].

3.4.3 Drift Chamber

The drift chamber region was designed to track charge particle trajectories as they pass through the magnetic field produced by the toroidal magnetic coils[18]. The layout of the chambers allow for a large acceptance of decay angles. The detector has a polar angle range from 8° to 142°, and covers nearly 80% of the azimuth angles. To reduce the loss of acceptance, all the non-active components were built to reside within the shadow of the magnetic coils. The magnet bends charged particles away from or towards the beam line, but has little effect upon the azimuthal angle.

The drift chamber system is composed of six sectors separated by superconducting toroidal magnetic coils[18]. There are three layers of drift chambers within each sector, giving a total of 18 drift chambers. The interior of the drift chambers are partitioned into thousands of thin and long hexagonal drift cells. The field wires are at the vertices of each hexagonal cell, with a sense wire at its center. The sense wires are made of tungsten plated with gold, with a diameter of 20.1 μm. This choice allows for the smallest possible diameter to maintain the required tension. The field wires are made of gold-plated aluminum (5056 alloy) and have a diameter of 140 μm.

Each of the drift chambers are filled with a 9:1 mixture of argon and carbon dioxide. Charged particles ionize the gas molecules as they traverse the chamber. The freed electrons are then collected by the sense wires. The time it takes for the electrons to arrive on the sense wire is measured to determine the drift distance of the particle to the sense wire. The hexagon design of the cells allows for drift time to drift distance relation to be reasonably independent of angle of entry to the cell. This process is applied to all three regions to determine the particle's trajectory.

Independently and together the three separate layers of the drift chambers can yield significant information about a charged particles trajectory. The central (second) layer experiences the greatest strength of the magnetic field. At this point the particle momentum could be evaluated at the point of maximal curvature. The inner and outer layers experience the lowest magnetic field effects and can be used to determine the initial and final direction of a charged particles path.

3.4.4 Time of Flight Paddles

As the name implies, the time-of-flight system's primary purpose is the measurement of the particles flight time. However, in some situations, the system is also used to for energy-loss measurements and velocity determination[18]. It can also be used for the CLAS Level 1 trigger. The multiple functionalities of the TOF system impose a number of requirements on this system design. It must have excellent timing resolution for particle identification, as well as strong segmentation for variable triggering and pre-scaling. The system must also be capable of operation in a high-rate environment.

To meet these requirements, several factors in the TOF system design were considered. The size of the paddles had to be configured for optimization of the time resolution and needed to cover most of the angular distribution within each sector. For the forward angles, the scintillators were made 15 cm wide with 2 inch PMTs, due to space constraints. At the large angles the scintillators were 22 cm wide with 3 inch PMTs. The PMTs had to be properly shielded from the magnetic fields of the toroidal magnets. Since the regions behind the coils are inactive, the PMTs were located there with extra shielding. The light from adjacent TOF paddles must be summed for separation of intersecting events. The LeCroy 4413 leading-edge discriminator was chosen instead of the constant-fraction discriminators. Despite the constant-fraction discriminator's, better timing, the offline time-walk corrections from the leading-edge discriminators proved superior. The system must be able to record rates up to 1500 Hz to achieve time resolutions between 100 and 200 ps. The LeCroy 1872A Mod 100 time-to-digital converter (TDC) was selected for this requirement.

The ionized radiation from a charged particle passing through a scintillator will excite the material, which then radiates the photons. A portion of radiated photons are internally reflected down the length of the scintillator's light guides, then into the PMTs at each end. The arrangement of these scintillators and PMTs provide a timing resolution between 150 ps and 250 ps. The resolution varies based on the length of the scintillators. The neutral particle's hadronic interactions produce significantly less radiation which makes them difficult to detect with the TOF paddle.

3.4.5 Electromagnetic Calorimeter

The forward electromagnetic calorimeter (EC) has three primary purposes[21]. It can be used to distinguish the electron events from the pion. Many of the pion events can be eliminated if their momentum is less than 3 GeV/c. For greater momentum, the energy of the particle deposited must be compared to its trajectories within the drift chambers. Secondly, the EC can be used to separate the neutron events and photon based on timing. The photon information can be used for the reconstruction of the π^0 and η decays, while the neutron is key information for a number of experiments. With the use of the TOF system, it is possible to distinguish between the neutrons and photons. For this research study, the detection of neutrons is the primary interest.

There are six EC modules that correspond with the six sectors of the CLAS detector. The 39-layer lead-scintillator stack has a triangular shape, with a 'projective' geometry (that is, the area of each subsequent layer is increased). Each scintillator layer is 10 mm thick and is made up of 36 strips parallel to one side of the triangle. The lead strip has a thickness of 2.2 mm. As can be seen in Fig. 3.16, the orientations of the strips are rotated by 120° for each layer. This gives three different orientation planes, which are labeled *U*, *V* and *W*. A fiber optic light readout is used to transfer the scintillators light on to the PMTs at the base of the stack.

After a particle enters the EC, the high *Z* of the lead offers a high probability for the charged particle to interact electromagnetically. The position of the hit can then be measured within each layer by the comparison of their three strips (U, V, and W). This can be done straightforwardly by observing overlap of the hit channels of each strip. It can also be done for each strip independently by finding the hit distance from the readout edge. Software is then used to reconstruct the energy of each particle event by summing up the energies of each layer. The events are then sorted by their respective energies.

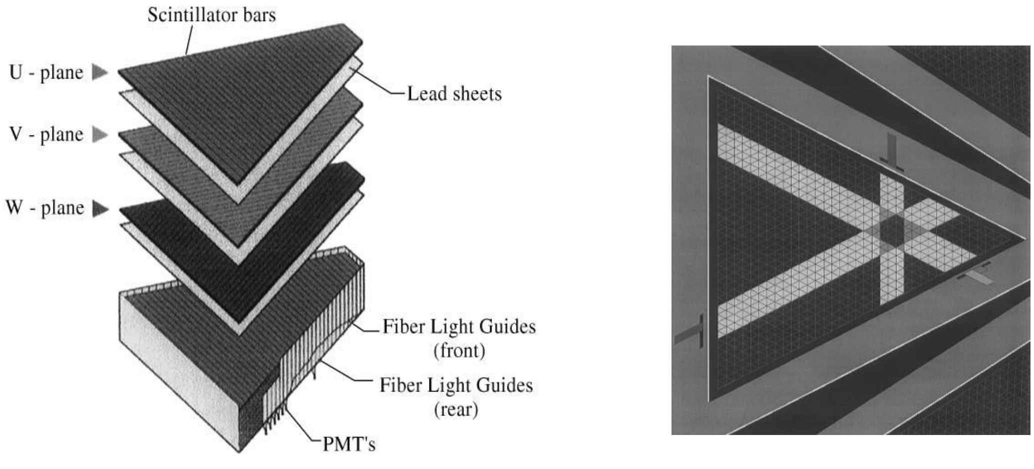

(a) (b)

Figure 3.13: Cross-sectional view of one of the electromagnetic calorimeter modules[18], (a) The three strips of a single layer layer and (b) the reconstruction of position using the three layers with their varying alignments

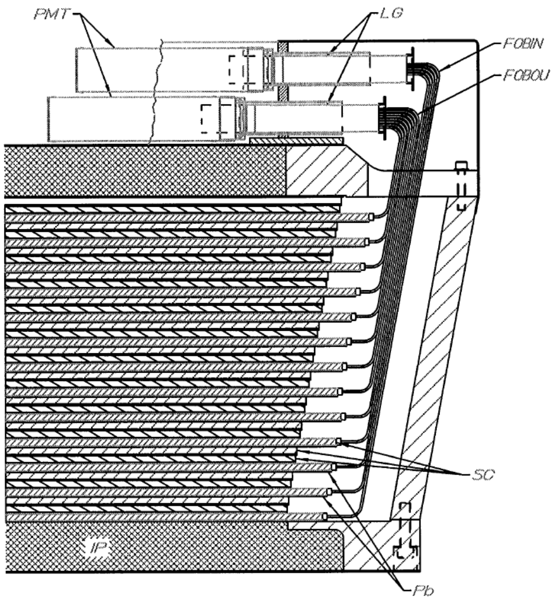

Figure 3.14: Sketch of the EC light readout system, with the light guide (LG), scintillators (SC), lead sheets (Pb), inner plate (IP), fiber optic bundle inner (FOBIN) and fiber optic bundle outer (FOBOU)[18]

3.5 g13 Experiment Overview

The g13 experiment was split into two parts called g13a and g13b. The g13a portion used a circularly polarized photon beam, while the g13b portion used a linearly polarized photon beam. A 40-cm unpolarized liquid-deuterium target was used for both portions of the experiment, and a -1500 A current was used in the torus magnet to bend negatively charged particles away from the beam line. This maximizes the acceptance of low-momentum π^- resulting from the decays of hyperons. Of all the data collected in the g13 experiment, only data from the g13a portion of the experiment were used for this analysis[21].

3.5.1 Circularly Polarized Photons

The g13a experiment ran at two electron energy beam levels (1.99 and 2.655 GeV) for approximately an equal amount of time. The majority of the g13a experiment started in late October of 2006 and lasted through December of the same year. An additional week of runs occurred in March of 2007. CEBAF supplied a longitudinally-polarized electron beam at currents between 33 and 45 nA, which resulted in narrow beam brunches of between 412 and 562 electrons every 2 ns. A two-section tagger was used to select events to record. Approximately 20 billion events were recorded in the two-month experiment. The g13a provides the ideal data for the cross section measurements are restricted to that data.

Figure 3.18 shows the incident of the longitudinally-polarized electron beam on a 10^{-4} radiation-length gold-foil radiator. It produced a circularly polarized photon beam[22]. The photon energy magnitude directly affected the amount of polarization transferred from the photon beam[23]. The 1.99 GeV and 2.655 GeV beam energies were chosen for this reason to maximize the photon beam's polarization in these N* production regions. The electron beam polarization was approximately 84% for the

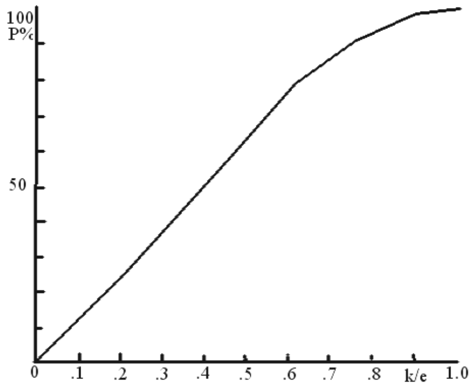

Figure 3.18: Polarization transfer from longitudinally polarized electrons to circularly polarized photons in bremsstrahlung radiation[24].

1.990 GeV data and 78% for the 2.655 GeV data. A 6.4 mm tungsten collimator allowed approximately 90% of the photon beam to pass on to the target. This resulted in a photon flux rate at the target on the order of 10^7 Hz.

3.5.2 Linearly Polarized Photons

The g13b experiment started mid-March 2007 and continued through to June of the same year. These runs used eight different electron beams energies between 3.3 GeV and 5.16 GeV. The beam currents ranged between 5 to 12 nA. The electrons arrived in bunches ranging from 62 to 150 electrons every 2 ns. Approximately 30 billion event triggers were recorded with a single sector event trigger.

This diamond radiator produced a linearly polarized photon with approximately 200 MeV coherent peaks between 1.1 GeV and 2.3 GeV[18]. As seen in Fig. 3.19, the radiated photon energy distribution forms a large coherent peak in the results. Smaller peaks at higher photon energies can also be observed in the results. These smaller peaks are caused by scattering on higher-order planes[25].

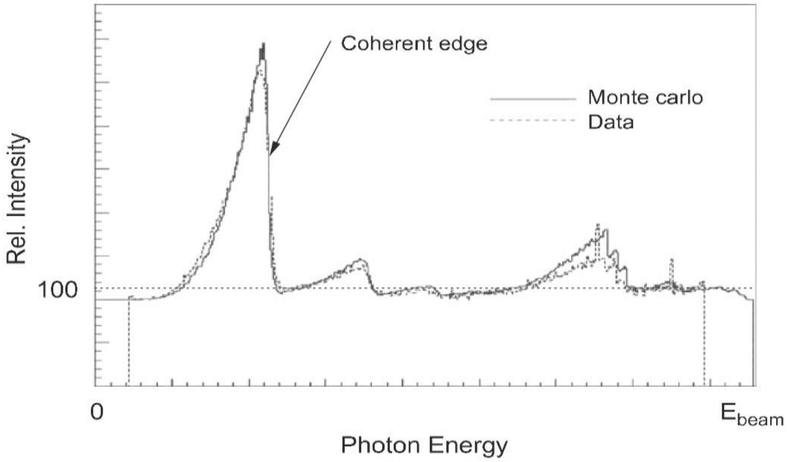

Figure 3.19: Collected data with the Monte-Carlo simulated photon energy distributions produced from an electron beam incident on a diamond radiator[26].

3.5.3 Event Triggering

The data acquisition (DAQ) system is used for event triggering in the CLAS detector. This system receives singles from the other detector subsystems to find and select desired events for recording. While the DAQ system is recording events, it cannot accept signals from other subsystems. Signals sent during this period are lost. This period is called the dead time. The g13 recorded events at a rate of approximately 10 kHz, with a dead time of approximately 15%. Approximately 20 billion events were recorded for g13a and 30 billion events were recorded for g13b[25].

There are two levels to the trigger system[25], for two different degrees of discrimination from background events. The level 1 trigger was designed with no dead time. This allows it to quickly process signals from the other components of the detector system. All the prompt PMT signals are processed within 90 ns, which are then sent to a trigger supervisor (TS) module. The level 2 trigger was set up to look for events that do not match trajectories from within the drift chamber (such as cosmic-ray events). The dual g13 experiments both exclusively used the level 1 trigger. The g13a used at least two of the six CLAS sectors to record events with coincidence between the start counter (ST) and TOF scintillators. The g13b required only one of the sectors to record a coincidence between the ST and TOF. By using the level 1 trigger and recording multiple sectors, the background accidental detector hits were minimized, and the DAQ rate for charged-particle physics events was maximized.

A 28 ns pulse signal is sent to the Level 1 trigger in a sector when a signal is detected in a scintillator paddle of the ST that is greater than the pre-trigger voltage threshold. A 120 ns pulse signal is sent for the TOF scintillators. The DAQ receives events when the strobe in the level 1 trigger found a coincidence between the ST and

TOF that satisfies the triggering conditions. The sectors that were in coincidence are then saved by a 20 ns latch. This includes those that had an ST and TOF coincidence 15 ns later in the next sampling. The trigger losses due to missed coincidences were negligible due to the lengths of these pulse signals.

Chapter 4

Extraction of the Experimental Yield

The g13a dataset was used to extract the $\gamma n \rightarrow K_S\Lambda$ cross section. This dataset was collected with a circularly polarized photon beam incident upon an unpolarized deuterium target. Before analysis, the data was “cooked”; meaning the data from all the sub-detector systems are matched together into new database files. The database sorts the information by “events” into multiple banks, using correction constants from a calibration database. These events correspond to multiple detected particles that can be associated with a single photon event within the target. The cooking is an iterative process where the constants in the calibration database are modified until the timing between the sub-systems is consistent and are working in concert. Once the cooked data has been properly calibrated, the analysis can begin.

The analysis can be described in three primary stages: yield extraction, flux determination, and acceptance studies. The *yield extraction* is determined from the selection of events from the data and the reconstruction of the representative $K_S\Lambda$ missing mass. The photon *flux determination* is used to determine how many photons were needed to produce the measured $K_S\Lambda$ events. Finally, the *acceptance* is determined by performing a Monte Carlo simulation. All three stages require special corrections for events and the tracks within them, based on the CLAS systems limitations. These corrections were discussed at the end of each section. This chapter will focus on the first stage, *yield extraction*. Specifically, the extraction of the $\gamma n \rightarrow K_S\Lambda$ reaction yields. At the end this chapter we will show the photon flux determination. The next chapter addresses the systematics studies to include the cuts and corrections made. Chapter 6 is focused on the detector acceptance.

4.1 Event Reconstruction

For both the $\gamma n \rightarrow K_S\Lambda$ and $\gamma n \rightarrow K_S\Sigma^0$ reactions the intermediate kaon and hyperons (Λ and Σ^0) being neutral and short lived makes their direct detection essentially impossible. Therefore they are reconstructed through their primary decays: $K_S \rightarrow \pi^+\pi^-$, $\Lambda \rightarrow p\pi^-$ and $\Sigma^0 \rightarrow \Lambda\gamma \rightarrow p\pi^-(\gamma)$. Having no particles directly measured from the production vertex requires a more vigorous analysis, particularly with vertex reconstruction. The pre-skimmed files require an event to have at least two positive and two negative tracks for events consistent with $\pi^+\pi^-\pi^-p$.

4.1.1 Particle Sorting and Selection

Since the final-state particles of this analysis are all pions and protons, the identification of the measured particles is relatively straightforward. Because of this ease of identification, a matrix sorting approach was used during the initial screening of events. The particle's charge and mass were used for loose cuts for the initial particle identification. Each particle track within an event was then sorted into a matrix. The rows are defined by the possible detected particles, while the columns correspond to the ordered instances for each particle. Each column entry is the track number stored in the banks. The last column with an entry indicates how many particles were detected of a specific type (e.g. a row with its last entry in the 3rd column would indicate three particles of that type were found). Table 4.1.1 illustrates a case were the event has the follow ordered tracks $\pi^+, p, \pi^-, \pi^-,$ and p. To improve the initial particle identification, timing and track velocity cuts were applied.

Table 4.1: Particle identification (PID) matrix for an event with tracks in the following order: $\pi^+, \mathrm{p}, \pi^-, \pi^-$, and p

	1st instance	2nd instance	3rd instance	4th instance
proton	2	5	0	0
Pi plus	1	0	0	0
Pi minus	3	4	0	0

Timing cuts were made to ensure that all the tracks being examined came from the same photon event. The time, t_{vertex}, for each track was determined by taking the difference of time, t_{tof}, measured by the time-of-flight (tof) paddles and the calculated time of flight:

$$t_{\text{vertex}} = t_{\text{tof}} - \frac{\ell}{\beta c} = t_{\text{tof}} - \frac{\ell\sqrt{m^2c^4+p^2c^2}}{pc^2}, \tag{4.1}$$

where ℓ is the decay length of the track, m is the mass of the particle, p is the momentum measured by the drift chambers, and β is the velocity of the particle ($\beta = v/c$). Since there are at least four tracks in final state, instead of taking a time difference for each pairing of tracks, the average was taken for all tracks. Tracks that were more than 6 nanoseconds away from the median were not put into the matrix.

Further evaluation of a particle's identity can be made by looking at its characteristic $\Delta\beta$ vs. momentum distribution. With $\Delta\beta$ is defined as:

$$\Delta\beta = \beta_{\text{calculated}} - \beta_{\text{measured}} = \frac{pc}{\sqrt{m^2c^4+p^2c^2}} - \frac{\ell}{c(t_{\text{tof}}-t_{\text{start}})}. \tag{4.2}$$

the particle's speed (β) and momentum are functions of the particles mass. This $\Delta\beta$ - p correlation allows for selective cuts on the distributions for each track. Since a pre-selection has already been made based on charge and mass, the $\Delta\beta$ vs. p plots were made for each potential particle type. Figure 4.1 shows the distribution of possible π^- tracks. The left plot is the β vs. p while the right is the $\Delta\beta$ vs. p. To limit how many misidentified kaons are in these distributions, a cut was made to maximum and minimum value functions. The functions are defined by taking the 3σ from a fit to projections with momentum binning.

Once the matrix for an event has been made, the surviving tracks will used to determine if this event has the minimum particle requirements. It was important to measure the missing mass of the spectator proton, so when selecting the events it is necessary require that all the final-state particles will have been detected. Initially the skims were designed to take exactly two π^-s, one π^+ and one proton. With simulated data, this does not count any lost events since the simulation does not produce all the background channels and phase space. However, the empirical data do have a

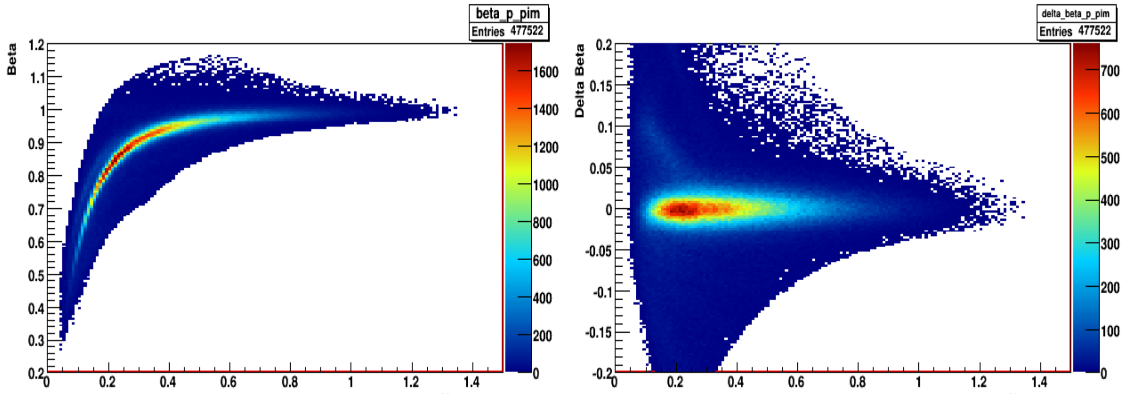

(a) (b)

Figure 4.1: (a) Beta vs. momentum plots for the measured π^- and (b) delta beta vs. momentum plots for the measured π^-. Both follow a loose mass cut and $|\Delta\beta| < 0.2$ cut.

significant number of events with more than one proton or π^+. To regain some lost events, the particle identification (PID) was modified to accept events with two protons and two π^+s. This accepts events that have an extra proton and/or pion mismatched from another event. Both protons were checked to see if their tracks reconstruct to Λ when matched with either of the π^- tracks. If both did or did not, the event is rejected; otherwise the single acceptable proton is passed on. A similar method is applied with events having the two π^+s to see if either could reconstruct a K_S. Roughly 2% of events were recovered when two protons were present and 1% with two π^+s.

4.1.2 Reconstruction of the Intermediate Particles

Once the candidate events with all the required particles are identified, their tracks are paired to reconstruct the possible K_S and Λ particles. The K_S will decay 69% of the time into a $\pi^+\pi^-$ pair, while the Λ has a 64% branching ratio to the $p\pi^-$ channel. It cannot be certain which of the two π^-s belong to the proton or π^+, so both combinations are introduced into the data. Mass and momentum cuts will remove most of the combinatorial background as discussed above. Figure 4.2 shows the reconstructed masses of the proton with the π^- vs. the masses of the π^+ and π^- for each event. Distributions can be seen along the *x*- and *y*-axis corresponding to the masses of the Lambda and kaon. The peak at the crossing of the two mass distributions indicates the reactions that produce both the Lambda and kaon together.

From Fig. 4.3 we can see the effects of the cuts on the mass to reduce background. The leftmost column shows the full invariant mass distributions, and the middle column zooms in on the two visible peaks. Looking at the previous histogram, we can see the trailing distributions outside the peak, which correspond to events that

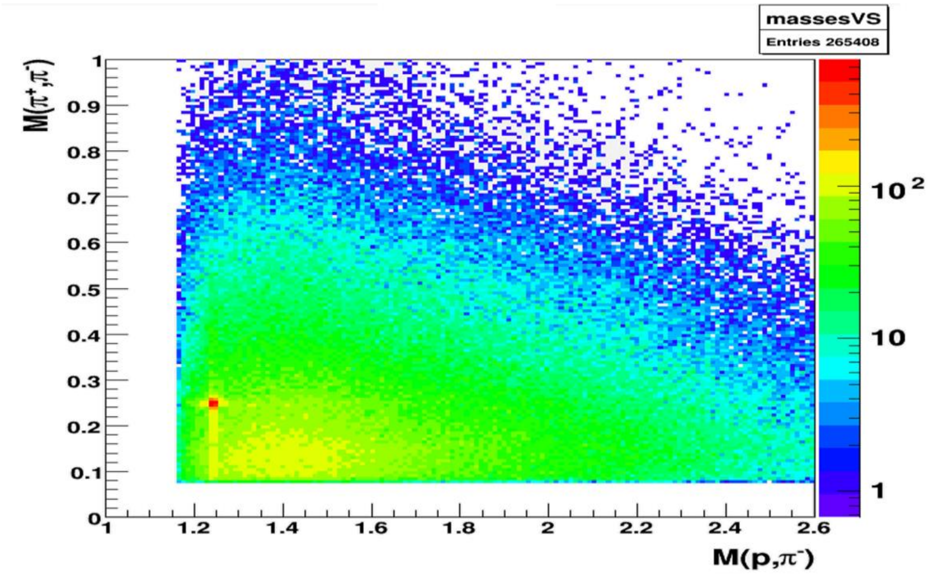

Figure 4.2: Plot of the invariant mass of the Lambda particle, M(p,π⁻) vs the invariant mass of the kaon, M(π⁺,π⁻) in GeV. The peak indicates the events were both a lambda and a kaon were reconstructed.

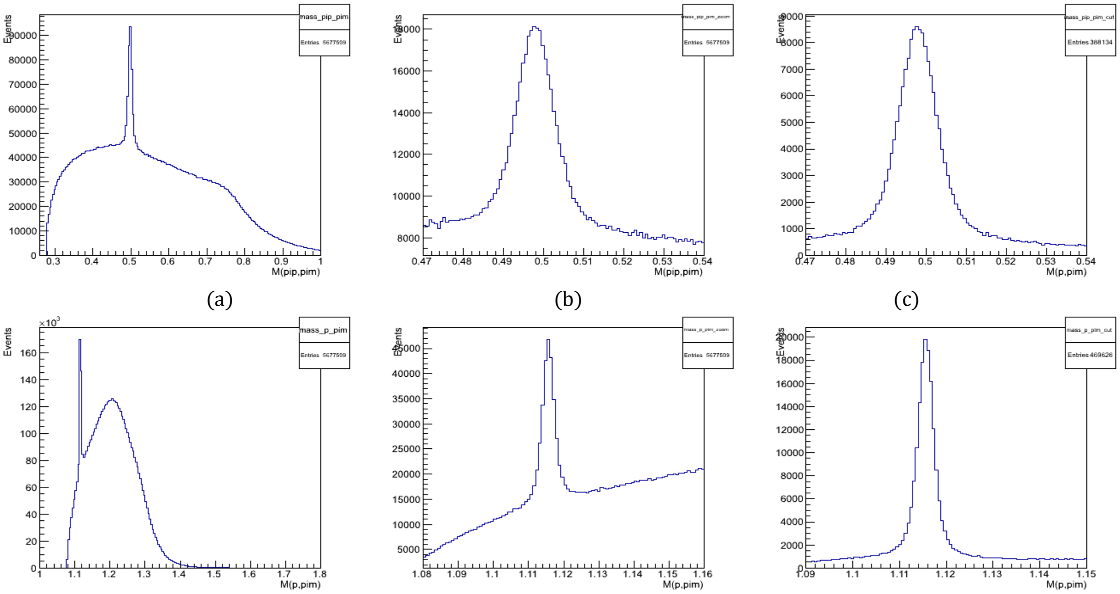

(a) (b) (c)

(d) (e) (f)

Figure 4.3: Mass of the K_S and Λ particles. (a) Mass distribution of the π⁺ and π⁻ combinations, (b) zoomed in view of the hadron mass peaks, (c) background reduced by placing the cut $1.108 < M(p, \pi^-) < 1.122$ GeV for the π⁺ and π⁻ combinations, (d) mass distribution of the proton and π⁻ combinations, (e) zoomed in view of the proton and π⁻ combinations, (f) background reduced by using the cut $0.485 < M(\pi^+, \pi^-) < 0.51$ GeV for the proton and π⁻ combinations

contain one of the required reconstructed particles, but not the other. By cutting on 3σ of the peak for the K_S mass, the unwanted $p\pi^+$ combinations outside of the peak were removed. Similar cuts were made with the Λ mass for the K_S. The background was reduced further by adjustment of all the preceding cuts. The rightmost column in Fig. 4.3 shows the K_S and Λ mass peaks after the cuts were made.

4.1.3 Combinatorial and Phase Space Backgrounds

Up to this point all of the events are effectively being double counted because the primary decay particles (K_S and Λ) both have a π^- in their final state. In the process of event selection, 3σ cuts were placed on the invariant mass distributions for the kaon and Lambda. Events where both combinations of the proton and π^+ with the negative pions surviving contribute to the *combinatorial background*. However, this background was shown to be less than 0.1% of the peak events after the invariant mass cuts. As can be seen in Fig. 4.4, the combinatorial background is significantly smaller than the phase space background. From this it was determined that contributions from events in the combinatorial background can be ignored.

The *phase space background* represents events with the final-state particles $p\pi^-\pi^-\pi^+$, but do not belong to the resonance. These events would mostly be reactions with no intermediate kaons or hyperons. This flat region could also include events with misidentified positive kaons. The ratio of the resonant to non-resonant events (or the phase space ratio) was determined using a double Gaussian fit to the resonant peak and a linear fit to the non-resonant (see Fig. 4.5). A Monte Carlo simulation was used to determine the number of real $K_S\Lambda$ events that end up in the non-resonant region (see

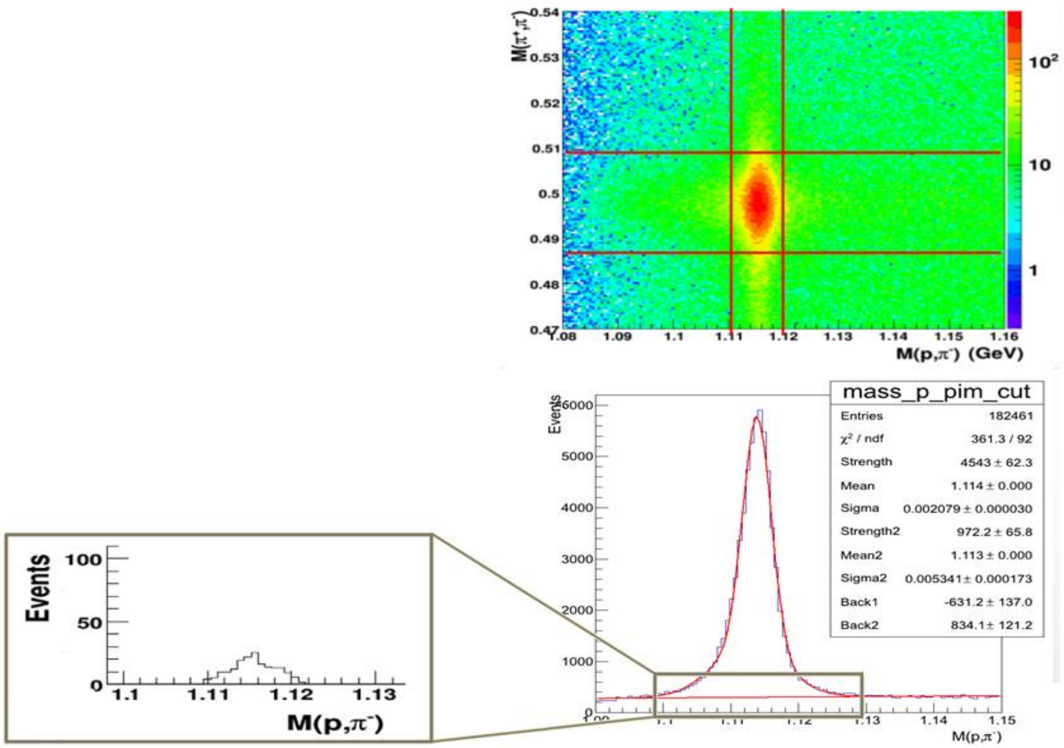

Figure 4.4: The invariant mass cuts on both the kaon and Lambda mass peaks almost completely remove the events where both combinations of $\pi^-\pi^+$ pairing survive. The top figure shows the invariant mass of $p\pi^-$ verses the invariant mass of the $\pi^-\pi^+$. For the invariant mass of the K_S, three-sigma cuts were placed on the Λ peak. The same cuts were made for the K invariant mass.

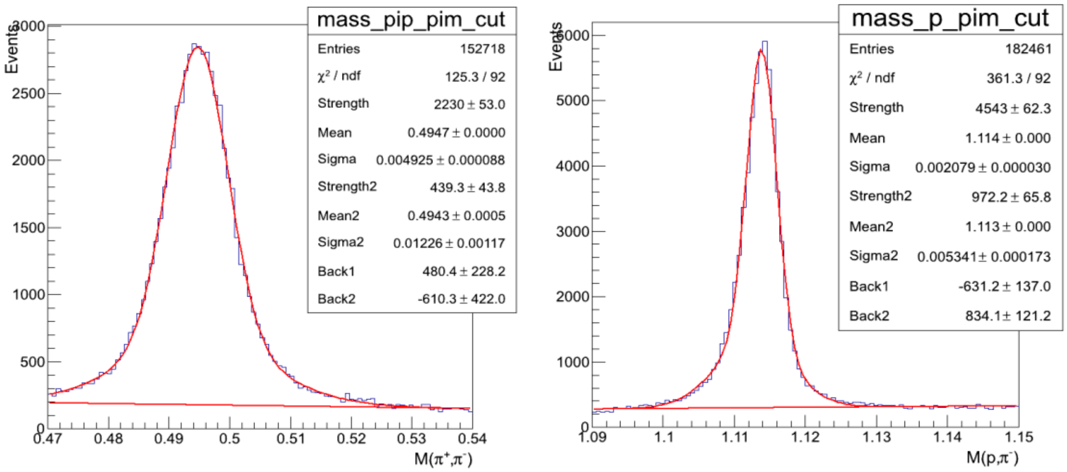

.

Figure 4.5: The fits to the kaon and Lambda peaks. The fits were used to determine the ratio of the resonant region to the non-resonant background.

chapter 6). This fraction was then used to correct phase space ratio. The phase space ratio is then used to correct the total yields.

4.1.4 Vertex Reconstruction

Two key steps are needed before we can build a reliable missing mass for the $\gamma n \rightarrow K_S\Lambda$ reaction. The energy of the photon must be determined so the total energy of the reaction can be used. However, each event on average has 6 different possible originating photons. The photons are stored in the tagger bank based on their vertex time, which is determined by the photon's separation from the center of the 40-cm target. Therefore to choose the correct photon (along with its time), we must first know where the production vertex is.

As mentioned in the first chapter, the vertex reconstruction is somewhat more complicated in this analysis because none of the original decay particles were measured directly. The vertex positions and times (with their associated photons) are stored for each particle independently. This can introduce a problem as can be seen in Fig. 4.6. The decay of the kaon and the Lambda mask their original trajectory. This can lead to the occasional disagreement between the times recorded for each of the detected particles on which photon produced the reaction. The vertex position is also directly related to decay length of each decay particle. The decay length can be used to determine the lifetime of the track. Therefore a check of the lifetime could be used to verify the vertex reconstruction and the particle identification.

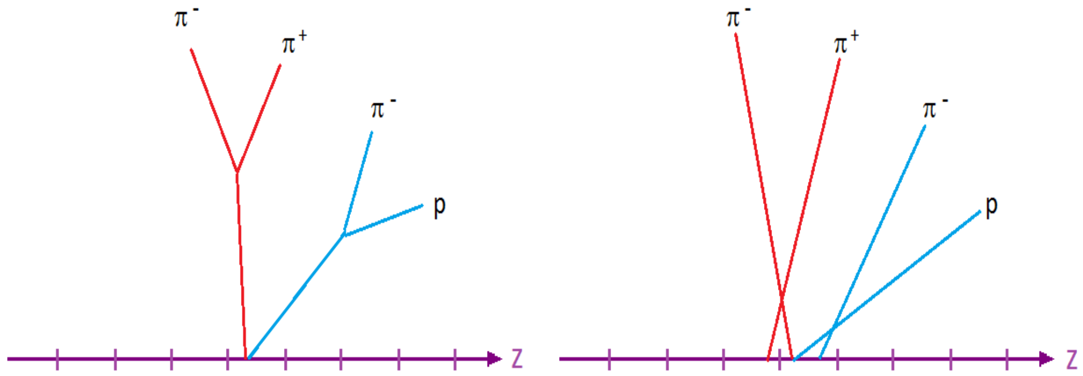

Figure 4.6: The path of the original decay particles seen on the right are not well represented by the tracks reproduction in the data banks. The scales are exaggerated for clarity. The final state particle paths are 2 orders of magnitude greater in length.

The distance of closest approach (DOCA) method was used to determine the vertex points of the K_S and Λ particles. This method assumes that both paired particles measured in CLAS came from the same production vertex. The difference in the databank would be due to measurement uncertainty. In the case of secondary decays, it would also be due to the miscalculation of the decay vertex. To find the correct value, the tracks of both particles are compared to find the two points at which the distance between them is the smallest (see Fig. 4.7). At these points, the line between them would be completely orthogonal. This is usually not the case, and a correction needs to be made.

To make this correction, we take the normal of each track at the vertex point from the banks and then compare them. If we define the tracks by $\mathbf{p}_1$ and $\mathbf{p}_2$, we can define $\hat{\boldsymbol{n}}_1$ and $\hat{\boldsymbol{n}}_2$ as the unit vectors of their normals at points P_1 and P_2 respectively. By using the difference between points we can then define the normals from each track and correct their positions. We define:

$$\boldsymbol{n}_1 = \Delta\boldsymbol{P} \cdot \hat{\boldsymbol{n}}_1 = (\boldsymbol{P}_1 + \boldsymbol{P}_2) \cdot \hat{\boldsymbol{n}}_1 \tag{4.3}$$

$$\boldsymbol{n}_2 = \Delta\boldsymbol{P} \cdot \hat{\boldsymbol{n}}_2 = (\boldsymbol{P}_1 + \boldsymbol{P}_2) \cdot \hat{\boldsymbol{n}}_2 \tag{4.4}$$

$$R = \hat{\boldsymbol{n}}_1 \cdot \hat{\boldsymbol{n}}_2 \,, \tag{4.5}$$

where $\boldsymbol{n}_i$ are the normals to each track path at points $\boldsymbol{P}_i$, and $R = cos\theta$, which is the cosine of the angle between the two normals. The points are then corrected by their relations to center of the target:

$$\boldsymbol{P}_{1-\mathrm{corr}} = \boldsymbol{P}_2 + \left(\frac{\boldsymbol{N}_1 - R\boldsymbol{N}_2}{R^2 - 1}\right) \cdot \hat{\boldsymbol{n}}_1 \tag{4.6}$$

$$\boldsymbol{P}_{2-\mathrm{corr}} = \boldsymbol{P}_1 + \left(\frac{R\boldsymbol{N}_1 - \boldsymbol{N}_2}{R^2 - 1}\right) \cdot \hat{\boldsymbol{n}}_2 \tag{4.7}$$

When the two normal unit vectors are parallel, R goes to zero and equations 4.8 and 4.9 reduce to the simple addition or subtraction of vectors with respect to the origin.

The vertex of the event (decay or production) is then determined by taking the DOCA point. The DOCA point is generally determined by taking the midway point of the DOCA vector. If one particle has better statistics than the other track, the DOCA point can be chosen closer to its track by applying a weighting factor.

Figures 4.10 and 4.11 show the results of the vertex reconstruction for the K_S (top) and Λ (bottom) decays. The first plot in each group shows the DOCA lengths. The other three plots show the decay vertices for each event in the xy-plane, xz-plane, and yz-planes. The target was 40 cm long with a 4 cm diameter. The beam spread was less than 3 mm. From the figures, it is clear that most of the secondary decays occur within the target. The Λ is significantly more likely to decay outside the target than the K_S. This is in agreement with the expectations since both strange hadrons have short lifetimes, where the K_S has a shorter lifetime than the Λ.

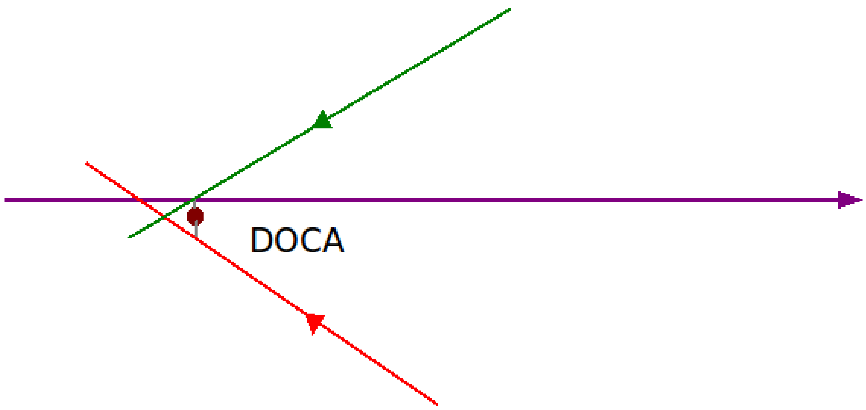

Figure 4.7: The distance of closest approach (DOCA) method. Two tracks are compared to find the path of shortest difference between them. A point is chosen somewhere on this line as the DOCA point, based on the importance weighted to each track.

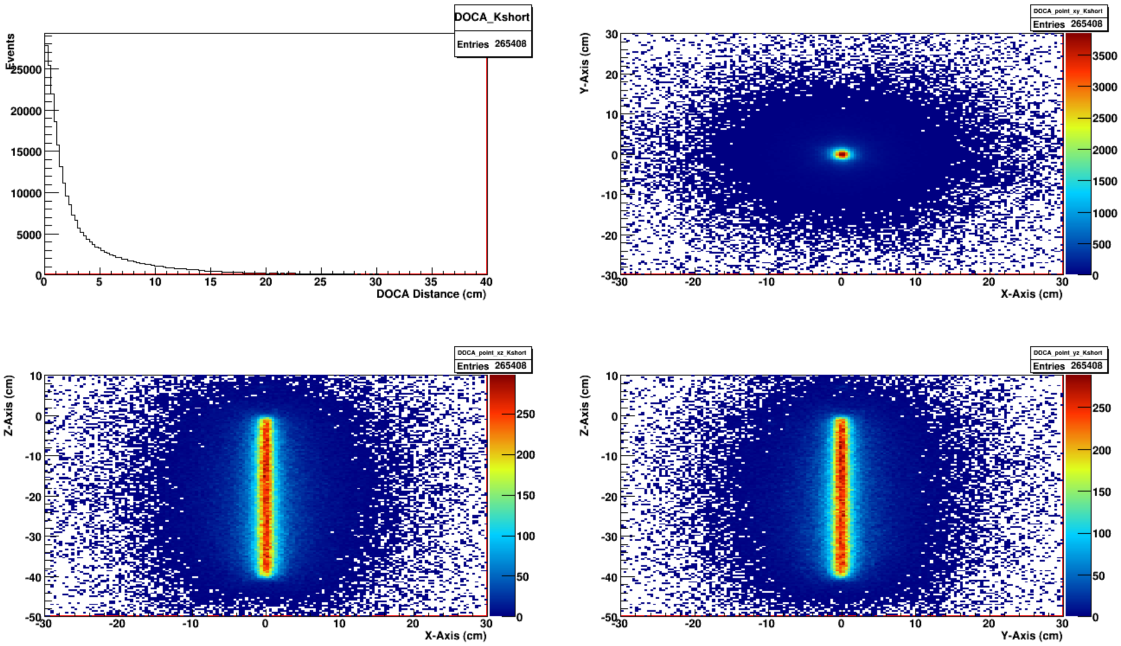

Figure 4.8: The reconstruction of the K_S decay vertex. The first histogram shows the DOCA lengths while the other three are the *xy*, *xz,* and *yz* planes. Most of the short kaons do not make it out of the target.

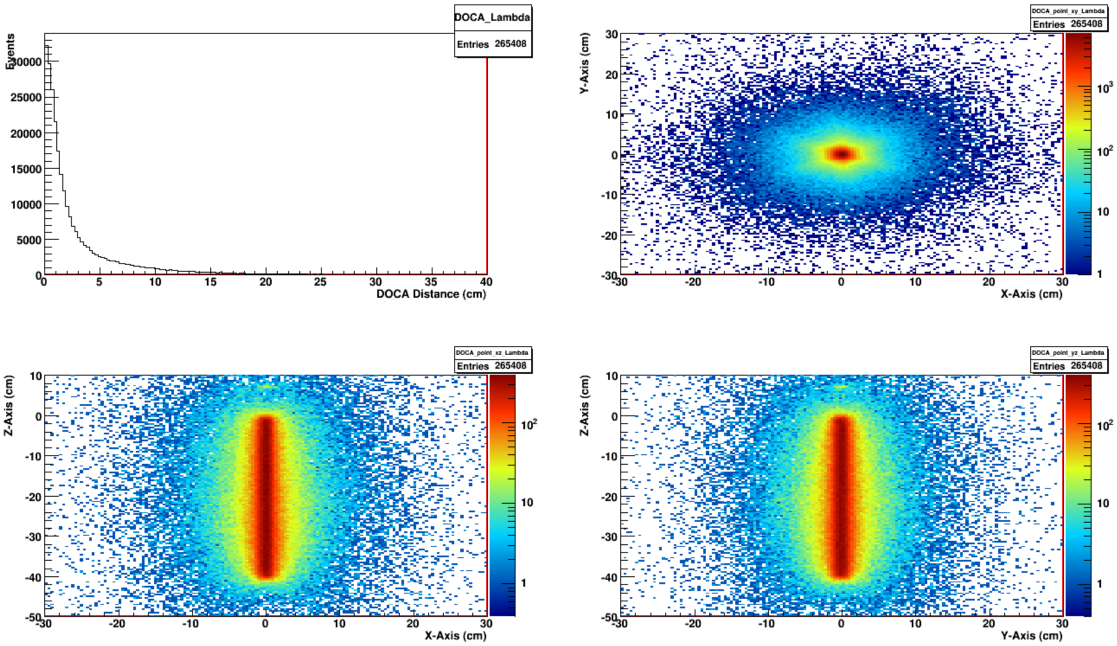

Figure 4.9: The reconstruction of the Λ decay vertex. The first histogram shows the DOCA lengths while the other three are the *xy*, *xz,* and *yz* planes. Most of the Λs do not make it out of the target.

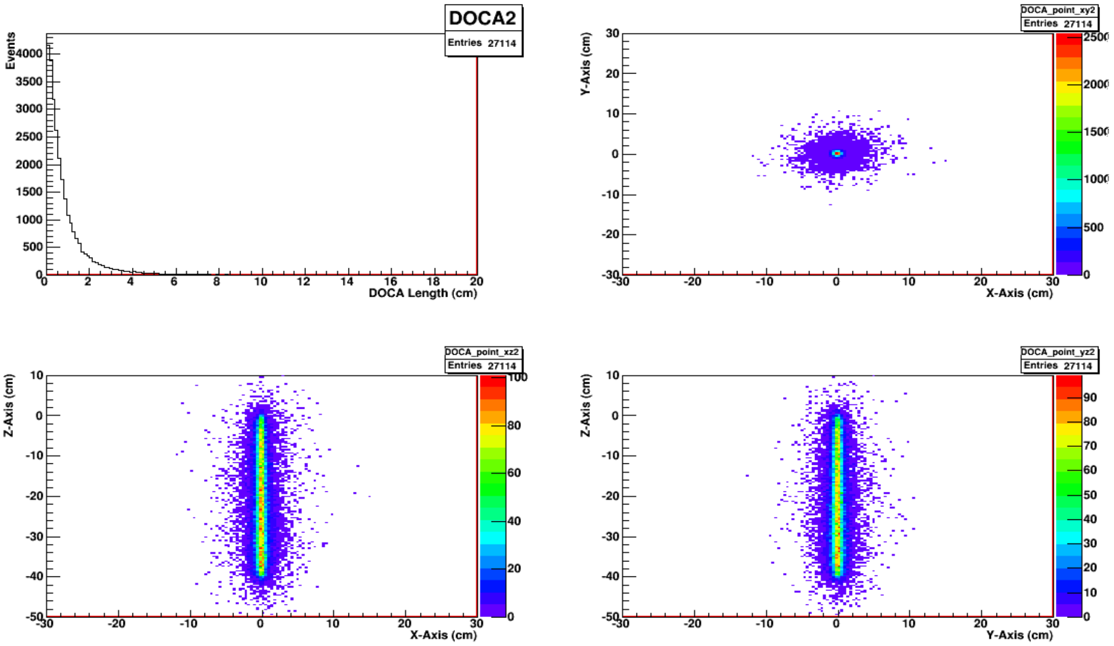

Figure 4.10: The reconstructed production vertex using method 1. The first histogram shows the DOCA lengths while the other three are the *xy*, *xz*, and *yz* planes. Essentially all of the events occur within the radius of the beam.

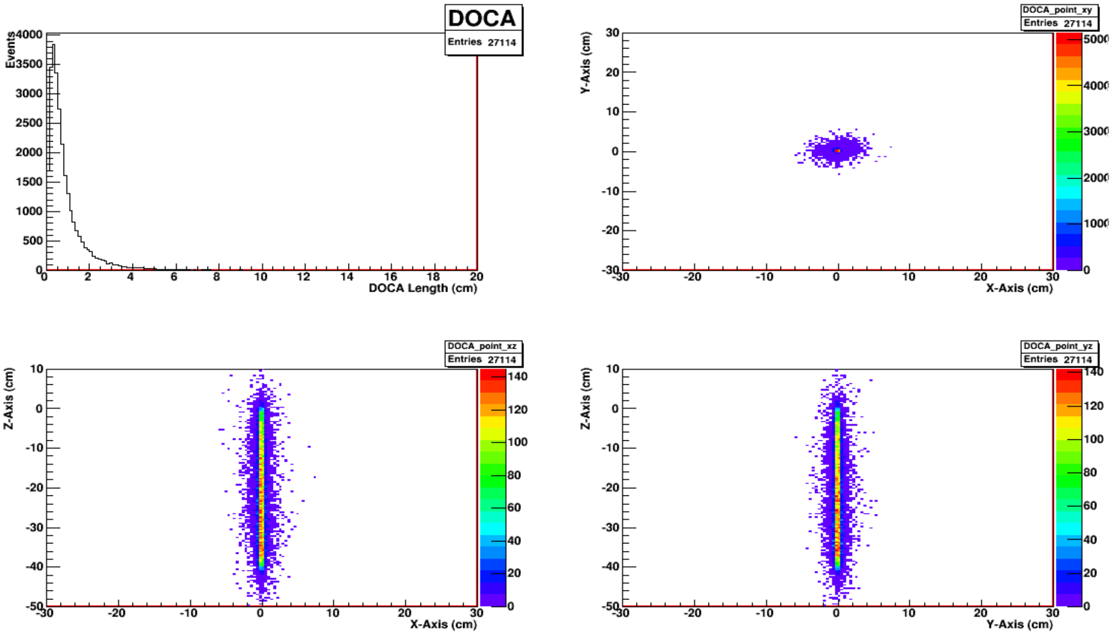

Figure 4.11: The reconstructed production vertex using method 2. The first histogram shows the DOCA lengths while the other three are the *xy*, *xz*, and *yz* planes. Essentially all of the events occur within the radius of the beam.

After the K_S and Λ vertices were reconstructed, it was necessary to use their newly constructed tracks, in turn, to reconstruct the production vertex. Each vertex reconstruction has an uncertainty. If it were applied a second time, the uncertainty could significantly increase with the newly constructed paths. To understand this effect, two methods were developed for the reconstruction of the event vertex (see Fig. 4.12). The first method directly compares the paths of the K_S and Λ tracks. It is expected that the interaction would occur within the photon beam; therefore the second method uses the assumption that the production vertex is the same as the recorded beam position. In most cases the beam the x and y positions were very near zero. The DOCA point was calculated for both the K_S and Λ tracks with respect to the beam path. The average of their positions was used to determine the production vertex.

From Figs. 4.10 and 4.11, it can be seen that both methods show the production vertex occurs within the beam. However, the distributions produced by the first method are more dispersed than the second method. This was expected since the second method ties both neutral tracks directly to the beam line.

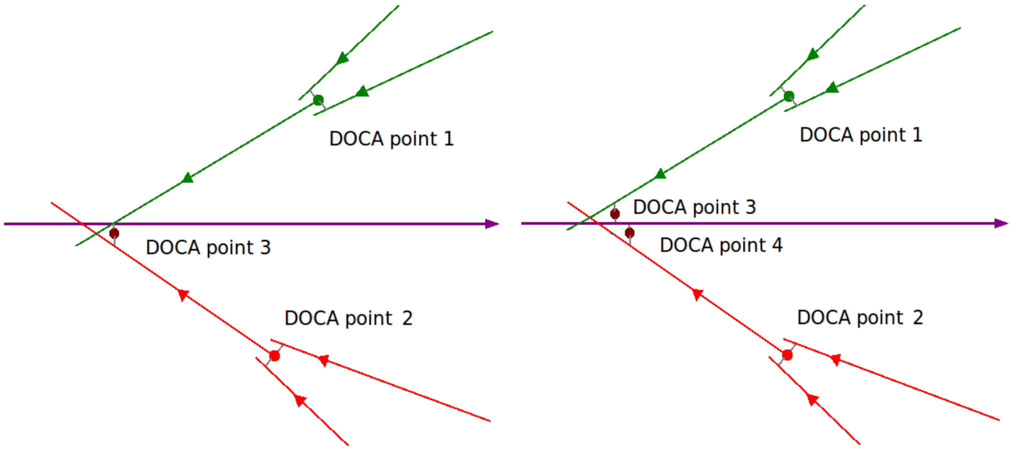

Figure 4.12: The two methods used to determine the production vertex. Both methods use the distance of closest approach method (DOCA) for each vertex position. In the first method the two reconstructed tracks are compared together for the production vertex, while the second method compares them to the beam line and then takes their average.

4.1.5 Vertex Verification

The reconstruction of the vertex was verified through the Monte Carlo simulation. The phase space generator (fsgen) begins at the hadronization stage. User defined parameters were used to produce the position, momentum, and primary decay modes for the initial decay particles. The generated particles were then propagated through the simulated CLAS detector using the GSIM package[27]. GSIM is built from the GEANT particle simulation code from CERN. The data is then processed through the GPP code to correct the tracks for detector inefficiencies and dead paddles or wires. The final-state particles are then recorded in the same banks as the real data (such as EVNT and TAGR). The original particle information is stored in simulation-independent banks MCTK and MCVX. The simulation process will be explained in more detail in Chapter 6 on acceptance and flux determination.

The simulated data is then treated the same as real data. After the files are cooked, they are processed through the skimming and analysis codes. The reconstructed vertex can now be compared to the "real" vertex position from the simulation banks. Figures 4.13 and 4.14 show the reconstructed vertex positions for the simulated data. Similar to the real data, most of the K_S and Λ decay vertices are within the target. The range difference between the kaon and Lambda particles reflect the data as well. In the next two figures (4.15 and 4.16), we see even less difference between the two methods. The first method is closer to the beam center in the simulation than in the experimental data. This is not surprising since the MC simulation does not perfectly take into account all the system's imperfections. However, similar to the real data, method one's distribution does show a little more deviation from the beam line than that of method two's.

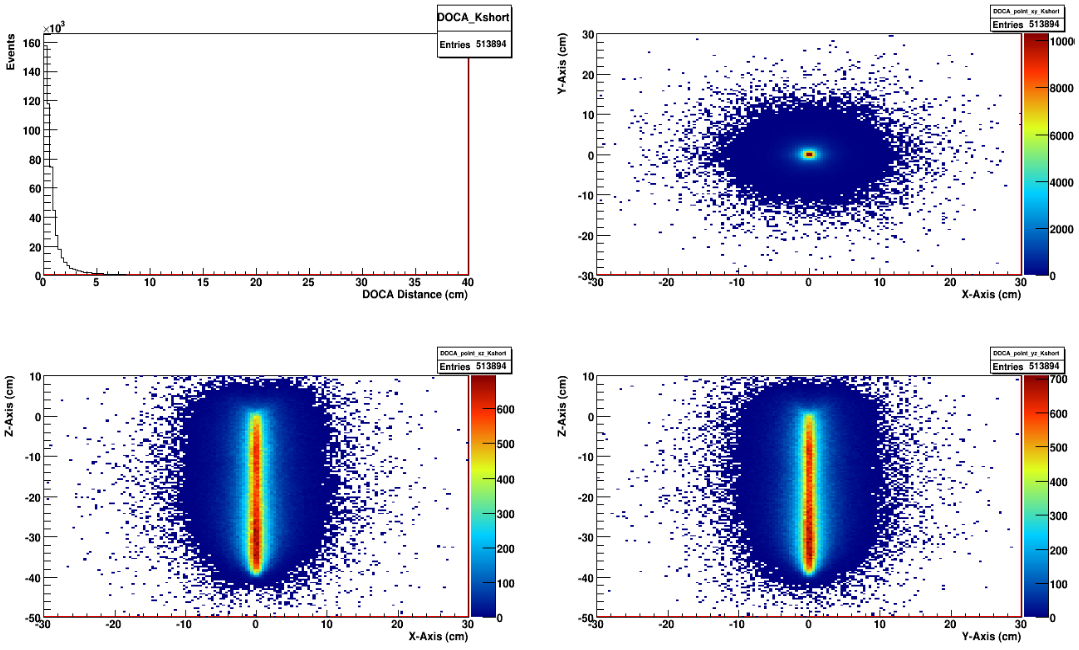

Figure 4.13: The reconstruction of the simulated K$_S$ decay vertex. The first histogram shows the DOCA lengths while the other three are the xy, xz, and yz planes. The distribution closely matches that of the data seen in figure 4.8.

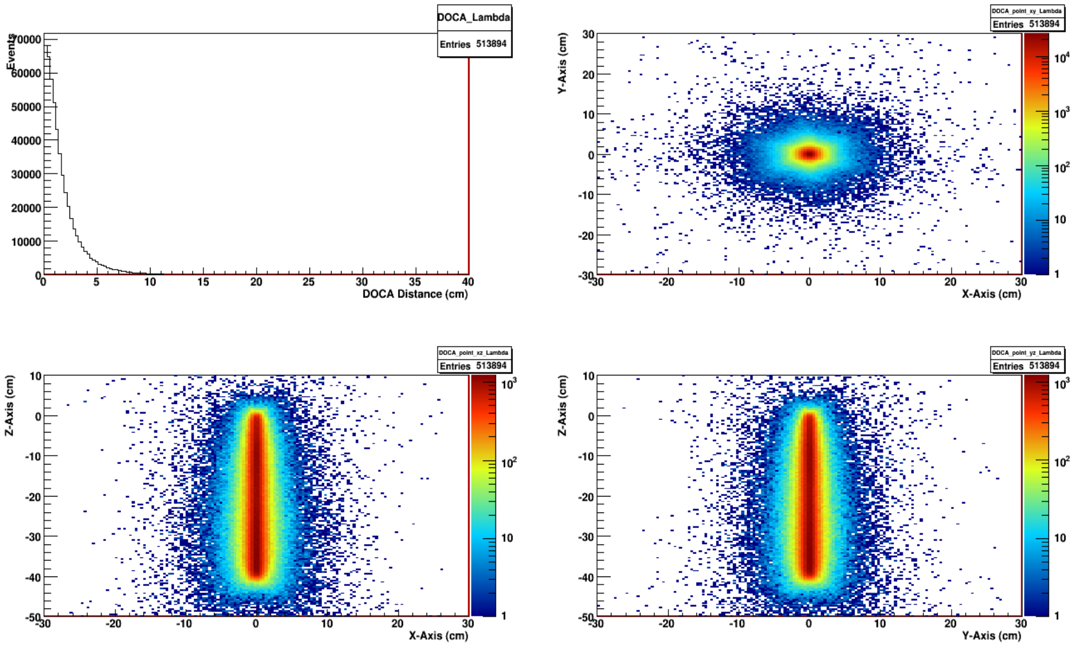

Figure 4.14: The reconstruction of the simulated Λ decay vertex. The first histogram shows the DOCA lengths while the other three are the *xy*, xz, and *yz* planes. The distribution closely matches that of the data seen in Fig. 4.9.

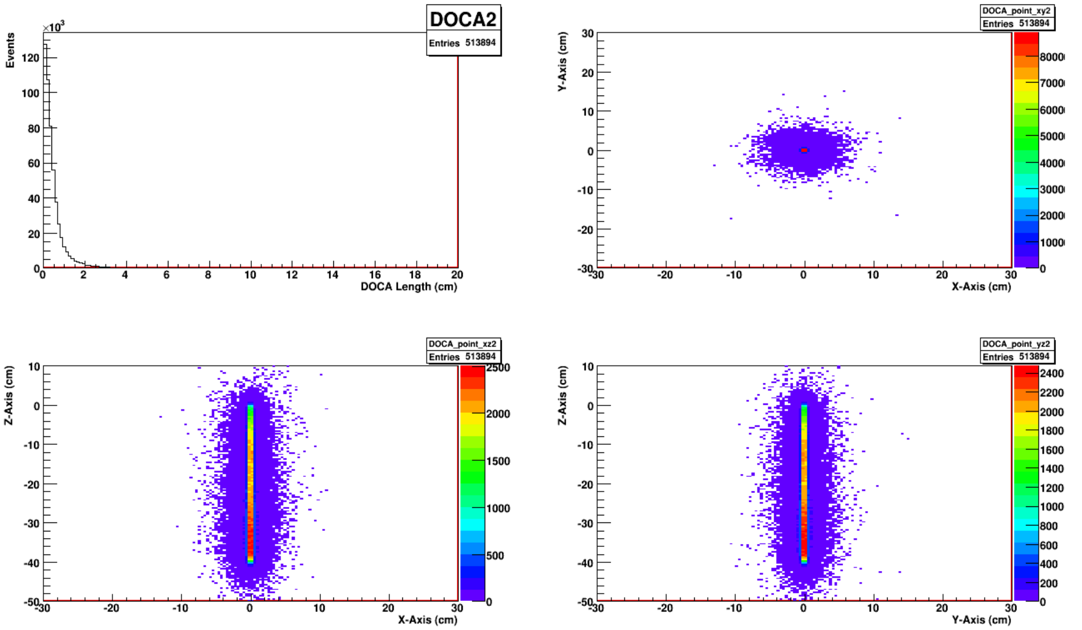

Figure 4.15: The reconstructed production vertex using method one for the simulated data. The first histogram shows the DOCA lengths while the other three are the *xy*, *xz*, and *yz* planes. The distribution is in good agreement with the real data (Fig. 4.10), though not as well as method 2.

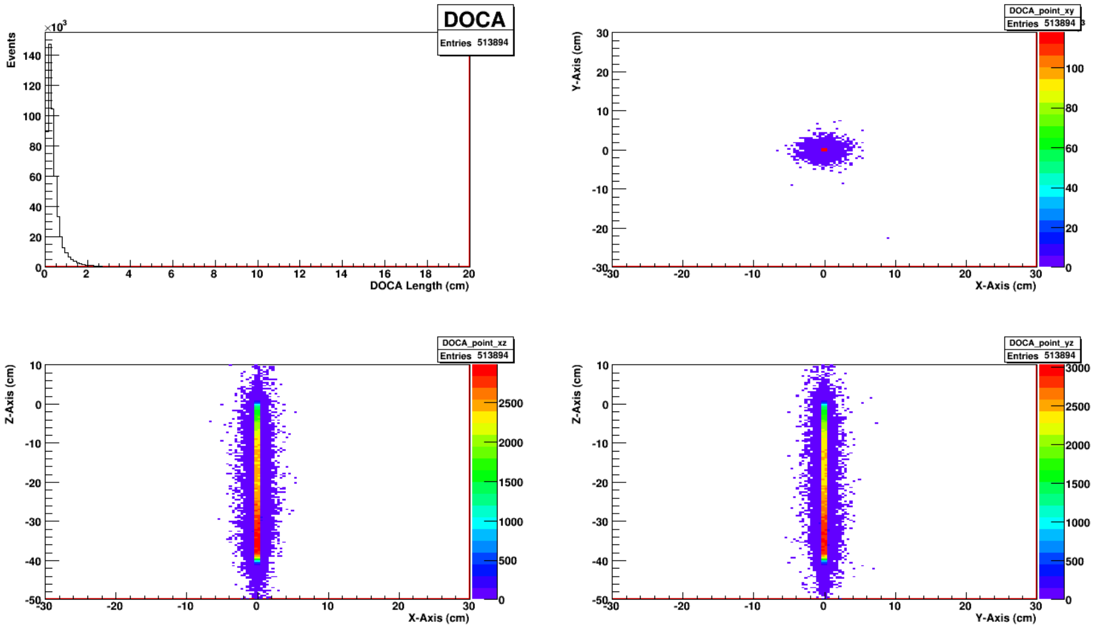

Figure 4.16: The reconstructed production vertex using method two for the simulated data. The first histogram shows the DOCA lengths while the other three are the *xy*, *xz*, and *yz* planes. The distribution is in very good agreement with the real data (Fig. 4.11).

Finally, in Fig. 4.17 the difference between the reconstructed vertex and original vertex position in the simulated data is reasonably small. This validates the reconstruction method used in the code and allows us to conclude the reconstructed positions in the real data are accurate to at least 5 mm.

4.1.6 K_S and Λ Decay Lengths and Lifetimes

With accurate vertex positioning, it is now possible to determine the proper decay length and lifetime of the particle. The proper decay length is simply the difference between the primary and secondary decay vertex corrected relativistically. Dividing this length by the particle's velocity and we have the lifetime of the particle. From a distribution of lifetimes we can determine the mean lifetime of the possible K_S and Λ

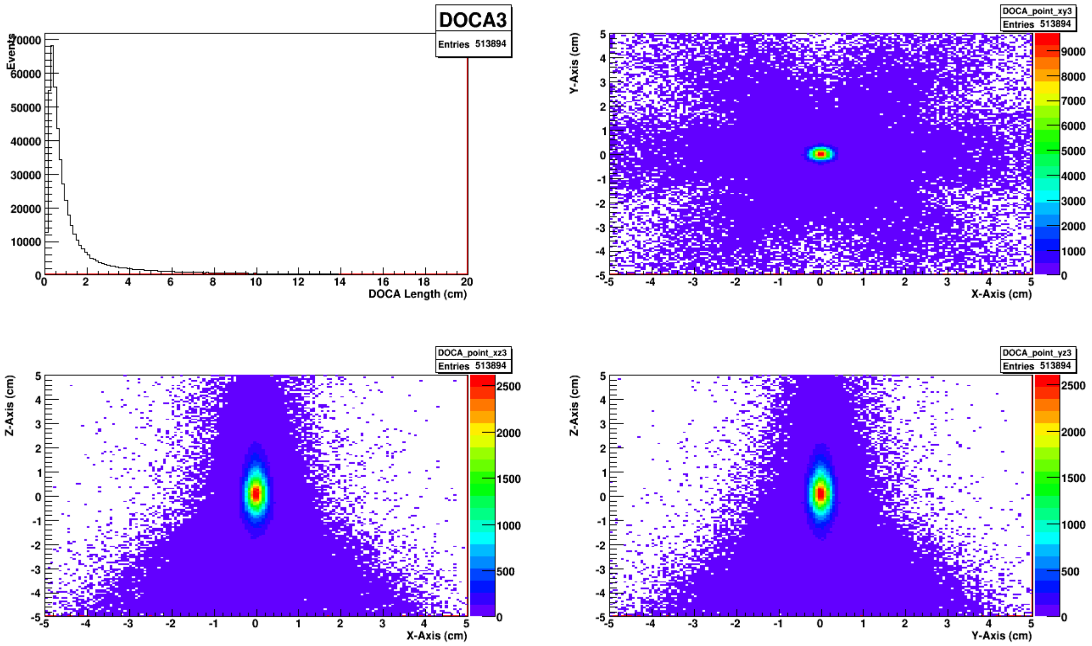

Figure 4.17: Difference between the reconstructed vertex and the "real" vertex on the simulated data using method 2

particles. The mean life is given by the inverse exponential slope of a fit to the time distributions. This corresponds to the probability of decay for an unstable particle:

$$N(t) = N_0 e^{-t/\tau} \tag{4.8}$$

where $\tau = 1/\lambda = T_{1/2}/\ln 2$, and λ is the decay constant and $T_{1/2}$ is the half life of the particle.

By looking at Fig. 4.18, we can see that the decay lengths very closely matched the Ks and Λ particles identified in the g10 dataset. The top histograms show that the decay lengths using vertex reconstruction method 1 and 2 very closely match in the g13a measurement. Figure 4.19 is the distribution of the difference of decay length between method 1 and method 2 for each particle. As can be seen, both vertex reconstructions produce some difference (most less than 3 mm) when looking at the total decay length of each particle. With respect to the total decay length, these differences would yield approximately 4% uncertainty in particle position. However as we have seen from the distribution, these differences become significantly reduced when taking the whole dataset.

From Fig. 4.20, the lifetime distributions are now plotted and fit to find the decay rate (the inverse of the mean lifetime). The data is fit between 0.18 and 0.5 ns. The lower range is cut out due to lower probabilities of measurement and the higher decay times were not included because of statistical uncertainties. The fits were made independently for each vertex reconstruction method, though the plots in Fig. 4.20 only show the fit for method 2. The results from the fit for method 2 are shown in Table 4.1 along with the particle data group (PDG) decay constants for the K_S and Λ particles.

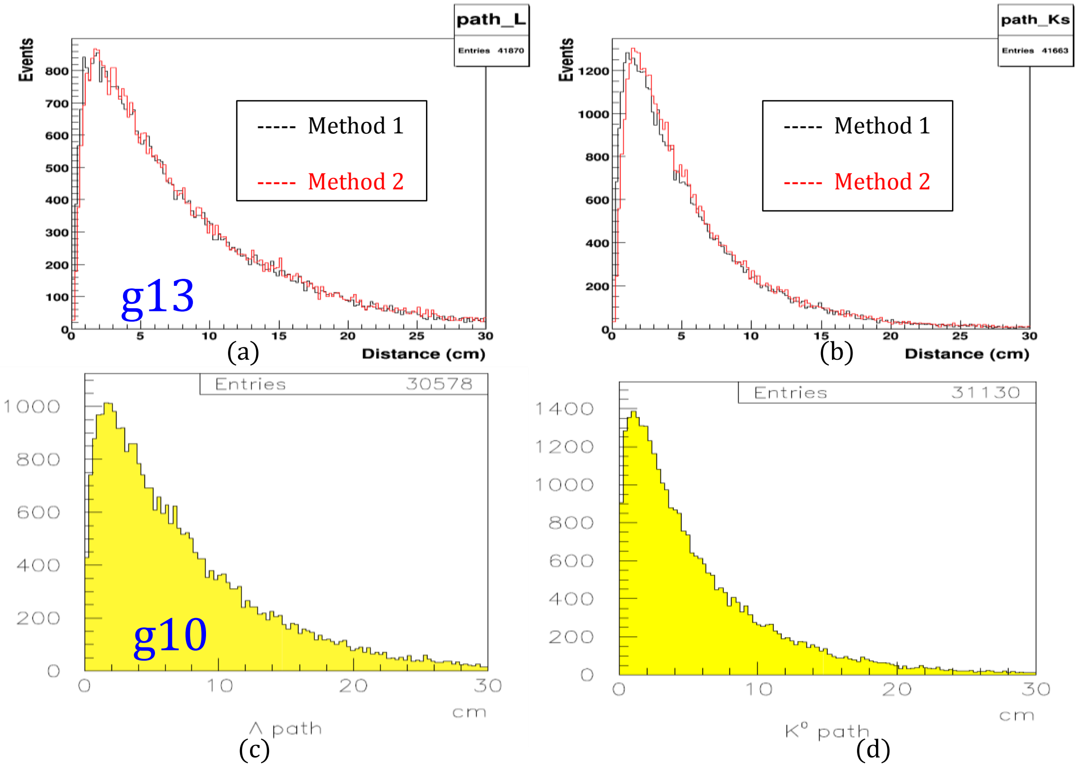

(a) (b)

(c) (d)

Figure 4.18: The top (a) and (b) distribution show the decay length for the Lambda and kaon, respectively, for the g13 experiment. The bottom (c) and (d) show the measured values for the g10 experiment. As can be seen in the g13 plots, both methods yield the same decay length distributions. These distributions for the g13a dataset are consistent with similar g10 measurements or the K_S and Λ particles.

With a fixed beam width (6.4 mm), most of the uncertainty in the vertex determination is along the length of the beam line. Smaller angles can introduce larger uncertainty in the z position of the event vertex (see Fig. 4.21). Therefore by removing the lower angle events, the mean lifetime can be further improved. There is a clear decrease in lifetimes as the lower angles are excluded. Mean lifetimes above 30 degrees are closer to the PDG values; currently their statistics are too low. Current values are taken after dropping events where either decay path is less than 25 degrees. The measured lifetimes verifies that the correct particles have indeed been identified. Current results are within approximately 5% and 8% of the PDG values for the K_S and Λ decay constants, respectively.

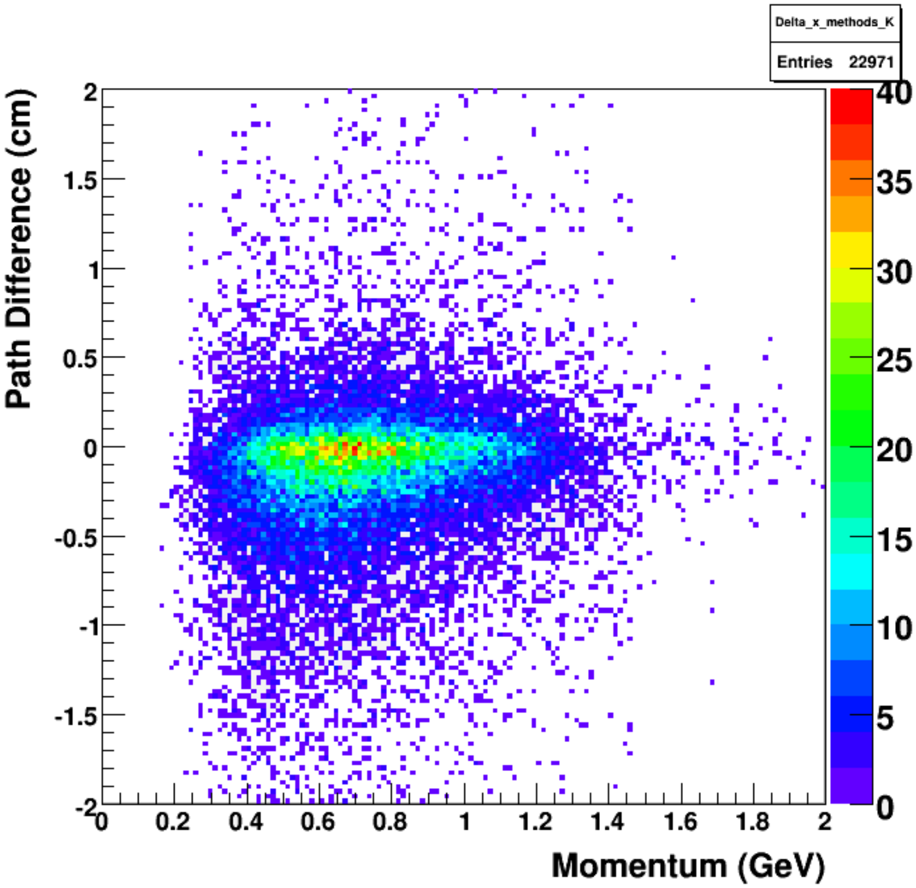

Figure 4.19: Comparison of the production vertex for both methods. The total decay length is determined by taking the difference between the primary and secondary decay vertices. The difference between method 1 and 2 are then plotted with respect to the momentum of the particles.

Table 4.2: Measured mean lifetime of the fit to the time distribution of the data.

Particle	Measured Mean Lifetime (ns)	PDG Measured Mean Lifetime (ns)
Ks	0.095 ± 0.006	0.0895 ± 0.0003
Λ	0.286 ± 0.006	0.263 ± 0.002

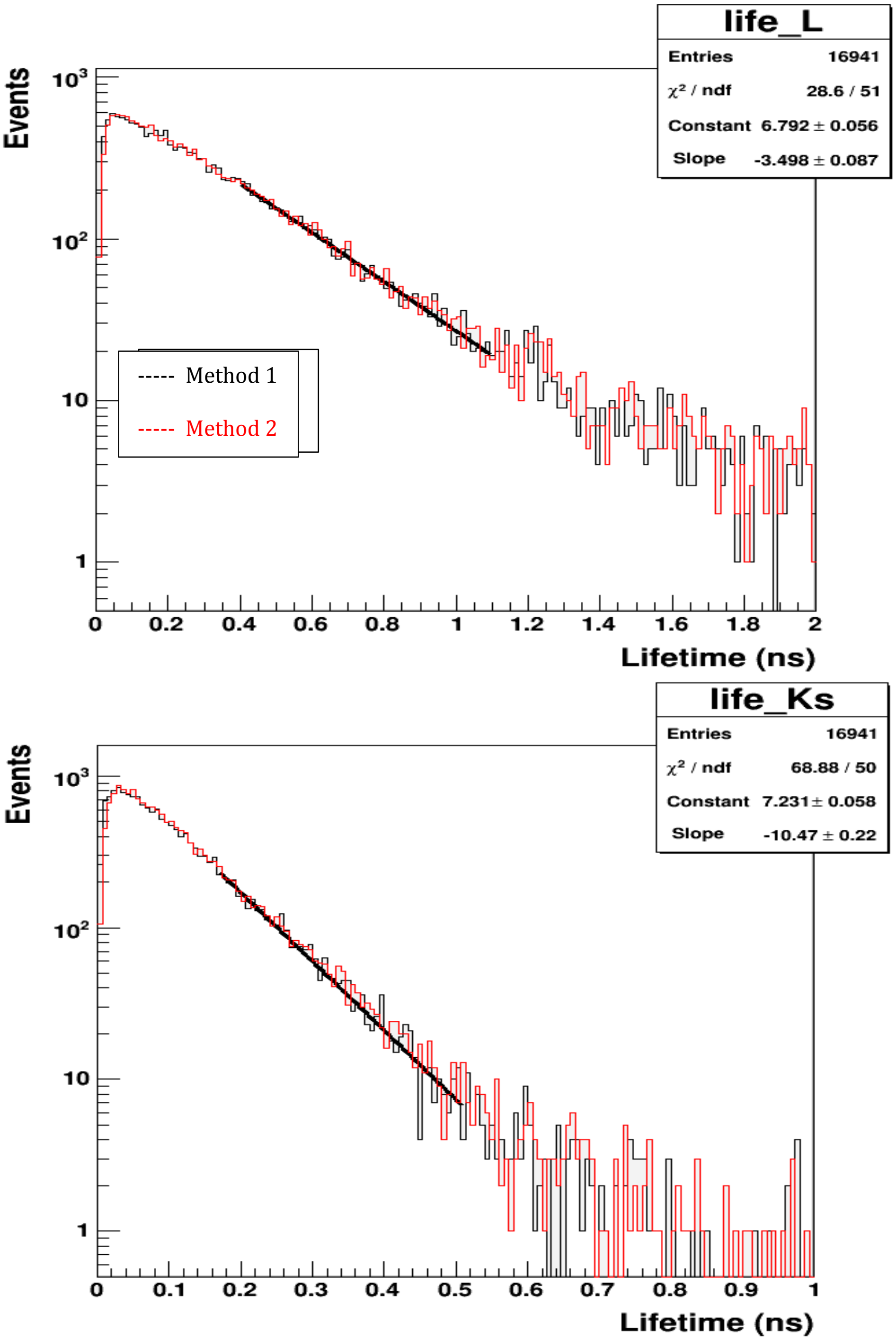

Figure 4.20: Lifetime distributions of the reconstructed K_S and Λ particles. The fit was made between 0.18 and 0.5 ns to avoid inefficiencies at the shorter and longer times.

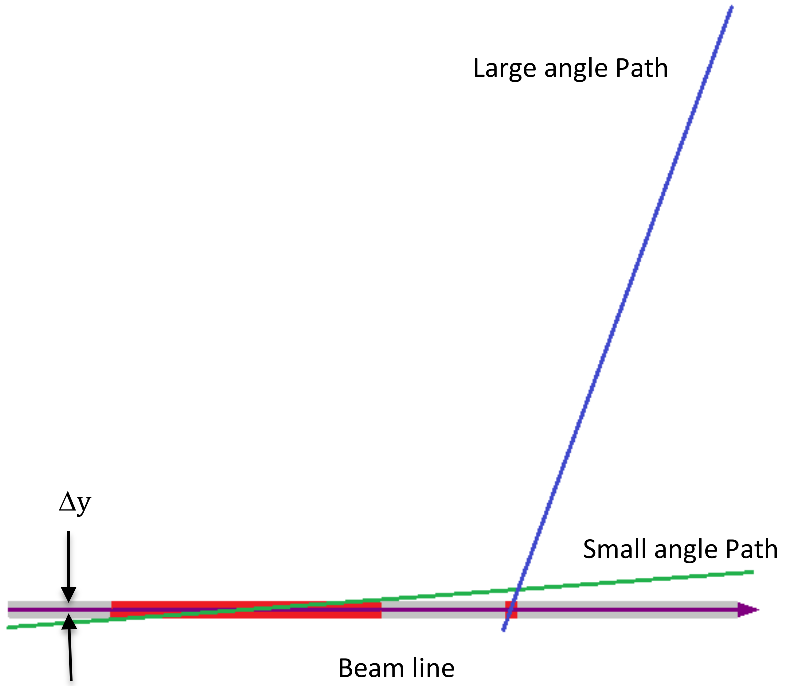

Figure 4.21: Smaller angles can introduce larger uncertainty in the *z* position of the event vertex. There is a clear decrease in lifetimes as the lower angles are excluded. Though lifetimes above 30 degrees are closer to the PDG values, currently their statistics are too low. Current values are taken after dropping events where either decay path is less than 25 degrees

Table 4.3: Measured mean lifetimes of the fit to the time distribution of the data, with various cuts on minimum allowable angle. Though the cut of everything below 30⁰ was closer to the PDG, its statistics were low. Therefore the 25⁰ cut was used for the production of histograms.

Min Angle	K_S Measured Mean Lifetime (ns)	Λ Measured Mean Lifetime (ns)	K_S Ratio (Measured/PDG)	Λ Ratio (Measured/PDG)
0^0	0.113± 0.005	0.307± 0.005	1.157	0.796
5^0	0.113± 0.005	0.307± 0.005	1.157	0.797
10^0	0.113± 0.005	0.306± 0.005	1.153	0.799
15^0	0.111± 0.005	0.303± 0.005	1.139	0.809
20^0	0.105± 0.005	0.296± 0.005	1.113	0.858
25^0	**0.096± 0.005**	**0.285± 0.005**	**1.074**	**0.942**
30^0	0.090± 0.005	0.271± 0.006	1.02	1.000
35^0	0.220± 0.005	0.593± 0.010	2.232	0.409

4.1.7 Photon Selection

Before the missing mass is determined, the photon for the event is selected. Choosing the correct photon is essential in obtaining the correct total energy of this photo-initiated event. Initially, the skim code used the photon that was selected when the data was cooked. Later it was refined to iterate over the various photons so as to find the best candidates. This was done by using the reconstructed event vertex to calculate the correct time of the event, with respect to the center of the target. The closest photon to this time was used for the event. Later it became necessary to examine the timing windows of the particles and look for cases where there exist multiple candidate photons. Since this reaction requires at least four detected particles, an accurate vertex reconstruction allowed for a better selection of the event photon than would be offered by other channels.

4.1.8 Exclusive $K_S\Lambda$ Event Selection

With the data reduced to events containing both K_S and Λ particles, it now becomes necessary to conserve the four-momentum to determine the momentum of the parent particles. With the energy of the photon, it is possible to look for the missing mass and missing momentum of the reaction. If the missing mass gives the mass of the spectator proton, we know we have found these events arising from the neutron. However, there are other competing background channels- namely: $\gamma D \rightarrow K_S\Sigma^0(p) \rightarrow K_S\Lambda\gamma(p)$ and $\gamma D \rightarrow K_S\Sigma^{*0}(p) \rightarrow K_S\Lambda\pi^0(p)$[28]. These reactions will produce additional peaks and background within the mass distribution. They can more clearly be seen by plotting the missing mass of $K_S\Lambda$ with the missing mass of just the K_S (see Fig. 4.22). Removing the background from the peak of the spectator proton can be evaluated either by fitting the peaks and doing a subtraction or by cutting out the upper half of the peak. Each of these methods was evaluated in this study.

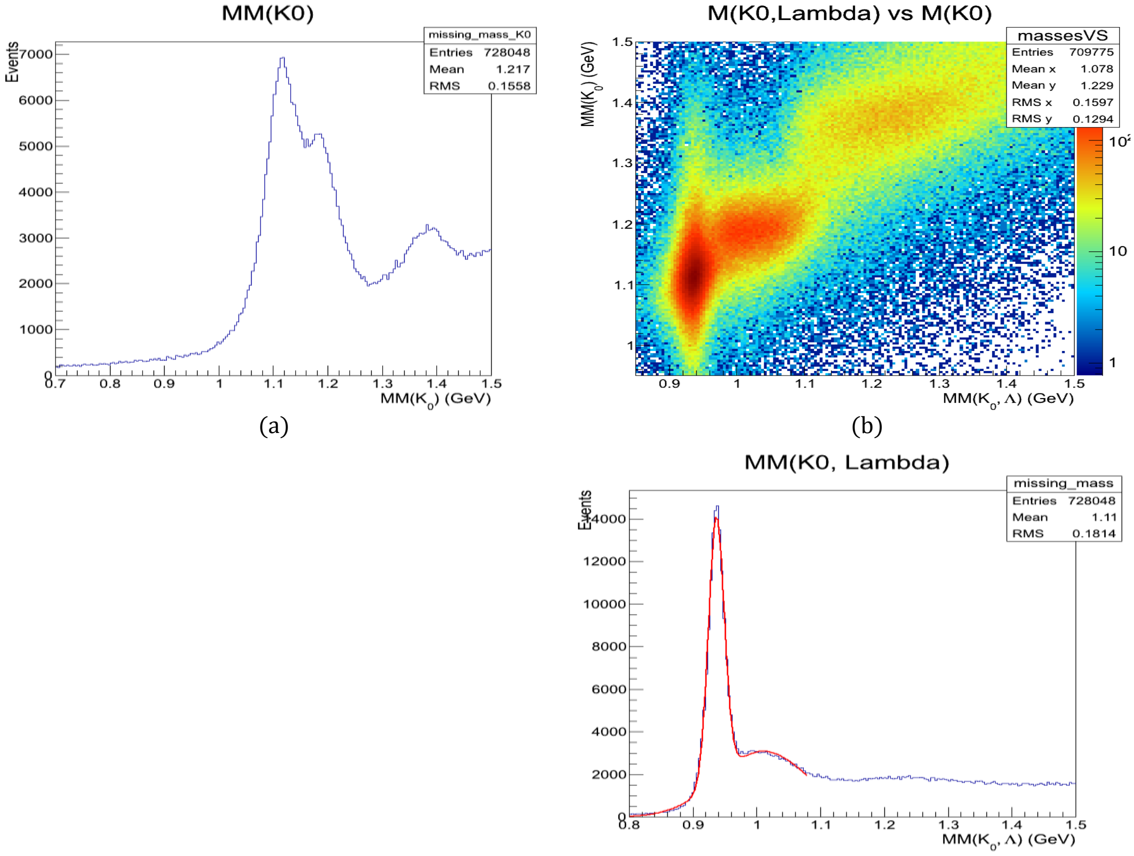

(a) (b)

(c)

Figure 4.22: Missing mass of the $K_S\Lambda$ channel. (a) The sharp peak corresponds to the mass of the spectator proton, while the secondary peak relates to the γ from the competing channel $\gamma n \rightarrow K^0\Sigma^0 \rightarrow K^0\Lambda\gamma$. The tail is the contribution from the $\gamma n \rightarrow K^0\Sigma^{*0} \rightarrow K^0\Lambda\pi^0$ channel. (b) The MM(K_S,Λ) vs. MM(K^0) offers a clear picture of the Σ^0 signal.

4.1.9 Quasi-Free Event Selection

Additional information can be gained by making a histogram with the missing momentum verses the missing mass of the $K_S\Lambda$ or verses the cosθ angle (Fig. 4.23). From the first histogram, the vertical distribution corresponds to the mass of a proton at approximately 0.938 GeV (the PDG is 0.93827 GeV). The offset from zero momentum illustrates the Fermi momentum within the nucleus. The smear above it corresponds to rescattering events. The other distributions with excessive momentum and mass indicate that an extra particle exists within the reaction. The right histogram shows angular distribution of the events, after placing a cut on the missing mass of the $K_S\Lambda$. The quasi-free neutrons should have no preferred direction. However both in and above the flat distribution, it can be seen that some events have a forward preference. These events are removed by placing a cut on the missing mass of the neutral kaon alone.

With a cut on the missing mass temporarily applied, we can now review all the previous cuts to see if there are any clear areas where events that do not contribute to the final distributions could be cut. By reversing the cut on the missing mass of the $K_S\Lambda$, it is possible to examine the beta, momentum, and mass distributions again. With the absence of the resonance it is possible to more clearly see the effects of the background phase space. Once the mass and momentum peaks have been optimized to their ideal widths and amplitudes, we can remove the missing mass cuts and use a fit to its peak to extract the yield of the channel. This analysis further gives insight into the overall systematic variation of our cuts and whether the cuts are order dependent.

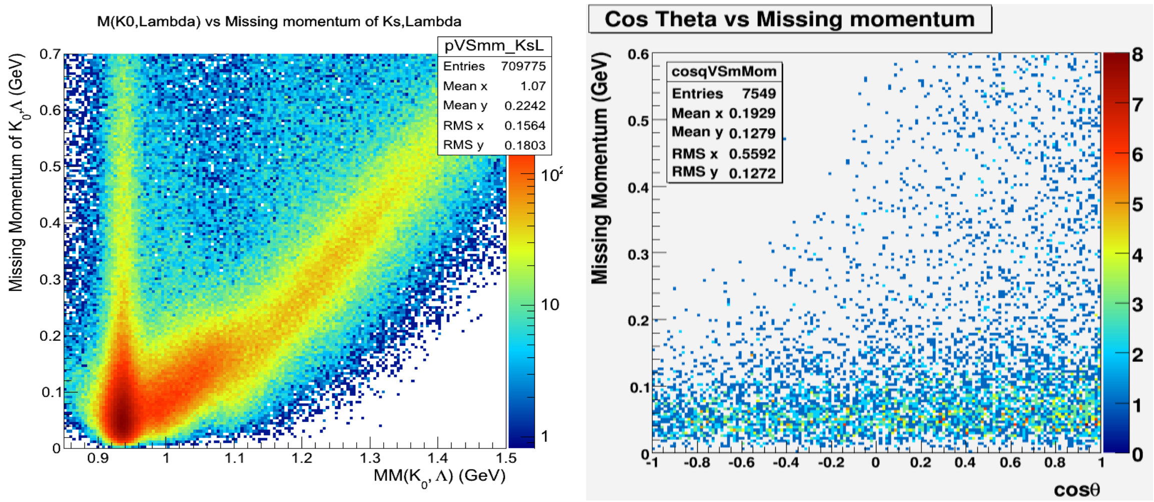

Figure 4.23: (a) The missing mass of the K^0, Λ vs. its missing momentum, the proton can be seen by the vertical distribution, while the diagonal distribution implies events where a extra particle exists within the reaction. (b) The cosine angle vs. the missing momentum of the K^0, Λ. The band along the bottom of the plot shows the quasi-free neutrons, while the rest shows the forward bias of the interaction.

4.3 Flux Determination

Before extracting the cross section, it is necessary to first measure the photon flux incident on the target. The *gflux* method was used for the g13 dataset. This method counts the number of "good" electrons in the tagger and compares them with the number of photons measured with the total absorption counter (TAC), which has a well-known efficiency. From these normalization runs, a tagging ratio is produced. This ratio is then applied when the data is cooked to normalize the photon flux. A normalization run was made every few hundred runs. A normalization run uses a thinner bremsstrahlung radiator and operates at 10% of the production beam current, since the TAC cannot handle a higher flux. The tagging ratio is independent of the photon flux intensity [29].

4.3.1 Photon Flux Code

The *gflux* software[31] was used for the calibration and correction to the photon flux for each run. For the calibration the code counts the number of "good" electrons measured in the tagger and compares them to the TAC values, and returns the tagging ratio. The term "good" electrons correspond to "out-of-time" electron measurements within the tagger that could not be involved in a physics event trigger. The "good" electrons can be seen in Fig. 4.24 by the τ window to the right of the trigger peak. When an event is triggered in the T-counter, the signal is split into two signals. When the right trigger conditions are met with the first signal, the T-counter TDCs begin counting. The counting continues for a short duration while the second signal passes through very long cables (which provide sufficient time for the trigger to decide if the event is worth recording). Once the second signal reaches the TDCs, the counting is stopped. The "out-of-time" electrons are assumed to follow a Poisson distribution. Therefore the τ window is defined by the user to only include flat accidental background events.

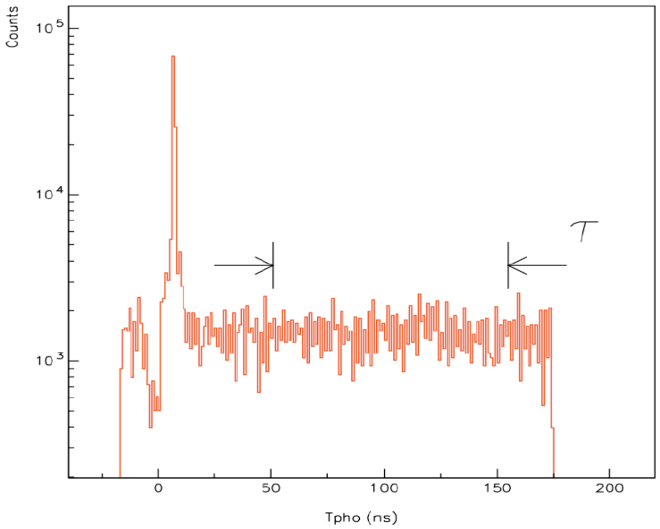

Figure 4.24: Distribution of the photon times associated with the electrons measured in the tagger for a single T-counter, with respect to the center of the target. The peak corresponds to a physical trigger, while the flat region is the accidental background.

The number of "good" electrons can be determined by summing the rates over each time interval, or:

$$N_{e^-}^T = \sum_i R^{TS} \cdot t_{\text{scalar}} \cdot t_{\text{live}} , \tag{4.9}$$

where R^{TS} is the rate of "good" electron hits, t_{scalar} is the time scalar interval and t_{live} is the live-time during the scalar interval. The live-time calculated from predefined fractions of the number of triggers that were needed by the data acquisition software to start recording the event. The rate, R^{TS}, was take to be the Poisson distribution of "good" electron hits within the first-hit T-counter within the time interval τ.

The tagging ratio is defined by the total number of "good" tagged electrons in coincidence with total number of photons measured by the TAC:

$$\epsilon^T = \frac{N^T \cdot TAC}{N^T} \quad . \tag{4.10}$$

The tagging ratio is shown per timing counter in Fig. 4.25. The number of tagged photons per T-counter can now be calculated by multiplying $N_{e^-}^T$ by the tagging ratio, ε^T, and dividing by the correction of the TAC to g13 target dimensions:

$$N_\gamma^T = \frac{N^T \cdot \epsilon^T}{1 - \alpha} \quad . \tag{4.11}$$

The α factor is determined by the fraction of photons lost from the physics target to the the TAC. This factor is typically between 3.6% and 4.4%. The development of this factor can be found in the CLAS Note 01-010[24].

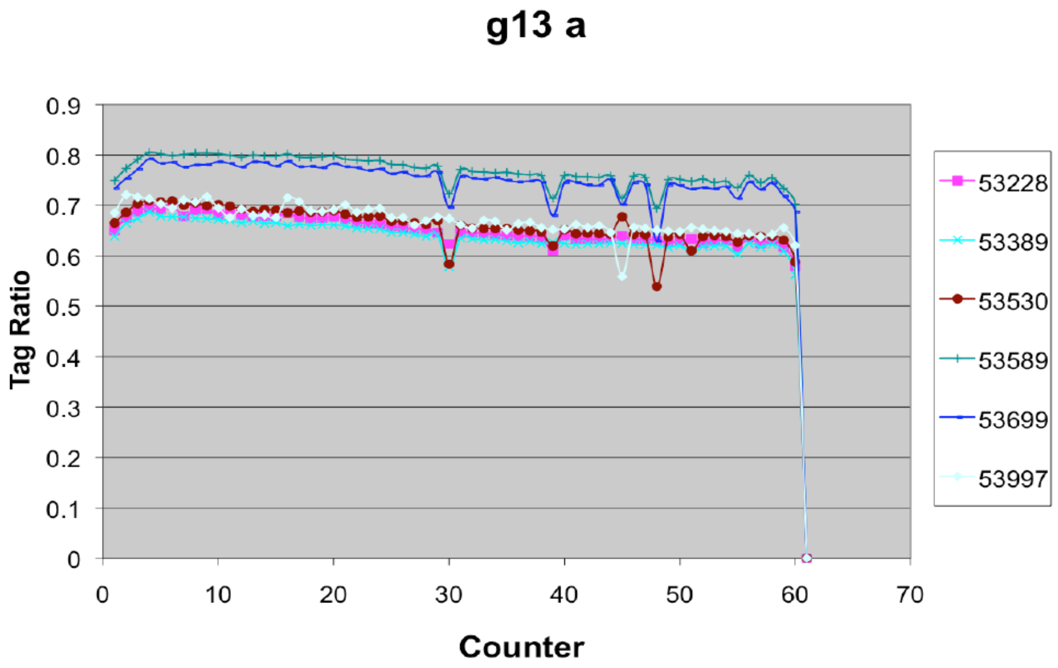

Figure 4.25: The tagging ratios for g13a. The run numbers correspond to normalization gflux runs, which require the use of the total absorption counter (TAC) for real photon flux determination. Fluctuations can be seen in various T-counters.

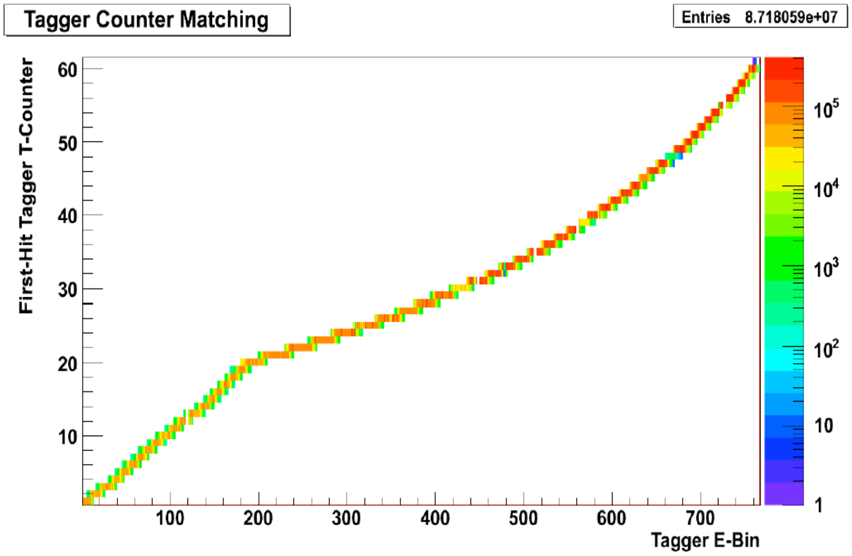

Figure 4.26: Tagger counter matching. The relationship between the energy bins and the timing bins of the electron/photon tagging system.

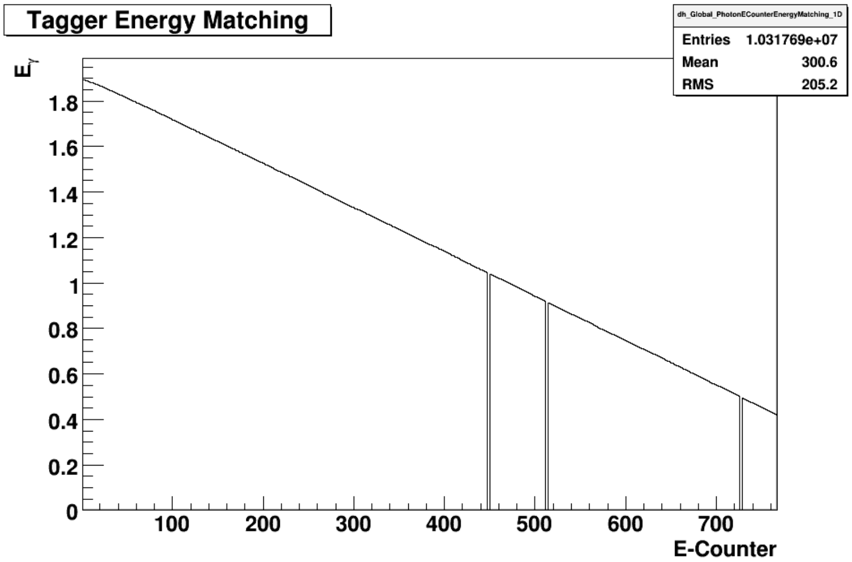

Figure 4.27: The corresponding photon energy factor for the 736 energy bins (corresponding to the 368 overlapping E-counters). The linear fit was determined by the max and min photon energies.

The *gflux* code produces a two-dimensional occupancy matrix (called the ET matrix) of the T-counter with respect to the binning of "good" electrons in the tagger. The occupancy of the E-counters vs T-counters is illustrated in Fig. 4.26 for each element in the ET matrix. The *gflux* code calculates the probability of a hit in each E-bin for each T-counter.

Figure 4.27 gives the conversion of E-bins to its corresponding energy. This histogram has to be independently calculated. The minimum bin is set to the maximum photon energy while the maximum bin is set to the minimum energy. Dead paddles were set to zero energy, of which there were only four.

4.3.2 Photon Flux Measurements

After the normalization runs are completed, *gflux* can be run on the productions runs. This is usually done in the regular cooking process. A bundle of histograms are produced for each run, giving the conversion factors as well as the total flux. The histograms have already been corrected by the tagging ratio. Figures 4.28 and 4.29 show the photon flux for the three-pass (E_e = 1.99 GeV) and the four-pass (E_e = 2.65 GeV) runs, respectively. The dips correspond to counters with poor efficiency or ones that are completely dead. When the analysis is being performed, the data is integrated into the same bins used in the yield partitions.

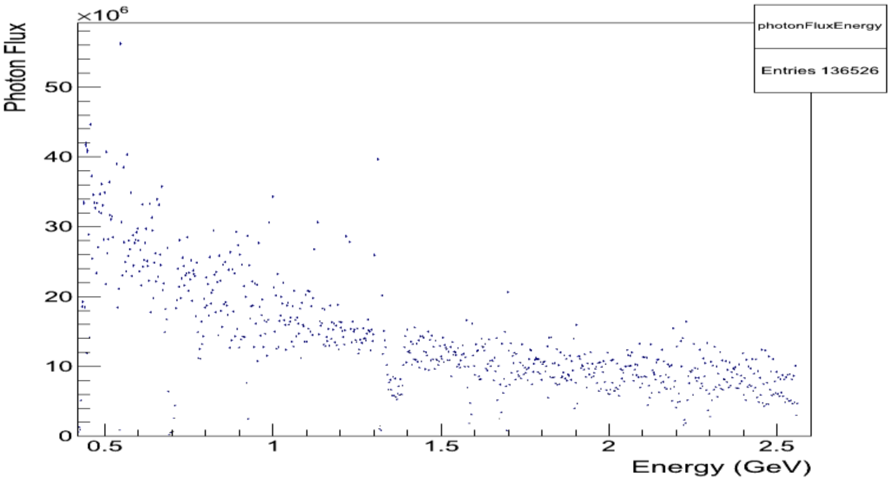

Figure 4.28: Photon flux for the three-pass (E_e = 1.99 GeV) runs.

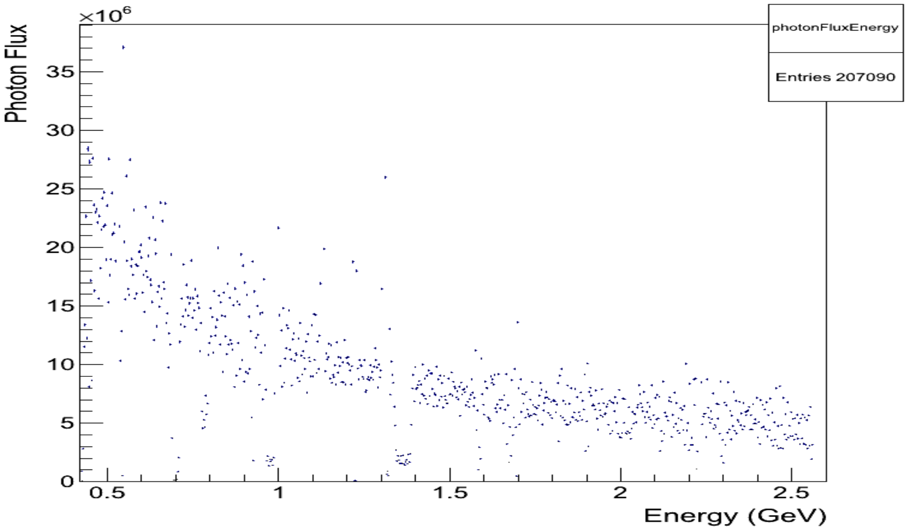

Figure 4.29: Photon flux for the four-pass ($E_e = 2.65$ GeV) runs

4.4 Yield Extraction

The distributions in Fig. 4.30 illustrate the clean distributions of the missing mass corresponding to the $\gamma n \rightarrow K_S\Lambda$ and $\gamma n \rightarrow K_S\Sigma^0$ reactions. The cuts on momentum and the missing mass of the K_S remove events that would require the associated production of a pion– such as in the case of the higher-mass hyperons Σ^* and Λ^*. The yields for both of these reactions can be determined by fitting the two missing mass peaks surviving all the cuts. Both the proton peak (corresponding to the missing mass of the $K_S\Lambda$) and the proton plus photon peak ($K_S\Sigma^0$) are fit with a single Gaussian. Integration of each fit is used to remove contributions from the other missing mass peak.

For full development of the differential cross sections, the data will be binned in terms of both photon energy and $\cos(\theta_{K_S}^{CM})$ and their values will then be normalized to the photon flux. The yields will then need to be acceptance-corrected from the results of the Monte Carlo simulation, which will be discussed in the Chapter 6. First, the yield correction factor will need to be calculated by studying how many good events are lost as functions of varying the cuts. This will give measure of the systematics. Similarly, the acceptance needs to be calculated using a realistic representation of the CLAS detector in the GEANT simulation.

The final yield is determined after several iterations of corrections to the cuts on the Δβ vs. momentum, track timing, invariant mass, missing mass of the K_S, and missing momentum. Fiducial cuts of the CLAS detector and corrections to the photon beam energy and track momentum must also be made. These steps are discussed in detail in the next chapter on systematic studies.

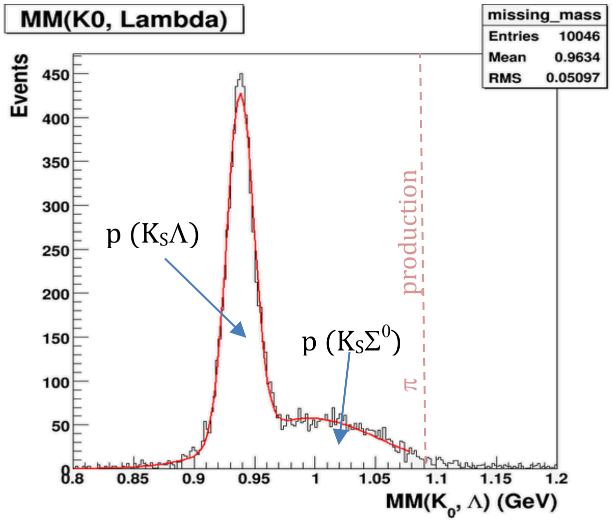

Figure 4.30: Missing mass distribution of the proton from $K_S\Lambda$ and with the distribution from the proton plus photon associated with the $K_S\Sigma^0$. Because of the cuts used in the code, events with Σ* do not survive.

Chapter 5

Systematic Studies and Corrections

Before the final yield could be extracted from the dataset, several particle track corrections must be applied and cuts checked for their effects on the final results. Inefficiencies, tagger sag, and "blind" spots required corrections for both the momentum and energy of the final-state particles. Additionally, due to the yield's sensitivity to the cuts made, it was necessary to justify the choice for each cut by their impact on both the yield and other essential particle properties. There effects were recorded and are presented in this chapter.

Whenever possible, fits are preferential to cuts to reduce the loss of events. However, cuts are always needed in a rich data set such as the g13 collection. Initial cuts were made during the actual cooking of the dataset. Scripts were run to create new data files which required specific final states– such as events with two positive/one negative tracks or two positive/two negative. Timing cuts are made on particles with times unique enough to question their involvement with the current event. Events are also cut if any of their tracks occur within inefficient time-of-flight (TOF) paddles. As part of particle identification, the analysis code separates particles first into positive, negative, and neutral tracks and then makes loose cuts on mass. After the track momentum and energy corrections are made, cuts are made on the invariant mass of the reconstructed intermediate particles (the candidate K_S and Λ particles). The final two related cuts are on the hyperons in the missing mass of the K_S distribution and on the missing mass of the $K_S\Lambda$ channel.

Before the reconstruction of the neutral-decay particles, it was necessary to correct the energy of the photon and the momentum of the final-state particles. The gravitational sag in the tagger system creates a small offset of the binning for electron (hence photon) energies. The T-counter and E-counters inefficiencies are fixed in the same energy correction method used for the tagger sag. The momentum needs to be corrected for both the energy lost in the target and the start counter before it reaches the drift chambers and the inefficiencies of the drift chambers. The standard eloss package[34] and Mattione's[35] drift chamber correction methods were used for this analysis.

5.1 Standards of the Systematic Studies

When choosing the cuts for any analysis, we must keep in mind what the criteria will be for maximizing the yield while maintaining quality data. For the $\gamma n \rightarrow K_S\Lambda$ reaction, there are three primary factors to be observed as cuts are applied– are the events exclusive, are they mostly from quasi-free neutrons, and will the cut exclude too many events? The percentage of exclusive events can be determined by fitting the peak (resonant) and background (non-resonant) for the distributions of the K_S and Λ masses. Changes in the ratio between the resonant to non-resonant integrals can be observed as various cuts are made. Since the target neutron is not truly free, the selection of events includes only events with the expected Fermi momentum from the deuteron nucleus. Events with extra momentum from rescattering can produce inaccurate missing mass and widen the proton peak. The effects of these cuts were also observed in the simulated data.

The calculated errors are a combination of statistical and data-range variation. The 4-pass (four passes through the accelerator loop) data was partitioned into four sequential data ranges to study the systematic variation within the dataset. The errors are then propagated to the complete 3- and 4-pass datasets. These segments are then used to observe variation in the effects from the cuts.

5.1.1 Exclusive Event Selection

After events have been reduced to those with the required final state, it is still necessary to determine which events come from a resonant ($K_S\Lambda$, $K_S\Sigma^0$ or $K_S\Sigma^*$) or a non-resonant ($p\pi^-\pi^-\pi^+$ or $p\pi^-\pi^-K^+$) event. In the case of the missing mass, there are only two clear signals after placing a cut on the missing mass of the neutral kaon (see Fig. 5.1). These two peaks can be clearly identified as the $K_S\Lambda$ and $K_S\Sigma^0$ channels. The cut is below the threshold of pion production, so it is unlikely other resonant channels are present. Both the Λ and Σ^0 yields can be independently extracted. There are, however, cases were non-resonant events are present; that is events which go straight to the $p\pi^-\pi^-\pi^+$ or $p\pi^-\pi^-K^+$ final states. These states are more visible if we go back a step and review the invariant masses of the neutral particles.

From the mass of the neutral decay particles (see Fig. 5.2) we can see a pronounced resonant peak on top of the non-resonant background. With a fit to the background and peak, the signal-to-noise ratio can be determined. Ideally these peaks come from the same resonance on top of the same non-resonant background and both should have the same ratio. As a quality check the fluctuation of these ratios and possibly overall decrease can be used to determine the quality of a cut or correction on the data. With good statistics there should be little variation in this ratio.

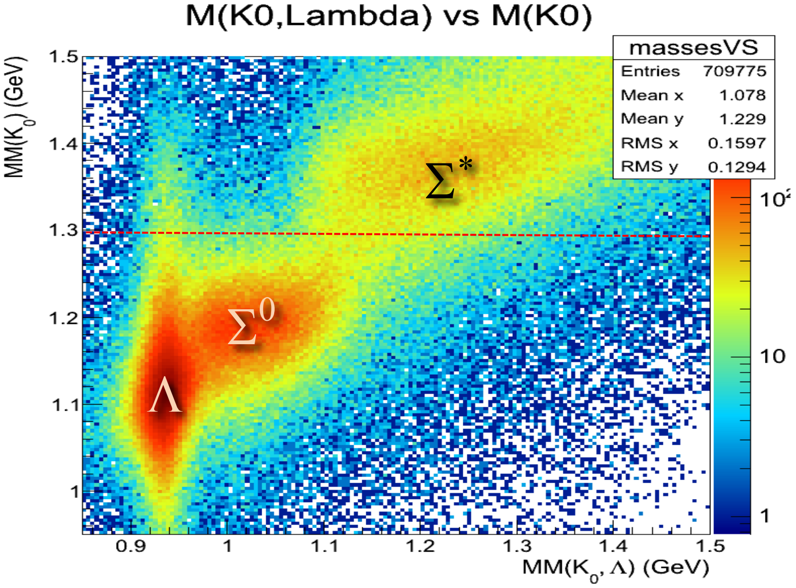

Figure 5.1: Missing mass of the $K_S\Lambda$ vs the missing mass of the K_S alone. The distributions are the mass of the proton (representing the Λ), the mass of the proton plus a photon (Σ^0), and the proton plus a pion (Σ^*). From the distributions we see that the Σ^* can be mostly removed with a cut on the $MM(KS) = 1.3$ GeV. However, the Σ^0 cannot be removed due to the strong overlap with the Lambda.

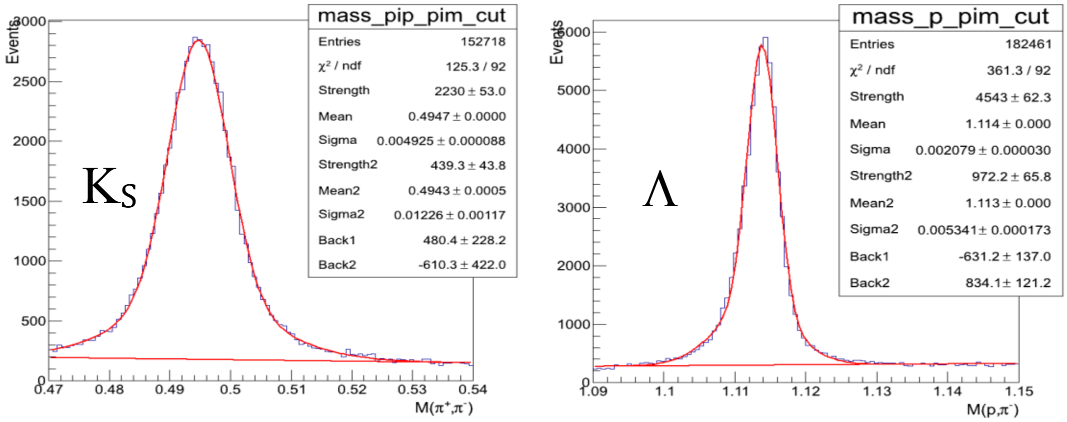

Figure 5.2: The fits to the kaon and Lambda peaks. The fits were used to determine the ratio of the resonant region to the non-resonant background. A double Gaussian was used to fit the peaks, corresponding to the energy resolution of the detector system and the uncertainty associated with the longer lifetimes of the particles. The background was locally fit with a linear function.

5.1.2 Quasi-Free Event Selection

The quasi-free events are primarily selected by the cut on the missing mass of the K_S, selecting mostly just the Λ and Σ^0 hyperons. A cut is also placed on the missing momentum of the spectator to remove many of the remaining events due to rescattering. Arguably, the order of these cuts can be reversed because of the direct relationship between the events with the heavier hyperons and the resultant excessive missing momentum. By plotting the missing mass vs. the missing momentum of the $K_S\Lambda$ channel (Fig. 5.3), we again see the hyperon distributions and their momentum dependence. Most of the protons reside withint the Fermi momentum (~50 MeV) uncertianty, with the vertical tail from rescattering. The Σ hyperons both have a linear relationship between their missing mass and missing momentum due to the extra particles not being exclusively measured (a γ or π, respectively).

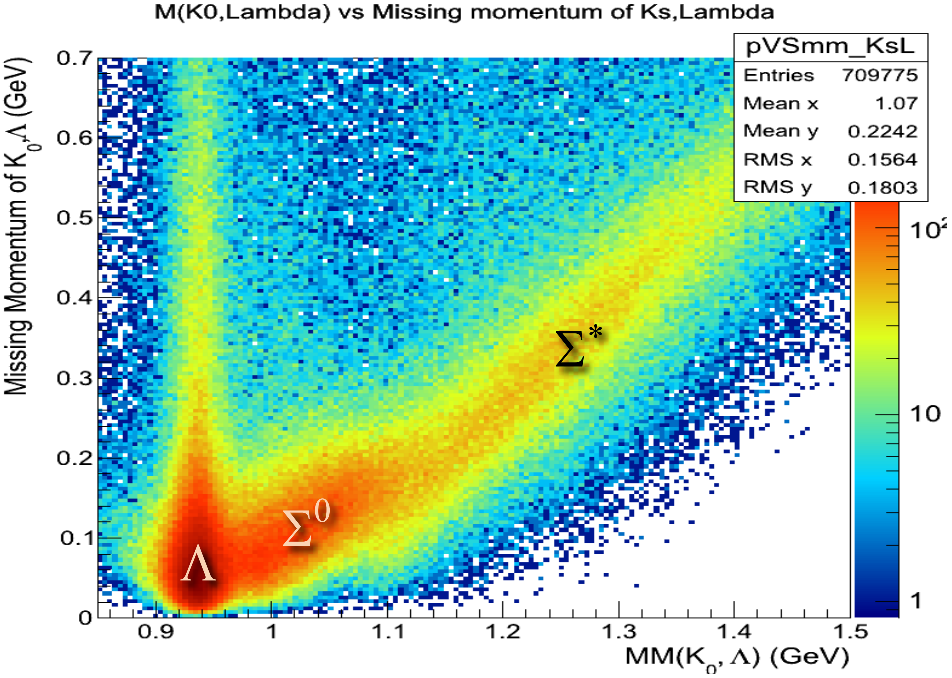

Figure 5.3: The missing mass of the K^0, Λ vs. its missing momentum, the proton can be seen by the vertical distribution, while the diagonal distribution implies events where an extra particle exists within the reaction.

The quality of cuts can then be determined by examining the slope of the missing particles' cosine theta verses its momentum. The slope is normalized to the yield for each run range, with the same cuts and corrections. Figure 5.4 illustrates how the angle of the missing momentum is used to check how many events are from quasi-free neutrons. The missing mass of the K_S cut has already been made in the right histogram. The top left histogram shows the projection of the cosine theta of the

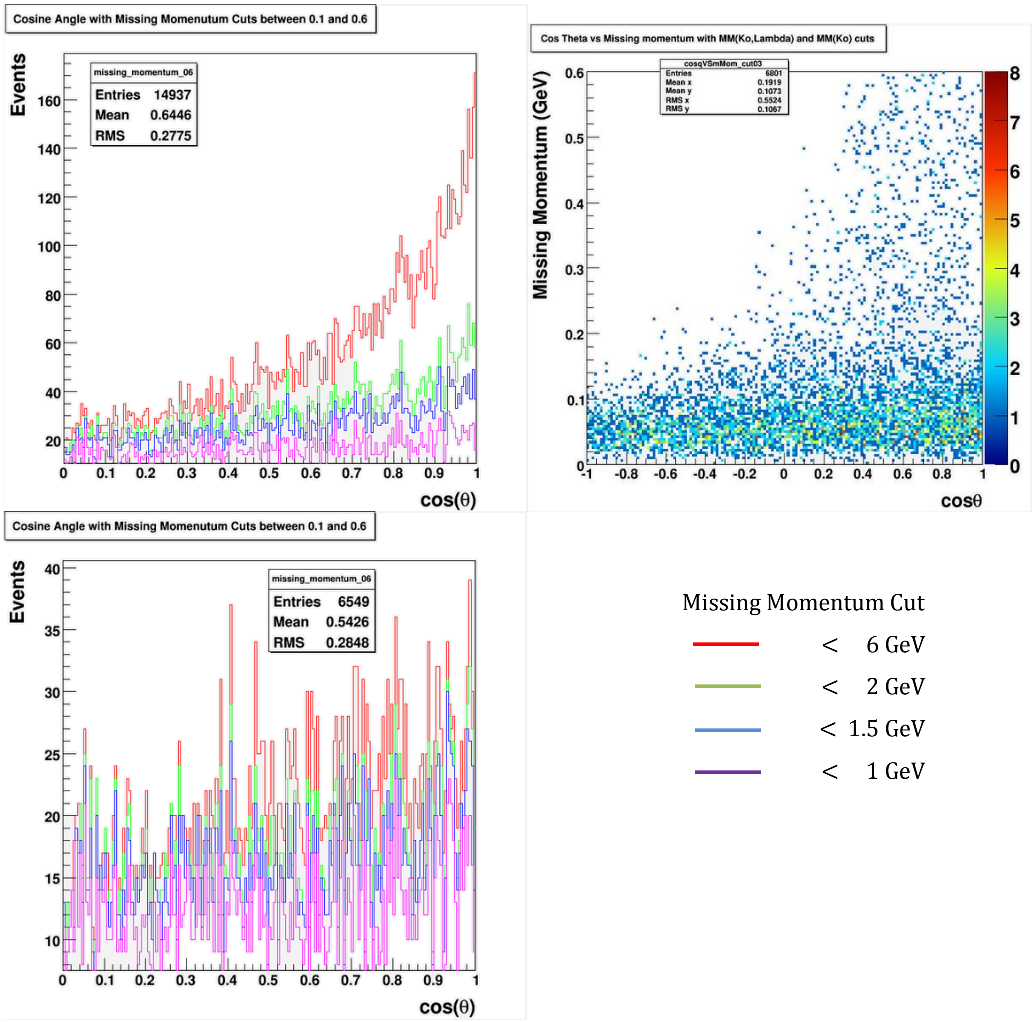

Figure 5.4: The angle of the missing momentum is used to check how many events are from quasi-free neutrons. The top left histogram shows the projection of the cosine theta of the missing particle (in the lab frame) verses its missing momentum with various cuts on the missing momentum. The bottom histogram shows the same projections but with cuts on the missing mass of the K_S.

missing particle verses its missing momentum with various cuts on the missing momentum. The spectator is expected to have no preferential direction (i.e. it should be isotropic). With wide cuts on the missing momentum (<6 GeV), there is strong evidence of events with extra momentum. This means that the neutron or one of its daughters scattered or there was an extra particle besides the proton in the missing mass. The bottom histogram shows the same projections but with cuts on the missing mass of the K_S. As can be seen in Fig. 5.5, there is little change with missing momentum cuts.

5.1.3 Yield Loss

The yield's decrease (and in some cases increase) must be evaluated as cuts and track corrections are applied. The absolute knowledge of the differential cross section relies entirely on our clear understanding of the systematics.

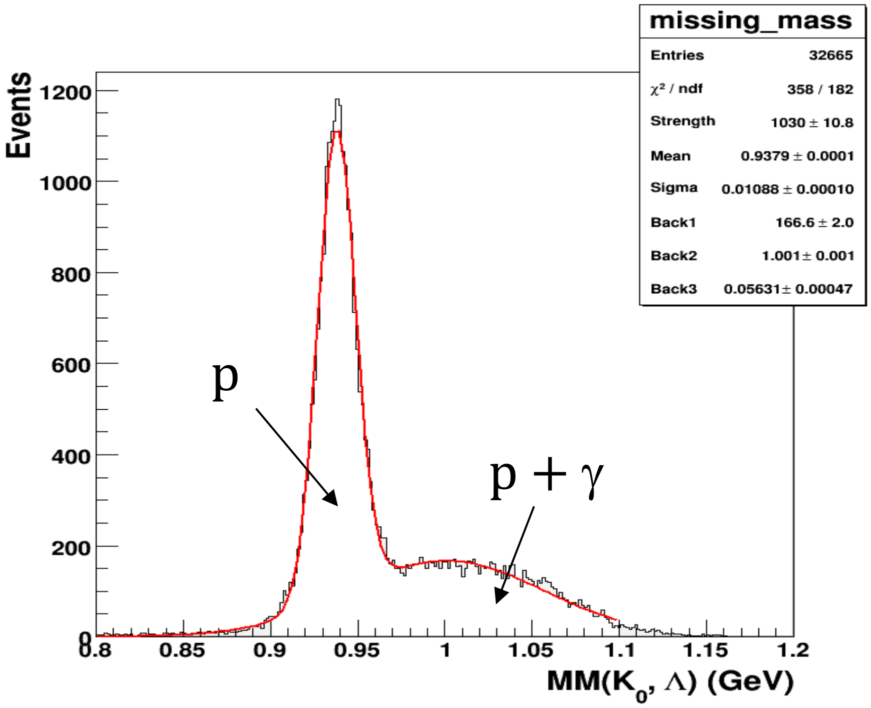

Figure 5.5: The missing mass of the $\gamma D \rightarrow K_S\Lambda(p)$ reaction, is used to determine the differential cross section of the reaction. This peak is one of the key checks when making corrections to the data.

5.2 Data Quality

The g13a dataset had approximately 202 billion triggers; yet a significant faction of these triggers could not be used. The largest portions of lost events were lost due to detector inefficiencies or unstable beam, though some were lost to corrupted or missing data tables. Table 5.1 shows the general run ranges for g13a. The first and last sets of runs were dropped because of their use of a hydrogen target, which is not applicable for this analysis. The run range 53095-53326 had significant loss of photon flux information and was not used in the reconstruction of the $\gamma n \rightarrow K_S\Lambda$ cross section. The full list of acceptable runs is given in Appendix B.1. Runs taken during the installation and calibration of various subsystems were also excluded, as were runs with failing systems. Runs with unstable beam were further excluded. Some additional runs are cut because of bad tagger counters or malfunctioning time-of-flight paddles. Most of these ranges were determined by studies performed by Mattione[35].

Table 5.1: General run ranges for g13a. The first and last ranges were not used due to difficulties in either photon flux reconstruction or to simulation difficulties.

Run Range	Target	Beam Energy (GeV)
53095-53163*	LH_2	1.99018
53164-53326*	LD_2	1.99018
53333-53429	LD_2	1.99018
53430-53537	LD_2	1.99018
53538-53862	LD_2	2.65458
53863-54041*	LH_2	2.00014

* not used in the reconstruction of the $\gamma n \rightarrow K_S\Lambda$ cross sections

5.2.1 Skim Files and Missing Banks

As the data is sorted into the data banks of the BOS files (databanks with CLAS table format) during the cooking process, additional *skim* files are produced accepting only events with the minimum number of charged tracks. For this analysis the skim file datasets with at least two positive and two negative tracks were used. Skim files are much smaller than the BOS files and allow for much faster analysis jobs on the batch farms. They also introduce a new possible source of data loss if not all the qualifying events are correctly copied to the skims. To examine this possibility several runs were used to compare both the initial BOS files and the skim files. Checks were made to ensured files lost on the batch farms during processing or copying to the work disks were excluded from both the BOS and skims. Final results showed absolutely no difference between the skimmed and BOS files. Therefore, the skimmed files were used for the analysis instead of the BOS files.

It is also necessary to track how many events are lost from empty banks and from channel-specific skimming. There were many reasons an event was rejected during the selection process. Before they were processed through particle identification checks, the data was checked for integrity. While the data is catalogued, rejected events are tallied into three areas– EPICs drops, EVNT or TAGR drops and too few tracks, as tabulated in Table 5.2. The percentage of loss from the first two columns also applies to the second two columns (corresponding to the skim files). These percentages were not applied in the skim lost percentages; the events lost from the skim files are measured independently. The EPICS bank contains all the channels of the various detector systems and scalars. EVNT has the basic information for each track in an event, to

Table 5.2: Events lost from the analysis before and during the analysis process from initial event and track requirements. The first two columns' percentage of loss also applies to the second two columns of the skim file losses. However, they are not applied. The events lost from the skim files are independently tallied.

	BOS Files		**Skim Files**		**Simulated**	
Reason Event was Dropped	*Average*	*Standard Deviation*	*Average*	*Standard Deviation*	*Average*	*Standard Deviation*
EPICS event missing	0.0081%	0.0002%	1.25%	0.0423%	0.0%	0.0%
EVNT missing	16.58%	0.0090%	1.28%	0.09%	37.10%	1.26%
TAGR missing	0.0%	0.0%	0.0%	0.0%	0.0%	0.0%
Too Few Tracks	62.59%	0.0742%	0.0%	0.0%	55.96%	1.88%
Too Few Final State	20.62%	0.0833%	64.82%	0.22%	5.10%	0.17%

Table 5.3: Events lost from the analysis before and during the analysis process due to secondary requirements on the tracks. The first two columns' percentage of loss also applies to the second two columns of the skim file losses. However, they are not applied. The events lost from the skim files are independently tallied.

3+ π^-	0.0005%	0.0%	0.0780%	0.0059%	0.0003%	0.0002%
3+ π^+	0.0%	0.0%	0.0042%	0.0030%	0.0%	0.0%
3+ proton	0.0004%	0.0001%	0.0635%	0.0102%	0.0001%	0.0001%
both protons rejected	0.0143%	0.0004%	2.25%	0.0843%	0.0013%	0.0004%
both protons qualified	0.0009%	0.0%	0.1302%	0.0035%	0.0027%	0.0005%
both π^+ rejected	0.0035%	0.0004%	0.5291%	0.0391%	0.0024%	0.0004%
both π^+ qualified	0.0001%	0.00003%	0.0142%	0.0039%	0.0008%	0.0002%
extra Λ	0.0%	0.0%	0.0%	0.0%	0.0%	0.0%
extra K	0.0%	0.0%	0.0%	0.0%	0.0%	0.0%

include momentum, mass, charge, beta, and position. It also records the status of the primary subdetectors of CLAS during this event (e.g. drift chamber, start counter, etc). The TAGR bank stores the information of each photon in the vicinity of the target length during the event. As can be seen in Table 5.2, few events are lost from EPICS. However, in the BOS files, nearly 17% is lost from the EVNT bank. When the EVNT bank existed for an event, the TAGR bank was always present. For the simulated events, 37% are lost as the generated particles are propagated through the modeled CLAS system and cooked into the standard BOS format. Both real data and simulated lose around 60% of the events due to having too few tracks. Since the skimmed files follow from the BOS files, it is expected that very few losses occur at this point. Filtering by the required final-states particles in the skim files reveals that only about 35% of the particles are real candidates. Approximately 26% of the BOS events and 49% of the simulated qualified for $K_S\Lambda$ reconstruction. The bookkeeping shows very few events have more than two π^- s, π^+ or protons in the final state.

Proportionately, the percentage of events lost from too many qualifying protons and pions (only one each is desired) are nearly the same with all three trials (see Table 5.3). The percentage of these lost events is clearly higher in the pre-skimmed files because they exclude events with less than four tracks. For this same reason, the percentage of events with both protons (or π^+) failing or passing the missing mass cuts increases in the pre-skims. None of the skims showed significant combinatoric background events.

5.3 Particle Identification Studies

Before possible events were selected, each particle in the event were catalogued by their charge, mass, momentum, and timing. By the deflection (bending inward or outward) of each particle in CLAS, the charge of the particle is identified. The mass is only used as a very loose separation of the pions and protons. This leaves the momentum and the timing as the primary tools for particle identification. Since there is no clear error associated with the values in the data banks, the variation due to the selection of beta and time cuts is used to determine the uncertainty.

As was discussed in section 4.1, a loose mass cut is put on the $\Delta\beta$ vs. momentum as can be seen in Figs. 5.4, 5.5, and 5.6. Initial skimming incudes a 0.2-$\Delta\beta$ cut and a 6-ns track timing cut. The initial loss of events was determined by looking at the percentage of lost Λ and K_S candidates (as can be seen in Table 5.3). Due to the losses from both neutral hadron candidates, roughly 6% of the events are lost from the missing mass of the reaction. Studies were performed to see if tighter cuts improve the yield extraction, resonant mass extraction, and percentage of quasi-free neutrons reactions.

Table 5.4: Initial loss of events from the pre-PID cuts on the beta and track time.

	Lambda Mass Mean	**Lambda Sigma**	**Loss (%)**	**Kaon Mass Mean**	**Kaon Sigma**	**Loss (%)**
No cut	1.116	0.00187	0	0.4977	0.00477	0
Beta cut	1.116	0.001942	1.03	0.4978	0.004726	0.86
Beta and timing cut	1.116	0.00194	2.72	0.4978	0.004894	3.65

5.3.1 Beta Cuts

Figures 5.6 through 5.8, illustrate the development of distributions for the π^-, π^+, and proton respectively. The isolation of each track distribution in the histograms illustrates the initial loose mass cuts. The 0.2-GeV cuts on each Δβ has already been applied. The top left histogram shows the beta distribution for each track and the top right shows the difference between the measured and calculated β (the Δβ). The bottom left shows the momentum versus the beta and the bottom right the momentum verses beta difference. The calculated β uses the fixed PDG values for the particle mass, forcing tracks with the correct mass (and therefore similar β) to have a Δβ near zero.

To refine these cuts on Δβ, the events were binned into 0.1-GeV momentum bins. The peaks were then fit with a Gaussian. The sigma of peak was then used to determine cuts for each momentum bin. The σ, 2σ, and 3σ cuts were compared to evaluate the changes in the event selection. Figure 5.9 shows the mean with its 3σ for each momentum bin for both pions and the proton.

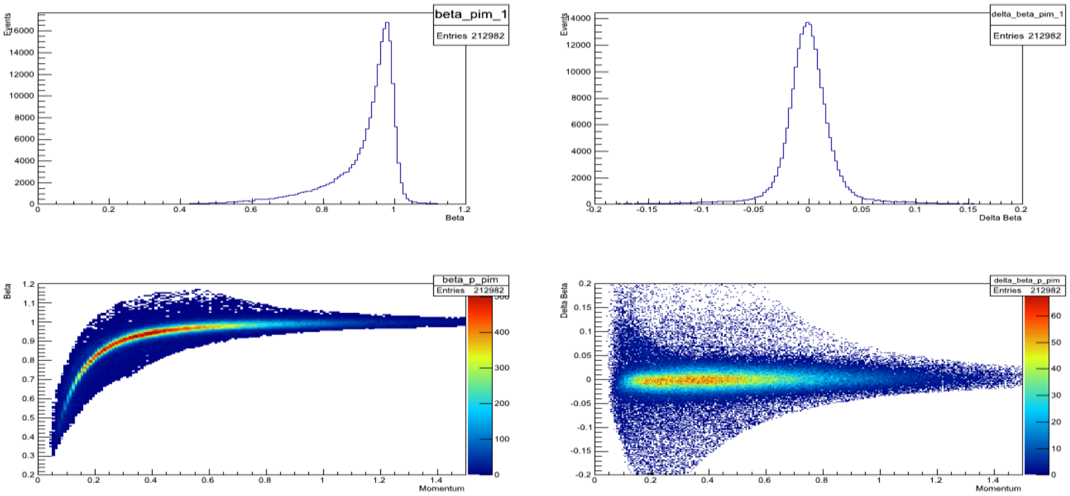

Figure 5.6: Beta histograms for the π^-. For the particle identification, the mass was taken to be between −0.1 and 0.1 GeV. The difference of the measured beta and the calculated are shown in top right plot. The bottom left and right show the β and Δβ vs. the momentum of each particle, respectively.

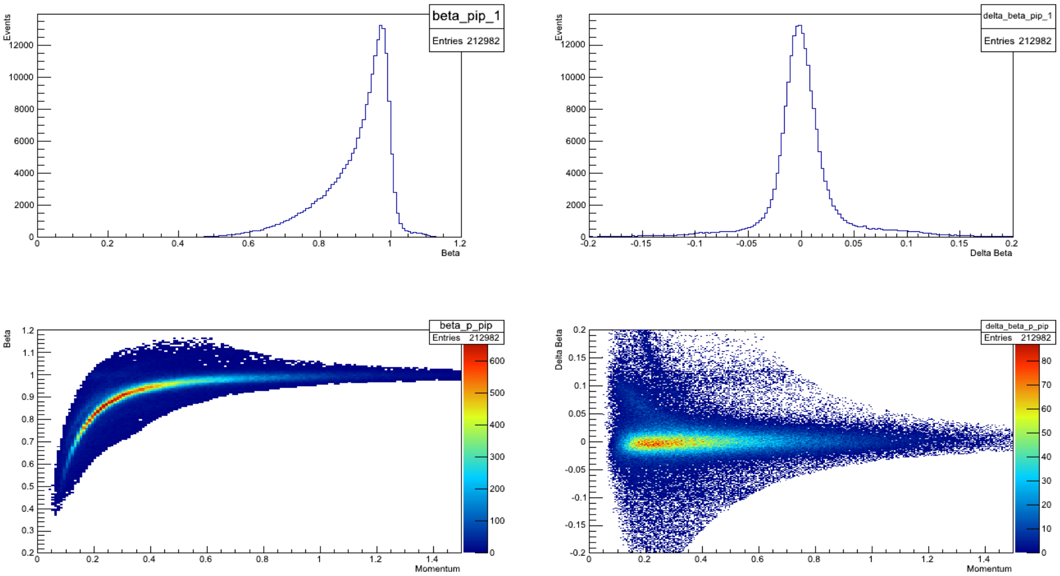

Figure 5.7: Beta histograms for the π+. For PID, the mass was assumed to be between –0.1 to 0.1 GeV. The difference of the measured beta and the calculated are shown in top right plot. The bottom left and right show the β and Δβ vs. the momentum of each particle, respectively.

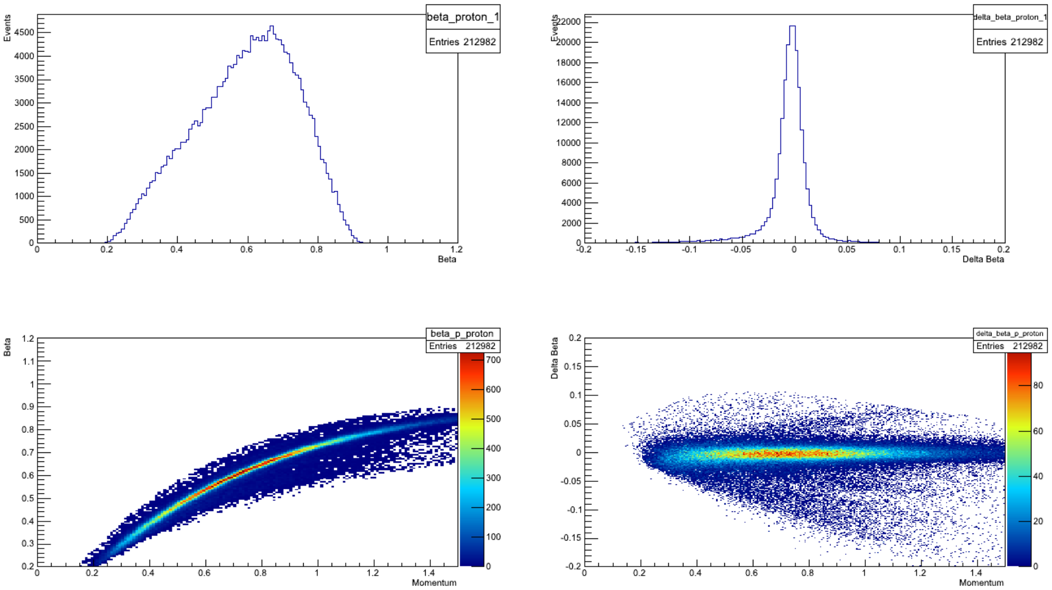

Figure 5.8: Beta histograms for the proton. For PID, the mass was assumed to be at least 0.5 GeV. The measured beta of the particle is shown in the first histogram. The difference of the measured beta and the calculated are shown in top right plot. The bottom left and right show the β and Δβ vs. the momentum of each particle, respectively.

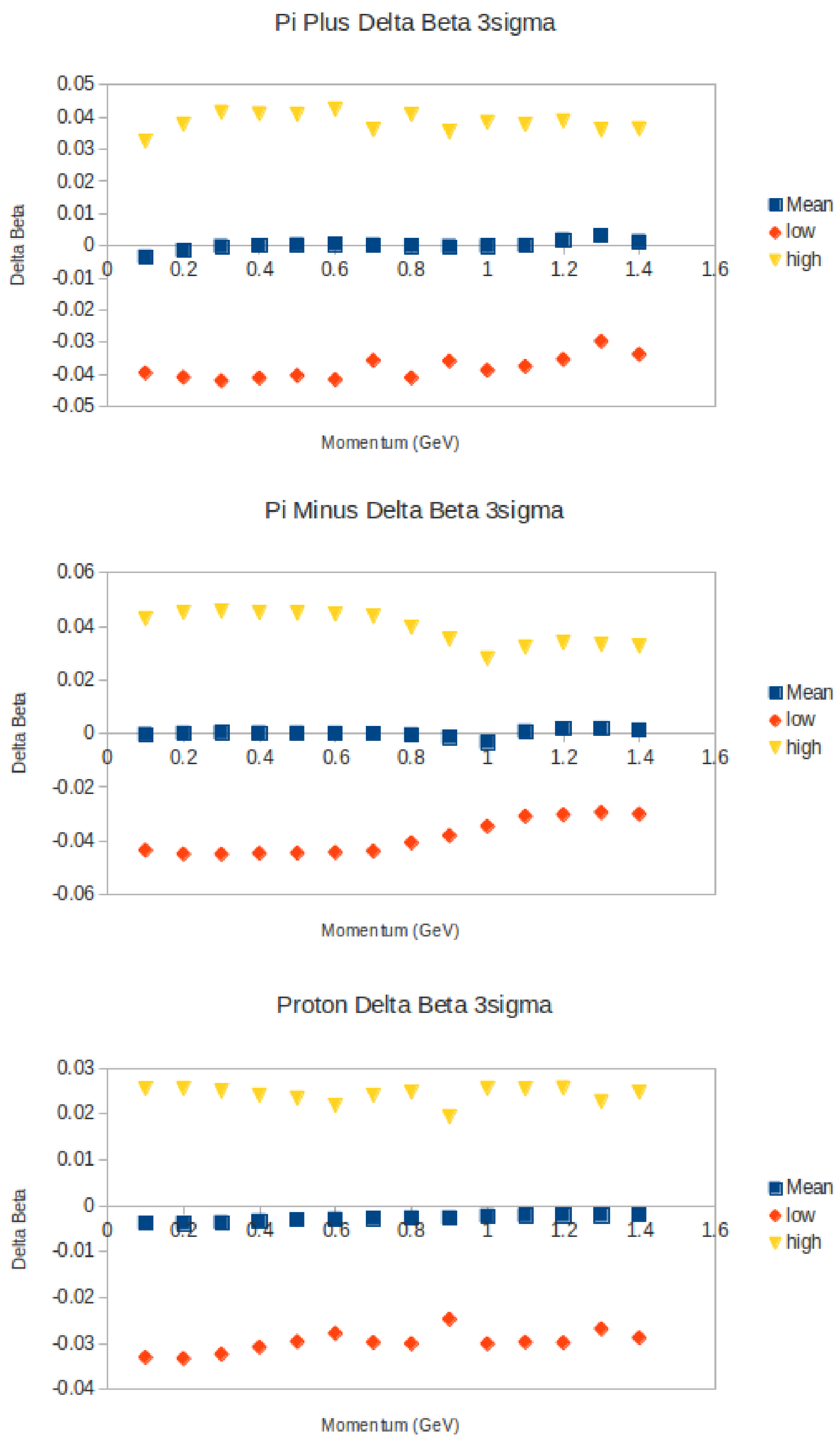

Figure 5.9: The Δβ was binned by momentum and fit with a Gaussian. The 3σ give the limits to use for cutting events from the analysis. The plots show the mean and high and low 3σ values for each momentum bin.

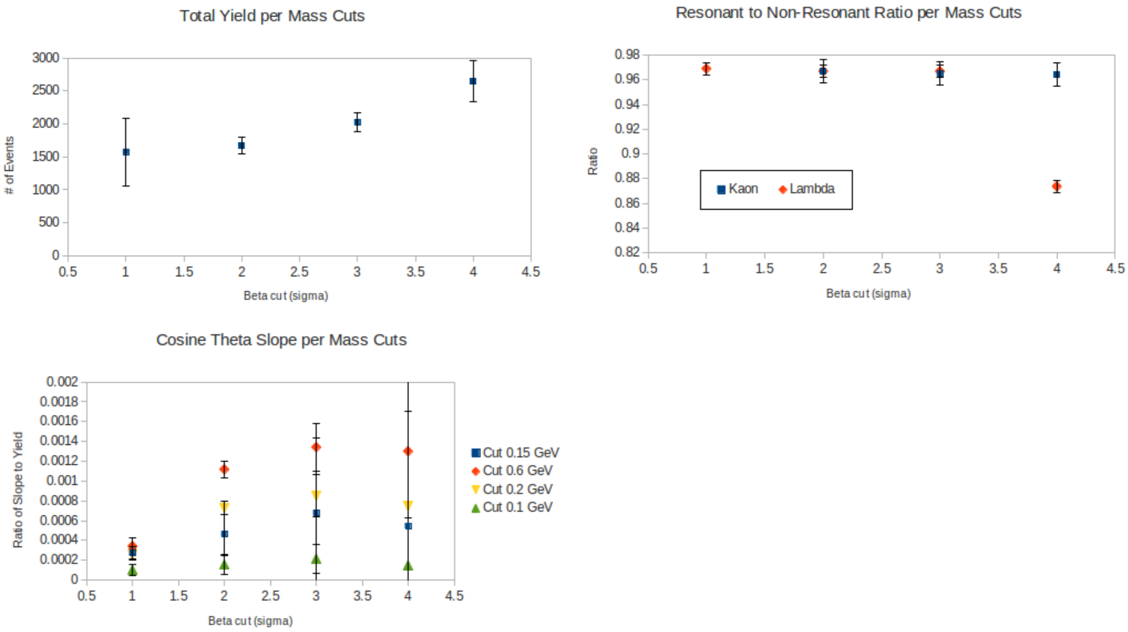

Figure 5.10: The top left histogram shows that the 3σ cuts on the Δβ binned by momentum, which only has a minor effect on the yield. The top right plot shows the resonant to non-resonant ratio for the invariant mass peaks. The 3σ has the greatest difference with 0.006, which is too small to be concerned with. In the yield-normalized slope of the missing mass angle, the 3σ has the greatest slope, though still small.

The results of the cuts can be seen in Fig. 5.10. As one would full expect, the tightening of cuts on the Δβ distribution has a notable effect on the distribution of the cosine theta of the missing momentum. The tighter cuts would remove poorly identified particles as well as events with poorly-reconstructed momentum values from inefficient detectors. The 3σ and tighter cuts do show a significant improvement in the invariant mass ratios with respect to each other, while 4σ has a quick fractional loss to the Λ particle ratio. To minimize the loss of yield, the cut was kept at 3σ.

5.3.2 Timing Cuts

During the initial particle section of the skim code, a cut was placed to exclude any track that was greater than six nanoseconds from the average time of all tracks in the events. Tracks were usually within 1 ns of each other. However, to reduce the likelihood of extraneous particles contributing to the event, further refinement to the cuts were made to evaluate their effects on event selection and the final yield.

Using the corrected event time, the events with any final-state tracks outside of a variable timing window were excluded. As can be seen in Fig. 5.11, the most significant change is due to the loss in the upon total yield. The mass ratios and missing mass's cosine theta distributions remained relatively unchanged. This is reasonable since the reconstruction of the K_S and Λ masses would remove most of the out-of-time events. Since little benefit was gained from tightening the track timing window, it was decided to leave the window at 6 nanoseconds to maximize the yield.

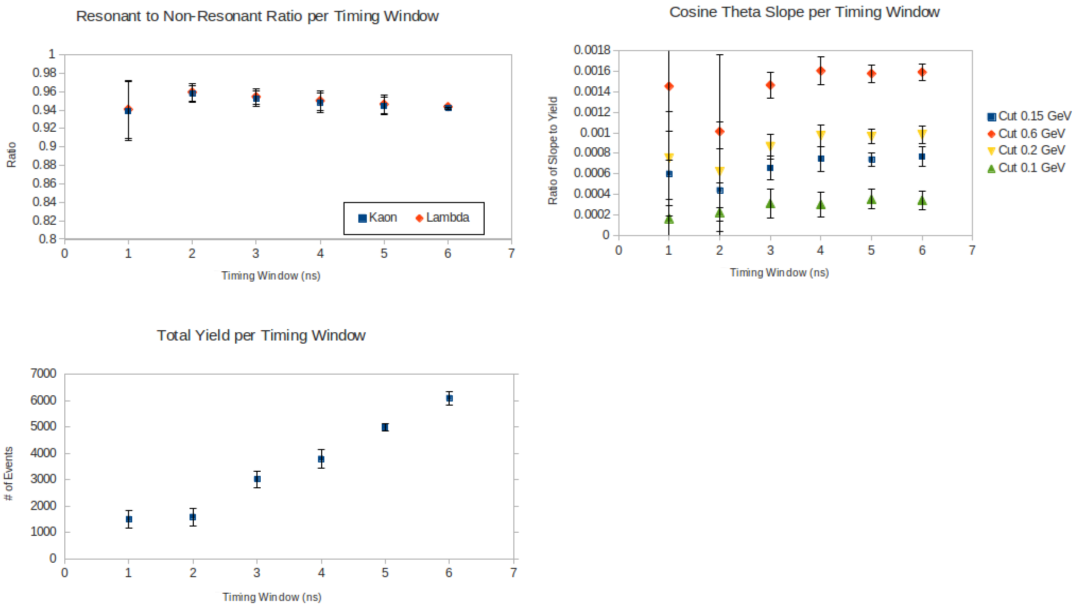

Figure 5.11: The top-left histogram shows the loss in total yield with decreasing track timing window. The top-right and bottom-left show the nearly constant resonant mass ratio and normalized slope, respectively. Since there is little improvement in the exclusive selection of events and the percentage of quasi-free events, it was decided to keep the timing window to six nanoseconds.

5.4 Yield Extraction Studies

There are three important checks to make in coding the analysis process when finding the total and differential yields. First, the quality of the cuts on the invariant masses of the neutral decay particles was examined, as well as the cut made on the missing mass of the K_S. If the cuts are not robust (i.e. highly sensitive) appropriate adjustments would be necessary. It was also important to test the fits to the missing mass of the $\gamma n \rightarrow K_S\Lambda$ and $\gamma n \rightarrow K_S\Sigma^0$ reactions.

5.4.1 Invariant Mass Cuts

After particle identification and track pairing, the key cut is the invariant mass cut. It is clear that unduly tightening the cut would reduce the yield. Less clear is that the resonant to non-resonant ratio remains essentially constant (as was observed in the data seen in Fig. 5.12). This behavior is most likely expected with a linear phase-space, and reaffirms the choice of the fit used for the non-resonant background. Since the ratio does not change and the invariant mass cut is not selective on particle momenta, it is not unexpected that changes with the slope or the anisotropicity of the spectator proton's angle appear to only fluctuate within expected statistical uncertainties and do not appear to follow any systematic errors. Due to the larger uncertainty of the yield and slope using the 4σ cut (due to the excessive quantity of non-resonant events), the 3σ was used for the invariant mass cuts.

5.4.2 Missing Mass of the K_S Cuts

Figure 5.13 shows the hyperon distributions by plotting the missing mass of the $K_S\Lambda$ reaction against just the missing mass of the K_S. While it is clear that the majority of Σ^* can be removed from the Λ distribution, the Σ^0 has significant overlap requiring fits to

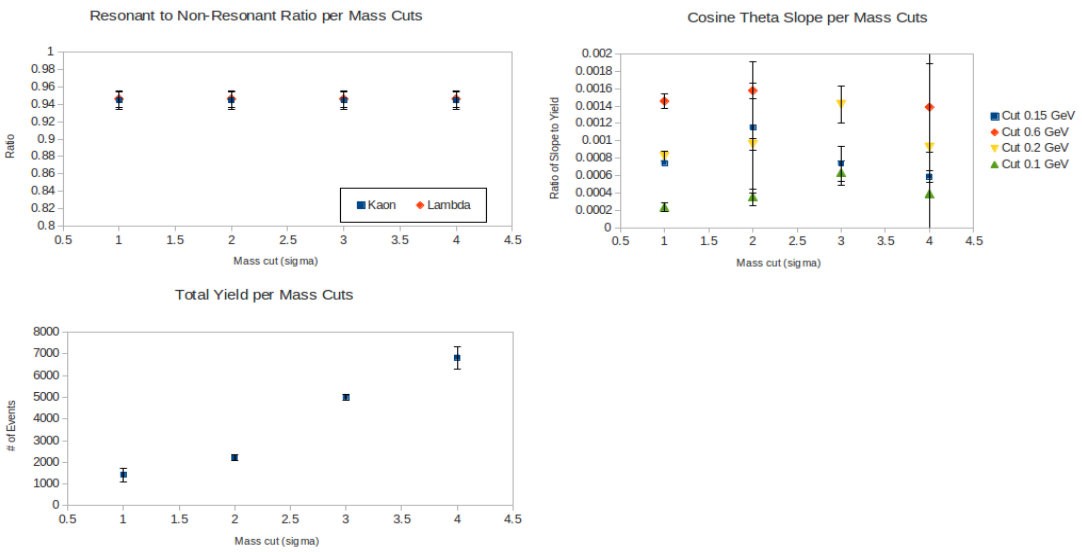

Figure 5.12: Changes in the yield, resonant to non-resonant ratio and slope of the spectator proton's angular distribution with changes to the invariant mass cuts. The *x*-axis shows the number of sigmas used for each evaulation. For each point, the 4-pass data was divided into four ranges of data.

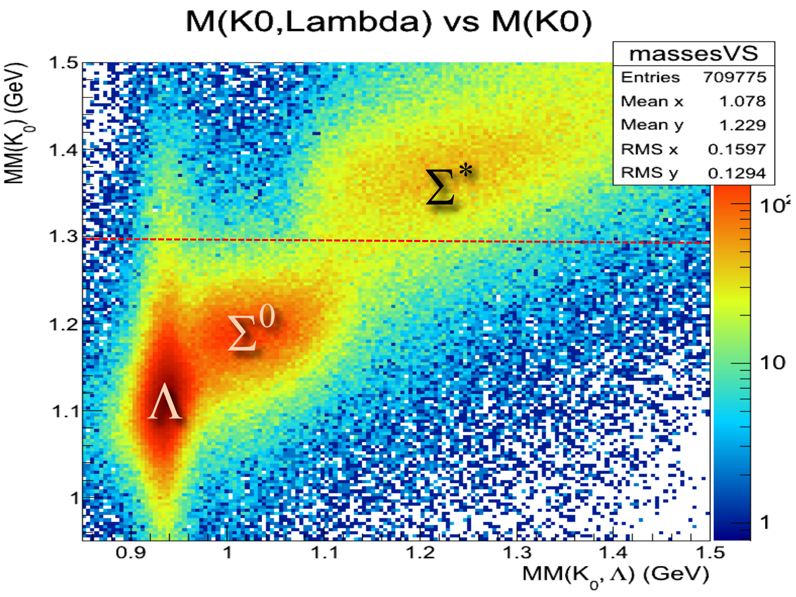

Figure 5.13: The hyperon distributions can be seen with the plot of the missing mass of the $K_S\Lambda$ reaction against just the missing mass of the K_S.

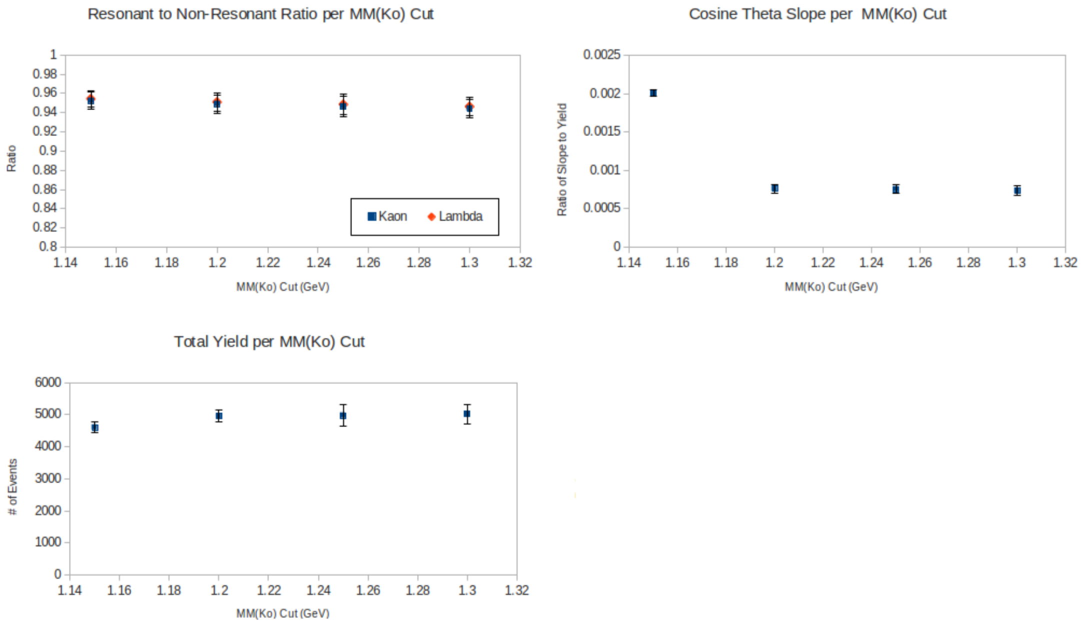

Figure 5.14: Changes in the yield, the resonant to non-resonant ratio, and slope of the spectator proton's anglular distribution with changes to the K_S missing mass cuts. The *x*-axis shows the number of sigma used for each evaulation. For each point, the 4-pass data was divided into four ranges of data.

separate the two peaks. However, cutting the Σ^* out does remove some of the Λs. This loss can be seen in Fig. 5.14 with the decreased sigma in the first histogram.

With the missing momentum cuts in place, most of the contributions from the Σ^*s have been removed. From the bottom plot in Fig. 5.14, it can be seen that with a missing momentum cut of 200 MeV, the slope of the spectator proton's angular distribution remains constant until the cut nears the center of the Λ peak.

With these momentum cuts, we can also go back and check the ratio of resonant to non-resonant with the invariant mass. The choice of cutting on the missing mass of the K_S does not affect the signal-to-noise ratio. Once the Σ^* has been essentially removed (momenta $>$ 1.3 GeV), only the Σ^0 overlaps with the Λ distribution. As can be seen in Fig. 5.3, both distributions share similar momentum. Therefore, the lower the cut on the missing mass of the K_S cannot distinguish between the two channels.

5.5 Track Corrections and Cuts

With a Gaussian fit to the peak of the missing proton mass, we can find a preliminary yield of the $K_S\Lambda$ channel. However, before this yield can be final, several corrections must still be applied to account for various systematic uncertianties. First, the standard energy-loss corrections must be investigated. While the particles pass through the start counter, they lose information on the 4-momentum from dE/dx losses and multiple scattering. This loss can be approximated by the Bethe-Bloch equation[30], which can be corrected with the *eloss* software package[31]. The *eloss* correction was applied during the reconstruction of the neutral Lambda and kaon particles from the charged daughter products. It will also be necessary to apply a momentum correction for the particle's track through the drift chambers. This correction makes use of a kinematic fit of the $\gamma D \rightarrow pp\pi^-$ reaction[32].

Energy corrections were also needed. The beam delivered to Hall B does not exactly match the requested or recorded beam energy. Again, the $\gamma D \rightarrow pp\pi^-$ reaction was used as a method of applying corrections. The energy was also corrected for the systematic uncertainties in the binning of electron energy in the tagger hodoscope due to gravitational sag to the E-counters.

In addition to these corrections, it was also necessary to cut events. Events were removed when they involved an inefficient tagger counter, dead SC paddle, or enter regions of the detector where the toroidal coils block detection (fiducial cuts). Paul Mattione performed the initial studies on the efficiencies for the tagger, time-of-flight, beam energy corrections, and the detector fiducial cuts for g13a. He wrote C++ libraries that apply the corrections from his studies. His methods are being used by several studies on the g13 dataset[33].

5.5.1 Tagger Corrections and Cuts

Due to the distortion of the tagger's focal plane from the weight of the system, electrons are potentially arriving at the wrong energy bins[34]. This effect can shift the knowledge of the photon energy by as much as 0.2%. This correction factor is not large, but can have some impact on the differential cross section. The correction is E-counter dependent, as can be seen in Fig. 5.15.

As described in section 3.2, the photon tagger system has 61 T-counters (with a non-uniform distribution) and 384 E-counters with a 1/3 overlap. Inefficient or dead overlapping counters can lead to the incorrect binning of the photon's energy. Therefore, the skim code and simulation were set up to reject events from inefficient T- and E-counters.

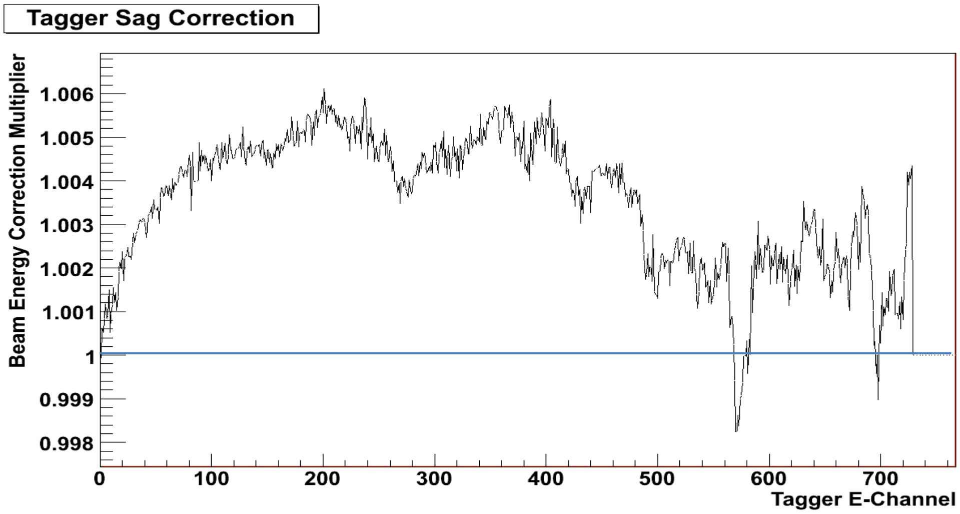

Figure 5.15: The photon correction multiplier for the energy[36]. This correction is due to the sag in the tagger under its own weight, which will shift the position of the counters from the "true" position.

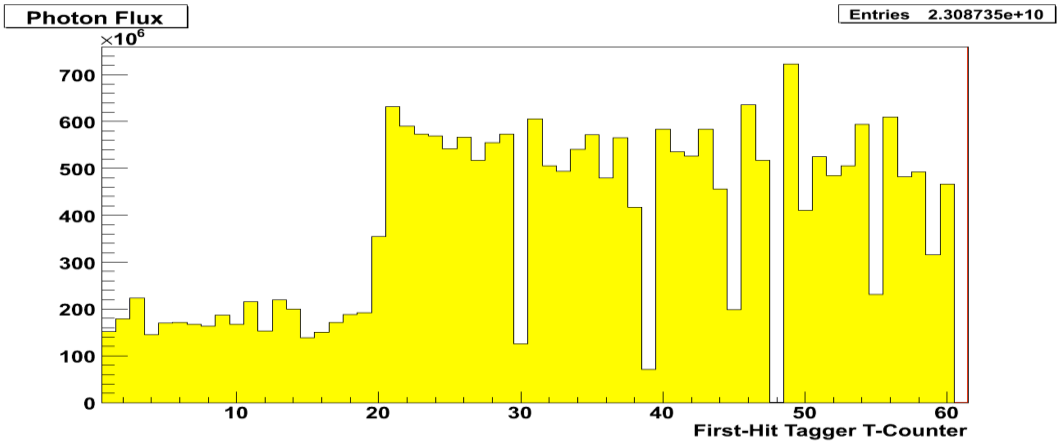

(a)

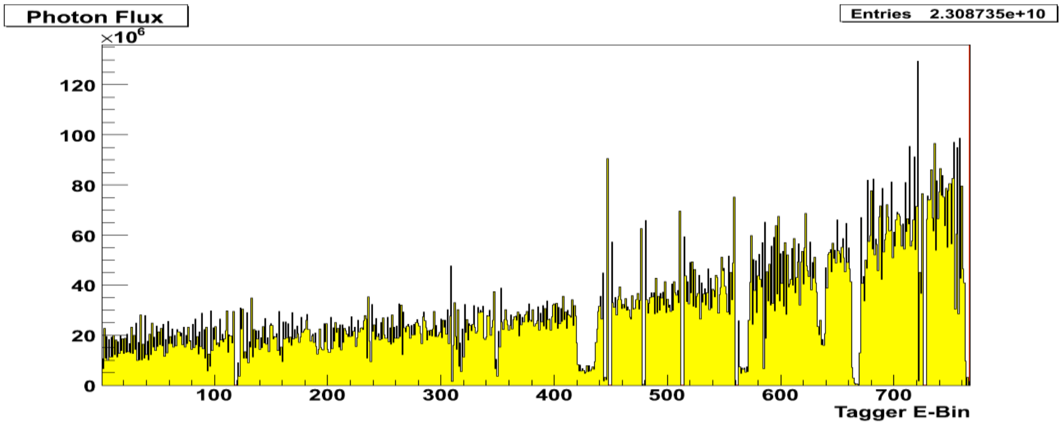

(b)

Figure 5.16: (a) The T-counter first-hit vs. the photon flux and (b) the E-counter first-hit vs. the photon flux. The holes are due to the dead or inefficient counters. The images were taken from Paul Mattione's dissertation [32]. The highest bin corresponds to the lowest E_{γ}.

In Fig. 5.16, the efficiencies of the counters can be seen by looking at the photon flux and particle yields as a function of the counters. Counters were considered inefficient if they had less than half the flux of the neighboring counters. From the photon flux per first-hit T-counter it is clear that the counters 30, 39, 45, 48, and 55 had weak counts, while counter 61 was completely dead. The flux distributions for the E-counters reveal the dead or low count E-counters 60, 225, 240, 257, 281, and 364.

5.5.2 Time-of-Flight Paddle Cuts

The time-of-flight scintillator (SC) paddles surrounding the body of the CLAS system, in conjunction with the start counter, were used for the stop time of the particle tracks. This time can also be constructed using the start counter time and the momentum determined from the track deflection in the drift chambers. Specifically:

$$t_{calc} = t_{ST} + \frac{\ell\sqrt{m^2c^4+p^2c^2}}{pc^2}, \tag{5.1}$$

Where t_{ST} is the start counter time, and ℓ is the path length of the particle. The difference between the calculated and measured SC paddle time was used to determine which paddles were dead or inefficient, as shown in fig 5.17. Scintillator paddles with low or no counts can be seen as vertical disruptions in the distributions of Δt_{ST}. Some of the paddles show poor alignment or double peaking. Most of these uncalibrated paddles are in the backward region.

Table 5.5 lists the paddles per sector removed from both the experimental and simulated data. Paddle 8 in sector 1 was dead for a larger portion of the g13a data set, while the other dead counters remained that way for the duration of the experiment. It was not possible to replace some of the dead photomultiplier tubes (PMTs) because of their position behind the electromagnetic calorimeter and hence were completely inaccessible.

To ensure few events were lost, CLAS was designed with a large overlap of the two TOF planes. Despite the effectiveness of this configuration, it was not precisely modeled in the GSIM code. Because of this, paddle 23 for all sectors was excluded from all analysis.

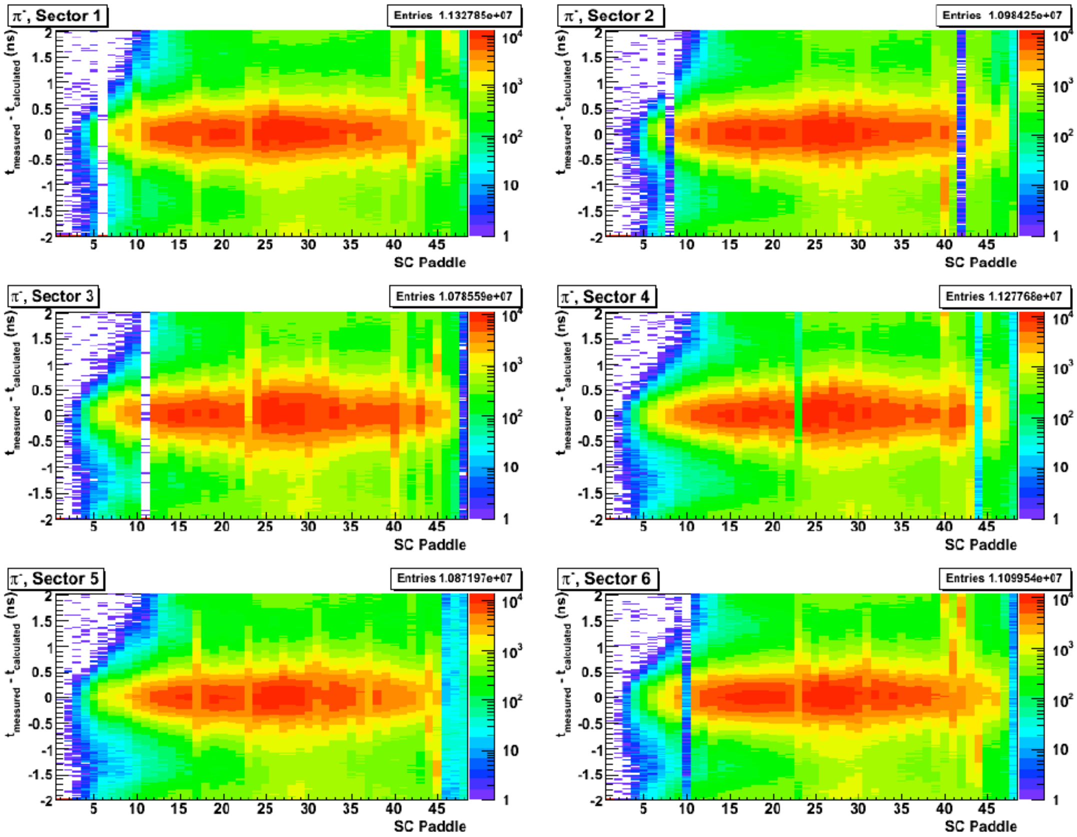

Figure 5.17: The difference between the calculated and measured stop times for different SC paddles, from the systematic studies of Mattione[32]. The dead, inefficient, and dead paddles can be seen in the otherwise symmetric distribution. Events with tracks on these SC paddles were cut from both the empirical data and the simulated studies.

Table 5.5: Dead, inefficient and uncalibrated paddles per sector. Both experimental and simulated events with tracks entering these paddles are removed from the analysis

Sector	Dead Paddles	Inefficient Paddles	Uncalibrated Paddles
1	6	10, 24	23, 40 - 48
2	8		23, 40 - 48
3	11		23, 40 - 48
4	-		23, 40 - 48
5	-	24, 29, 30, 31, 37	23, 40 - 48
6	24, 25, 31	24, 25, 31	23, 40 - 48

5.5.3 Fiducial Cuts

As with most detector systems, the efficiency of particle detection for the CLAS drift chamber decrease at the boundary regions. These regions are defined by the six sectors segmented by the toridial magnets and the support frames for the chambers. The GSIM simulation poorly models the loss of events within these regions. Therefore, it becomes necessary to apply angular fiducial cuts in both azimuth and polar distributions for both the measured and simulated data. For this study, Paul Mattione's methods and routines were used[32].

From Fig. 5.18, we can see the distribution of events within the drift chambers. The edges correspond to the areas of transition between chambers azimuthally, as well as the theta angle acceptance. The figures shown were made for both negative (left) and positive (right) pions at all theta and phi angles, but for the just the first few centimeters of the target. The 10-centimeter bins were necessary because of the change in cuts needed for the backward angles. From Fig. 5.18 it can be seen that the positive tracks have some momentum dependence at the small theta angles. This is due to the positive tracks being bent into the beamline and while the negative are bent away.

For the fit to the distribution, the code uses a function of the form:

$$\phi = \begin{cases} C_1\left(1 - e^{C_1\theta + C_2}\right), & C_3 < \theta \\ \left(C_4 + C_5\theta + C_6\theta^2\right), & C_3 > \theta \end{cases} \tag{5.2}$$

where the C_i are the parameters of the function fit. A high and low cut were also placed on the theta angles. Two different equations can be used, depending on θ, (defined by parameter C_3). The function form is not a direct function C_3, but does depend on it for choice of which curve to use. The negative phi angles were assumed be symmetric with

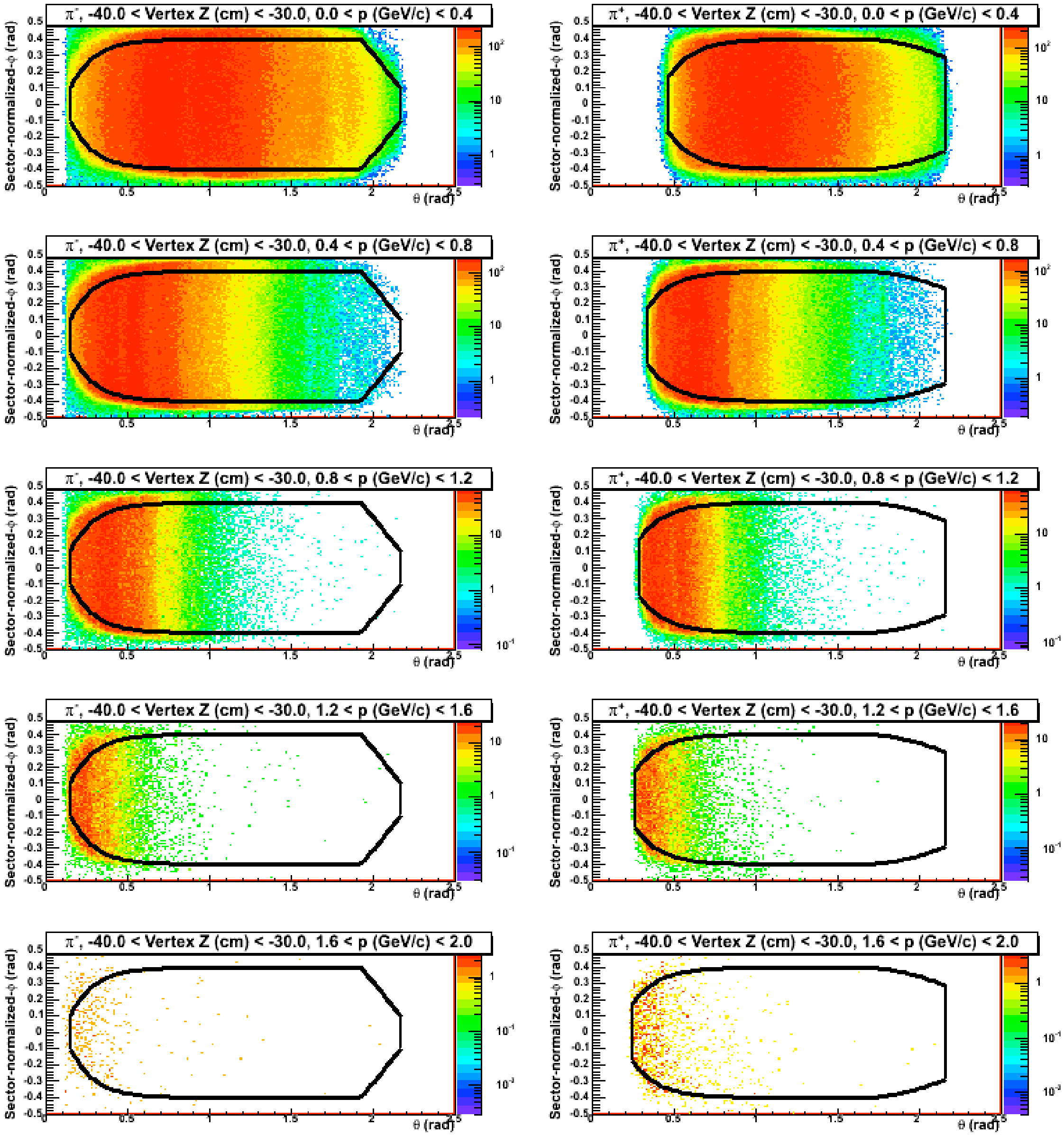

Figure 5.18: Illustration from Mattione's thesis of the distributions of reconstructed for all six sectors of the CLAS system[35]. The histograms are binned by theta and sector normalized phi for the first 10 cm of the target. The left histograms show the π^-s and the right the π^+s. The black lines indicate the fit results for the fiducial cuts.

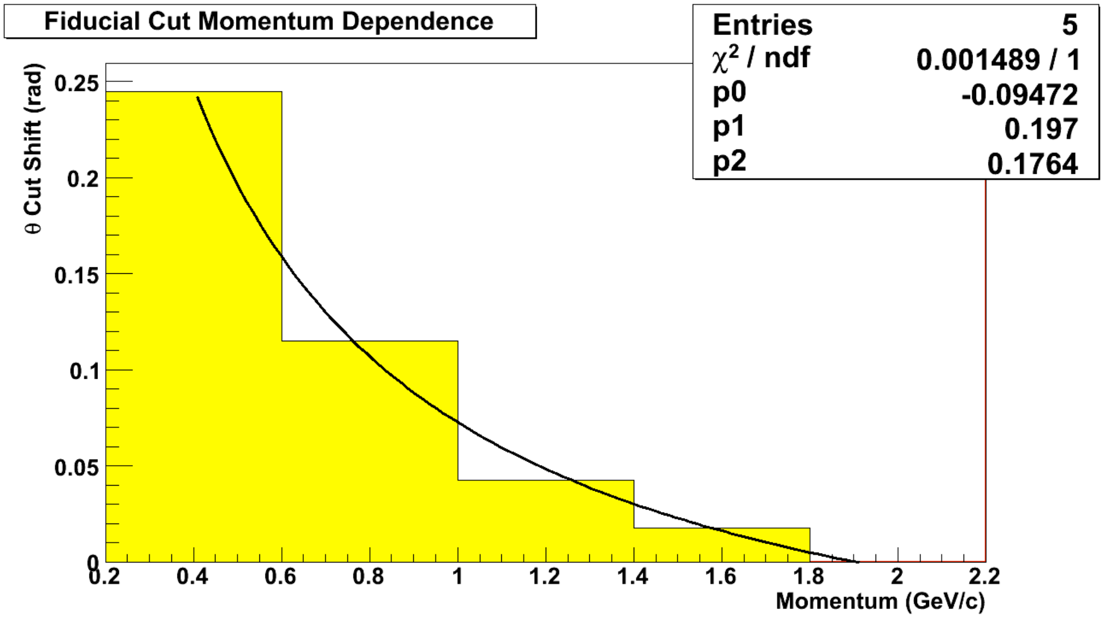

Figure 5.19: The distribution of the theta shift of the positive tracks. Mattione's routines use the fit to this distribution to adjust the fiducial cuts of the positive pion tracks[35].

the positive. Mattione manually adjusted all the constants used in his method until most of the inefficient reconstruction regions at the edges of the drift chambers were removed. The theta was shifted manually to observer the changes in momentum. The momentum dependence θ_{shift} vs. momentum for the positively charged tracks are illustrated in Fig. 5.19. The fit to this distribution is used for determining the shift for the fiducial cut to the positive pions- namely:

$$\theta_{\text{Shift}} = D_o + D_1/(p + D_2), \tag{5.3}$$

The one-dimensional plots seen in Fig. 5.20 where produced by Mattione to check the cuts applied in the methods. These plots show the slices of the 2-dimentional π^- histograms seen in Fig. 5.20.

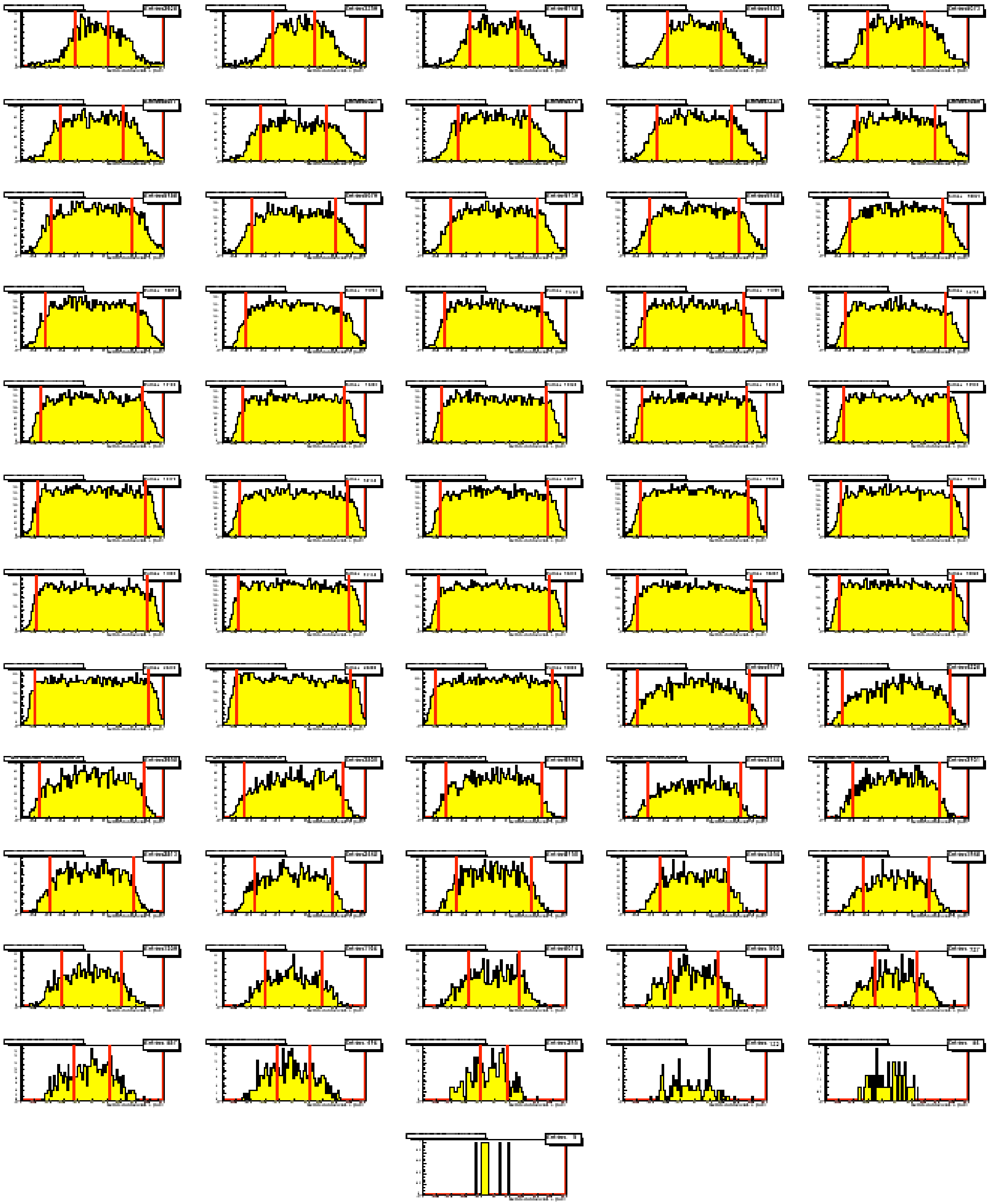

Figure 5.20: The sector-normalized phi distribution for the πs within the first 10 cm. The red lines correspond to the black line in Fig. 5.18 for the fiducial cuts.

5.5.4 Momentum Corrections

During the g13 experiment there were several sources of systematic uncertainties. There were differences between the calculated field map used for track reconstruction and the actual toroidal magnetic field. There were also drift chamber misalignments and energy losses in the drift chambers. To account for these additional momentum corrections, Mattione's code uses kinematic fits for the γD → ppπ⁻ reaction on runs 53630 through 53650; the electron beam was stable during this period[35]. The reconstruction was checked by requiring the conservation of the 4-momentum. The least-squares error of the measurement is minimized. The magnitudes of the track momenta were treated as unknown. The constraint of the 4-momentum was defined as;

$$\begin{pmatrix} E_\gamma + E_D - E_p - E_p - E_{\pi-} \\ p_{x_p} + p_{x_p} + p_{x_{\pi-}} \\ p_{y_p} + p_{y_p} + p_{y_{\pi-}} \\ p_{z_\gamma} - p_{z_p} - p_{z_p} - p_{z_{\pi-}} \end{pmatrix} = 0, \tag{5.1}$$

where E_i is the energy and p_{xi} are the momentum components of of the individual particles.

The missing energy of the γD → ppπ⁻ reaction was centered on zero, as shown in Fig. 5.21. A histogram of this distribution was generated after placing the cuts detailed in Section 5.2 to isolate the γD → ppπ⁻ events. The track momentum measurement errors were fit for the protons and the π⁻. The adjustments to the fit were determined by using the mean difference between the kinematic fit and measured momentum of the particles. The paths of particles are dependent on their charge and momentum within any particular magnetic field, and had to be treated separately depending on their charge. The drift chamber misalignments and other errors in the magnetic field map were applied to all particles of the same charge. These momentum corrections for the proton were applied to K^+s and π^+s as well. However, the energy losses in the drift chambers were dependent on the particle's velocity. The polarity of the magnetic field is set to bend negative particles outward, while the positive are deflected inward. This means that positive tracks have a higher chance of entering the uncovered forward region. Therefore, the π^+s used the π^- energy. Similarly, the π^- corrections were assigned to the K^+ are as well since K^+s have a similar momentum-dependent behavior as pions.

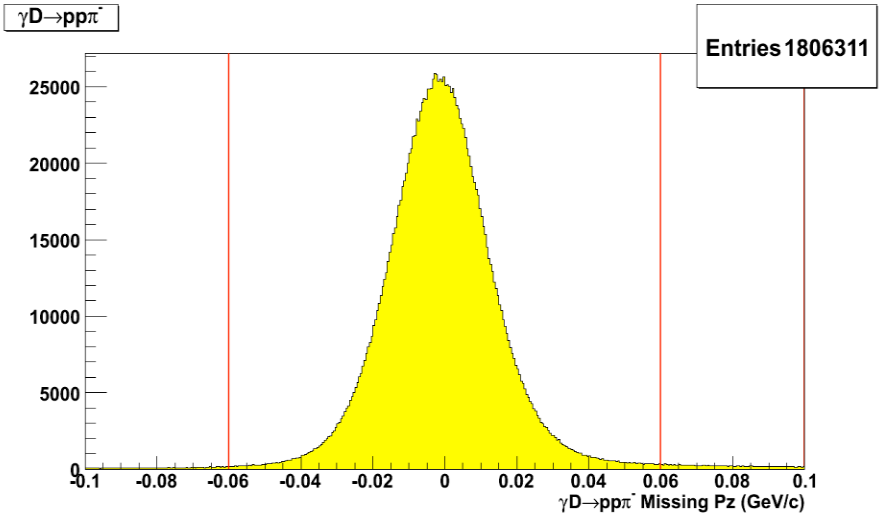

Figure 5.21: The missing momentum of the $\gamma D \rightarrow pp\pi^-$ reaction. The red lines indicate the ± 0.06 GeV/c missing-momentum z cuts[34].

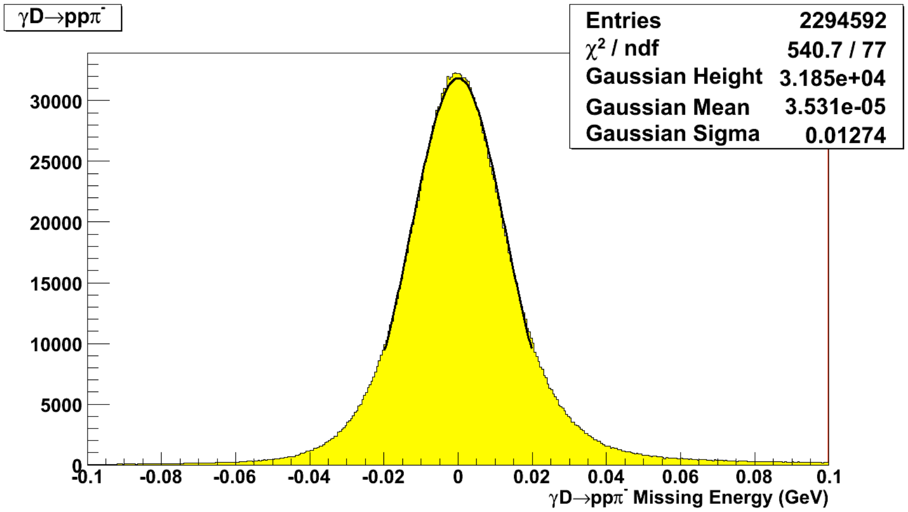

Figure 5.22: Initial missing energy distribution of the $\gamma D \rightarrow pp\pi^-$ reaction for runs 53630 through 53650 of g13a. The Gaussian fit to the peak is centered around zero, indicating a suitable run range for determining momentum corrections[34].

The measurements were assumed to have a Gaussian distribution about their true value. The confidence level is determined by how well the parameters of the measurement fit to the constraints (Eq. 5.1). The CL represents the probability of obtaining a larger χ^2 for the system and is defined by taking it as the integral of the probability function $f(\chi^2,N)$[34]:

$$CL = \int_{\chi^2}^{\infty} f(x,N)dx, \tag{5.2}$$

where N is the number of degrees of freedom. With large enough sampling range, the confidence level exhibits a flat distribution between 0.2 and 1.0 (see Fig. 5.23).

The "pull" distributions were used to check the effect of each individual track parameters used in momentum correction code. The pull was defined as the deviation between its fit and the measured values. Their distributions can be determined with a Gaussian distribution of known true events (see Fig. 5.24). Using a single standard deviation, if the pull for an event was less or greater than the normal distribution

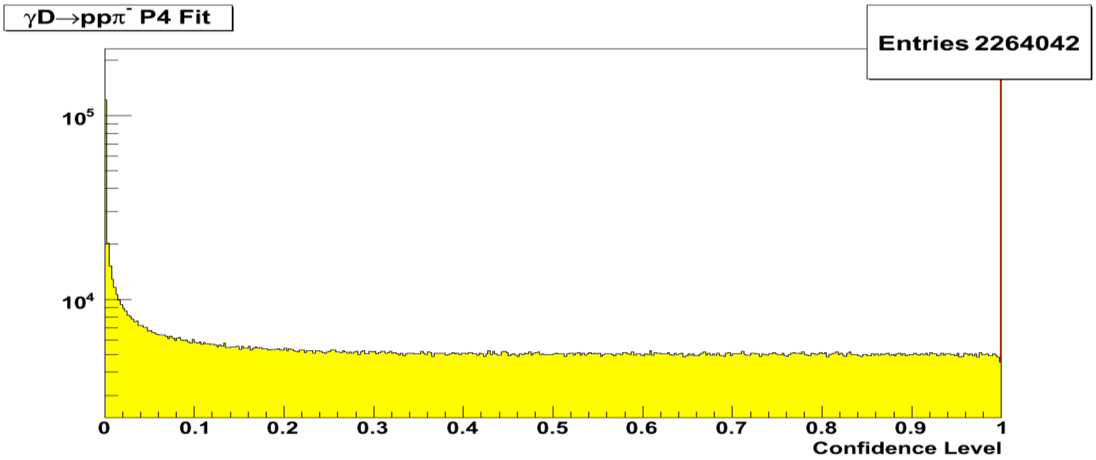

Figure 5.23: The confidence level distribution for the kinematic fit of the reaction $\gamma D \rightarrow pp\pi^-$ with the magnitudes of the track momenta treated as unknown. The large spike near zero confidence corresponds to background events.

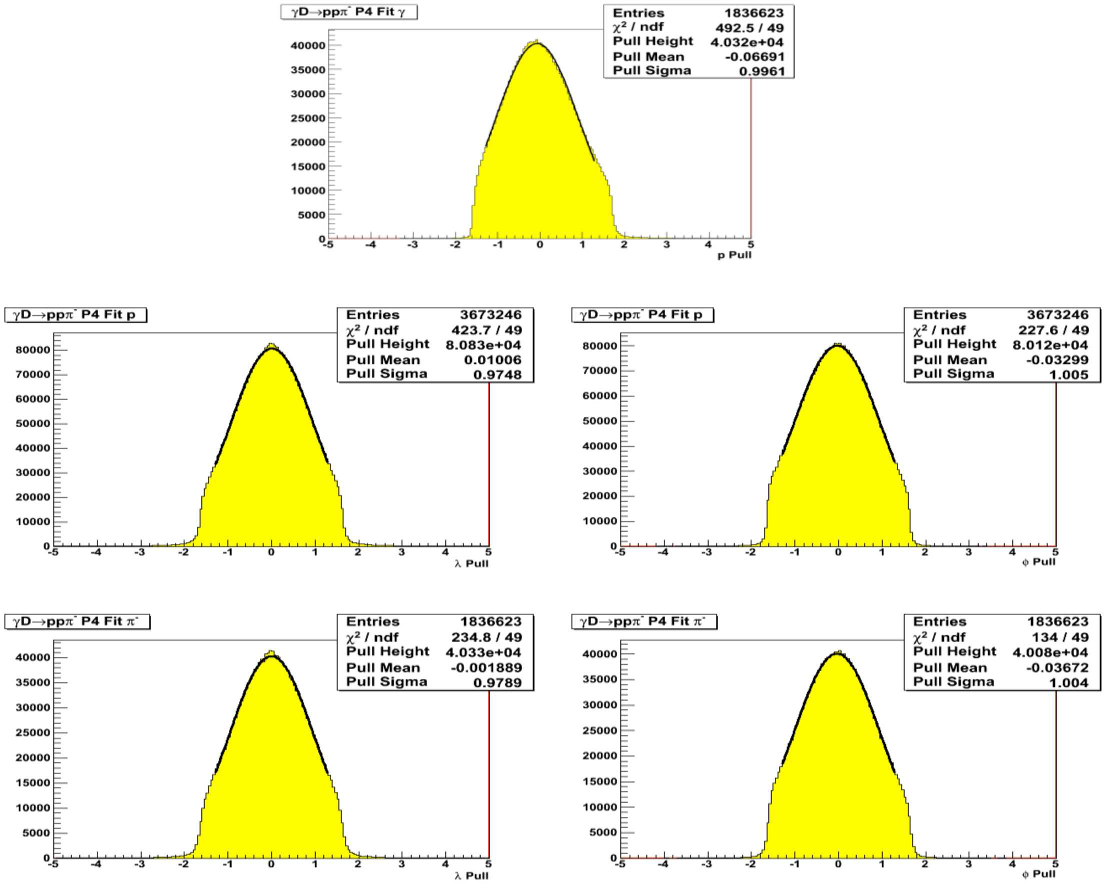

Figure 5.24: Pull distributions of the track measurements from the kinematic fit of the reaction $\gamma D \rightarrow pp\pi^-$ with the magnitudes of the track momenta treated as unknown for the (A) photon, (B) protons, and (C) π^-s. Events with a confidence level less than 10% were cut to remove background events, but this cut also removed the tails of the Gaussian distributions. The coordinate system used for the kinematic fit is defined in Reference [35].

then the event is determined to be overestimated or underestimated. Poorly estimated events required track corrections.

The $\gamma D \rightarrow pp\pi^-$ reaction required four-momentum conservation with the magnitudes of the track momenta of the protons and π^- treated as unknown to make a kinematic fit. $\boldsymbol{\Delta} p$ was analyzed for each particle in each sector of the detector. The protons and the π^- uncertainties on the track momentum measurements were fit independently.

Figure 5.25 shows $\boldsymbol{\Delta} p$ vs. p, ϕ, and θ for Sector 1 of the CLAS detector for the proton and π^- after the *eloss* corrections. The ϕ is the azimuthal angle from the middle of Sector 1, and θ is the polar angle from the beamline within the lab coordinate system. These skewed charged particle momentum can reach 10 MeV/c. These peaks can be attributed to energy losses not taken into account by the *eloss* package, misalignments of the drift chambers, and differences between the actual and calculated magnetic fields. The error in the results of the track momentum was largest for low-momentum protons.

The path of the track traversing the drift chambers was used for calculating the momentum of the charged particles. The length of a charged particle's path within a magnetic field is proportional to:

$$x \sim \frac{\left|\int \vec{B} \times d\vec{\ell}\right|}{p}. \tag{5.2}$$

The uncertainties in the momentum scale as the reciprocal of the momentum. This is difference between the inverse of the fit momentum and the inverse of the detected momentum after *eloss* corrections. The p, ϕ, and θ were used for the corrections to the track paths. Each were fit in different stages to isolate their contributions. Several iterations were performed until the momentum corrections converged to a mean $\boldsymbol{\Delta}p$ of zero. Figure 5.26 shows the mean difference between the fit and corrected momentum binned by p, ϕ, and θ for Sector. After the corrections most of the distributions show a nearly flat distribution.

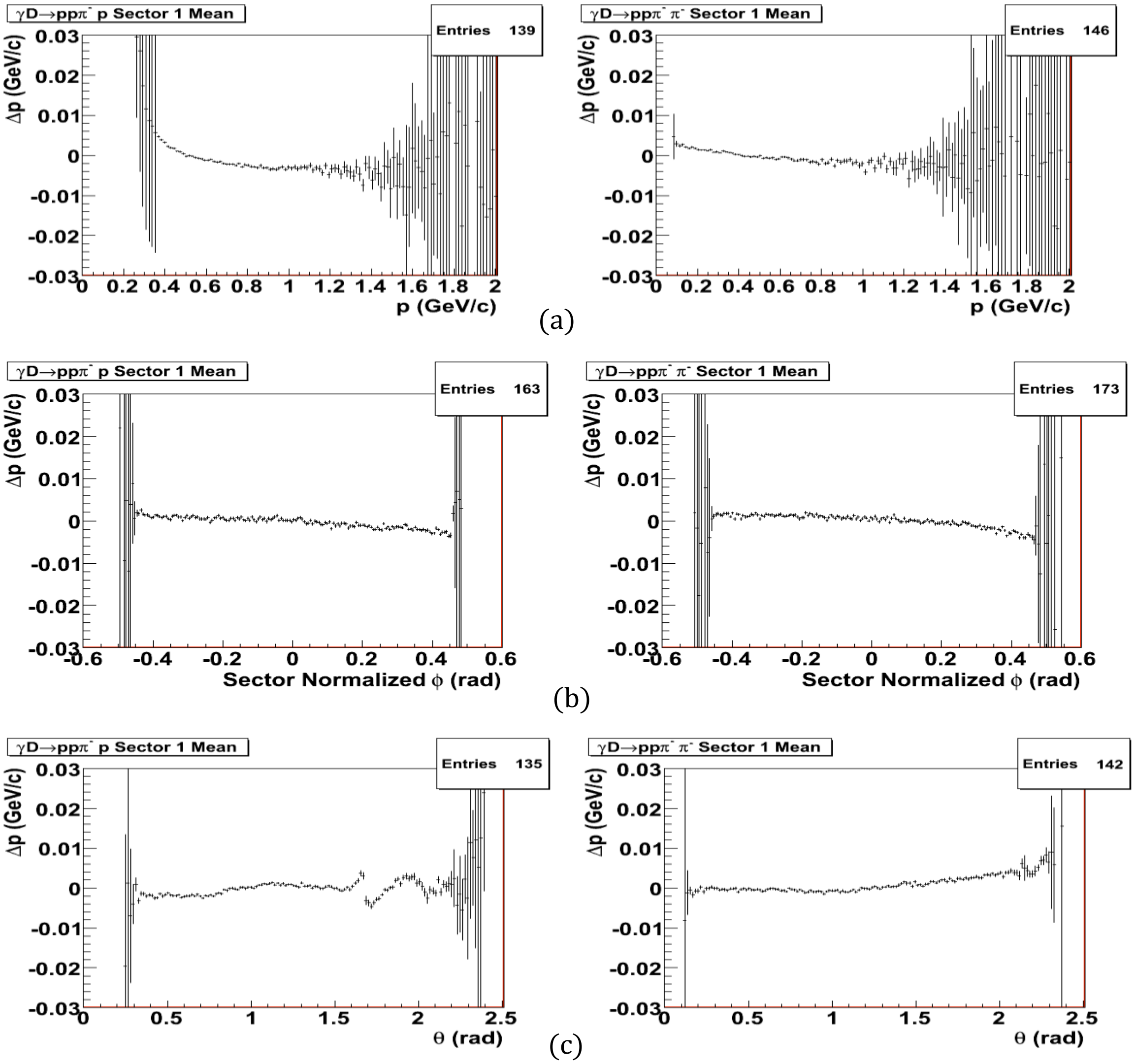

(a)

(b)

(c)

Figure 5.25: Sector 1 fits from Mattione's momentum correction[35]. Each shows the difference between the fit and detected momentum after *eloss* corrections as a function of (a) momentum, p, (b) azimuthal angle, ϕ, and (c) polar angle, θ for for the proton(left) and π^-(right). In (c), the inefficient drift chambers and TOF scintillator paddles caused several "hole" regions. These are seen in each of the sectors.

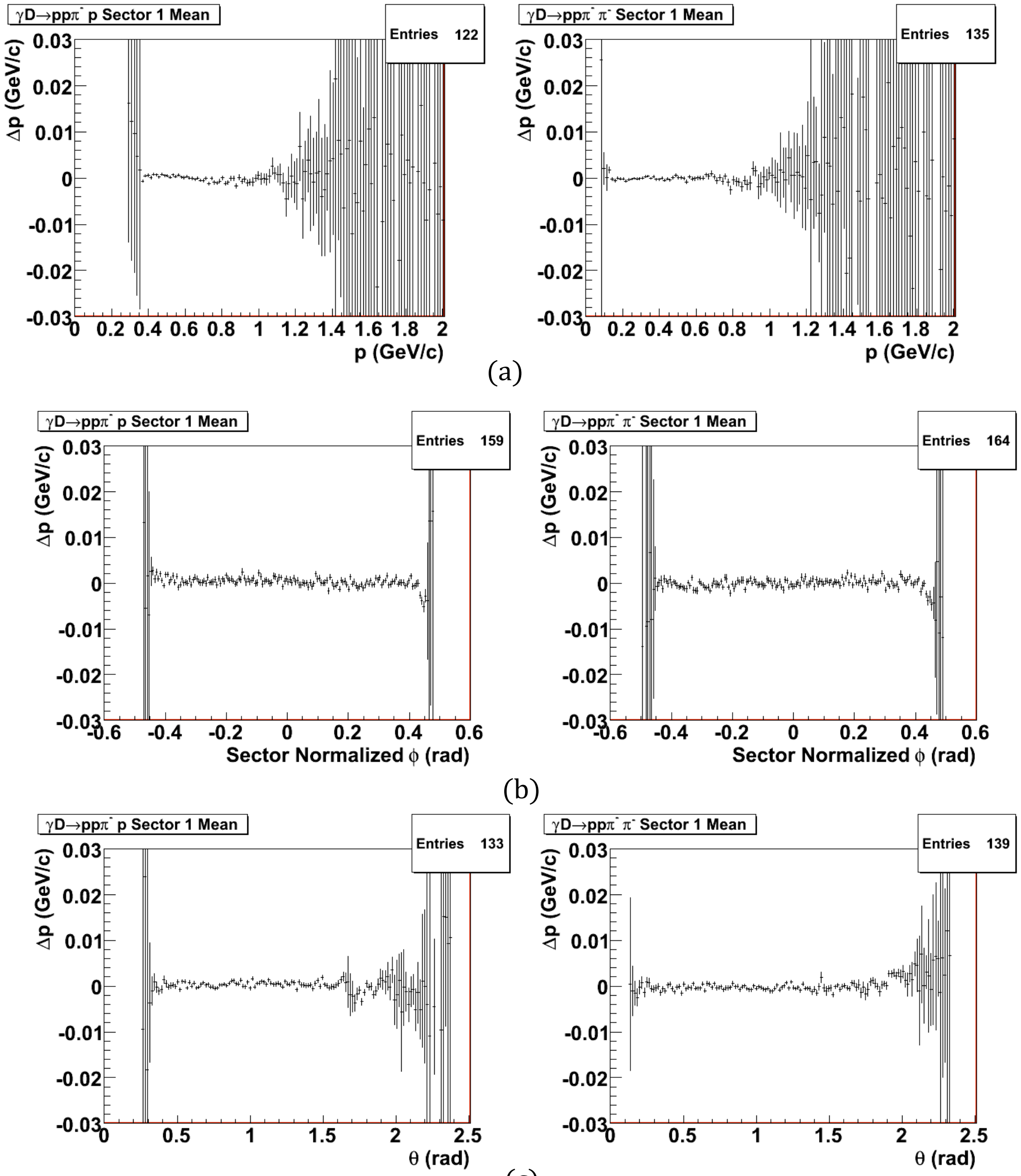

(a)

(b)

(c)

Figure 5.26: Sector 1 fits from Mattione's momentum correction[35]. Each shows the difference between the fit and detected momentum after the momentum corrections have been applied. They are plotted as functions of (a) momentum, p, (b) azimuthal angle, ϕ, and (c) polar angle, for the positive(left) and negative (right) pions.

The plots in Fig. 5.26 show the effects on the momentum after the eloss and drift chamber corrections for the π^+. When looking at the distribution of momentum for each final-state track with its corrected momentum, little difference is seen. However, when the change is plotted per momentum interval, the effects of the corrections become more visible. With just the eloss correction, an exclusively positive corrections is found with stronger corrections at the lower momenta. However, when the drift chamber corrections are applied, an unbiased smearing is seen.

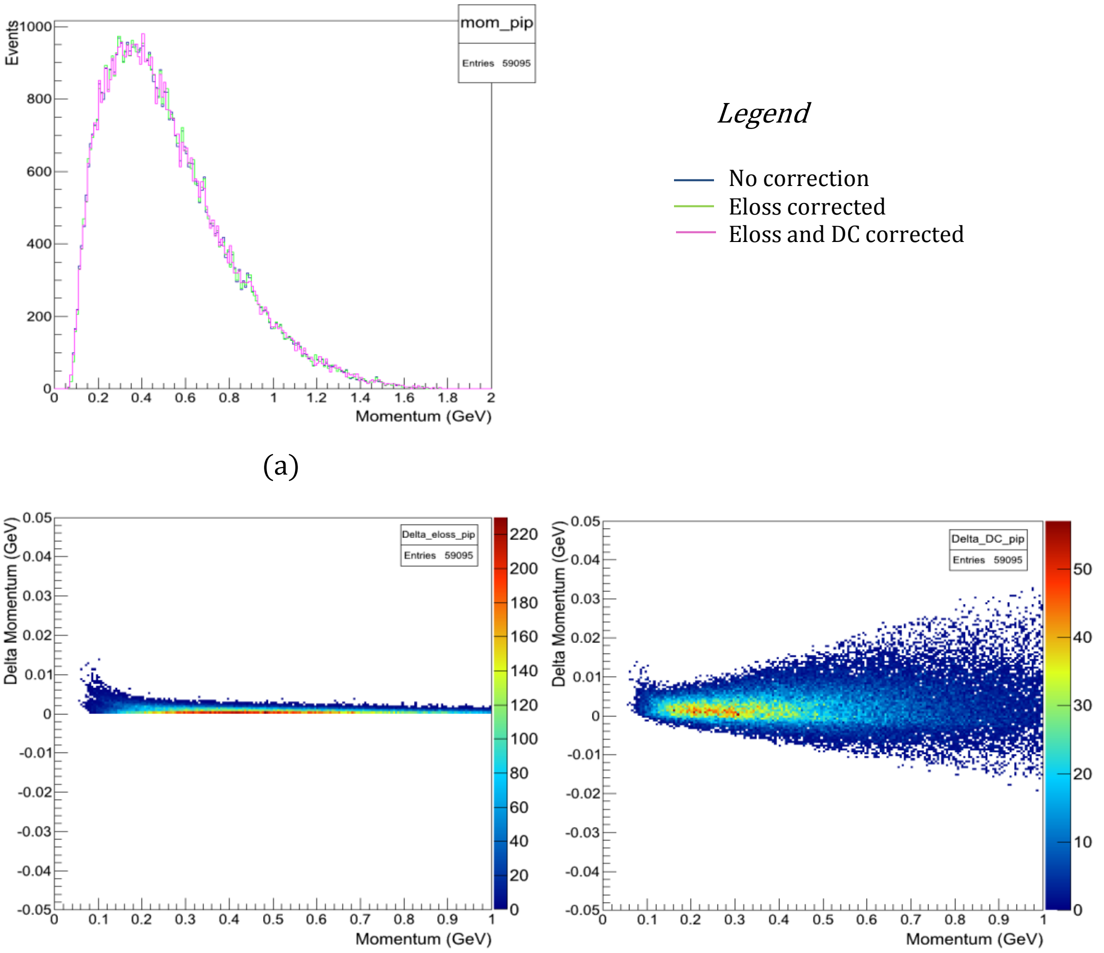

(a)

(b) (c)

Figure 5.27: Corrections to the positive pion's momentum. In (a) little difference is seen between the distributions of original track momentum and the two corrected. However (b) when the difference of the eloss correction is plotted per momentum interval, a positive skewing in momentum can be seen. (c) With both eloss and drift chamber corrections applied, an unbiased smearing is seen in the change of momentum.

Because of the poor resolution and larger uncertainties at lower track momentum (as can be seen in a plot of the track momenta, as is evident in Fig. 5.27), events with protons below 400 MeV and pions below 100 MeV are not used in this study.

5.5.5 Beam Energy Corrections

The energy of the electron beam has no direct measurement in the CLAS detector system. Instead the electron energy is assumed to be the reported energy from the CEBAF accelerator, which should be near the requested energy (1.990 and 2.655 GeV). Initial checks were made on the fluctuation of the beam energy with that requested, by comparing with energies measured in simultaneous experiments made in Hall A and C. Drifts in energy were typically around 2 MeV. Their cause could be due to beam steering, beam dispersion, and variation in the cryogenic cooling.

For Mattione's beam correction code, the $\gamma D \rightarrow pp\pi^-$ reaction was again used. The energies were corrected by individual runs based on their mean missing energies per event. A correction factor (CF) was developed to apply to the BOS bank values and was defined as:

$$\mathrm{CF} = (E_\gamma - E_{\mathrm{Missing}})/E_\gamma \;, \tag{5.3}$$

where E_{Missing} is the average missing energy in the $\gamma D \rightarrow pp\pi^-$ reaction.

Figure 5.28 shows the calculated multiplicative energy corrections used in Mattion's code for both energy ranges in the g13a dataset. An average 1 MeV variation is seen with the corrections.

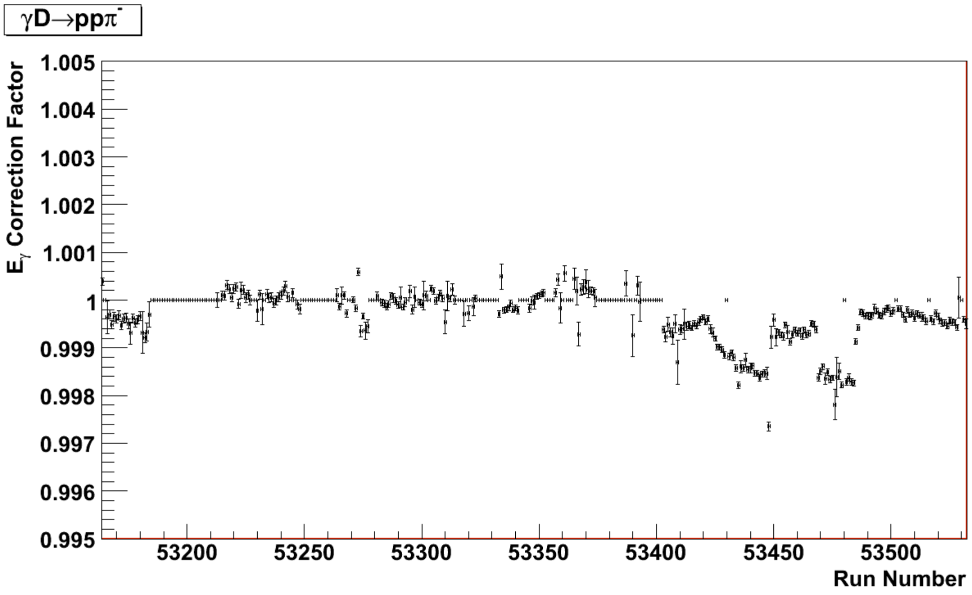

(a)

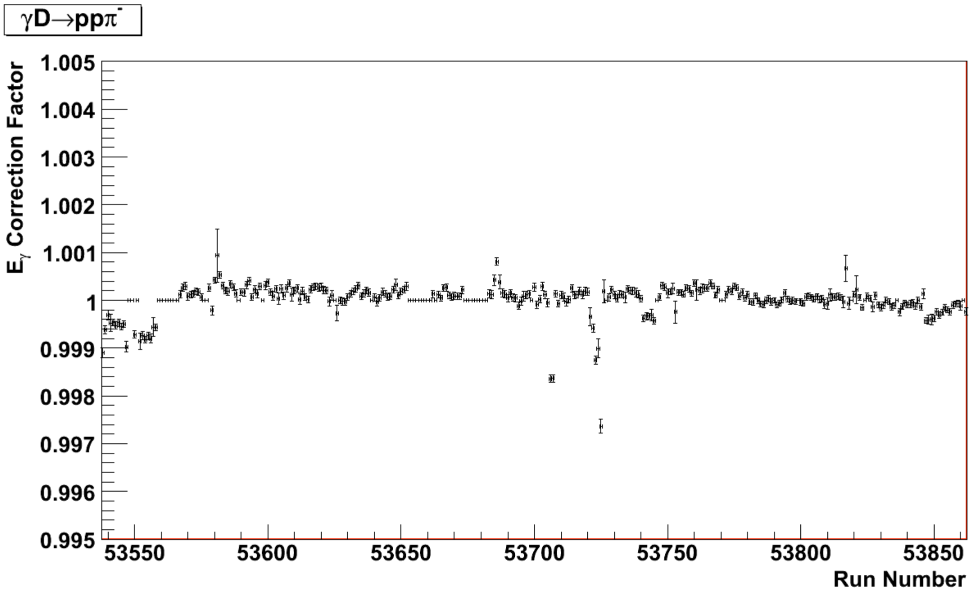

(b)

Figure 5.28: The energy correction factors used by Mattion's method[34], for (a) the electron energy 1.990 GeV and (b) for 2.655 GeV.

5.6 Photon Selection Studies

For this analysis, three methods where employed for the photon selection. The first method simply took the event photon from the banks, which was determined during the cooking process. The next two methods both used a voting scheme. The vertex time for each track is used to vote for a specific photon. The photon voting is weighted to favor the pions (particularly the negative pion), to avoid tied votes. The first method uses the vertex position for each track as the correction to the vertex time. The second uses the corrected production vertex position to calculate a new vertex time for each track. Though there is an intermediate decay for these tracks, the vertex time will not experience a significant change. It is, however, sensitive to the z position within the target.

5.6.1 Method Comparisons

The different methods were compared by looking at the photons chosen for each event. In cases where the photons chosen are not in agreement, a value of 50 is assigned. This allowed for visual representation of the disagreement with the photon selection. When comparing the photon selection from the vertex corrected method with the photon selected in the cooking process, we see approximately a 10.5% difference. This clearly indicates that the bank vertex values cannot be trusted in events without any measured tracks from the production. Likely, reliable values could be taken from the bank in similar reactions if a photon or an extra pion is in the final state with the $K_S\Lambda$. This extra particle would originate from the event vertex. If the vertex corrected method is then compared to the method using the initial track vertices, a difference of 3.6% is seen. This further illustrates the necessity of vertex reconstruction of the intermediate and event particles.

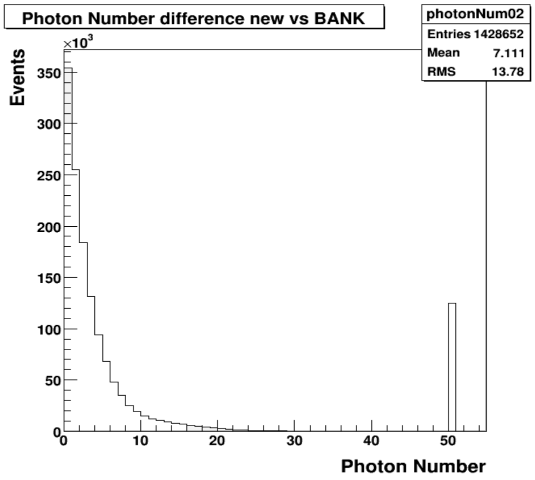

Figure 5.29 Photon column number selected for each event. If using the new calculated event vertex gives a different photon number from the detected particle's positions, the photon value was set to 50.

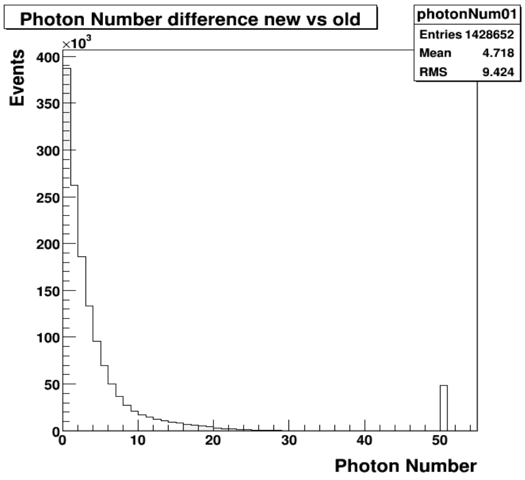

Figure 5.30: Photon column numbered selected for each event. If using the new calculated event vertex gives a different photon from what is stored in the banks

Chapter 6

CLAS Acceptance

In principle the CLAS detector provides 4π acceptance, but in reality, the detector has several "blind" spots and low regions of efficiency. Monte Carlo simulation was used to model these inefficiencies. The simulation can be used to study the limitations in the analytical code use for the channel reconstruction. The simulation only generates $K_S\Lambda$ or $K_S\Sigma^0$ events. This fact can be used to examine cuts to see how many "real" events are being lost by some of the chosen cuts. The GSIM code used for GEANT already has the details of the CLAS detector system encoded. Some modifications were made to adjust the data to the specifics of the g13 experiment– namely *gpp* and the code created for this analysis.

6.1 Monte Carlo Simulation

How one simulates the hadronization process is of fundamental importance. When the parton (collectively quarks and gluons) shower is finished, low momentum transfers dominate. Currently there are concrete theories on this process; however, there are several empirical models. PYTHIA is the most notable code for processing parton showers. For this study, fsgen (a FORTRAN code which uses the PYTHIA framework) was used for the event generator. For practical reasons, fsgen uses pre-generated "Lund" tables to begin the event generation. These tables hold the decay tables for many of the hadrons. The generated events are then passed to the GSIM GEANT package where their tracks are traced through the simulated CLAS detector. The distribution of the tracks is then corrected by the *gpp* software to account for inefficient or dead detectors not modeled in GSIM (mostly in the drift chambers and the time-of-flight systems). Finally, the simulated data is cooked the same way as the empirical data and processed by the same analysis code. Some final cuts are made to account for dead and inefficient detectors and to correct for event triggering.

6.2.1 Event Generation

The decay or scatter of the excited nucleon is not performed with fsgen. Instead, the event generation begins with the section of photon energy. With this energy, the Fermi momentum is determined using the Bonn distribution and the center-of-mass energy and momentum is determined. The Bonn potential is based on the exchange of mesons between the nucleons[36]. In its simplest form (before the Fourier transform), the potential can be written as;

$$V_\pi^{(loc)}(\boldsymbol{r}) = -\frac{g_\pi^2}{4M^2}\frac{(\boldsymbol{\sigma_1}\cdot\boldsymbol{k})(\boldsymbol{\sigma_2}\cdot\boldsymbol{k})}{\boldsymbol{k}^2+m_\pi^2}, \tag{6.1}$$

where g is the coupling constant for the pN interaction, M is the mass of the nucleon, $\boldsymbol{\sigma_i}$ are the Pauli spin matrices, and $\boldsymbol{k}$ is the difference of the relative 4-momenta in their initial and final states. The code then uses two factors to calculate the angular distribution of the decay/scatter hadron– a user defined function for the cosine theta and a defined t-slope value, where the t slope is b in the differential cross section:

$$\frac{d\sigma}{dt} = \sigma_o e^{-bt}. \tag{6.2}$$

Here σ_0 is the amplitude of the cross section and t is the squared 4-momentum transfer as discussed in section 2.5. The t slope can be varied to a user defined method.

Initially the distribution of angles for the neutral kaon and Lambda decay particles cannot be known. This determination has to be done through an iterative process. For the first iteration of the simulation, a phase space (isotropic in ϕ and cosθ) distribution is used. The acceptance is calculated by the number of events extracted from the missing mass peak of the spectator proton divided by the total number of events generated. It is known that the two hadrons decay back to back, so when reporting the differential cross sections, only the kaon center-of-mass angle is used. The resulting cross section of each iteration is then used to correct the next.

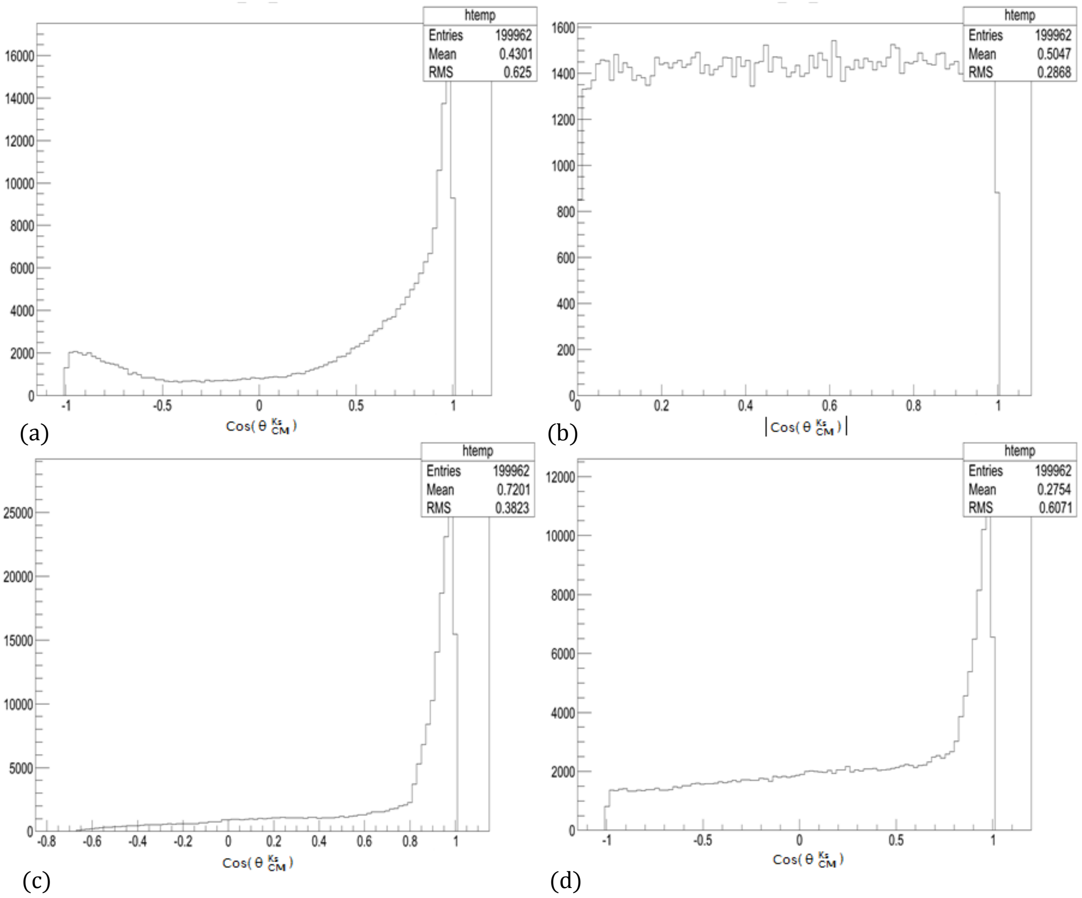

Figure 6.1: The *fsgen* input distributions for the cosine theta of the K_S track. The standard *t*-slope distribution (a) the phase space distribution (b) and the input cross sections without (c) and with (d) a 10% phase space are each input into the *fsgen* event generator for 200,000 events for each run submission. 512 runs were submitted for each iteration. The phase space (b) is presented in absolute value by the inspection code when checking before submission. The fsgen histogram reports the full distribution for the sum of particles.

With every iteration, the new cross section is submitted into fsgen. This is done by assigning each event a number between 0 and 1 and checking it with the normalized distribution. If its random number is less than the normalized cross section value for its θ bin, it is rejected and a new event takes its place. The total number of desired events is then produced with the shape of the angular cross section. However, it is important to make sure each normalized value does not approach zero when using the cross section to produce the new distribution of K_S in cosine theta. Small values tend to induce wild fluctuations with each iteration. This is easily avoided by assuming each angle has at least 10% chance of having a K_S, while the remaining 90% conform to the cross section (see Fig. 6.1). Bins with strong slope also have stronger uncertainty associated with the slope function.

The *fsgen* code can perform secondary decays of the particles into specified channels. However for this study, the decay options were turned off and the decay was performed by the GSIM as the particles are being translated through the simulated CLAS system. This allows for more realistic vertex reconstruction within the simulated data.

It is important to note that when boosting tracks in the generated event BOS files, the neutron is treated as the only target. Its momentum, however, is not treated as zero. The neutron is calculated to have the Fermi momentum it shares with the proton while in the deuteron. The simulation BOS files only store the Fermi momentum of the proton; however the neutron's Fermi momentum is equal and opposite to that of the proton and is easily derived.

6.2.2 Event Processing

Once the quality of the generated events has been verified, they are passed to the GSIM code, which propagates them through a simulated CLAS system. The short-lived K_S and Λ particles are decayed during this stage of the simulation. Most of the neutral particles decay before they reach the start counter. Their decay products are then propagated through the rest of the system. The trajectories and energies of the final-state particles are recorded into the data banks as individual measurements of subdetector systems. The simulated BOS files have the same structure as the real BOS files, but have additional MC banks. The MCTK bank stores the track information for the neutral particles in addition to the final state tracks. The originating vertices for each track are stored in the MCVX bank. Before these files are cooked and analyzed it is important to first correct for the detector inefficiencies by running the gpp package.

The gpp code serves two primary purposes– it modifies the tracks to represent the inefficiencies in the current CLAS detector system and it can smear the track's path through the drift chambers to better model the uncertainty of detectors as seen in the experimental data. It also smears the time of the event photon. Initially, the smear values are all set to the maximum unit value of 1. In later simulations, the photon time smearing was adjusted to test the analysis codes selection of event photon.

When the analysis code is run on simulated data, extra steps are made during the cataloguing of track values. The MC banks are used to compare the original generated event values to the reconstructed values. This method was described in some detail in section 5.1.5, when examining the reliability of the vertex reconstruction. The use of the banks is very important when evaluating the analysis codes accuracy. With the original event information, it is possible to determine how many good events are rejected during the particle identification, photon selection, and invariant mass cuts. These factors are considered when generating the yield correction factor for the final development of the cross sections.

6.2.3 Simulation Results

With the absence of background channels in the simulated data, we expect to see clear distributions of the final-state and intermediate particles. In Fig. 6.2 the reconstructed masses of the neutral kaon and Lambda are shown. Their form closely resembles that of the experimental data with a much lower background. That there is any background at all in the simulated data indicates uncertainty in the reconstruction of the analysis code and/or effects of the CLAS detector's simulated efficiency. The yield correction factor accounts for this discrepancy.

Similar to Fig. 4.22, the missing mass of the proton is shown in Fig. 6.3. The first histogram shows the missing mass of the $K_S\Lambda$ vs. the missing mass of the K_S alone. This gives the missing mass of the proton vs. that of missing mass of the hyperon. In the case of simulated data, the only hyperon is that of the Lambda.

6.2.4 Simulation Start Counter Cuts

The triggering from the start counter introduces subtle loss of events that is present in the real data, but not in the simulated set. The simulated CLAS system does not account for the relative long life of the Λ (and to a lesser degree, the K_S). The Λ has a proper decay length of 7.9 cm. Though it is not usual, the Λ particle can decay outside the start counter. Because it is a neutral particle, it is unlikely to generate a hit if it decays outside of the start counter. The level 1 trigger used in g13a required 2 sector hits to record an event. Even if the K_S (or the Λ if the K_S decayed outside) registers a hit the start counter an event would not be recorded.

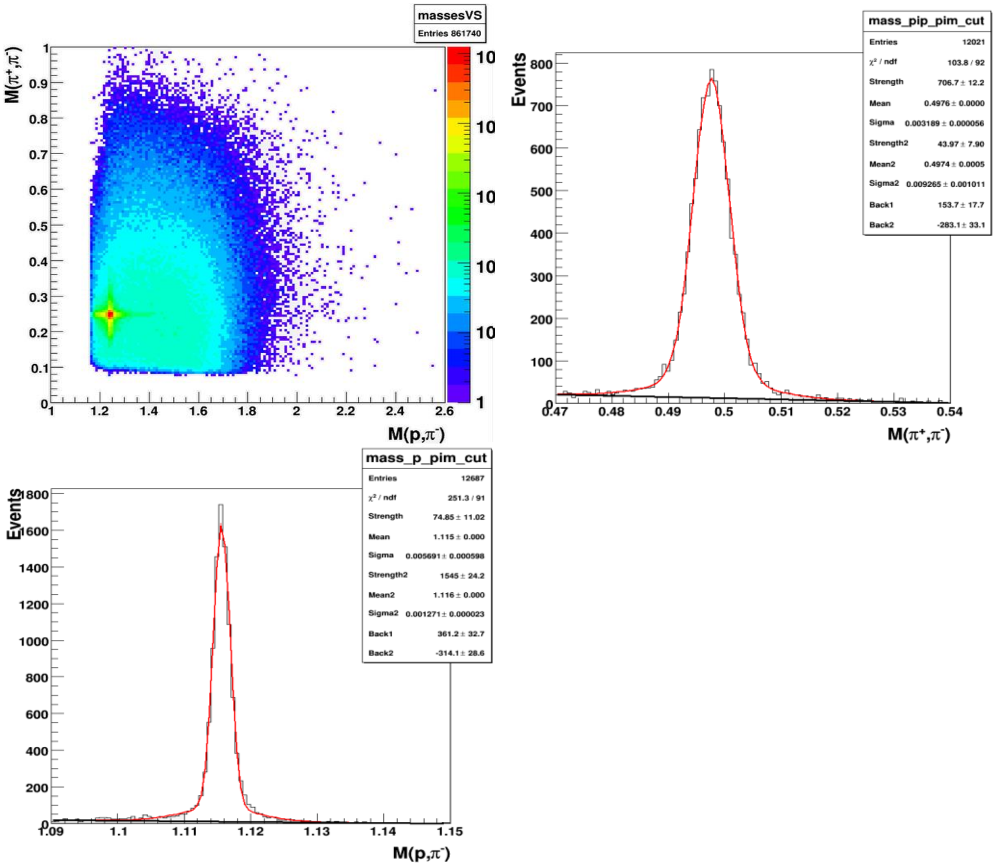

Figure 6.2: The invariant mass distributions of the simulated K_S and Λ particles. Since only "real" $K_S\Lambda$ events were generated, the slope in the $\pi^+\pi^-$ invariant mass indicates that some $K_S\Lambda$ events are being poorly reconstructed. This could be due to distorted data during the tracks path through the GSIM simulated CLAS detector or efficiency corrections in gpp.

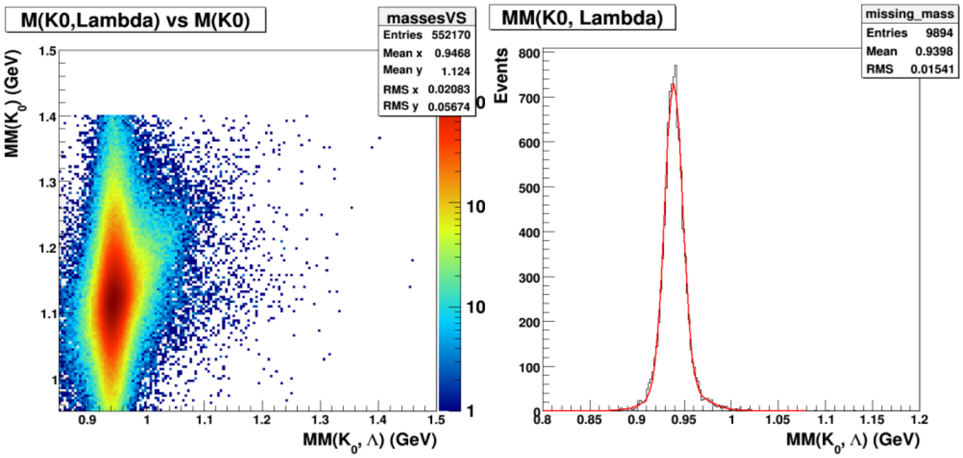

Figure 6.3: Missing mass of the simulated data, from the reconstructed K_S and Λ particles

The Monte Carlo simulation does not account for hits in the start counter, but instead assumes all particles were registered. The analysis code accounts for this with cuts on the decay vertex position. The GSIMS code decays both the Λ and K_S during its propagation through the CLAS detector system, with the probability of decay being in its proper frame;

$$P = e^{-t/\tau}, \tag{6.3}$$

where τ is the mean lifetime and t is the random track lifetime. It records the start positions of all the initial, intermediate, and final-state particles. If the either of the particles decayed outside of the target, the event is rejected.

6.2.5 Evaluation of Competing Channels

Before the final cross sections were determined, a comparison of channels was made as a simple study of acceptances. Equal number of events were generated for the $K_S\Lambda$ channel and the two lowest energy competing background channels– the $K_S\Sigma^0$ and K(892)*Λ channels. Phase space was used for the event generation. The final results show a very familiar missing mass distribution. The near absence of the K(892)*Λ channel reflects the low total cross section for the reaction, and the events that do occur have a low very low acceptance. It is unlikely the experimental data has many K(892)*Λ events. Since both the $K_S\Lambda$ and $K_S\Sigma^0$ channels have a distribution ratio very similar to that of the empirical results, it would be reasonable to expect the total cross sections of the $K_S\Lambda$ and $K_S\Sigma^0$ channels to be within one order of magnitude. However, to truly understand the relation between the two reactions, the cross section for both channels must be extracted simultaneously.

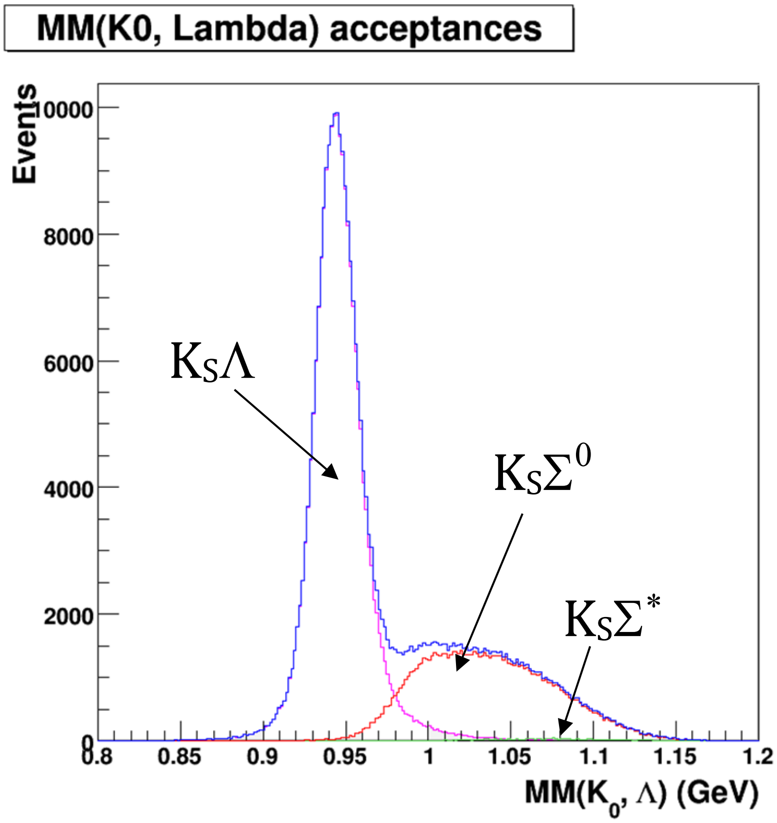

Figure 6.4: Comparison of acceptances for different reactions. Two hundred and fifty thousand events were generated for each. The green distribution is the K*Λ channel, and shows very little contribution.

6.3 Yield Correction Factor

The simulation of the CLAS detector allows for the correction of lost events in the CLAS system. It also allows the evaluation of the analysis code itself with the development of the yield correction factor. This correction factor is determined by taking the ratio how many events are lost in the particle identification and invariant mass cuts in the experimental data vs. the simulated events. For this analysis, the yield correction factor was determined by:

$$Y_{CF} = \frac{(1-C^{S}_{\mathrm{TIME}})(1-C^{E}_{\mathrm{MASS}})(1-C^{s}_{TC})}{(1-C^{E}_{\mathrm{TIME}})(1-C^{S}_{\mathrm{MASS}})(1-C^{E}_{\mathrm{TC}})}, \tag{5.4}$$

where C^{S}_{TIME} is the faction of cut events from poor timing, C^{S}_{MASS} is the percentage of lost events from the invariant mass cut to the simulated data, and C^{S}_{TC} is the fraction of events where both track combinations survive the cuts. The variables C^{E}_{PID}, C^{E}_{TIME}, and C^{E}_{MASS} correspond to the same fractions for the experimental data. We find the correction factor to be 1.003.

6.4 Acceptance

The acceptances for the $K_S\Lambda$ and $K_S\Sigma^0$ channels were calculated by taking the original number of events generated and comparing them with the number events that survived after they were passed thought the simulated CLAS detector and reassembled through the same code as the real data. Originally the events are generated in a flat phase space. That is to say isotropically with $d(\cos\theta)$ and $d\phi$ being uniform in the center of mass frame. With small enough bin size this is a reasonable assumption. However, when bin sizes get larger, the slopes within each bin can cause poor representation of the true functional form of the values within each bin. To reduce the effect from large binning, the cross section produced after the first iteration is used to generate the events for the next.

6.4.1 The $\gamma n \rightarrow K_S \Lambda$ Acceptance

Figure 6.5 shows the acceptances for the $K_S\Lambda$ channel, binned by cosine theta of the kaon and the energy of the interaction. The cosine theta distributions all exhibit the typical form seen in the experimental data, with a mostly forward bias. It is difficult to be certain on what the real contributions are for the simulated acceptances; however, there appears to be a forward and central distribution. The forward distribution remains strong at each of the measured energies; however, the middle distribution loses its prominence after 2.0 GeV. At this point, only the statistical errors are shown. The systematic errors are presented independently in section 6.5.1.

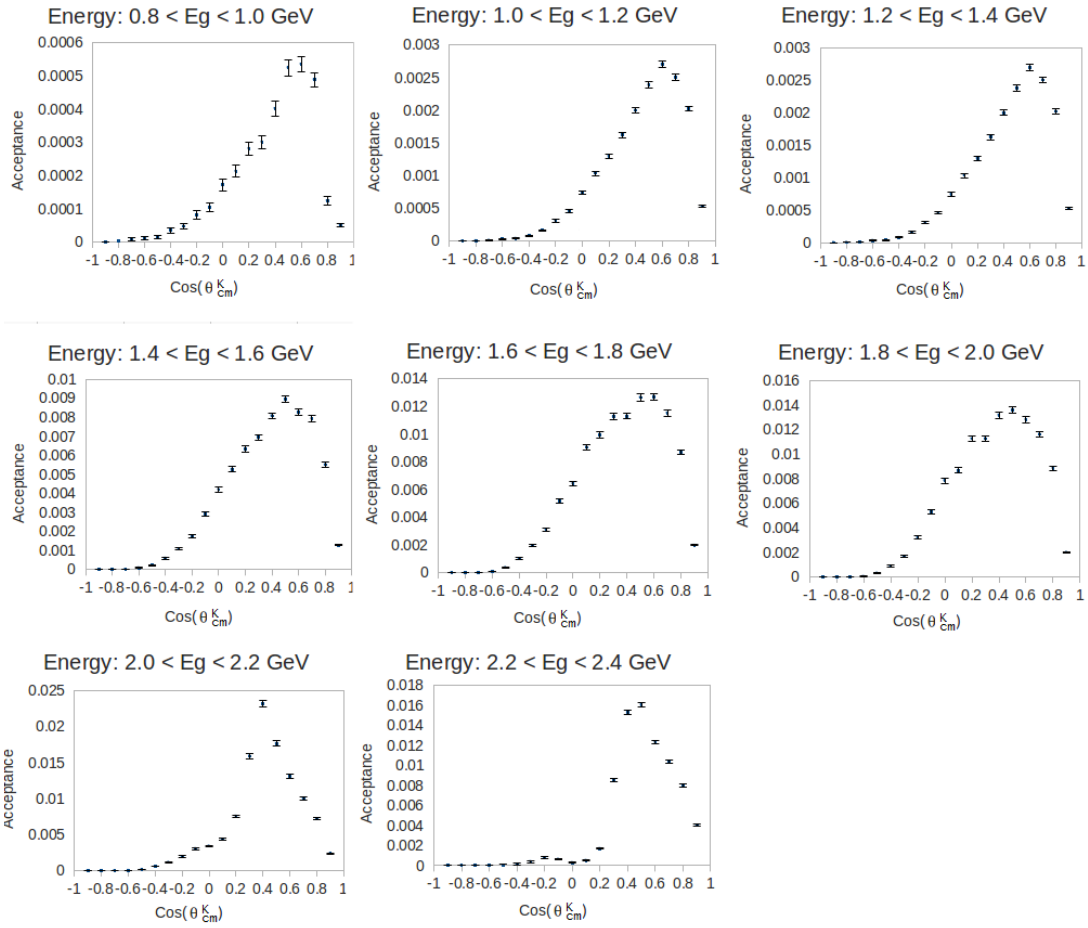

Figure 6.5: Acceptance of the CLAS detector system for the $\gamma n \rightarrow K_S \Lambda$ reaction, binned by energy and cosine theta.

6.5 Acceptance Uncertainties

Two methods were applied to determine the uncertainties of the acceptance. For the statistical, I used Yordanka Ilieva's method for the time-of-flight uncertainty. This technique does a comparison of the number of generated events verses the number of events measured. Michael McCracken's method of acceptance-corrected yields was used for the systematic uncertainties. His method matches the simulated acceptance with the experimental yield for each sector to estimate the variation.

6.5.1 Systematic Uncertainties

The CLAS detector was designed for 4π acceptance in the boosted reference frame. That is to say, it was built to have the same coverage over nearly all azimuthal and polar angles. With a large enough data sample, it could be expected that each of the six azimuthal sectors would have roughly the same yield. Yet in reality each sector has systematic losses in detector efficiency (due to lost TOF paddles, dead DC wires, etc). The simulated CLAS in GSIM was modeled to try to account for these weak or dead detectors. The clearest way to check this is to normalize the yields for each sector by the simulated acceptance. Lost systems are not symmetric and become visible when comparing the each sector to the average of the acceptance-normalized yield.

Figures 6.6 and 6.7 show the yields by sector and acceptance-normalized yields by sector, respectively. With a perfect model, the acceptance-normalized yields per sectors would mostly line up. However no model is perfect and experimental detector efficiencies are not constant. Therefore, significant variance can be seen between the sectors. Figure 6.8 shows the ratio of the acceptance-normalized yields per sector verses the mean. These deviations were used in the calculation of the systematic uncertainty of the acceptance.

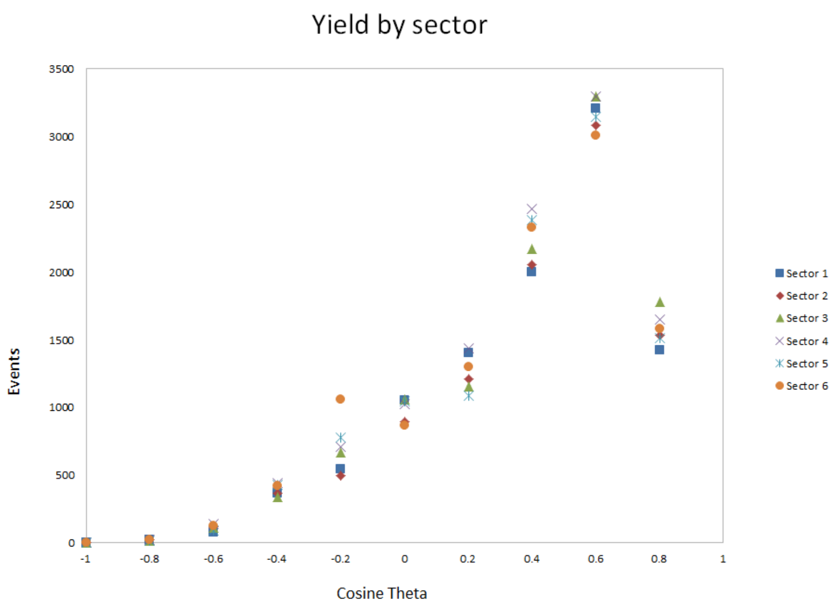

Figure 6.6: The sector-dependent yield for each sector. The 2.64 GeV g13a data set was used for this uncertainty measurement. The design for 4π acceptance implies that each sector should have nearly the same yield; however, some fluctuation can be seen. Most variance is due to the failed detectors within the CLAS system.

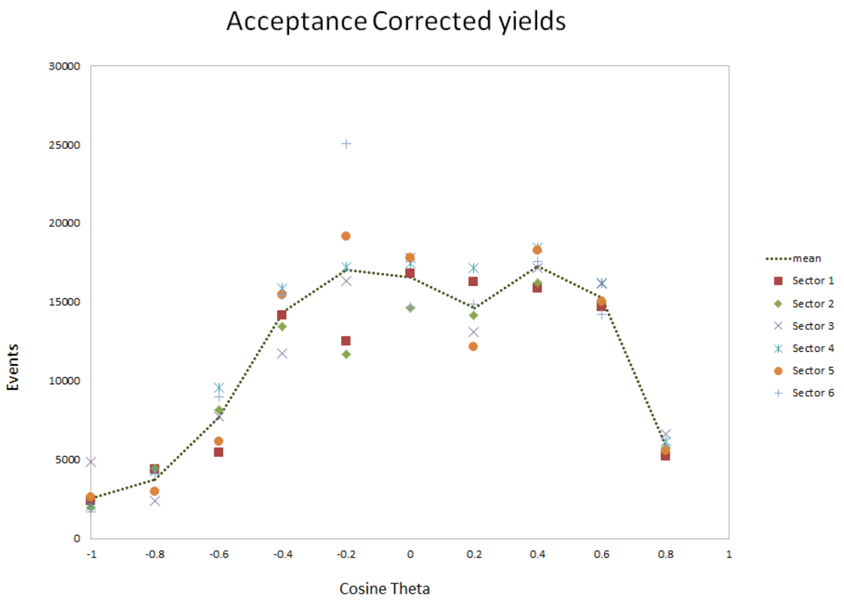

Figure 6.7: The acceptance-normalized yield for each sector can be used to see the variation in the simulated model from the experimental efficiency of the CLAS system. Each sector's value can be compared to the mean value for its uncertainty.

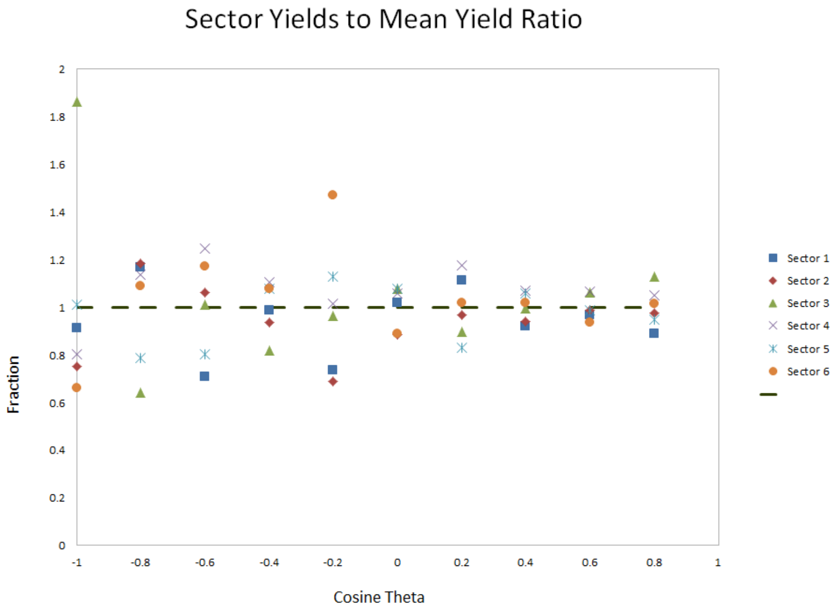

Figure 6.8: The ratio of each sector's yield to the mean of all sector yields can be used for determining the final systematic uncertainty of the acceptance.

6.5.2 Statistical Uncertainties

The statistical uncertainties were determined using the same method applied to the original TOF studies for CLAS. This method employs a straightforward comparison of total measured events with those actually generated[37]. The efficiency of a simulated event can be determined by:

$$\varepsilon\left(E, cos\theta_{CM}^{Ks}\right) = \frac{A}{C} = \frac{A}{A+B}, \tag{6.5}$$

where A is the number of simulated events in the final reconstruction, B is the number of events which did not make it into the reconstruction and C = A + B is the total number of events. The inefficiency is found in a similar manner:

$$\varepsilon'\left(E, cos\theta_{CM}^{Ks}\right) = \frac{B}{C} = \frac{B}{A+B}. \quad (6.6)$$

The efficiency and inefficiency together account for all events, therefore their sum must equal one. This means that their change must also equal, and that ΔA = ΔB. The value of C has treated as a fixed number and has no statistical uncertainty, so:

$$\frac{\Delta\varepsilon}{\varepsilon} = \frac{\Delta A}{A} \text{ and } \frac{\Delta\varepsilon\prime}{\varepsilon\prime} = \frac{\Delta B}{B} \quad (6.7)$$

By summing both terms in eq. 6.5, we can express $\Delta\varepsilon$ as:

$$\Delta\varepsilon = \varepsilon\varepsilon'\left(\frac{C}{AB}\Delta A\right). \quad (6.8)$$

The change in the accepted events, ΔA, is expressed by:

$$\Delta A = \sqrt{\frac{AB}{C}}, \quad (6.9)$$

and

$$\Delta\varepsilon = \sqrt{\frac{AC}{B^3}} . \quad (6.10)$$

Equations 6.9 and 6.10 are used in the final determination of the statistical uncertainty of the acceptance.

Chapter 7

Differential Cross Section

In this chapter we discuss our results of extracting the differential cross section for the $K_S\Lambda$ channel as functions of center-of-mass angle and as functions of the center-of-mass energy. With the reconstruction of the $K_S\Lambda$ channel from the final-state particles $p\pi^-\pi^-\pi^+$, only the $K_S\Sigma^0$ survives the cuts, which in turn decays to the $K_S\Lambda$ plus a γ. Non-resonance phase space is negligible. In identifying the photoproduction of hyperons off neutrons, we take the missing mass of the total reaction; the peaks of the proton and the proton plus gamma overlap some.

The $K_S\Sigma^0$ is background for this work, but in future studies, we shall make use of our $K_S\Lambda$-channel identification tools for extracting the Σ^0s. The method of yield extraction for the $K_S\Sigma^0$ channel is similar; only the acceptance simulation will require an extra decay step in the event generation. The cross section for the $K_S\Sigma^0$ channel will be developed at a later time. These future studies will allow us to perform an independent coupled-channel analysis of the $K_S\Lambda$ and $K_S\Sigma^0$ reactions for cross checking the systematic uncertainties inherent in neutral-hyperon identification.

7.1 Cross Section Uncertainties

7.1.1 Systematic Uncertainties

In Chapter 5 we discussed in detail our systematic studies for extracting the $\gamma n \rightarrow K_S\Lambda$ cross section. Each cut and correction on the data was evaluated by systematically studying the effects on the exclusive selection of events, on identifying quasi-free neutrons, and on the total yield. The systematic uncertainties were determined both from varying the ratio of the invariant mass peak to the phase-space background as well as observing the momentum dependence of the angular distribution of the missing particle and its subsequent effect on the total yield itself.

Cuts were made on beta and time selections, the background of related invariant mass peaks, the heavy hyperon seen with the missing mass of the K_S, and on events having excessive momentum. Due to the gravitational sag in the tagger hodoscope, it was necessary to correct the energy of the photon and the momentum of the final-state particles. The momentum corrections are required to account for the energy lost in the target and in the start counter before the particle is measured in the drift chambers with the attendant systematic inefficiencies in various regions of the drift chambers.

The quality of the Monte Carlo simulation was also considered. This leads to more cuts on events with tracks entering bad T- and E-counters or SC paddles. The inefficiencies at the boundaries of the CLAS detector also required fiducial cuts for both the experimental and simulated data.

The overall uncertainty of the cross section varies significantly for each point. The range of uncertainties for the systematic studies is presented in Table 7.1. The minimum uncertainty has been calculated to be 7.30% with the worst points being 57.15%. The largest source of error comes from the acceptance uncertainty and yields fits. This is predominately due to low-count bins in energy and cosine theta that result in poor data fits.

7.1.2 Statistical Uncertainties

The statistical uncertainty of the acceptance was discussed in section 6.5.2. As can be seen in Fig. 7.1, the systematic uncertainties tend to dominate over the statistical.

However, the statistical contribution is significant in each energy bin and is therefore always factored into the total uncertainty. The difference in uncertainties in last two energy bins (2.0-2.2 GeV and 2.2-2.4 GeV) is particularly small.

The statistical uncertainty of the yields was determined from the fit to the missing-mass peak. The uncertainty of the yield shows a similar dominance of the systematic uncertainty. Yet the statistical uncertainty still has a significant presence and is considered for all of the total uncertainty calculations.

Table 7.1: The assorted uncertainties associated with data cuts, corrections, and individual system measurement limits. Chapter 5 covers the development of most of these values. Others were taken from reference indicated. The largest source of error is from the acceptance uncertainty and yields fits.

Category	System	Source	Uncertainty
Final-State Identification	PID Cuts	Beta cut checks	0.30% − 22.00%
	Time Difference Cuts	Timing cut checks	2.48% − 4.28%
Yield Extraction	Ks Invariant Mass cuts	Mass cut checks	2.48% – 7.46%
	L Invariant Mass cuts	Mass cut checks	2.49% – 7.48%
	Missing Momentum Cuts	Missing momentum fits	3.79% 6.76%
	Correction factor	$\gamma n \rightarrow K_S\Lambda$	> 0.1%
	KsΛ fits	$\gamma n \rightarrow K_S\Lambda$	> 0.1% 32.1%
	KsΣ^0 fits	$\gamma n \rightarrow K_S\Lambda$	> 0.1% 16.5%
CLAS Acceptance	Fiducial Cuts	Mattione [32]	1.70% – 6.20%
	Acceptance Uncertainty	$\gamma n \rightarrow K_S\Lambda$	3.02% − 32.29%
	Trigger Simulation	$\gamma n \rightarrow K_S\Lambda$	2.11
Miscellaneous	Target Length	Christo *et al.* [38]	0.03%
	Target Density	Williams [6]	0.11%
	BR(K_S, $\pi^+ + \pi^-$)	Nakamura *et al.* [39]	0.05%
	BR(Λ, $p + \pi^-$)	Nakamura *et al.* [39]	0.05%
	Photon Flux	Williams [6]	1.80%
Overall	Systematics	Total of above uncertainties	7.10% – 55.18%
	Statistical	Taken from yield	1.67% − 14.88%
	Total		7.30% − 57.15%

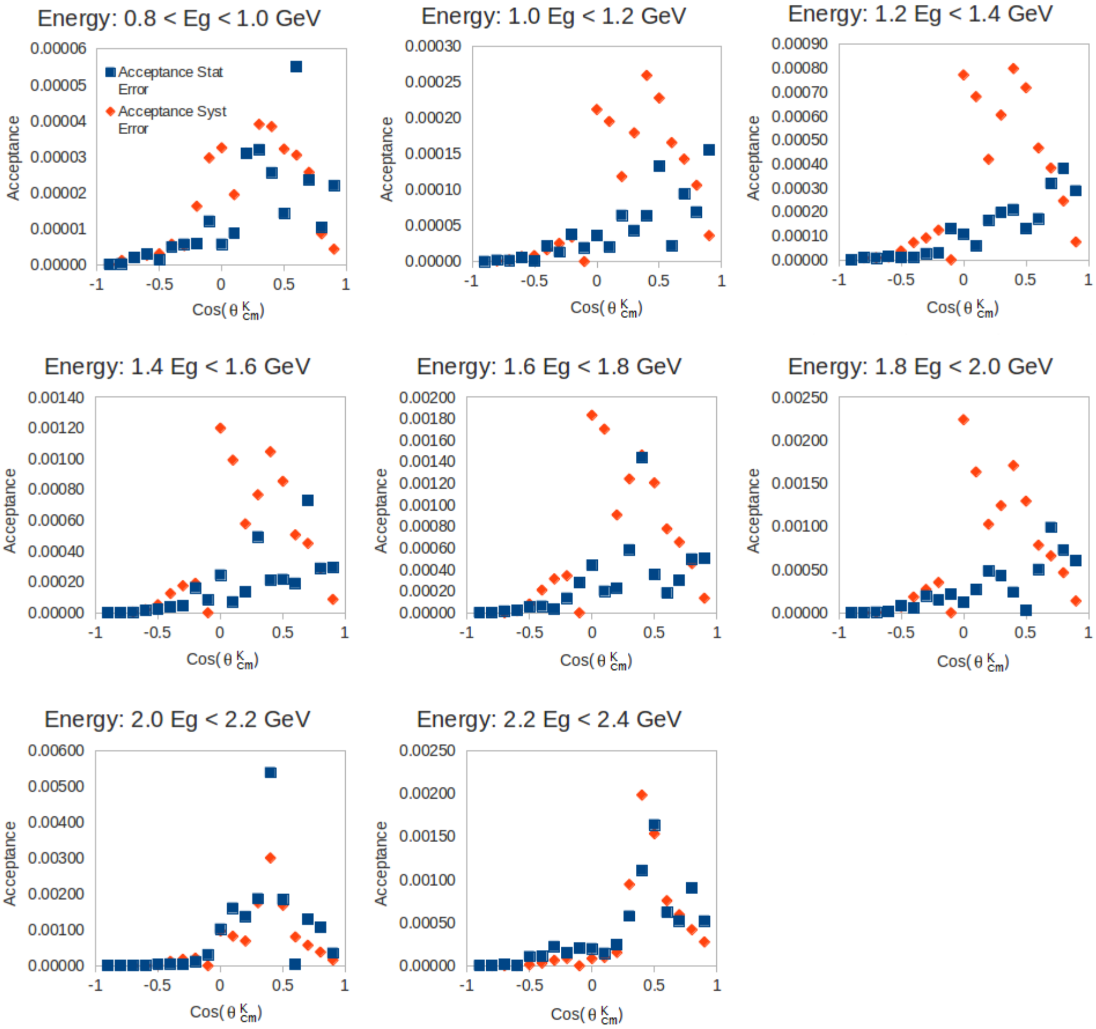

Figure 7.1: The statistical and systematic uncertainties for the acceptance of the γn → $K_S\Lambda$ reaction. For $cos(\theta_{CM}^{K^0})$, the systematic uncertainties tend to dominate over the statistical. The uncertainties in last two energy bins (2.0-2.2 and 2.2-2.4 GeV) have similar magnitudes. The statistical contribution is significant in each energy bin and is always factored into the total uncertainty.

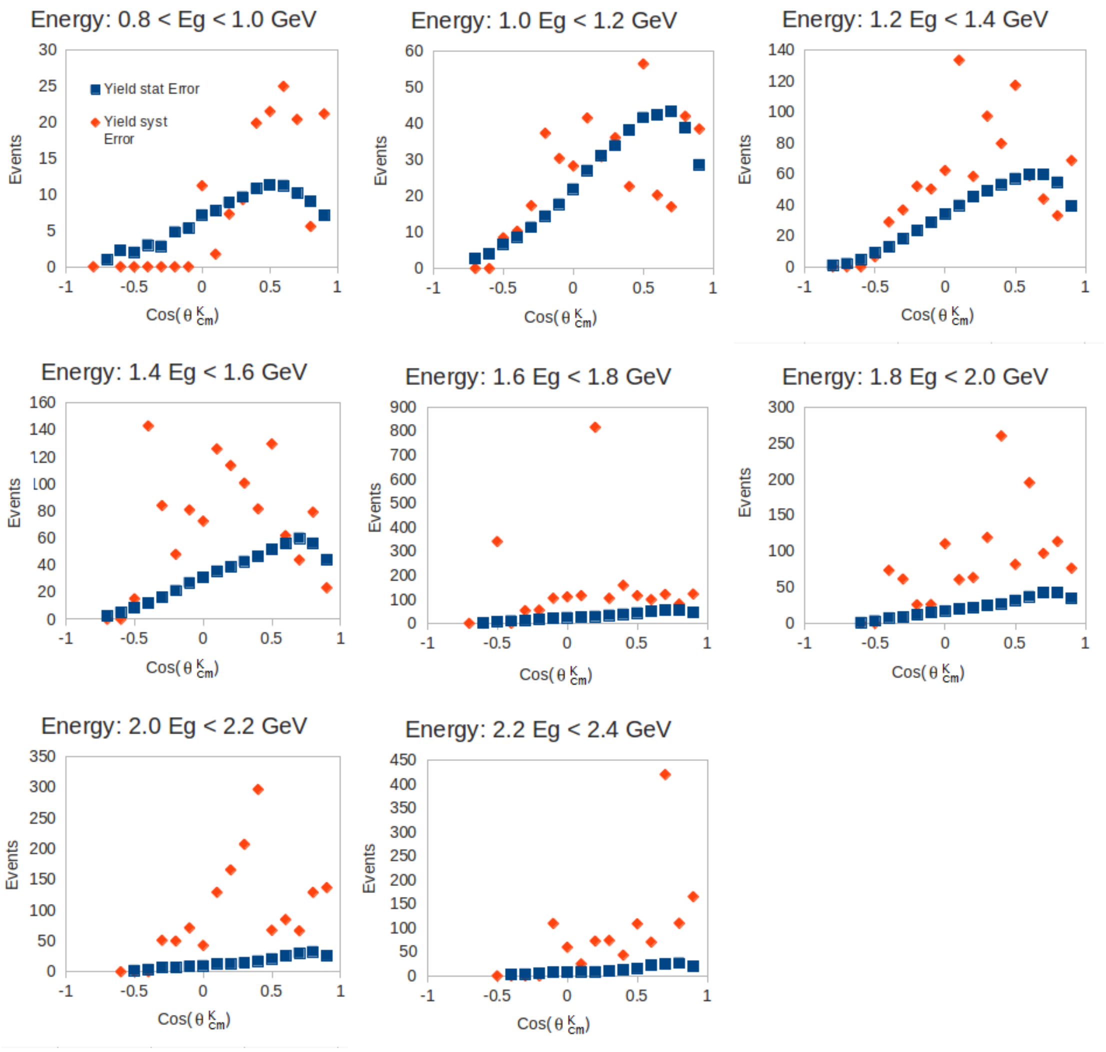

Figure 7.2: The statistical and systematic uncertainties for the yield of the γn → $K_S\Lambda$ reaction. For $cos(\theta^{K^0}_{CM})$, the systematic uncertainties tend to dominate over the statistical. Though the statistical contribution remains significant in each energy bin and is therefore always factored into the total uncertainty.

7.2 The $\gamma n \rightarrow K_S\Lambda$ Differential Cross Section

As discussed in section 2.6, the differential cross section for the $\gamma n \rightarrow K_S\Lambda \rightarrow p\pi^-\pi^-\pi^+$ reaction can be rewritten as:

$$\frac{d\sigma}{dcos\theta_{CM}^{K_S}} = \frac{A_{target}}{\rho\ell N_A}\frac{1}{\Delta cos\theta_{CM}^{K_S}}\frac{Y\left(\sqrt{s},\theta_{CM}^{K_S}\right)}{\phi_i\left(\sqrt{s}\right)}\frac{Y_{CF}}{\alpha\left(\sqrt{s},\theta_{CM}^{K_S}\right)}\frac{\Gamma_{K_S}}{\Gamma_{K_S\rightarrow\pi^+\pi^-}}\frac{\Gamma_\Lambda}{\Gamma_{\Lambda\rightarrow p\pi^-}}, \tag{5.1}$$

where A_{target} is the atomic weight of the target, ρ is the density of the target, ℓ is the length of the target, N_A is Avogadro's number, $\Delta\cos(\theta_{CM}^{K^0})$ is the bin width of the cosine theta, $Y\left(\sqrt{s},\theta_{CM}^{K^0}\right)$ is the yield, $\phi_i\left(\sqrt{s}\right)$ is the photon flux, Y_{CF} is the yield correction factor, $\alpha\left(\sqrt{s},\theta_{CM}^{K^0}\right)$ is the acceptance used, and $\frac{\Gamma_{K^0}}{\Gamma_{K^0\rightarrow\pi^+\pi^-}}$ and $\frac{\Gamma_\Lambda}{\Gamma_{\Lambda\rightarrow p\pi^-}}$ are the inverse branching ratios of the decay channels for the neutral hadrons.

After the final yield has been determined, several iterations are made in the development of the acceptance. The first step assumes that the K_S is projected into any angle, with the Λ hyperon being oppositely directed in the center-of-mass frame. The resultant cross section is then normalized and fed back into the event generator. Six iterations were performed for the final cross section. All but the first and last iterations used the previous iteration's cross section with a 0.1 phase space (at least a 10% chance that a K_S generated in a given angle will be kept). Without the requisite background phase space, certain bin values could approach zero and thereby produce highly uncertain and suspect values from the sloping function in the fsgen code. The phase space was reduced to 0.05 for the last iteration.

As can be seen in Fig. 7.3, the distributions are, more or less, consistent. They differ mostly for forward angles and energies above 2.2 GeV. These errors typically arise in bins with significant slope. After the first iteration using phase space, the distribution in the 2.2-2.4 GeV bin remain nearly the same. However, when the background is changed to 0.05 phase space, the peak magnifies. The fourth iteration was used for the development of the final cross section.

Figure 7.4 shows the flux-normalized yields for g13a, while Fig. 7.5 is the final differential cross section. In the two lower energy bins (0.8-1.0 and 1.0-1.2 GeV) for the $K_S\Lambda$ channel, the cross section is relatively flat. However, after 1.2 GeV, the cross section begins to resemble the standard *t*-slope distribution, implying that diffractive scattering

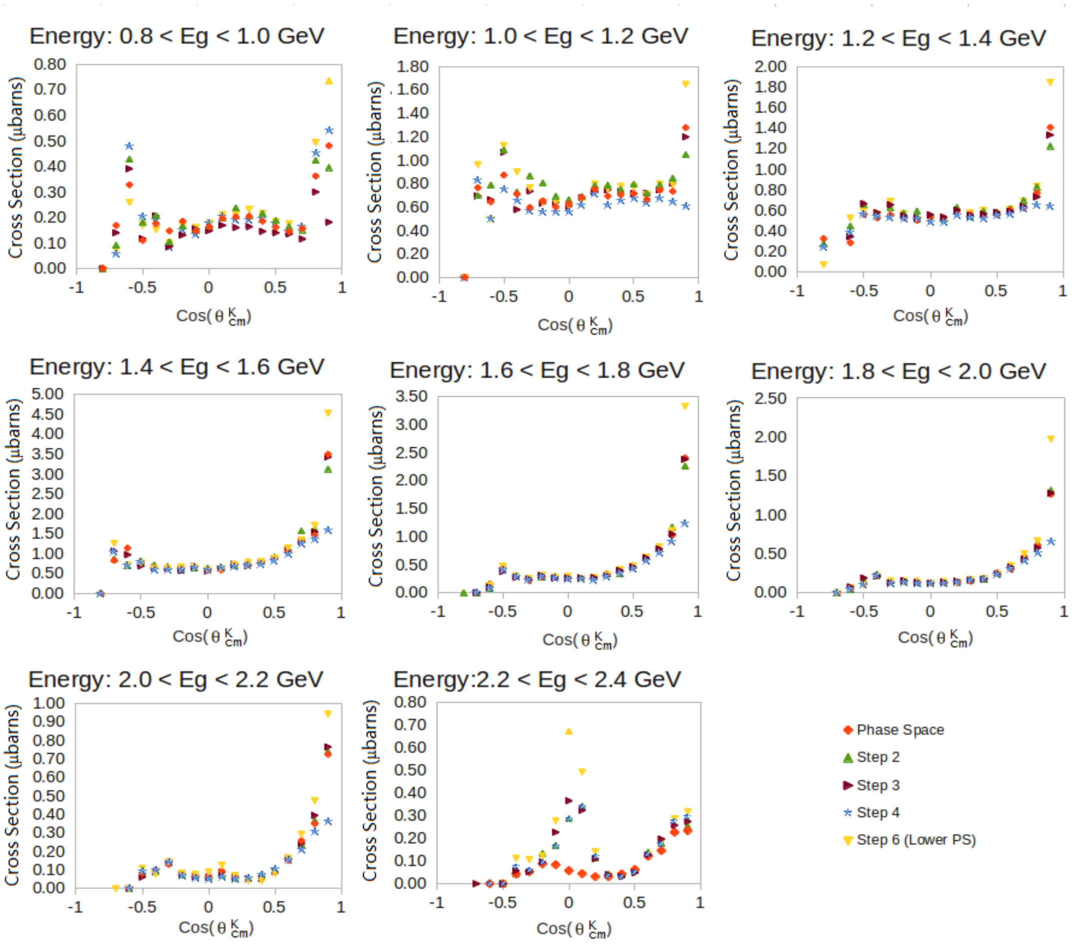

Figure 7.3: The evolution of the differential cross section with each iteration of the event generation. The distributions are mostly consistent, except at the most forward angles and above 2.2 GeV photon energy. Errors mostly arise in bins with significant slope. After the first iteration (using phase space), the distribution in the 2.2-2.4 GeV bin remain consistent. However, when the background is changed on the 6th iteration, the peak magnifies, due to the method used to generate the sloping function from the bin values.

dominates the reaction. By the energy range 2.2 to 2.4 GeV, there is a clear increase in cross section around $\cos(\theta_{CM}^{K^0}) = 0$. In the flux-normalized yield for the same energy bin, there is a clear opposite effect on the same region about zero. The effect of the peak clearly comes from the acceptance determination (see Fig. 6.5), which in turn is dependent on the results from the final yield. The increase in error bars in this region is due to the variation measured from the six iterations in the development of the acceptance; the error bars reflect the statistical and systematic uncertainties added in quadrature.

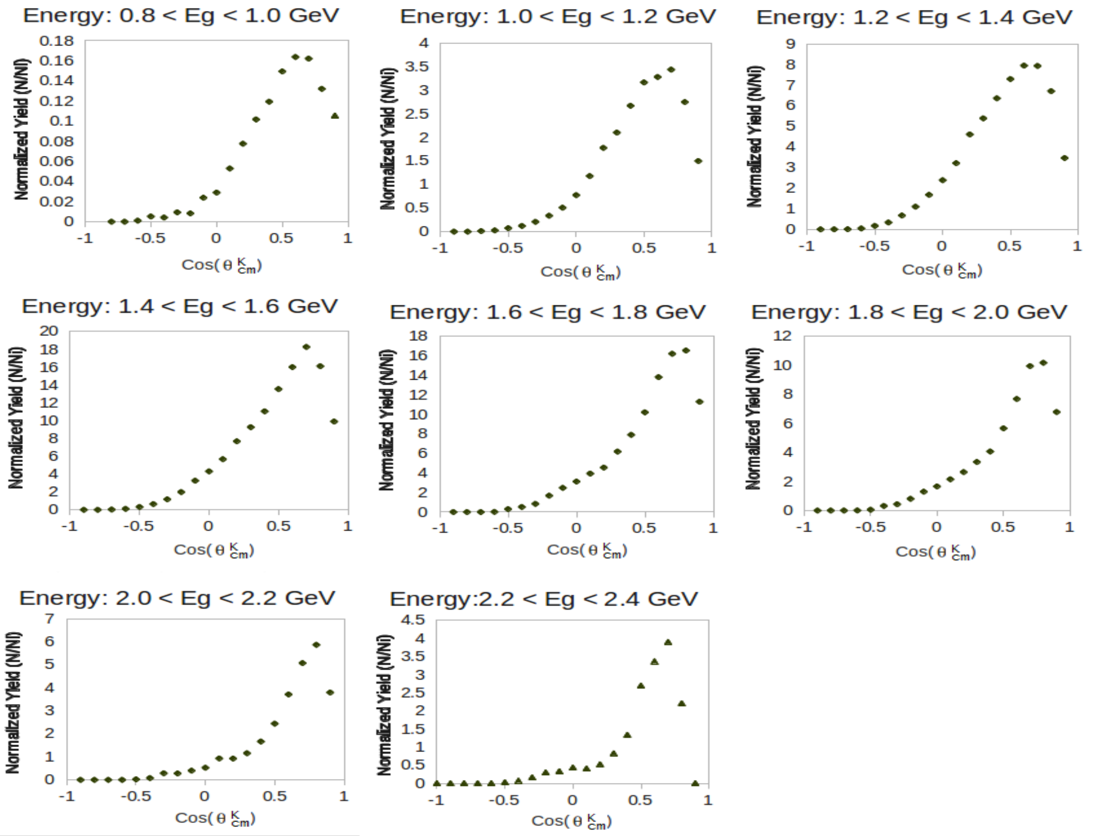

Figure 7.4: The normalized yields binned by both energy and cosine theta of the K_S track in the center of mass frame. The distribution has a clear forward bias in direction. Both the 2.0-2.2 and 2.2-2.4 GeV ranges show a decrease of events between 0 and 0.5 $cos(\theta_{CM}^{K^0})$.

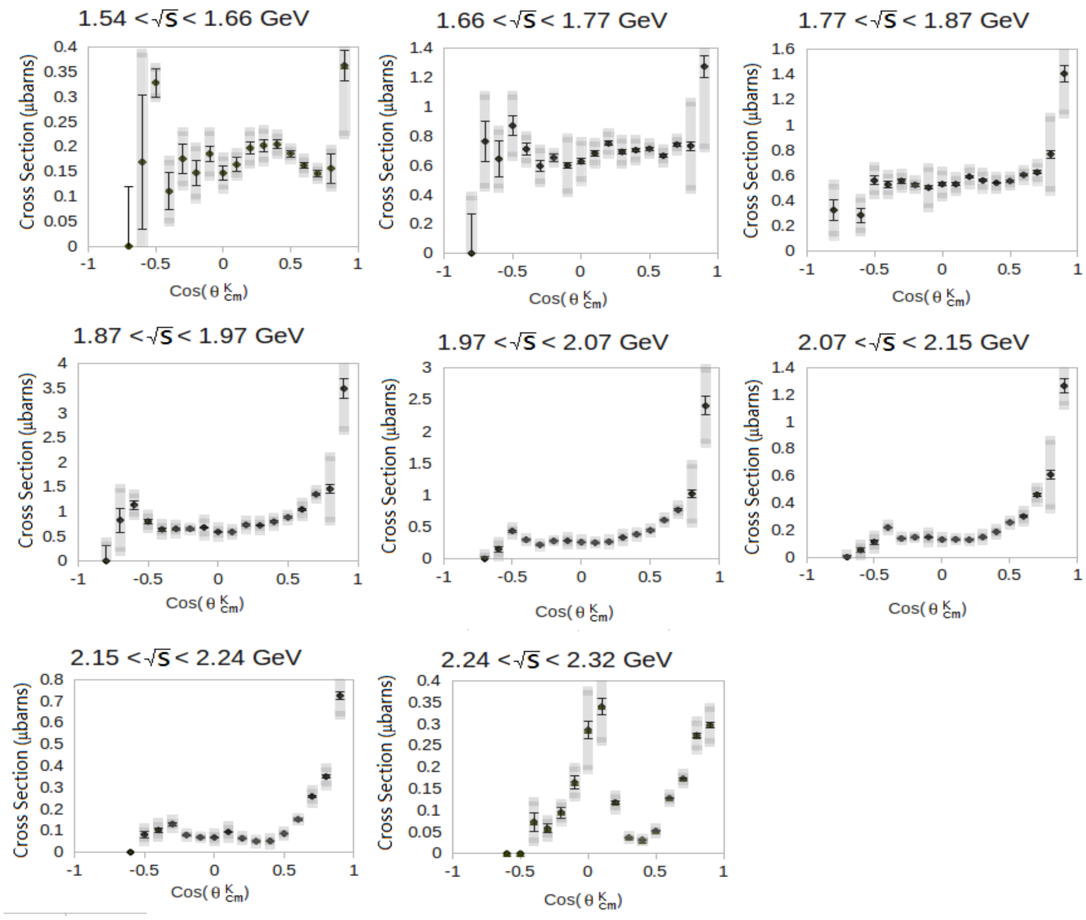

Figure 7.5: Differential cross section for the $\gamma n \rightarrow K_S\Lambda$ reaction, binned by energy and cosine theta. The first two energy bins show mostly an even cross section per $\cos(\theta^{K^0}_{CM})$ bin. However, the higher $\sqrt{s}$ energy bins exhibit a standard t-slope form, implying that scattering dominates in this reaction. Excess cross section can be seen about $\cos(\theta^{K^0}_{CM}) = 0$ in the 1.8-2.2 GeV range, which is consistent with results seen in similar channels (e.g. $K^+\Lambda$, and $K^{*+}\Lambda$). The error bars include both statistical and systematic uncertainties. The gray bar represents the variation in cross section from all the iterations of simulation before the cross section stabilized.

With the cross section plotted as a function of the center-of-mass energy (seen in Fig. 7.6), it is possible to further examine the trends of these energy-dependent distributions. The general distribution is similar with what is seen in the $K^+\Lambda$ channel[40],[42]. However, the $K^+\Lambda$ has one peak at ~1.8 GeV and, in this study, the $K_S\Lambda$ channel shows two peaks, at 1.7 and 1.9 GeV. The cross section quickly lowers with increased energy. Around 2.3 GeV, some uncertain structure manifests around cosine theta of zero.

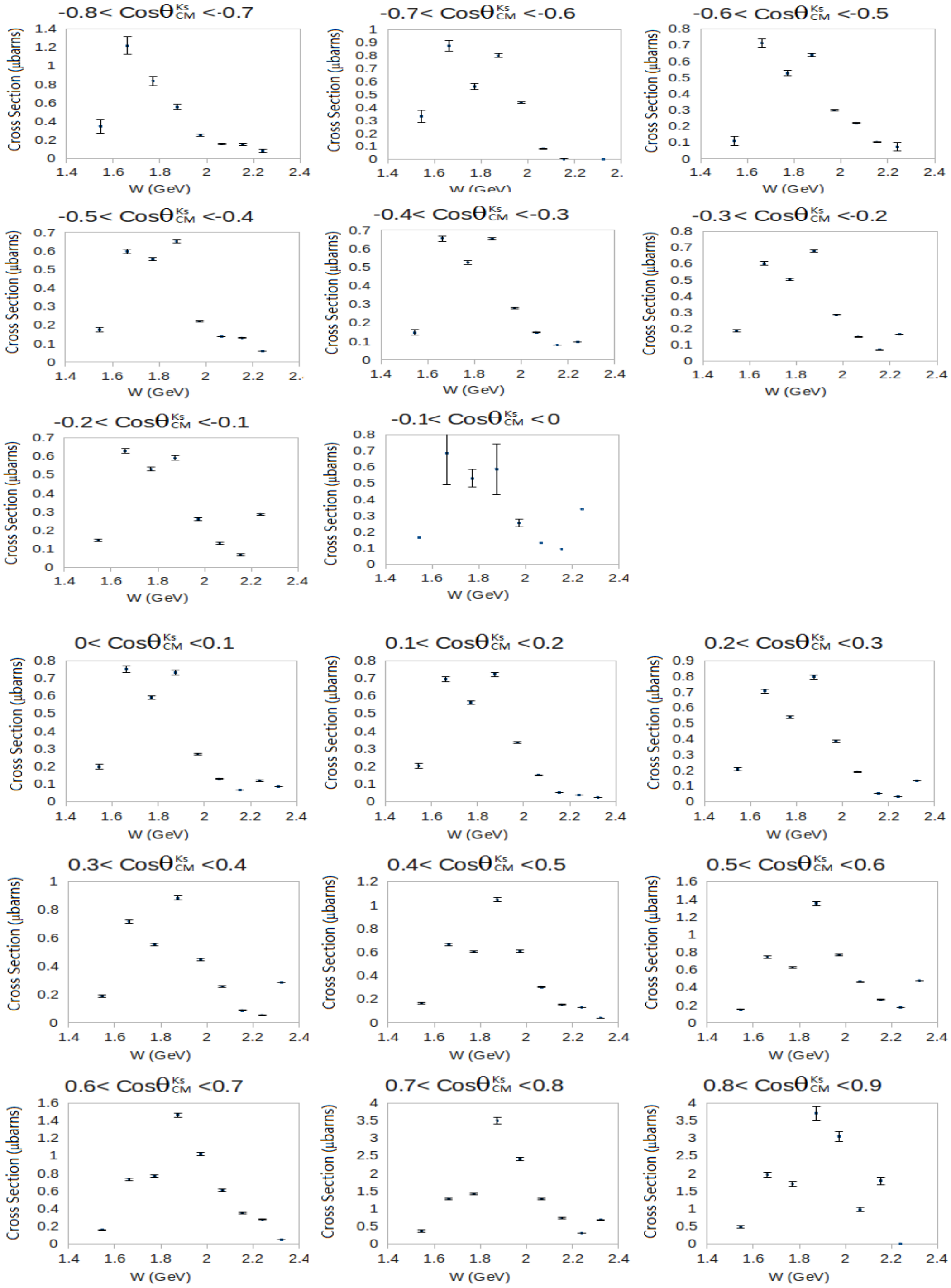

Figure 7.6: Differential cross section for the $\gamma n \rightarrow K_S\Lambda$ reaction, binned by cosine theta as a function of the center-of-mass energy. There is clearly a smooth increase at the lower and mid cosine theta angles as the energy bins are increased. The development of these structures can be seen with cm energy as low as 1.7 GeV and becomes more clearly pronounced by 1.9 GeV.

We have chosen to show the data “as is” as there are no prior measurements of this channel to form a direct comparison. We are also not aware of any specific predictions for this channel.

7.3 Summary

QCD-based theories predict a plethora of N* states. Although many of these low-lying states have been measured, we expect as new decay modes become kinematically accessible, more excited baryon will be identified. In the past, most of resonances were measured with pion beams. It is most likely that many of these yet unmeasured missing resonances will have a stronger coupling to photons than through interacting with pions. Specifically, the $\gamma n \rightarrow K_S \Lambda$ reaction is predicted to be sensitive to the contested “missing” $D_{13}(1900)$ resonance[1]. Some modified theories suggest alternate quark configurations. There are competing models for the quark symmetries and dynamics ranging from preferentially paired-quark distributions to hybrid gluonic excitations. The diquark model, for example, recalculates these resonances assuming that two of the quarks are tightly bound, the third in orbit about them. Identifying missing resonances will ultimately give measure of the underlying dynamics.

In this study, we measured the energy-dependent differential cross section for the $\gamma n \rightarrow K_S \Lambda$ reaction from the g13a dataset, which was collected in 2006 with the CLAS detector system at Jefferson Laboratory using a circularly-polarized photon beam between 1.3 to 2.3 GeV on a deuterium target. This cross section has not been previously measured. At the time of this study, we are unaware of any theories for the $\gamma n \rightarrow K_S \Lambda$ cross section. Even though the 13a experiment uniquely offers a circularly polarized beam onto a deuterium target, we chose to first extract the differential cross section, which we view as the necessary first step in understanding $K_S\Lambda$ production off neutrons.

Extracting the differential cross section is difficult, as one must have an extremely good understanding of the systematic uncertainties. The development of the differential cross section requires thorough tracking of the rejected events, as well as careful reproduction of the g13 experimental environment in the simulation. Flaws in the detector performance must be reflected in the simulation, and conversely, the limitations in the simulation must limit what is accepted in the empirical data. This channel is further complicated by the difficulty of reconstruction of the neutral K_S and Λ tracks. None of the detected final-state particles come from the production vertex. This required the reconstruction of the neutral decay vertices and, in turn, the event vertex. Additionally, the selection of the event photon needed special attention. Despite these challenges, we have solid results for the differential cross section.

We regard this work on the $K_S\Lambda$ energy-dependent differential cross section as the necessary first step in identifying the underlying physics in the resonance regime. The work will lay the foundation for further studies in extracting the polarization observables for circularly- and linearly-polarized photons from our analyzed dataset. Measurement of the differential cross section coupled with single- and double-polarization observables provide strong constraints on identifying the N* excitation spectrum. In the inestimable words of Lao-Tzu, the longest journey begins with a single step. We have made that crucial first step.

References

[1] R. Koniuk and N. Isgur, Phys. Rev. D 21, 1868 (1980).

[2] S. Capstick and N. Isgur, *Baryon decays in a quark model with chromodynamics*, Phys. Rev. D 34, N 9, 2809 (1986).

[3] S. Capstick and N. Isgur, *$N\pi$ decays of baryons in a relativized model*, Phys. Rev. D 45, N 5, 1994 (1993).

[4] W. Yao *et al*. *Review of Particle Physics*, J. Phys. G 33, 1 (2006).

[5] M. Williams, *Measurement of Differential Cross Sections and Spin Density Matrix Elements along with a partial Wave Analysis for $\gamma p \rightarrow p\omega$ using CLAS at Jefferson Lab*. Ph.D. Thesis, Carnegie Mellon University (2007).

[6] T. Mart and C. Bennhold, Phys. Rev. C 61, 012201 (1999).

[7] A. Waluyo, PhD thesis, Washington, DC: George Washington University, Washington, DC (2005).

[8] G. Penner and U. Mosel, *Vector meson production and nucleon resonance analysis in a coupled-channel approach for energies $m_N<\sqrt{s}<2$ GeV.* Phys. Rev. C 66, 055212 (2002).

[9] S. Capstick, and W. Roberts, Phys. Rev. D 58, 074011 (1998).

[10] C.J. Joachain, *Quantum Collision Theory*, North-Holland Publishing (1975).

[11] H. Garcilazo, J. Vijande, and A. Valcarce *Faddeev study of heavy-baryon spectroscopy*. Journal of Physics G 34 (5): 961–976. doi:10.1088/0954-3899/34/5/014, (2007).

[12] C. Garcia-Recio, V. K. Magas, T. Mizutani, J. Nieves, A. Ramos, L. L. Salcedo and L. Tolos, Phys. Rev. D 79, 054004 (2009).

[13] M.S. Sozzi, *Discrete symmetries and CP violation.* Oxford University Press (2008).

[14] H. Yamamura, *et al.* Phys. Rev. C 61, 014001 (1999).

[15] P.L. Cole, K. Livingston, *et al. Photoproduction of the ρ Meson from the Proton with Linearly polarized Photons*, Jefferson Lab PAC Proposal: Pr-94-109, (1994).

[16] P.L. Cole, F. Klein, *et al. Photoproduction of ω Meson with Linearly polarized Photons*, Jefferson Lab PAC Proposal: Pr-98-109, (1998).

[17] K. Livingston, Nucl. Instr. and Meth. A **603**, 205 (2009).

[18] D. I. Sober *et al.* (The CLAS Collaboration), Nucl. Instr. and Meth. A **440**, 263 (2000).

[19] P. Nadel-Turonski, *et al.*, Jefferson Lab PAC30 Proposal: PR-06-103, http://www.jlab.org/exp_prog/proposals/06/PR-06-103.pdf (2006).

[20] Y. G. Sharabian *et al.* (The CLAS Collaboration), Nucl. Instr. and Meth. A **556**, 246 (2006).

[21] M. Amarian, *et al.*, *The CLAS forward electromagnetic calorimeter*, (CLAS)*,* Nucl. Instr. and Meth. A **460**, 239-265(2001).

[22] P. Nadel-Turonski, *et al.*, Few Body Syst. **43**, 227 (2008).

[23] H. Olsen and L. C. Maximom, *Electron and Photon Polarization in Bremsstrahlung and Pair Production* , Phys. Rev. **114**, 887 (1959).

[25] U. Timm, *Coherent Bremsstrahlung of Electrons in Crystals*, Fortschr. Phys. **17**, 765 (1969).

[26] F. A. Natter *et al.*, Nucl. Instr. and Meth. B **211**, 465 (2003).

[27] M. Holtrop. *GSIM: CLAS GEANT Simulation*, http://www.physics.unh.edu/maurik/ Gsim/gsim current code dev.shtml.

[28] C. Amsler *et al.* (Particle Data Group), PL B667, 1 (URL: http://pdg.lbl.gov) (2008).

[29] E. Pasyuk, *Photon flux determination through sampling out of time hits with the Hall B photon tagger.*

[30] K. Nakamura *et al.* (The Particle Data Group), J. Phys. G **37**, 075021 (2010).

[31] E. Pasyuk, *Energy loss corrections for charged particles in CLAS*, CLAS-Note 2007-016 (2007). Jefferson Lab CLAS-Note 2005-002 (2005).

[32] P. Mattione, *$K^*(892)^0\Lambda$ and $K^+\Sigma^*(1385)^-$, Photoproduction on the Deuteron,* Doctoral dissertation*,* Rice University, (2011).

[33] N. Zachariou, *Determination of the Azimuthal Asymmetry of Deuteron Photodisintegration in the Energy Region Eg = 1.1 - 2.3 GeV*, Doctoral dissertation, George Washington University, (2012).

[34] K. Y. Kim, H. Denizli, J. A. Mueller, and S. A. Dytman, Jefferson Lab CLAS-Note 2001-018 (2001).

[35] M. Williams and C.A. Meyer, Jefferson Lab CLAS-Note 2003-017 (2003).

[36] R. Machleidt, *The high-precision charge-dependent Bonn nucleon-nucleon potential (CD-Bonn)*, University of Idaho, arXiv:nucl-th/0006014v1, (2008).

[37] Y.Y. Ilieva, *Analysis Note on Coherent Pion Photoproduction on Deuterium: $\gamma d\rightarrow\pi^+ d$*, CLAS –NOTE 2007-006, (2006).

[38] S. Christo, http://www.jlab.org/~christo/g11a%20target.html (2004).

[39] K. Nakamura *et al.* (The Particle Data Group), J. Phys. G 37, 075021 (2010).

[40] M.E. McCracken, *A Study of $K^+\Lambda$ Photoproduction in the CLAS g11a Dataset: Differential Cross Section, recoil Polarization and a Partial Wave Analysis*, Doctoral dissertation, Carnegie Mellon University (2008).

[41] V. Fanti, A. Lai, D. Marras, L. Musa, *et al.. A new measurement of direct CP violation in two pion decays of the neutral kaon.* Physics Letters B 465 (1–4), (1999).

[42] Biplab Dey, *Differential cross section and polarization extractions for* $\gamma n \rightarrow K^+ \Lambda$ *and* $\gamma n \rightarrow K^+ \Sigma^0$ *using CLAS at Jefferson Lab*, Doctoral dissertation, Carnegie Mellon University (2011).

Appendix A

Cross Section Tables

A.1 The $\gamma n \rightarrow K_S\Lambda$ Acceptance and Differential Cross Section

The table below gives the acceptance and differential cross sections discussed in chapter 6 for the $\gamma n \rightarrow K_S\Lambda$ reaction. The data is binned by energy and the cosine theta in the center of mass frame. The acceptance statistical errors were determined using the same method used by Ilieva[37] in the time-of-flight statistical uncertainty for coherent pion production. The systematic errors were determined using similar methods to McCracken's[40] detailed in chapter 7.

Table A.1: Tabulated differential cross sections for the $\gamma n \rightarrow K_S\Lambda$ reaction. Values are binned by both energy and cosθ in the center of mass frame

Energy $\sqrt{s}$ (GeV)	Cosine Theta	Acceptance	Acceptance Total Uncertainty	Yield	Yield Systematic Uncertainty	Cross Section $\frac{d\sigma}{\cos\theta_{cm}^{K}}$	Cross Section Total Uncertainty
1.74	-0.9	0.000E+00	0.000E+00	0.00	0.00	0.00000000	0.00000000
1.74	-0.8	2.118E-06	2.118E-06	0.00	0.00	0.00000000	0.00000000
1.74	-0.7	3.572E-06	2.526E-06	1.00	0.00	0.16889678	0.00000000
1.74	-0.6	9.195E-06	3.754E-06	5.00	2.24	0.32808862	0.13394320
1.74	-0.5	2.189E-05	5.651E-06	4.00	2.00	0.11026043	0.02846995
1.74	-0.4	3.094E-05	6.595E-06	9.00	3.00	0.17553133	0.03742498
1.74	-0.3	3.273E-05	6.682E-06	8.00	2.83	0.14745325	0.03010013
1.74	-0.2	7.483E-05	1.018E-05	23.00	4.80	0.18545209	0.02523942
1.74	-0.1	1.150E-04	1.240E-05	28.00	5.29	0.14689050	0.01584216
1.74	0	1.886E-04	1.612E-05	51.19	13.29	0.16372587	0.01399167
1.74	0.1	2.299E-04	1.690E-05	60.21	7.95	0.19681399	0.01447494
1.74	0.2	2.937E-04	1.795E-05	78.99	11.48	0.20204817	0.01234785
1.74	0.3	3.408E-04	1.903E-05	92.69	13.37	0.20434183	0.01141160
1.74	0.4	4.689E-04	2.254E-05	116.05	22.59	0.18595329	0.00894310
1.74	0.5	5.894E-04	2.482E-05	127.18	24.25	0.16213199	0.00683364
1.74	0.6	6.486E-04	2.507E-05	125.91	27.34	0.14585920	0.00564141

1.74	0.7	4.928E-04	2.057E-05	102.60	22.74	0.15643083	0.00653542
1.74	0.8	1.700E-04	1.391E-05	82.02	10.63	0.36256507	0.02967803
1.74	0.9	7.789E-05	4.888E-06	49.85	22.29	0.48082272	0.03017991
1.94	-1	0.000E+00	0.000E+00	0.00	0.00	0.00000000	0.00000000
1.94	-0.9	4.214E-06	2.107E-06	0.00	0.00	0.00000000	0.00000000
1.94	-0.8	8.578E-06	3.033E-06	7.00	2.65	0.76480729	0.27040398
1.94	-0.7	2.326E-05	4.850E-06	16.00	4.00	0.64476529	0.13444815
1.94	-0.6	4.851E-05	6.793E-06	45.13	10.81	0.87205836	0.12212306
1.94	-0.5	9.881E-05	9.465E-06	75.07	13.46	0.71201486	0.06821098
1.94	-0.4	2.026E-04	1.339E-05	128.96	20.73	0.59664900	0.03944255
1.94	-0.3	3.004E-04	1.597E-05	209.50	40.08	0.65359701	0.03475832
1.94	-0.2	4.920E-04	2.052E-05	315.34	35.22	0.60066908	0.02507314
1.94	-0.1	7.194E-04	2.453E-05	481.91	35.84	0.62780632	0.02142546
1.94	0	1.006E-03	2.825E-05	732.91	49.62	0.68301662	0.01921238
1.94	0.1	1.379E-03	3.307E-05	975.09	43.93	0.75143036	0.01805396
1.94	0.2	1.767E-03	3.689E-05	1152.66	49.61	0.69342044	0.01451785
1.94	0.3	2.209E-03	4.068E-05	1464.98	44.48	0.70495291	0.01302643
1.94	0.4	2.582E-03	4.432E-05	1736.55	70.24	0.71482743	0.01231789
1.94	0.5	2.875E-03	4.612E-05	1800.52	47.02	0.66584405	0.01073409
1.94	0.6	2.695E-03	4.336E-05	1885.80	46.65	0.74387620	0.01202468
1.94	0.7	2.183E-03	3.805E-05	1507.71	57.26	0.73406046	0.01284296
1.94	0.8	6.840E-04	1.534E-05	821.54	48.05	1.27681173	0.02870034
1.94	0.9	1.026E-04	3.852E-06	188.28	21.23	1.95149441	0.07335626
2.14	-1	0.000E+00	0.000E+00	0.00	0.00	0.00000000	0.00000000
2.14	-0.9	3.699E-06	2.616E-06	1.00	1.00	0.32387646	0.22901622
2.14	-0.8	1.822E-05	5.762E-06	4.00	2.00	0.00000000	0.08317818
2.14	-0.7	9.301E-05	1.290E-05	22.00	4.69	0.28339190	0.03930368
2.14	-0.6	1.794E-04	1.785E-05	83.71	11.16	0.55897063	0.05563141
2.14	-0.5	3.698E-04	2.505E-05	162.57	31.56	0.52673930	0.03569125
2.14	-0.4	7.061E-04	3.467E-05	327.32	40.88	0.55540078	0.02728680
2.14	-0.3	1.224E-03	4.538E-05	535.41	56.82	0.52421637	0.01945766
2.14	-0.2	1.946E-03	5.733E-05	815.05	57.72	0.50190435	0.01480956
2.14	-0.1	2.630E-03	6.637E-05	1161.60	70.84	0.52918972	0.01338133
2.14	0	3.536E-03	7.555E-05	1563.12	138.99	0.52955337	0.01134247
2.14	0.1	4.559E-03	8.396E-05	2043.13	73.75	0.58937755	0.01089247
2.14	0.2	5.620E-03	9.354E-05	2389.25	108.74	0.55906580	0.00934561
2.14	0.3	6.864E-03	1.045E-04	2819.75	95.58	0.54027015	0.00826512
2.14	0.4	7.676E-03	1.091E-04	3235.79	130.12	0.55439598	0.00792592
2.14	0.5	7.677E-03	1.072E-04	3523.46	83.49	0.60354789	0.00848048
2.14	0.6	7.420E-03	1.056E-04	3516.84	73.66	0.62329658	0.00892399
2.14	0.7	5.091E-03	8.169E-05	2974.11	63.72	0.76832747	0.01238718
2.14	0.8	1.435E-03	3.131E-05	1536.00	78.93	1.40754524	0.03078561
2.14	0.9	1.646E-04	6.544E-06	211.61	16.43	1.69043700	0.06724560
2.34	-1	0.000E+00	0.000E+00	0.00	0.00	0.00000000	0.00000000

2.34	-0.9	5.475E-06	3.871E-06	0.00	0.00	0.00000000	0.00000000
2.34	-0.8	1.908E-05	7.212E-06	6.00	2.45	0.82578015	0.31212117
2.34	-0.7	5.552E-05	1.184E-05	24.00	4.90	1.13533638	0.24206767
2.34	-0.6	2.317E-04	2.443E-05	70.40	17.23	0.79775807	0.08410995
2.34	-0.5	5.858E-04	3.924E-05	142.81	143.31	0.64023422	0.04289733
2.34	-0.4	1.055E-03	5.206E-05	261.10	85.50	0.65004324	0.03209704
2.34	-0.3	1.784E-03	6.576E-05	442.64	52.34	0.65169896	0.02404833
2.34	-0.2	2.805E-03	8.363E-05	724.26	85.12	0.67814834	0.02024726
2.34	-0.1	4.271E-03	1.029E-04	957.52	78.76	0.58870164	0.01420929
2.34	0	5.639E-03	1.187E-04	1259.65	130.72	0.58660928	0.01238585
2.34	0.1	6.137E-03	1.211E-04	1502.87	120.01	0.72991219	0.01444195
2.34	0.2	7.510E-03	1.370E-04	1814.28	109.21	0.72009407	0.01318699
2.34	0.3	8.107E-03	1.404E-04	2161.75	93.85	0.79480573	0.01382236
2.34	0.4	8.951E-03	1.456E-04	2649.06	139.33	0.88211726	0.01441441
2.34	0.5	8.938E-03	1.452E-04	3133.24	83.32	1.04491770	0.01705685
2.34	0.6	7.893E-03	1.318E-04	3575.38	74.10	1.35012846	0.02263488
2.34	0.7	6.438E-03	1.173E-04	3151.83	97.02	1.45917205	0.02668564
2.34	0.8	1.653E-03	4.092E-05	1937.62	49.75	3.49443238	0.08668846
2.34	0.9	1.282E-04	6.964E-06	159.15	32.31	3.70007265	0.20105532
2.54	-1	0.000E+00	0.000E+00	0.00	0.00	0.00000000	0.00000000
2.54	-0.9	0.000E+00	0.000E+00	0.00	0.00	0.00000000	0.00000000
2.54	-0.8	7.174E-06	5.073E-06	0.00	0.00	0.00000000	0.00000000
2.54	-0.7	6.373E-05	1.546E-05	3.00	1.73	0.15353662	0.03724005
2.54	-0.6	4.006E-04	3.769E-05	53.74	340.12	0.43762878	0.04118250
2.54	-0.5	1.019E-03	6.101E-05	93.08	9.65	0.29804876	0.01785879
2.54	-0.4	2.213E-03	8.737E-05	149.50	54.41	0.22034591	0.00870593
2.54	-0.3	3.508E-03	1.094E-04	299.15	57.54	0.27812914	0.00868790
2.54	-0.2	5.130E-03	1.309E-04	442.59	106.36	0.28141322	0.00719572
2.54	-0.1	6.987E-03	1.543E-04	558.47	112.49	0.26071786	0.00577295
2.54	0	9.056E-03	1.794E-04	704.44	118.25	0.25371324	0.00504172
2.54	0.1	9.917E-03	1.794E-04	815.01	815.51	0.26806063	0.00486633
2.54	0.2	1.081E-02	1.850E-04	1107.87	109.31	0.33425862	0.00574413
2.54	0.3	1.204E-02	1.963E-04	1414.47	162.24	0.38303967	0.00627027
2.54	0.4	1.334E-02	2.086E-04	1828.25	122.79	0.44688016	0.00701995
2.54	0.5	1.329E-02	2.039E-04	2471.39	110.28	0.60650085	0.00935350
2.54	0.6	1.233E-02	1.951E-04	2900.00	131.80	0.76702127	0.01219394
2.54	0.7	9.451E-03	1.649E-04	2959.40	96.79	1.02133221	0.01788751
2.54	0.8	2.741E-03	6.253E-05	2020.08	129.87	2.40358088	0.05495608
2.54	0.9	2.160E-04	1.042E-05	201.67	25.19	3.04473972	0.14692231
2.74	-1	0.000E+00	0.000E+00	0.00	0.00	0.00000000	0.00000000
2.74	-0.9	0.000E+00	0.000E+00	0.00	0.00	0.00000000	0.00000000
2.74	-0.8	4.035E-06	4.035E-06	0.00	0.00	0.00000000	0.00000000
2.74	-0.7	6.263E-05	1.566E-05	1.00	1.00	0.05208138	0.01302100
2.74	-0.6	2.929E-04	3.476E-05	10.00	3.16	0.11136881	0.01322011

2.74	-0.5	8.503E-04	5.912E-05	56.96	73.88	0.21851425	0.01519803
2.74	-0.4	1.836E-03	8.413E-05	77.26	61.95	0.13727082	0.00629457
2.74	-0.3	3.195E-03	1.107E-04	144.28	28.37	0.14727642	0.00510691
2.74	-0.2	5.101E-03	1.396E-04	231.56	30.18	0.14807183	0.00406032
2.74	-0.1	7.471E-03	1.728E-04	296.57	111.65	0.12946510	0.00300058
2.74	0	9.555E-03	1.950E-04	384.40	63.69	0.13121739	0.00268561
2.74	0.1	1.212E-02	2.296E-04	473.05	67.08	0.12731800	0.00242011
2.74	0.2	1.311E-02	2.316E-04	597.06	121.45	0.14848362	0.00263171
2.74	0.3	1.267E-02	2.246E-04	726.28	261.04	0.18690888	0.00332476
2.74	0.4	1.292E-02	2.206E-04	1011.46	87.62	0.25540445	0.00438038
2.74	0.5	1.487E-02	2.491E-04	1372.11	198.39	0.30099232	0.00506411
2.74	0.6	1.258E-02	2.144E-04	1777.36	105.69	0.46078594	0.00788354
2.74	0.7	9.734E-03	1.771E-04	1818.24	121.12	0.60926181	0.01112584
2.74	0.8	3.127E-03	7.228E-05	1212.17	83.91	1.26448176	0.02929783
2.74	0.9	2.204E-04	1.137E-05	65.75	10.72	0.97293359	0.05020348
2.94	-1	0.000E+00	0.000E+00	0.00	0.00	0.00000000	0.00000000
2.94	-0.9	0.000E+00	0.000E+00	0.00	0.00	0.00000000	0.00000000
2.94	-0.8	0.000E+00	0.000E+00	0.00	0.00	0.00000000	0.00000000
2.94	-0.7	3.251E-05	1.327E-05	0.00	0.00	0.00000000	0.00000000
2.94	-0.6	1.602E-04	2.976E-05	4.00	2.00	0.08142417	0.01512183
2.94	-0.5	4.466E-04	4.789E-05	14.00	3.74	0.10225048	0.01096600
2.94	-0.4	1.275E-03	8.356E-05	50.96	51.46	0.13039006	0.00854998
2.94	-0.3	2.036E-03	9.718E-05	49.73	50.23	0.07964827	0.00380296
2.94	-0.2	3.367E-03	1.248E-04	71.09	71.59	0.06886970	0.00255551
2.94	-0.1	4.483E-03	1.307E-04	93.82	43.72	0.06825707	0.00199346
2.94	0	5.780E-03	1.464E-04	166.03	129.42	0.09368590	0.00237796
2.94	0.1	8.347E-03	1.793E-04	165.21	165.71	0.06455696	0.00139013
2.94	0.2	1.332E-02	2.449E-04	206.73	207.23	0.05062761	0.00093424
2.94	0.3	1.884E-02	3.157E-04	297.73	296.26	0.05155690	0.00086792
2.94	0.4	1.654E-02	2.903E-04	436.16	70.50	0.08602048	0.00151611
2.94	0.5	1.426E-02	2.623E-04	663.34	88.52	0.15172703	0.00280114
2.94	0.6	1.146E-02	2.204E-04	906.60	72.97	0.25804951	0.00497953
2.94	0.7	9.789E-03	1.967E-04	1048.67	132.72	0.34940417	0.00704172
2.94	0.8	3.056E-03	7.602E-05	678.39	138.89	0.72403428	0.01804573
2.94	0.9	2.290E-04	1.320E-05	125.25	14.80	1.78379196	0.10286512
3.14	-1	0.000E+00	0.000E+00	0.00	0.00	0.00000000	0.00000000
3.14	-0.9	0.000E+00	0.000E+00	0.00	0.00	0.00000000	0.00000000
3.14	-0.8	0.000E+00	0.000E+00	0.00	0.00	0.00000000	0.00000000
3.14	-0.7	2.232E-05	2.232E-05	0.00	0.00	0.00000000	0.00000000
3.14	-0.6	1.371E-04	5.596E-05	0.00	0.00	0.00000000	0.00000000
3.14	-0.5	2.226E-04	6.713E-05	5.00	2.24	0.07324982	0.02208840
3.14	-0.4	7.311E-04	1.236E-04	13.00	3.61	0.05799477	0.00980690
3.14	-0.3	9.973E-04	1.288E-04	29.00	5.39	0.09483891	0.01225064
3.14	-0.2	1.054E-03	1.010E-04	53.21	109.53	0.16466159	0.01578210

3.14	-0.1	6.805E-04	5.005E-05	59.66	60.15	0.28593972	0.02103454
3.14	0	7.427E-04	4.084E-05	77.33	26.37	0.33963141	0.01868220
3.14	0.1	2.000E-03	7.053E-05	72.60	73.10	0.11838699	0.00417822
3.14	0.2	8.425E-03	1.574E-04	94.33	74.51	0.03651750	0.00068473
3.14	0.3	1.552E-02	2.188E-04	148.41	44.98	0.03119812	0.00044255
3.14	0.4	1.506E-02	2.183E-04	239.21	109.58	0.05179358	0.00075498
3.14	0.5	1.229E-02	1.877E-04	481.95	73.79	0.12792327	0.00196421
3.14	0.6	1.135E-02	1.789E-04	602.47	420.63	0.17320508	0.00274386
3.14	0.7	8.332E-03	1.387E-04	698.40	112.99	0.27338223	0.00457048
3.14	0.8	4.335E-03	9.278E-05	395.29	166.40	0.29739951	0.00638117
3.14	0.9	3.954E-04	2.818E-05	0.00	0.00	0.00000000	0.00000000

Appendix B

Data Cuts and Counting

This appendix offers some of the finer details of the cuts and fits made for the analysis. First the run ranges used for the analysis are listed. Next details are given on the beta development along with the cuts made to the final state particle's distributions. The final section shows the fit to the missing mass peaks used for each of the cross sections binned by photon energy and kaon angle.

B.1 Run ranges

The g13a dataset was taken over several run ranges. Table B.1 lists all of these runs with some description of their stand and end times, beam energy, target, and if the data was good. The first two ranges used a liquid hydrogen target, while the remaining used the liquid deuterium discussed in the target section in chapter 3.

Table B.1 List of run ranges and their associated information. The initial tabulation was made by Paul Mattione[32]

Run Range	Date Started	Date Finished	Beam Energy (MeV)	Target/ Quality	Golden Run
*53095 - 53139	10/28/06	10/28/06	1.99018	LH2 / Data	53121
*53140 - 53148	10/29/06	10/29/06	1.99018	LH2 / Data	53144
*53149 - 53163	10/30/06	10/30/06	n/a	Junk	53144
*53164 - 53326	10/30/06	11/06/06	1.99018	LD2 / Data	53220
*53327 - 53409	11/06/06	11/11/06	1.99018	LD2 / Data	53333

53410 - 53459	11/11/06	11/15/06	1.99018	LD2 / Data	53410
53460 - 53532	11/15/06	11/21/06	1.99018	LD2 / Data	53460
53533 - 53537	11/22/06	11/27/06	n/a	Junk	53460
53538 - 53569	11/28/06	11/30/06	2.65458	LD2 / Data	53554
53570 - 53767	11/30/06	12/15/06	2.65458	LD2 / Data	53570
53768 - 53862	12/15/06	12/22/06	2.65458	LD2 / Data	53768
53863 - 53969	12/22/06	03/09/07	n/a	Junk	53768
53970 - 53994	03/09/07	03/12/07	2.00014	LH2 / Data	53987
53995 - 53997	03/12/07	03/12/07	n/a	Junk	53987
53998 - 54035	03/12/07	03/15/07	2.00014	LH2 / Data	54023
54036 - 54041	03/15/07	03/16/07	n/a	Junk	54023

* Run ranges below 53333 are missing an important histogram needed for generating the conversions for calculating the photon flux. Otherwise the data is fine.

B.2 Beta Fits

The initial beta cuts only had loose charge and mass cuts as basic particle identification. To refine these cuts on the $\Delta\beta$ the events were binned into 0.1 GeV momentum bins. The peaks were then fit with a Gaussian. The sigma of peak was then used to determine cuts for each momentum bin. The σ, 2σ and 3σ cuts were compared to evaluate the changes in the event selection. Figure B.1 through B.3 show the fits to the beta peaks in various momentum bins.

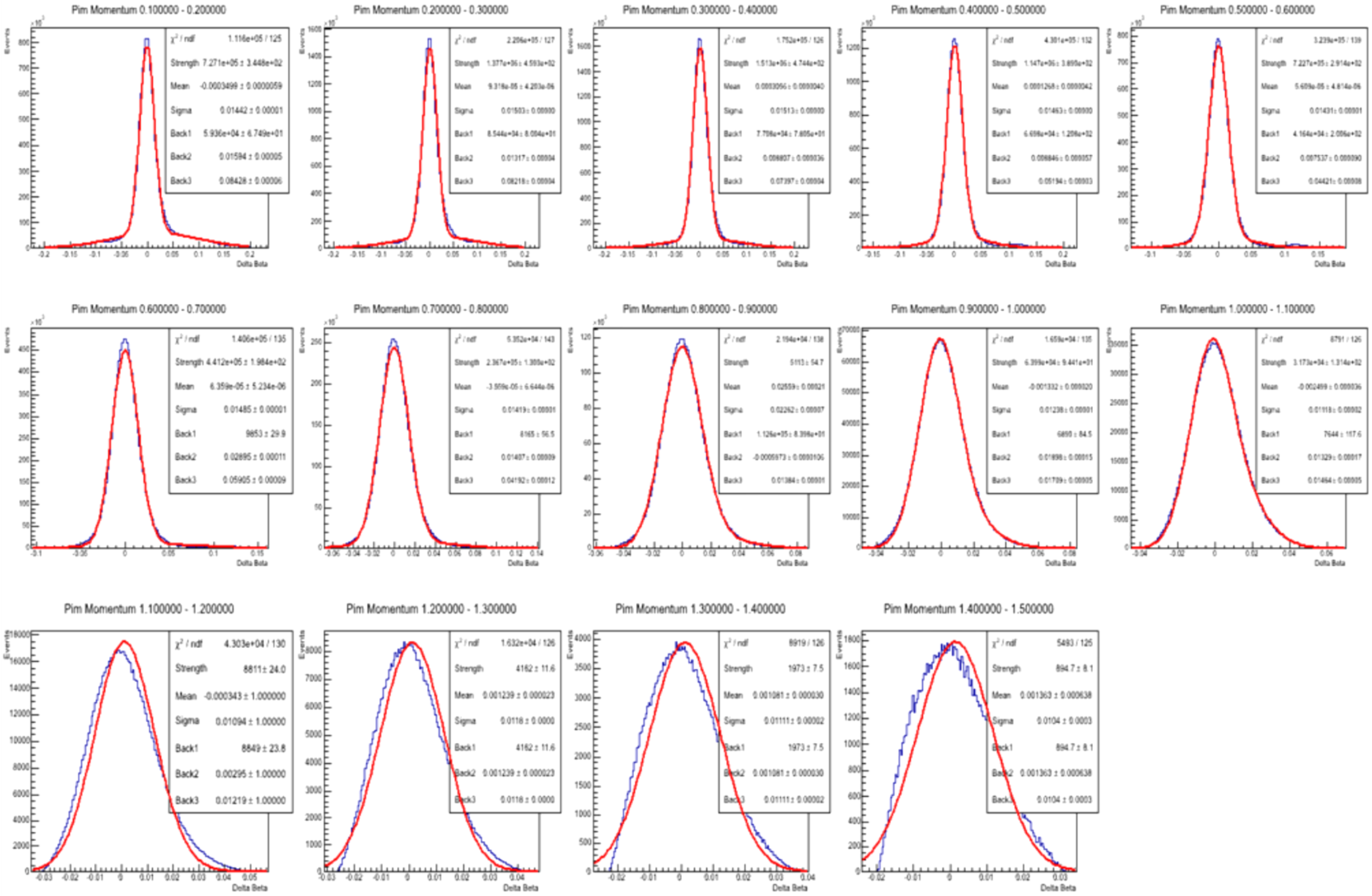

Figure B..1: Fits to the delta beta peaks, binned by momentum for the π^- candidates

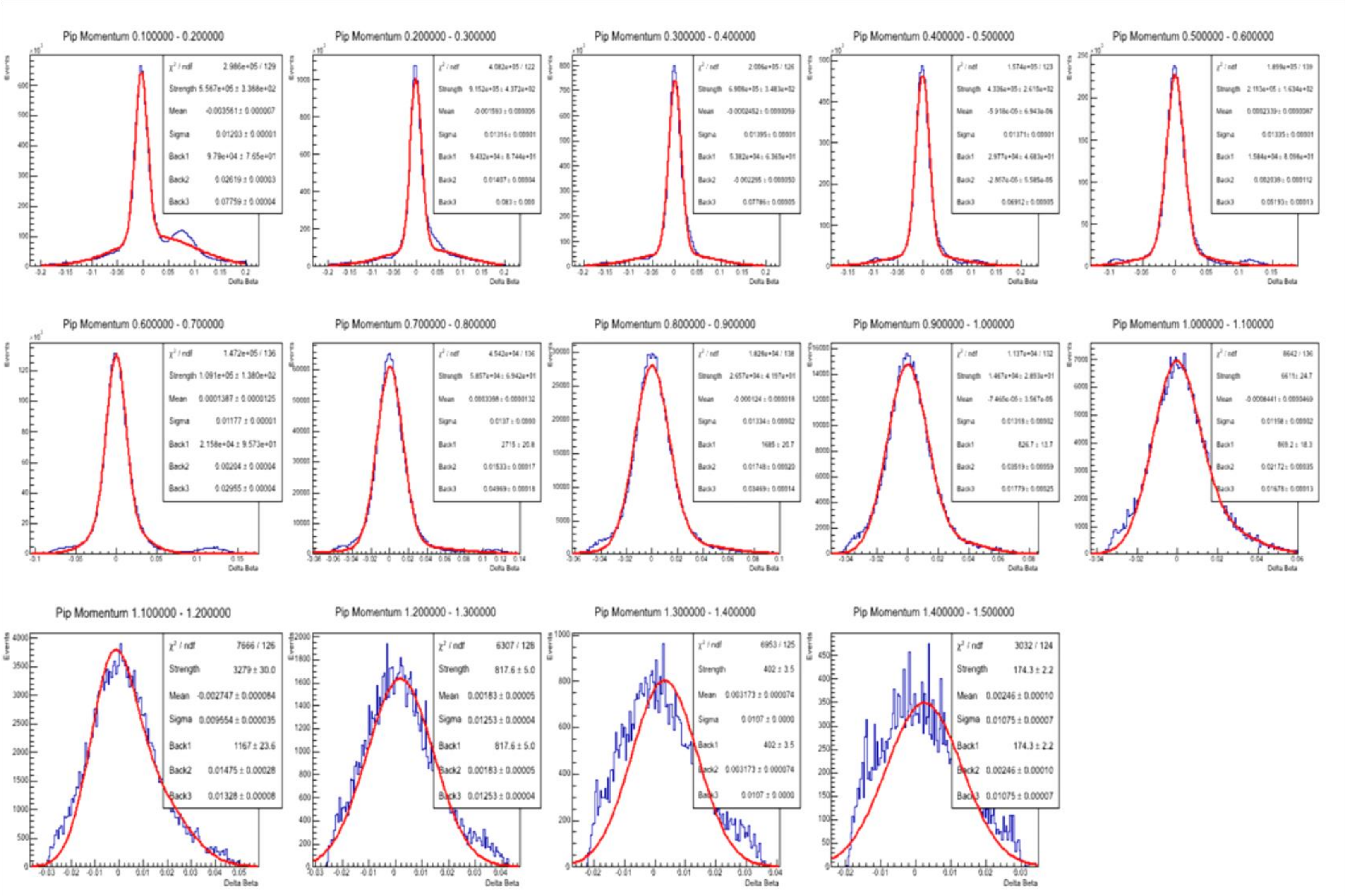

Figure B.2: Fits to the delta beta peaks, binned by momentum for the π^+ candidates

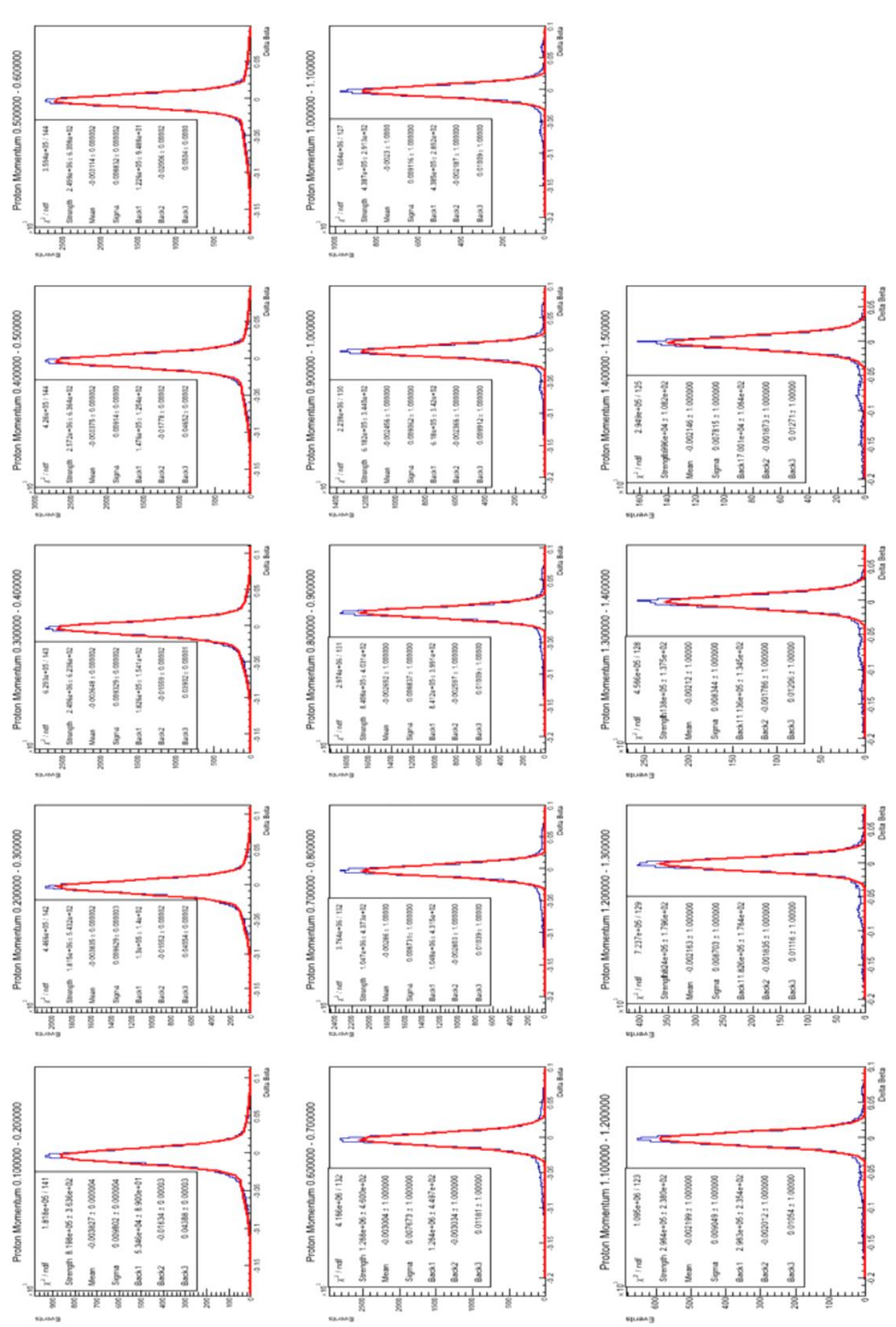

Figure B.3: Fits to the delta beta peaks, binned by momentum for the proton candidates

B.3 Missing Mass Fits

A routine was used to fit the missing mass peak for each $\cos\theta_{CM}^{K^0}$ and energy bin. The routine at times would not fit the peak correctly, and a visual check was required to ensure the quality of the fit. When the fit was found to be unsound, the missing mass peak was then individually fit for specific $\cos\theta_{CM}^{K^0}$ and energy.

B.3.1 Fits for the Experimental Data

The plots in the following plots show the fits to the low. Some energy and cosine theta bins did not fit properly while the routines were running. Sometimes the fit to the $K_S\Lambda$ channel peak worked, while the $K_S\Sigma^0$ did not. In such cases, they were fit independently to get a reliable yield. Bins with low counts, were counted instead of attempting to fit their peak. If they had significant counts in both the $K_S\Lambda$ and $K_S\Sigma^0$ channel regions, their error was estimated by the number of counts both peaks shared. Few counts were observed in the last energy bin 2.4 GeV. This bin range was left out of this report.

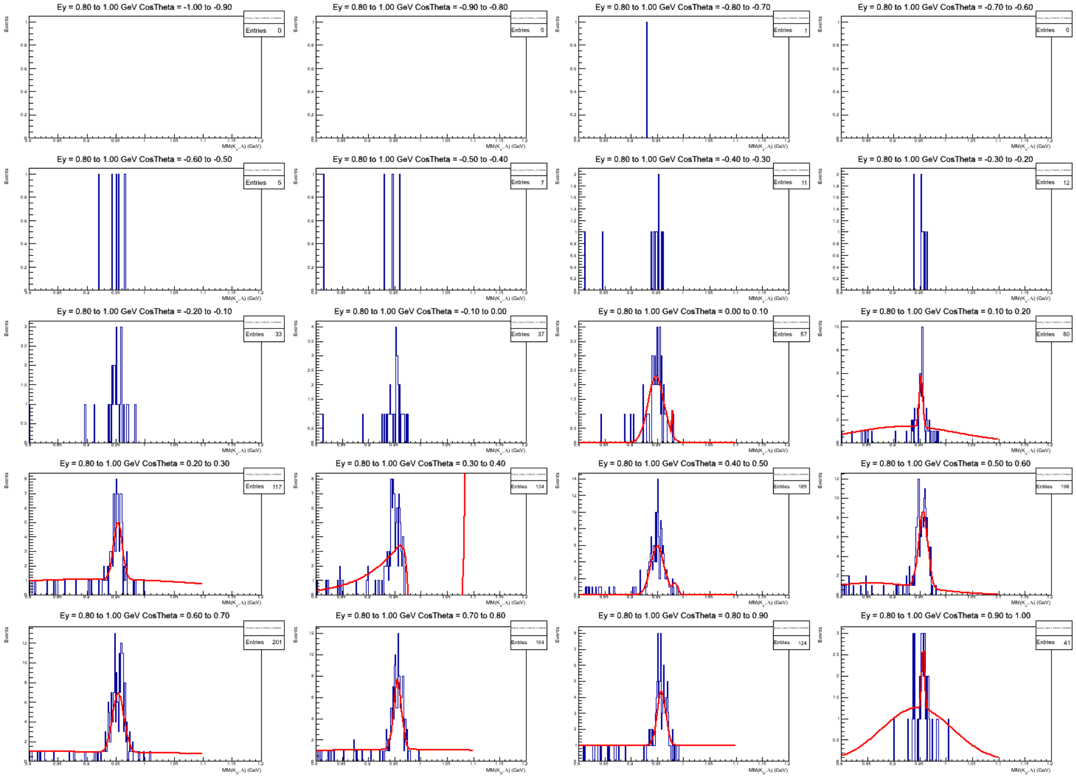
Ey = 0.80 to 1.00 GeV CosTheta = -1.00 to -0.90
Entries 0
Ey = 0.80 to 1.00 GeV CosTheta = -0.90 to -0.80
Entries 0
Ey = 0.80 to 1.00 GeV CosTheta = -0.80 to -0.70
Entries 1
Ey = 0.80 to 1.00 GeV CosTheta = -0.70 to -0.60
Entries 0
Ey = 0.80 to 1.00 GeV CosTheta = -0.60 to -0.50
Entries 5
Ey = 0.80 to 1.00 GeV CosTheta = -0.50 to -0.40
Entries 7
Ey = 0.80 to 1.00 GeV CosTheta = -0.40 to -0.30
Entries 11
Ey = 0.80 to 1.00 GeV CosTheta = -0.30 to -0.20
Entries 12
Ey = 0.80 to 1.00 GeV CosTheta = -0.20 to -0.10
Entries 33
Ey = 0.80 to 1.00 GeV CosTheta = -0.10 to 0.00
Entries 37
Ey = 0.80 to 1.00 GeV CosTheta = 0.00 to 0.10
Entries 57
Ey = 0.80 to 1.00 GeV CosTheta = 0.10 to 0.20
Entries 80
Ey = 0.80 to 1.00 GeV CosTheta = 0.20 to 0.30
Entries 117
Ey = 0.80 to 1.00 GeV CosTheta = 0.30 to 0.40
Entries 134
Ey = 0.80 to 1.00 GeV CosTheta = 0.40 to 0.50
Entries 189
Ey = 0.80 to 1.00 GeV CosTheta = 0.50 to 0.60
Entries 198
Ey = 0.80 to 1.00 GeV CosTheta = 0.60 to 0.70
Entries 201
Ey = 0.80 to 1.00 GeV CosTheta = 0.70 to 0.80
Entries 164
Ey = 0.80 to 1.00 GeV CosTheta = 0.80 to 0.90
Entries 124
Ey = 0.80 to 1.00 GeV CosTheta = 0.90 to 1.00
Entries 41
Events
MM(K, Λ) (GeV)

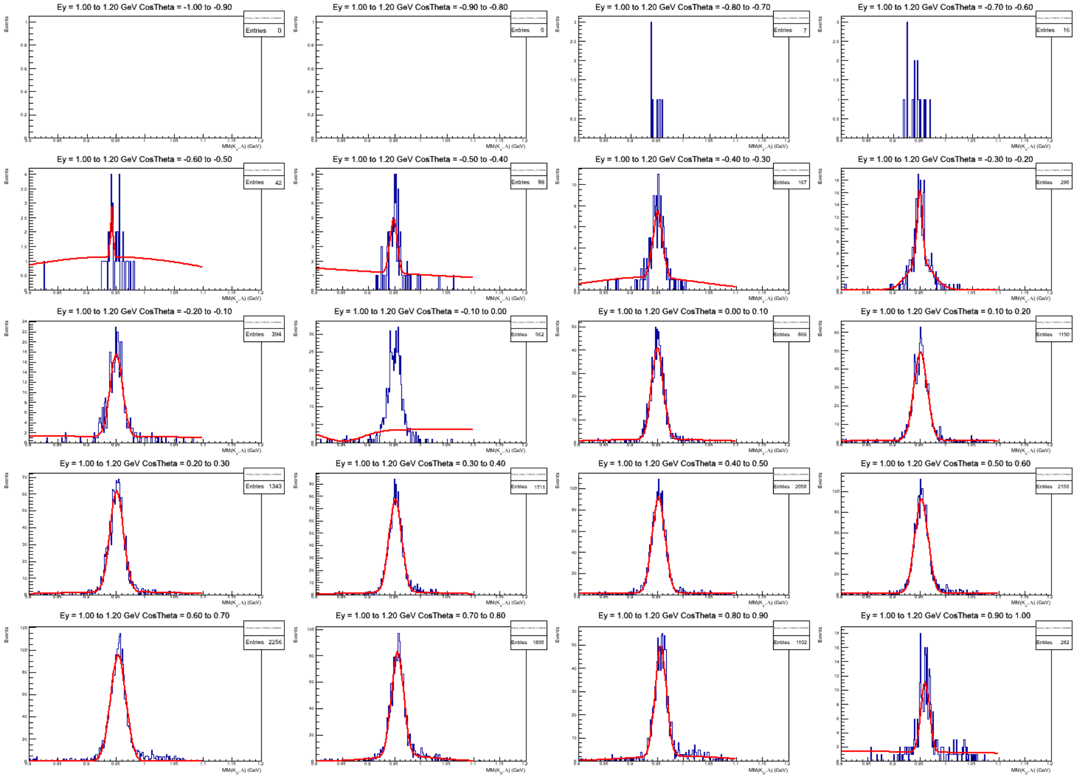
Ey = 1.00 to 1.20 GeV CosTheta = -1.00 to -0.90
Entries 0
Ey = 1.00 to 1.20 GeV CosTheta = -0.90 to -0.80
Entries 0
Ey = 1.00 to 1.20 GeV CosTheta = -0.80 to -0.70
Entries 7
Ey = 1.00 to 1.20 GeV CosTheta = -0.70 to -0.60
Entries 16
Ey = 1.00 to 1.20 GeV CosTheta = -0.60 to -0.50
Entries 42
Ey = 1.00 to 1.20 GeV CosTheta = -0.50 to -0.40
Entries 98
Ey = 1.00 to 1.20 GeV CosTheta = -0.40 to -0.30
Entries 167
Ey = 1.00 to 1.20 GeV CosTheta = -0.30 to -0.20
Entries 290
Ey = 1.00 to 1.20 GeV CosTheta = -0.20 to -0.10
Entries 394
Ey = 1.00 to 1.20 GeV CosTheta = -0.10 to 0.00
Entries 562
Ey = 1.00 to 1.20 GeV CosTheta = 0.00 to 0.10
Entries 866
Ey = 1.00 to 1.20 GeV CosTheta = 0.10 to 0.20
Entries 1150
Ey = 1.00 to 1.20 GeV CosTheta = 0.20 to 0.30
Entries 1343
Ey = 1.00 to 1.20 GeV CosTheta = 0.30 to 0.40
Entries 1711
Ey = 1.00 to 1.20 GeV CosTheta = 0.40 to 0.50
Entries 2050
Ey = 1.00 to 1.20 GeV CosTheta = 0.50 to 0.60
Entries 2150
Ey = 1.00 to 1.20 GeV CosTheta = 0.60 to 0.70
Entries 2256
Ey = 1.00 to 1.20 GeV CosTheta = 0.70 to 0.80
Entries 1890
Ey = 1.00 to 1.20 GeV CosTheta = 0.80 to 0.90
Entries 1102
Ey = 1.00 to 1.20 GeV CosTheta = 0.90 to 1.00
Entries 282
Events
MM(K, Λ) (GeV)

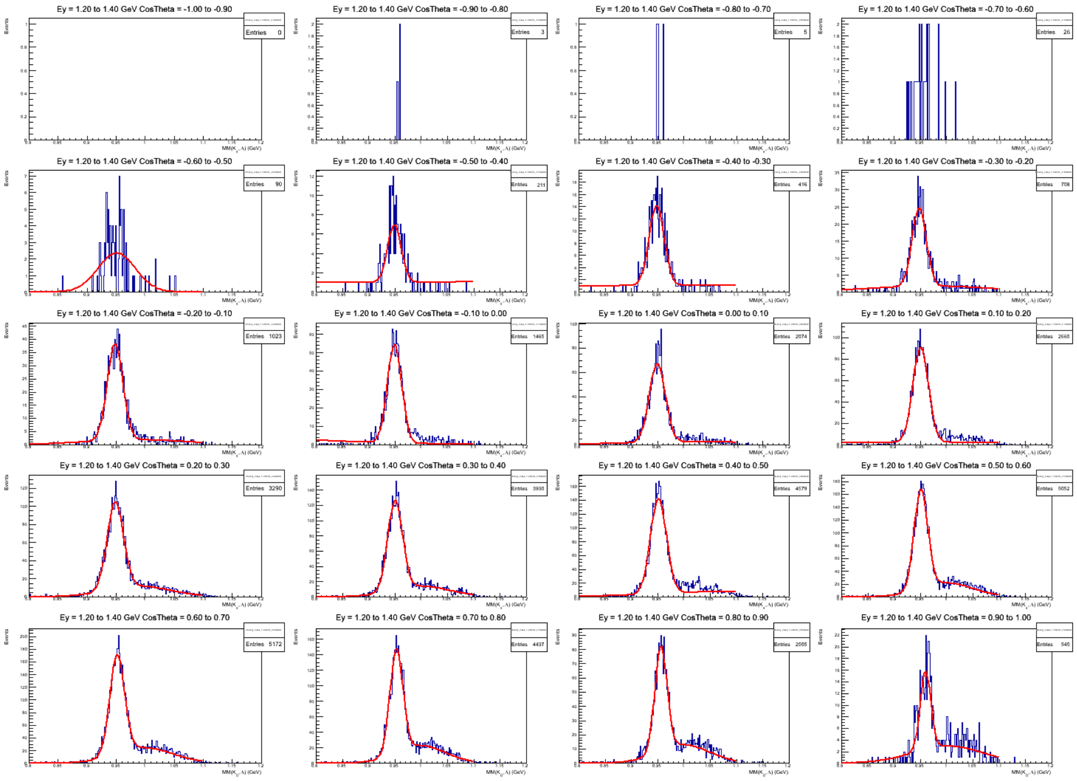
Ey = 1.20 to 1.40 GeV CosTheta = -1.00 to -0.90
Entries 0
Ey = 1.20 to 1.40 GeV CosTheta = -0.90 to -0.80
Entries 3
Ey = 1.20 to 1.40 GeV CosTheta = -0.80 to -0.70
Entries 5
Ey = 1.20 to 1.40 GeV CosTheta = -0.70 to -0.60
Entries 26
Ey = 1.20 to 1.40 GeV CosTheta = -0.60 to -0.50
Entries 90
Ey = 1.20 to 1.40 GeV CosTheta = -0.50 to -0.40
Entries 211
Ey = 1.20 to 1.40 GeV CosTheta = -0.40 to -0.30
Entries 416
Ey = 1.20 to 1.40 GeV CosTheta = -0.30 to -0.20
Entries 708
Ey = 1.20 to 1.40 GeV CosTheta = -0.20 to -0.10
Entries 1023
Ey = 1.20 to 1.40 GeV CosTheta = -0.10 to 0.00
Entries 1465
Ey = 1.20 to 1.40 GeV CosTheta = 0.00 to 0.10
Entries 2074
Ey = 1.20 to 1.40 GeV CosTheta = 0.10 to 0.20
Entries 2668
Ey = 1.20 to 1.40 GeV CosTheta = 0.20 to 0.30
Entries 3290
Ey = 1.20 to 1.40 GeV CosTheta = 0.30 to 0.40
Entries 3936
Ey = 1.20 to 1.40 GeV CosTheta = 0.40 to 0.50
Entries 4579
Ey = 1.20 to 1.40 GeV CosTheta = 0.50 to 0.60
Entries 5052
Ey = 1.20 to 1.40 GeV CosTheta = 0.60 to 0.70
Entries 5172
Ey = 1.20 to 1.40 GeV CosTheta = 0.70 to 0.80
Entries 4437
Ey = 1.20 to 1.40 GeV CosTheta = 0.80 to 0.90
Entries 2665
Ey = 1.20 to 1.40 GeV CosTheta = 0.90 to 1.00
Entries 540
Events
MM(K+, Λ) (GeV)

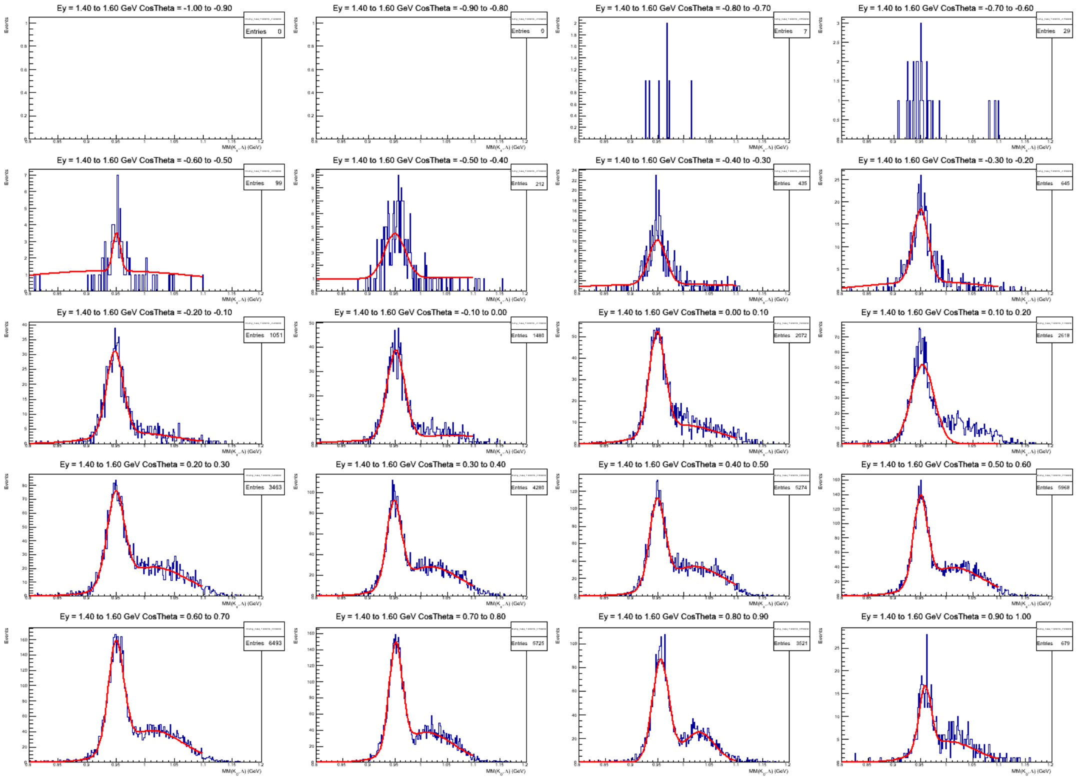
Ey = 1.40 to 1.60 GeV CosTheta = -1.00 to -0.90
Entries 0
Ey = 1.40 to 1.60 GeV CosTheta = -0.90 to -0.80
Entries 0
Ey = 1.40 to 1.60 GeV CosTheta = -0.80 to -0.70
Entries 7
Ey = 1.40 to 1.60 GeV CosTheta = -0.70 to -0.60
Entries 29
Ey = 1.40 to 1.60 GeV CosTheta = -0.60 to -0.50
Entries 99
Ey = 1.40 to 1.60 GeV CosTheta = -0.50 to -0.40
Entries 212
Ey = 1.40 to 1.60 GeV CosTheta = -0.40 to -0.30
Entries 435
Ey = 1.40 to 1.60 GeV CosTheta = -0.30 to -0.20
Entries 645
Ey = 1.40 to 1.60 GeV CosTheta = -0.20 to -0.10
Entries 1051
Ey = 1.40 to 1.60 GeV CosTheta = -0.10 to 0.00
Entries 1480
Ey = 1.40 to 1.60 GeV CosTheta = 0.00 to 0.10
Entries 2072
Ey = 1.40 to 1.60 GeV CosTheta = 0.10 to 0.20
Entries 2618
Ey = 1.40 to 1.60 GeV CosTheta = 0.20 to 0.30
Entries 3463
Ey = 1.40 to 1.60 GeV CosTheta = 0.30 to 0.40
Entries 4280
Ey = 1.40 to 1.60 GeV CosTheta = 0.40 to 0.50
Entries 5274
Ey = 1.40 to 1.60 GeV CosTheta = 0.50 to 0.60
Entries 5968
Ey = 1.40 to 1.60 GeV CosTheta = 0.60 to 0.70
Entries 6493
Ey = 1.40 to 1.60 GeV CosTheta = 0.70 to 0.80
Entries 5725
Ey = 1.40 to 1.60 GeV CosTheta = 0.80 to 0.90
Entries 3521
Ey = 1.40 to 1.60 GeV CosTheta = 0.90 to 1.00
Entries 679
Events
MM(K+, Λ) (GeV)

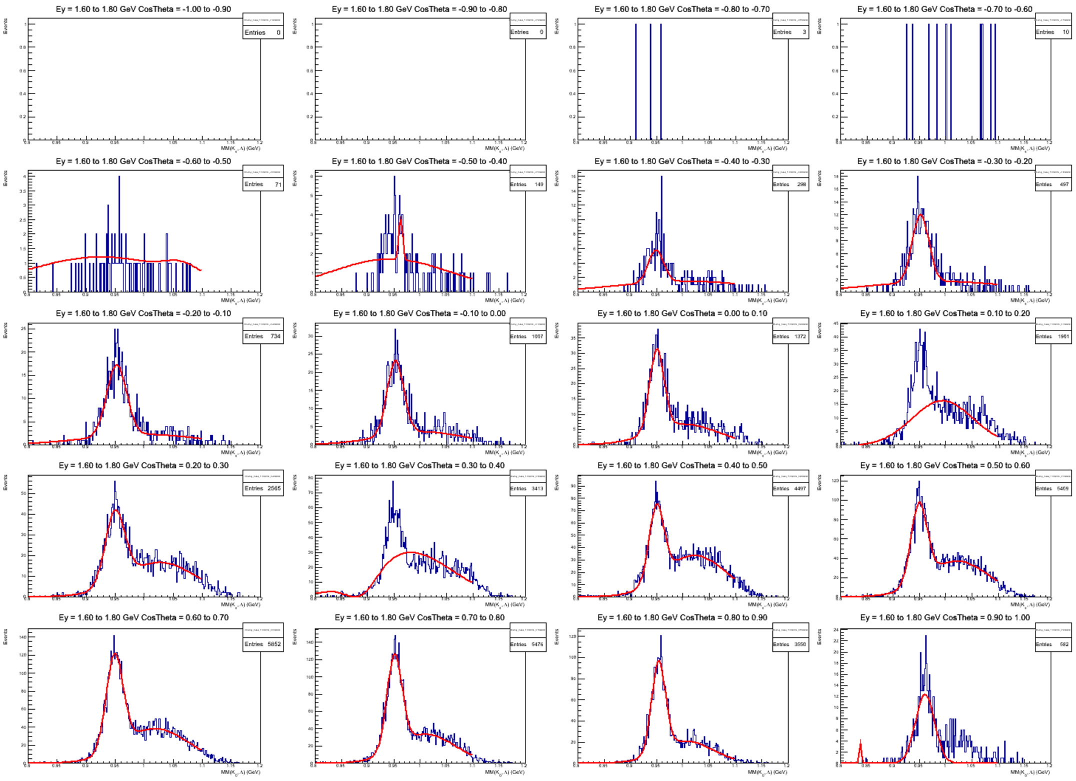
Ey = 1.60 to 1.80 GeV CosTheta = -1.00 to -0.90
Entries 0
Ey = 1.60 to 1.80 GeV CosTheta = -0.90 to -0.80
Entries 0
Ey = 1.60 to 1.80 GeV CosTheta = -0.80 to -0.70
Entries 3
Ey = 1.60 to 1.80 GeV CosTheta = -0.70 to -0.60
Entries 10
Ey = 1.60 to 1.80 GeV CosTheta = -0.60 to -0.50
Entries 71
Ey = 1.60 to 1.80 GeV CosTheta = -0.50 to -0.40
Entries 149
Ey = 1.60 to 1.80 GeV CosTheta = -0.40 to -0.30
Entries 298
Ey = 1.60 to 1.80 GeV CosTheta = -0.30 to -0.20
Entries 497
Ey = 1.60 to 1.80 GeV CosTheta = -0.20 to -0.10
Entries 734
Ey = 1.60 to 1.80 GeV CosTheta = -0.10 to 0.00
Entries 1057
Ey = 1.60 to 1.80 GeV CosTheta = 0.00 to 0.10
Entries 1372
Ey = 1.60 to 1.80 GeV CosTheta = 0.10 to 0.20
Entries 1961
Ey = 1.60 to 1.80 GeV CosTheta = 0.20 to 0.30
Entries 2565
Ey = 1.60 to 1.80 GeV CosTheta = 0.30 to 0.40
Entries 3413
Ey = 1.60 to 1.80 GeV CosTheta = 0.40 to 0.50
Entries 4497
Ey = 1.60 to 1.80 GeV CosTheta = 0.50 to 0.60
Entries 5469
Ey = 1.60 to 1.80 GeV CosTheta = 0.60 to 0.70
Entries 5652
Ey = 1.60 to 1.80 GeV CosTheta = 0.70 to 0.80
Entries 5476
Ey = 1.60 to 1.80 GeV CosTheta = 0.80 to 0.90
Entries 3558
Ey = 1.60 to 1.80 GeV CosTheta = 0.90 to 1.00
Entries 582
Events
MM(K+, Λ) (GeV)

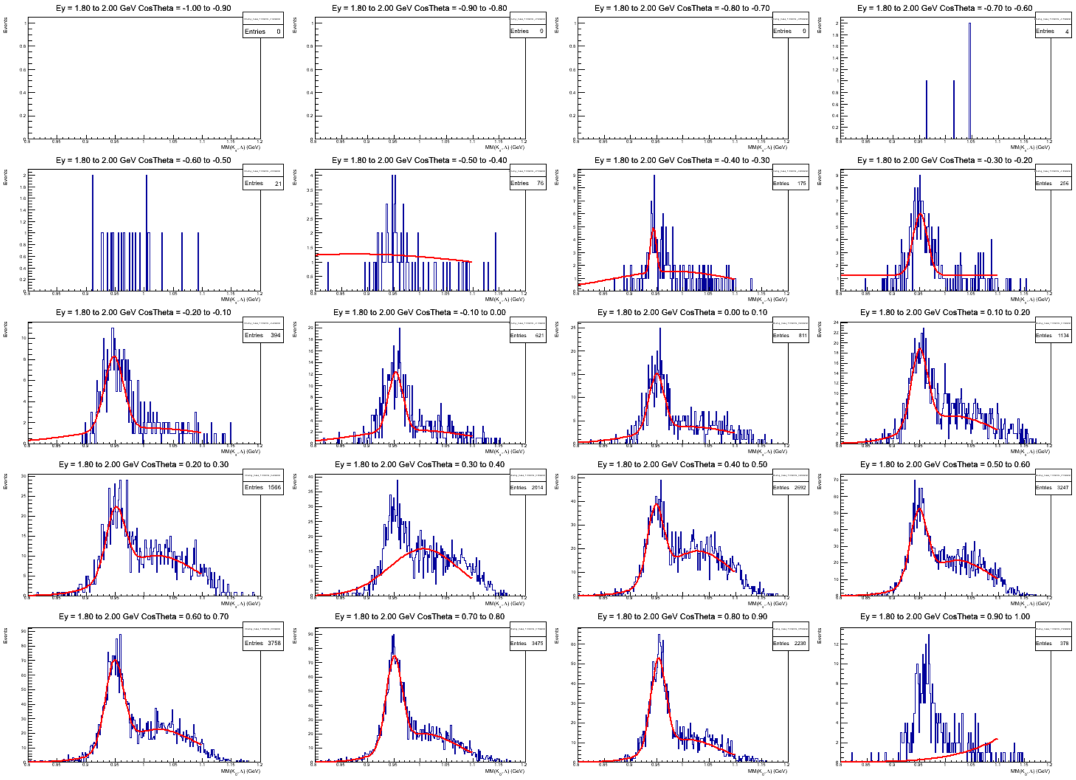
Ey = 1.80 to 2.00 GeV CosTheta = -1.00 to -0.90
Entries 0
Ey = 1.80 to 2.00 GeV CosTheta = -0.90 to -0.80
Entries 0
Ey = 1.80 to 2.00 GeV CosTheta = -0.80 to -0.70
Entries 0
Ey = 1.80 to 2.00 GeV CosTheta = -0.70 to -0.60
Entries 4
Ey = 1.80 to 2.00 GeV CosTheta = -0.60 to -0.50
Entries 21
Ey = 1.80 to 2.00 GeV CosTheta = -0.50 to -0.40
Entries 76
Ey = 1.80 to 2.00 GeV CosTheta = -0.40 to -0.30
Entries 175
Ey = 1.80 to 2.00 GeV CosTheta = -0.30 to -0.20
Entries 256
Ey = 1.80 to 2.00 GeV CosTheta = -0.20 to -0.10
Entries 394
Ey = 1.80 to 2.00 GeV CosTheta = -0.10 to 0.00
Entries 621
Ey = 1.80 to 2.00 GeV CosTheta = 0.00 to 0.10
Entries 811
Ey = 1.80 to 2.00 GeV CosTheta = 0.10 to 0.20
Entries 1134
Ey = 1.80 to 2.00 GeV CosTheta = 0.20 to 0.30
Entries 1566
Ey = 1.80 to 2.00 GeV CosTheta = 0.30 to 0.40
Entries 2014
Ey = 1.80 to 2.00 GeV CosTheta = 0.40 to 0.50
Entries 2692
Ey = 1.80 to 2.00 GeV CosTheta = 0.50 to 0.60
Entries 3247
Ey = 1.80 to 2.00 GeV CosTheta = 0.60 to 0.70
Entries 3758
Ey = 1.80 to 2.00 GeV CosTheta = 0.70 to 0.80
Entries 3475
Ey = 1.80 to 2.00 GeV CosTheta = 0.80 to 0.90
Entries 2238
Ey = 1.80 to 2.00 GeV CosTheta = 0.90 to 1.00
Entries 378
Events
MM(K+, Λ) (GeV)

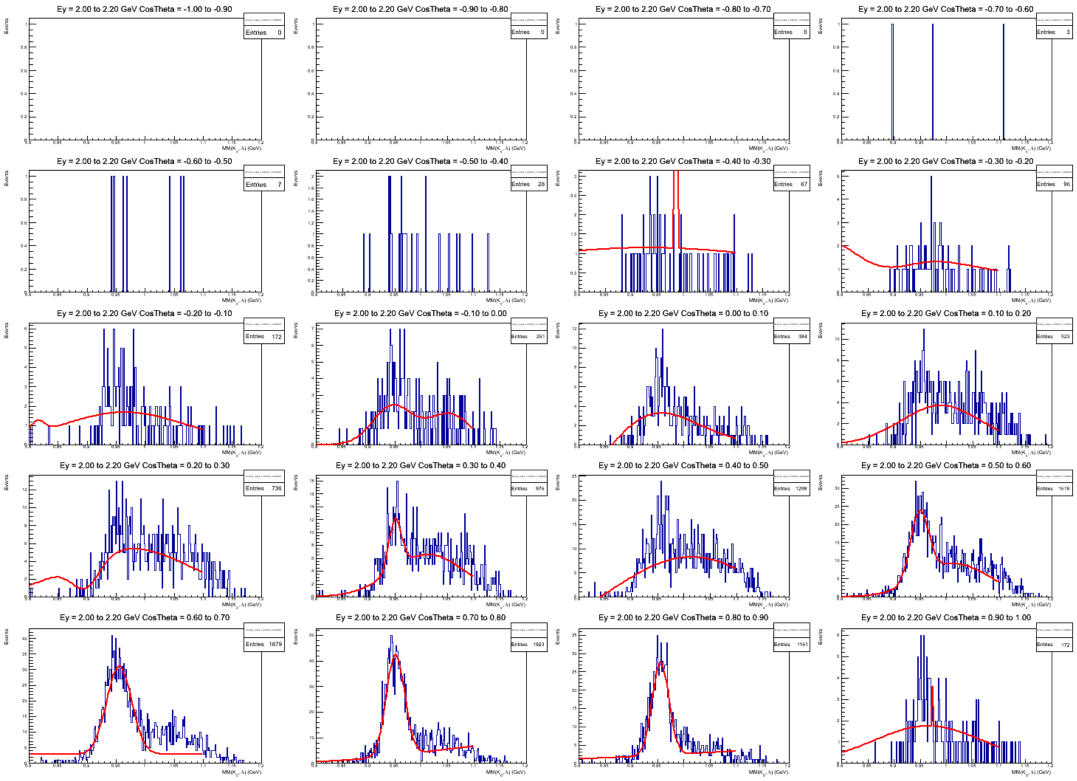
Ey = 2.00 to 2.20 GeV CosTheta = -1.00 to -0.90
Entries 0
Ey = 2.00 to 2.20 GeV CosTheta = -0.90 to -0.80
Entries 0
Ey = 2.00 to 2.20 GeV CosTheta = -0.80 to -0.70
Entries 0
Ey = 2.00 to 2.20 GeV CosTheta = -0.70 to -0.60
Entries 3
Ey = 2.00 to 2.20 GeV CosTheta = -0.60 to -0.50
Entries 7
Ey = 2.00 to 2.20 GeV CosTheta = -0.50 to -0.40
Entries 28
Ey = 2.00 to 2.20 GeV CosTheta = -0.40 to -0.30
Entries 67
Ey = 2.00 to 2.20 GeV CosTheta = -0.30 to -0.20
Entries 96
Ey = 2.00 to 2.20 GeV CosTheta = -0.20 to -0.10
Entries 172
Ey = 2.00 to 2.20 GeV CosTheta = -0.10 to 0.00
Entries 261
Ey = 2.00 to 2.20 GeV CosTheta = 0.00 to 0.10
Entries 384
Ey = 2.00 to 2.20 GeV CosTheta = 0.10 to 0.20
Entries 523
Ey = 2.00 to 2.20 GeV CosTheta = 0.20 to 0.30
Entries 736
Ey = 2.00 to 2.20 GeV CosTheta = 0.30 to 0.40
Entries 976
Ey = 2.00 to 2.20 GeV CosTheta = 0.40 to 0.50
Entries 1298
Ey = 2.00 to 2.20 GeV CosTheta = 0.50 to 0.60
Entries 1618
Ey = 2.00 to 2.20 GeV CosTheta = 0.60 to 0.70
Entries 1879
Ey = 2.00 to 2.20 GeV CosTheta = 0.70 to 0.80
Entries 1923
Ey = 2.00 to 2.20 GeV CosTheta = 0.80 to 0.90
Entries 1161
Ey = 2.00 to 2.20 GeV CosTheta = 0.90 to 1.00
Entries 172
Events
MM(K+, Λ) (GeV)

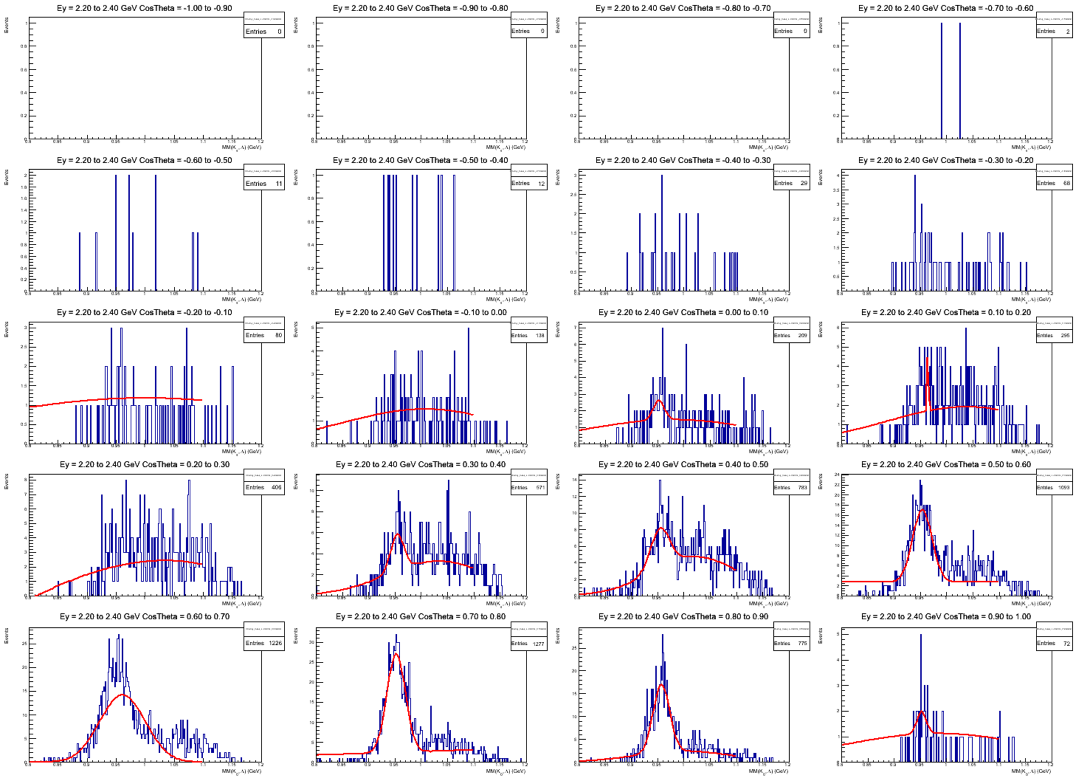
Ey = 2.20 to 2.40 GeV CosTheta = -1.00 to -0.90
Entries 0
Ey = 2.20 to 2.40 GeV CosTheta = -0.90 to -0.80
Entries 0
Ey = 2.20 to 2.40 GeV CosTheta = -0.80 to -0.70
Entries 0
Ey = 2.20 to 2.40 GeV CosTheta = -0.70 to -0.60
Entries 2
Ey = 2.20 to 2.40 GeV CosTheta = -0.60 to -0.50
Entries 11
Ey = 2.20 to 2.40 GeV CosTheta = -0.50 to -0.40
Entries 12
Ey = 2.20 to 2.40 GeV CosTheta = -0.40 to -0.30
Entries 29
Ey = 2.20 to 2.40 GeV CosTheta = -0.30 to -0.20
Entries 68
Ey = 2.20 to 2.40 GeV CosTheta = -0.20 to -0.10
Entries 80
Ey = 2.20 to 2.40 GeV CosTheta = -0.10 to 0.00
Entries 138
Ey = 2.20 to 2.40 GeV CosTheta = 0.00 to 0.10
Entries 209
Ey = 2.20 to 2.40 GeV CosTheta = 0.10 to 0.20
Entries 295
Ey = 2.20 to 2.40 GeV CosTheta = 0.20 to 0.30
Entries 406
Ey = 2.20 to 2.40 GeV CosTheta = 0.30 to 0.40
Entries 571
Ey = 2.20 to 2.40 GeV CosTheta = 0.40 to 0.50
Entries 783
Ey = 2.20 to 2.40 GeV CosTheta = 0.50 to 0.60
Entries 1093
Ey = 2.20 to 2.40 GeV CosTheta = 0.60 to 0.70
Entries 1226
Ey = 2.20 to 2.40 GeV CosTheta = 0.70 to 0.80
Entries 1277
Ey = 2.20 to 2.40 GeV CosTheta = 0.80 to 0.90
Entries 775
Ey = 2.20 to 2.40 GeV CosTheta = 0.90 to 1.00
Entries 72
Events
MM(K+, Λ) (GeV)

Ey = 2.40 to 2.60 GeV CosTheta = -1.00 to -0.90

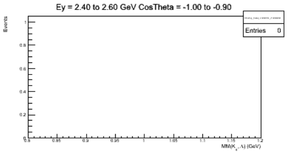

Ey = 2.40 to 2.60 GeV CosTheta = -0.90 to -0.80

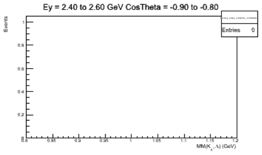

Ey = 2.40 to 2.60 GeV CosTheta = -0.80 to -0.70

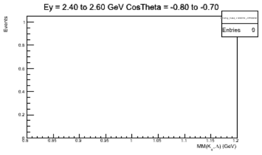

Ey = 2.40 to 2.60 GeV CosTheta = -0.70 to -0.60

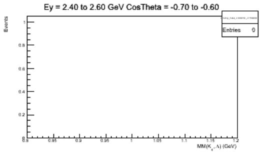

Ey = 2.40 to 2.60 GeV CosTheta = -0.60 to -0.50

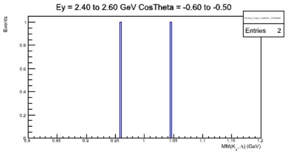

Ey = 2.40 to 2.60 GeV CosTheta = -0.50 to -0.40

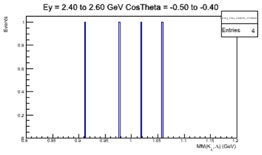

Ey = 2.40 to 2.60 GeV CosTheta = -0.40 to -0.30

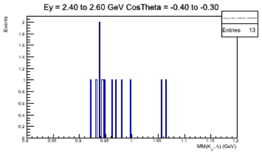

Ey = 2.40 to 2.60 GeV CosTheta = -0.30 to -0.20

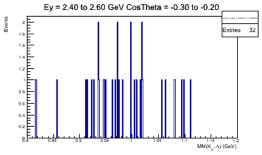

Ey = 2.40 to 2.60 GeV CosTheta = -0.20 to -0.10

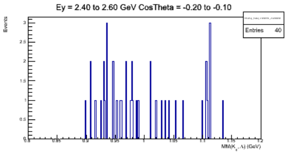

Ey = 2.40 to 2.60 GeV CosTheta = -0.10 to 0.00

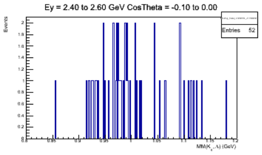

Ey = 2.40 to 2.60 GeV CosTheta = 0.00 to 0.10

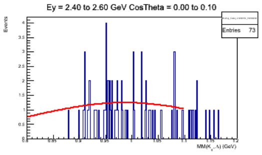

Ey = 2.40 to 2.60 GeV CosTheta = 0.10 to 0.20

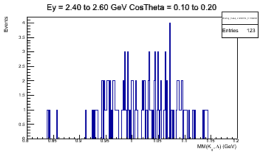

Ey = 2.40 to 2.60 GeV CosTheta = 0.20 to 0.30

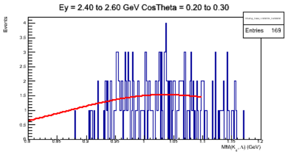

Ey = 2.40 to 2.60 GeV CosTheta = 0.30 to 0.40

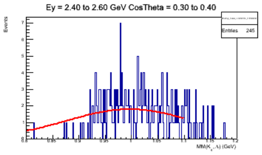

Ey = 2.40 to 2.60 GeV CosTheta = 0.40 to 0.50

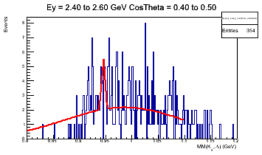

Ey = 2.40 to 2.60 GeV CosTheta = 0.50 to 0.60

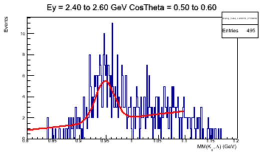

Ey = 2.40 to 2.60 GeV CosTheta = 0.60 to 0.70

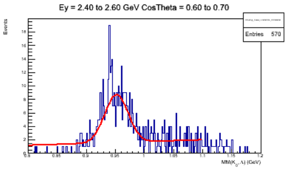

Ey = 2.40 to 2.60 GeV CosTheta = 0.70 to 0.80

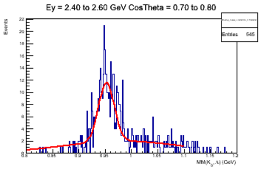

Ey = 2.40 to 2.60 GeV CosTheta = 0.80 to 0.90

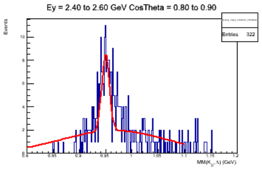

Ey = 2.40 to 2.60 GeV CosTheta = 0.90 to 1.00

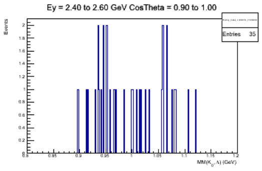

B.3.2 Fits for the Simulated Data for the $K_S\Lambda$ Channel

The plots in the following plots show the fits to the low. Some energy and cosine theta bins did not fit properly while the routines were running. In such cases, they were fit independently to get a reliable yield. Bins with low counts, were counted instead of attempting to fit their peak. The $K_S\Lambda$ channel had fewer problems with fitting than the empirical data. The dataset still required quite a bit of refitting. Very few events were observed in the 2.4 GeV energy bin. There plots have been left out.

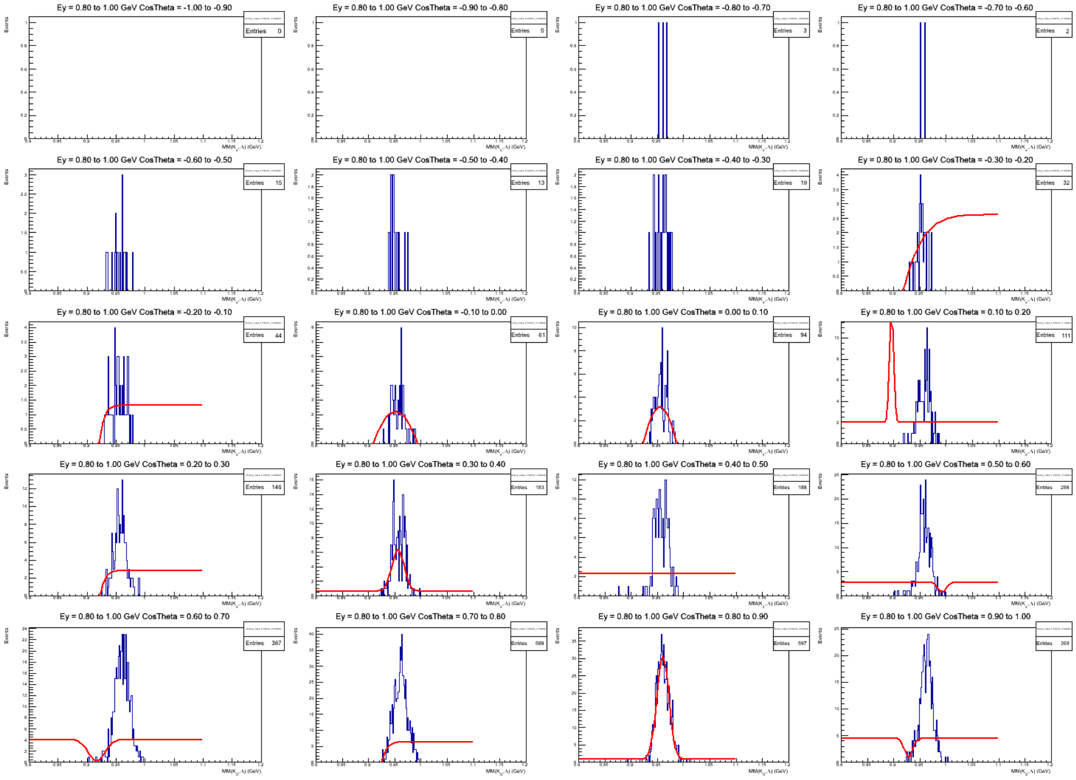

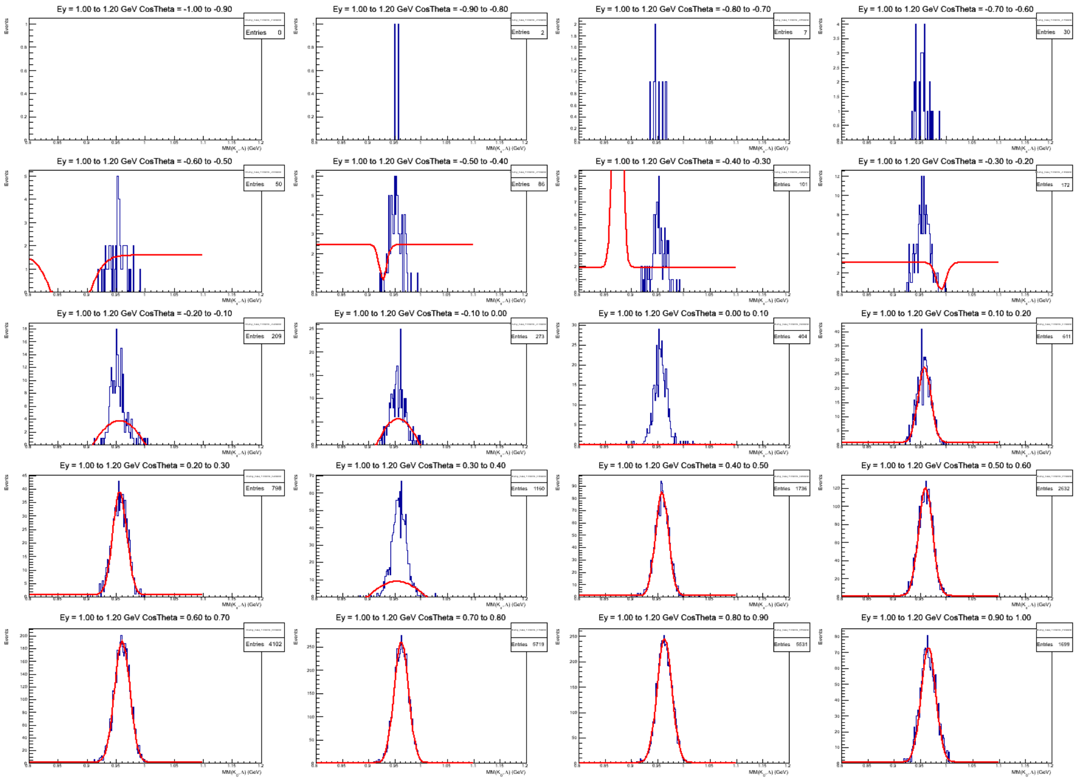
Ey = 1.00 to 1.20 GeV CosTheta = -1.00 to -0.90
Entries 0
Ey = 1.00 to 1.20 GeV CosTheta = -0.90 to -0.80
Entries 2
Ey = 1.00 to 1.20 GeV CosTheta = -0.80 to -0.70
Entries 7
Ey = 1.00 to 1.20 GeV CosTheta = -0.70 to -0.60
Entries 30
Ey = 1.00 to 1.20 GeV CosTheta = -0.60 to -0.50
Entries 50
Ey = 1.00 to 1.20 GeV CosTheta = -0.50 to -0.40
Entries 86
Ey = 1.00 to 1.20 GeV CosTheta = -0.40 to -0.30
Entries 101
Ey = 1.00 to 1.20 GeV CosTheta = -0.30 to -0.20
Entries 172
Ey = 1.00 to 1.20 GeV CosTheta = -0.20 to -0.10
Entries 209
Ey = 1.00 to 1.20 GeV CosTheta = -0.10 to 0.00
Entries 273
Ey = 1.00 to 1.20 GeV CosTheta = 0.00 to 0.10
Entries 404
Ey = 1.00 to 1.20 GeV CosTheta = 0.10 to 0.20
Entries 611
Ey = 1.00 to 1.20 GeV CosTheta = 0.20 to 0.30
Entries 798
Ey = 1.00 to 1.20 GeV CosTheta = 0.30 to 0.40
Entries 1160
Ey = 1.00 to 1.20 GeV CosTheta = 0.40 to 0.50
Entries 1736
Ey = 1.00 to 1.20 GeV CosTheta = 0.50 to 0.60
Entries 2532
Ey = 1.00 to 1.20 GeV CosTheta = 0.60 to 0.70
Entries 4102
Ey = 1.00 to 1.20 GeV CosTheta = 0.70 to 0.80
Entries 5719
Ey = 1.00 to 1.20 GeV CosTheta = 0.80 to 0.90
Entries 5531
Ey = 1.00 to 1.20 GeV CosTheta = 0.90 to 1.00
Entries 1699
Events
MM(K+, Λ) (GeV)

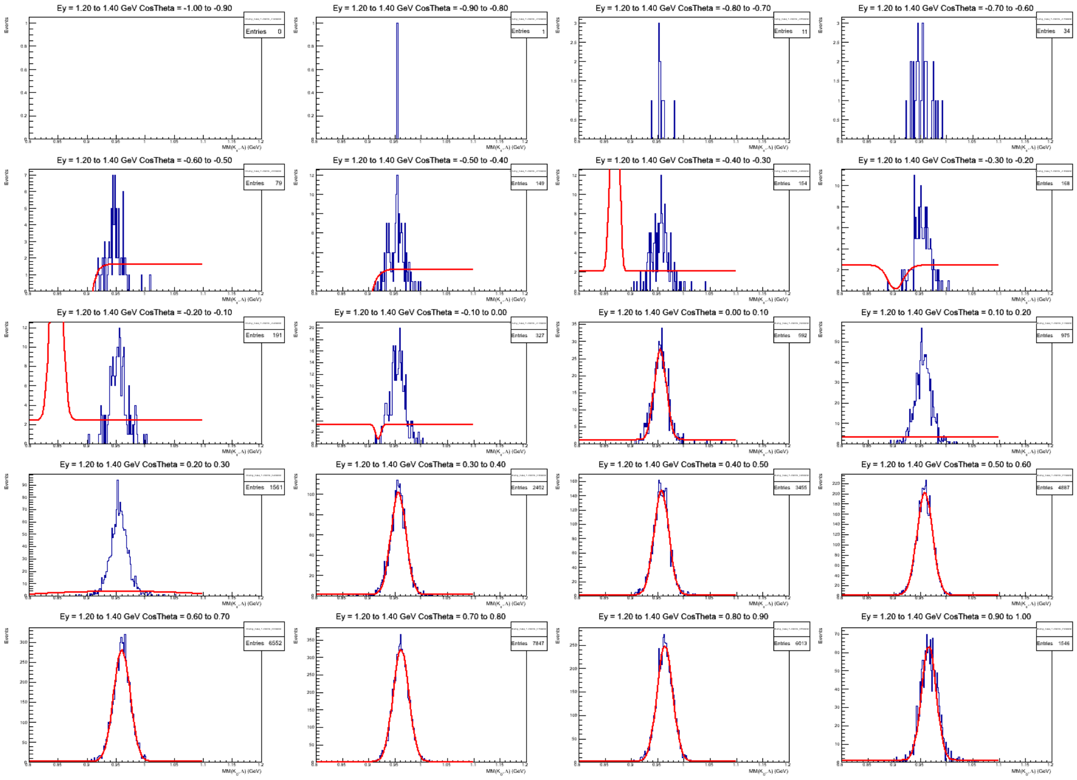
Ey = 1.20 to 1.40 GeV CosTheta = -1.00 to -0.90
Entries 0
Ey = 1.20 to 1.40 GeV CosTheta = -0.90 to -0.80
Entries 1
Ey = 1.20 to 1.40 GeV CosTheta = -0.80 to -0.70
Entries 11
Ey = 1.20 to 1.40 GeV CosTheta = -0.70 to -0.60
Entries 34
Ey = 1.20 to 1.40 GeV CosTheta = -0.60 to -0.50
Entries 79
Ey = 1.20 to 1.40 GeV CosTheta = -0.50 to -0.40
Entries 149
Ey = 1.20 to 1.40 GeV CosTheta = -0.40 to -0.30
Entries 154
Ey = 1.20 to 1.40 GeV CosTheta = -0.30 to -0.20
Entries 169
Ey = 1.20 to 1.40 GeV CosTheta = -0.20 to -0.10
Entries 191
Ey = 1.20 to 1.40 GeV CosTheta = -0.10 to 0.00
Entries 327
Ey = 1.20 to 1.40 GeV CosTheta = 0.00 to 0.10
Entries 592
Ey = 1.20 to 1.40 GeV CosTheta = 0.10 to 0.20
Entries 975
Ey = 1.20 to 1.40 GeV CosTheta = 0.20 to 0.30
Entries 1561
Ey = 1.20 to 1.40 GeV CosTheta = 0.30 to 0.40
Entries 2462
Ey = 1.20 to 1.40 GeV CosTheta = 0.40 to 0.50
Entries 3455
Ey = 1.20 to 1.40 GeV CosTheta = 0.50 to 0.60
Entries 4897
Ey = 1.20 to 1.40 GeV CosTheta = 0.60 to 0.70
Entries 6552
Ey = 1.20 to 1.40 GeV CosTheta = 0.70 to 0.80
Entries 7847
Ey = 1.20 to 1.40 GeV CosTheta = 0.80 to 0.90
Entries 6013
Ey = 1.20 to 1.40 GeV CosTheta = 0.90 to 1.00
Entries 1546
Events
MM(K+, Λ) (GeV)

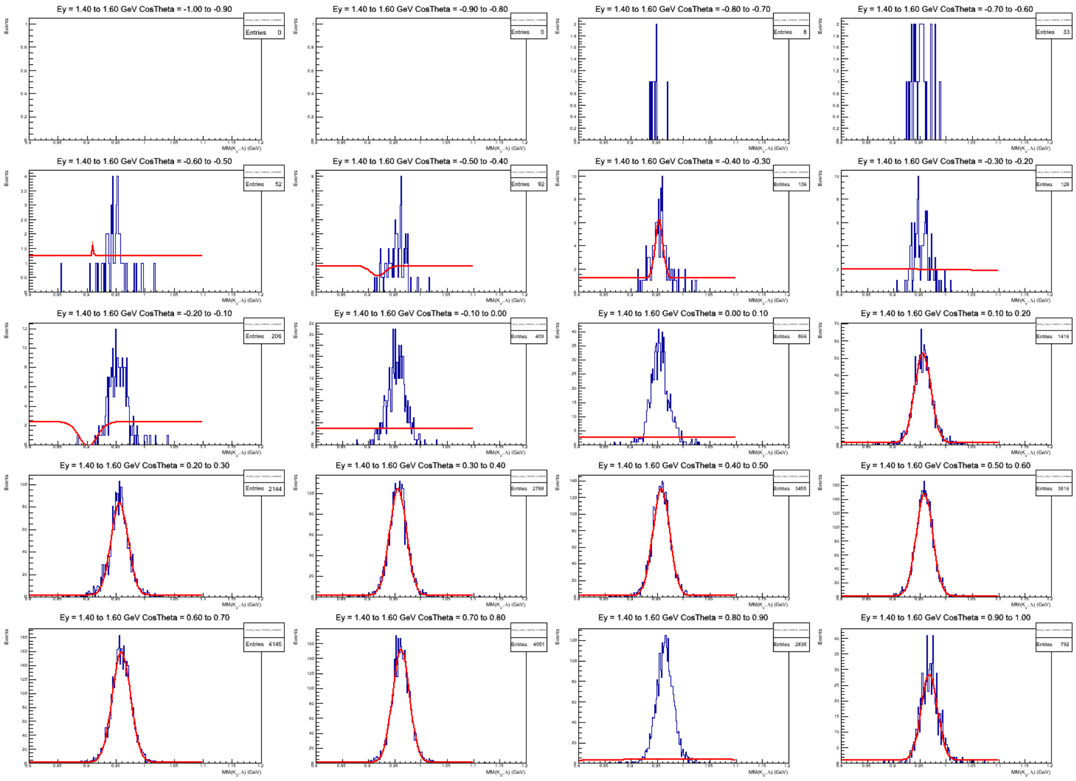
Ey = 1.40 to 1.60 GeV CosTheta = -1.00 to -0.90
Entries 0
Ey = 1.40 to 1.60 GeV CosTheta = -0.90 to -0.80
Entries 0
Ey = 1.40 to 1.60 GeV CosTheta = -0.80 to -0.70
Entries 8
Ey = 1.40 to 1.60 GeV CosTheta = -0.70 to -0.60
Entries 33
Ey = 1.40 to 1.60 GeV CosTheta = -0.60 to -0.50
Entries 52
Ey = 1.40 to 1.60 GeV CosTheta = -0.50 to -0.40
Entries 92
Ey = 1.40 to 1.60 GeV CosTheta = -0.40 to -0.30
Entries 136
Ey = 1.40 to 1.60 GeV CosTheta = -0.30 to -0.20
Entries 128
Ey = 1.40 to 1.60 GeV CosTheta = -0.20 to -0.10
Entries 206
Ey = 1.40 to 1.60 GeV CosTheta = -0.10 to 0.00
Entries 409
Ey = 1.40 to 1.60 GeV CosTheta = 0.00 to 0.10
Entries 866
Ey = 1.40 to 1.60 GeV CosTheta = 0.10 to 0.20
Entries 1416
Ey = 1.40 to 1.60 GeV CosTheta = 0.20 to 0.30
Entries 2144
Ey = 1.40 to 1.60 GeV CosTheta = 0.30 to 0.40
Entries 2788
Ey = 1.40 to 1.60 GeV CosTheta = 0.40 to 0.50
Entries 3455
Ey = 1.40 to 1.60 GeV CosTheta = 0.50 to 0.60
Entries 3816
Ey = 1.40 to 1.60 GeV CosTheta = 0.60 to 0.70
Entries 4145
Ey = 1.40 to 1.60 GeV CosTheta = 0.70 to 0.80
Entries 4001
Ey = 1.40 to 1.60 GeV CosTheta = 0.80 to 0.90
Entries 2830
Ey = 1.40 to 1.60 GeV CosTheta = 0.90 to 1.00
Entries 792
Events
MM(K_0, Λ) (GeV)

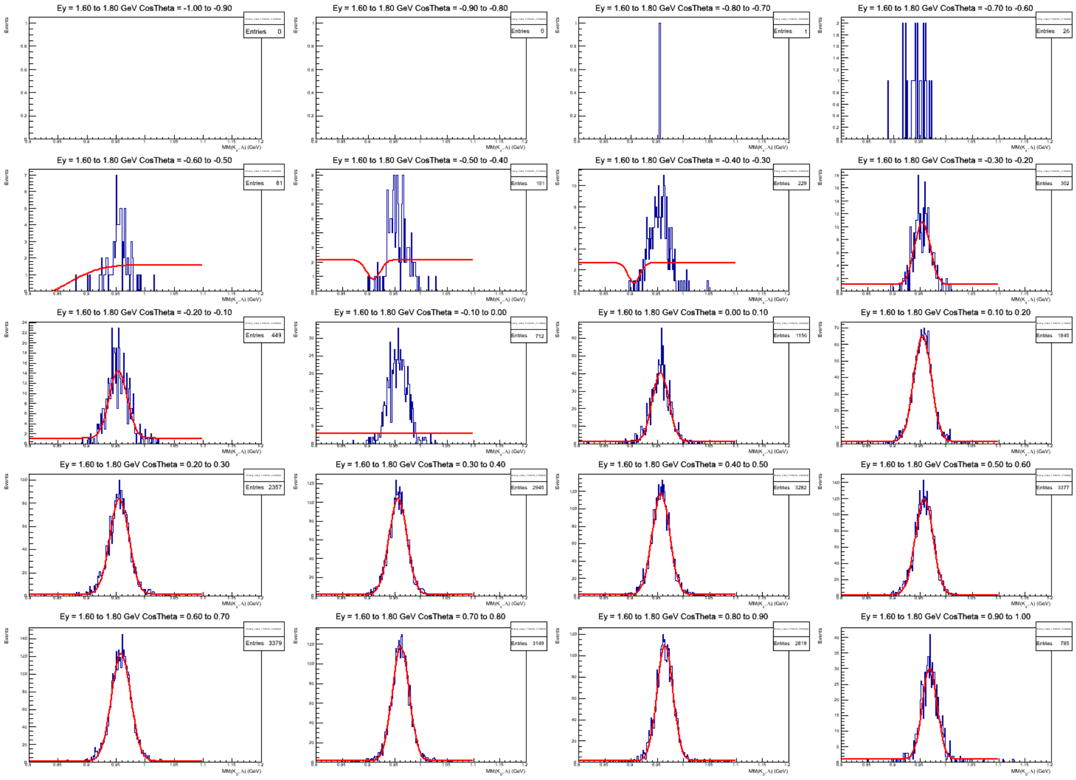
Ey = 1.60 to 1.80 GeV CosTheta = -1.00 to -0.90
Entries 0
Ey = 1.60 to 1.80 GeV CosTheta = -0.90 to -0.80
Entries 0
Ey = 1.60 to 1.80 GeV CosTheta = -0.80 to -0.70
Entries 1
Ey = 1.60 to 1.80 GeV CosTheta = -0.70 to -0.60
Entries 26
Ey = 1.60 to 1.80 GeV CosTheta = -0.60 to -0.50
Entries 81
Ey = 1.60 to 1.80 GeV CosTheta = -0.50 to -0.40
Entries 151
Ey = 1.60 to 1.80 GeV CosTheta = -0.40 to -0.30
Entries 229
Ey = 1.60 to 1.80 GeV CosTheta = -0.30 to -0.20
Entries 302
Ey = 1.60 to 1.80 GeV CosTheta = -0.20 to -0.10
Entries 449
Ey = 1.60 to 1.80 GeV CosTheta = -0.10 to 0.00
Entries 712
Ey = 1.60 to 1.80 GeV CosTheta = 0.00 to 0.10
Entries 1156
Ey = 1.60 to 1.80 GeV CosTheta = 0.10 to 0.20
Entries 1840
Ey = 1.60 to 1.80 GeV CosTheta = 0.20 to 0.30
Entries 2357
Ey = 1.60 to 1.80 GeV CosTheta = 0.30 to 0.40
Entries 2940
Ey = 1.60 to 1.80 GeV CosTheta = 0.40 to 0.50
Entries 3282
Ey = 1.60 to 1.80 GeV CosTheta = 0.50 to 0.60
Entries 3377
Ey = 1.60 to 1.80 GeV CosTheta = 0.60 to 0.70
Entries 3379
Ey = 1.60 to 1.80 GeV CosTheta = 0.70 to 0.80
Entries 3149
Ey = 1.60 to 1.80 GeV CosTheta = 0.80 to 0.90
Entries 2819
Ey = 1.60 to 1.80 GeV CosTheta = 0.90 to 1.00
Entries 785
Events
MM(K_0, Λ) (GeV)

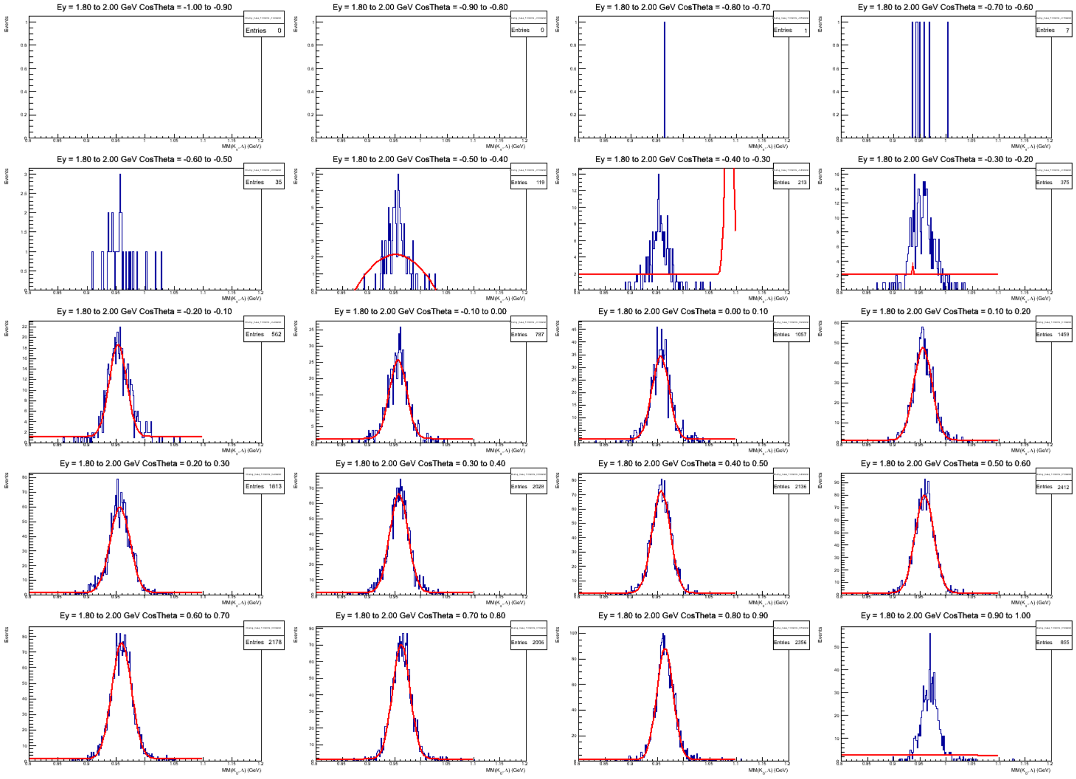
Ey = 1.80 to 2.00 GeV CosTheta = -1.00 to -0.90
Entries 0
Ey = 1.80 to 2.00 GeV CosTheta = -0.90 to -0.80
Entries 0
Ey = 1.80 to 2.00 GeV CosTheta = -0.80 to -0.70
Entries 1
Ey = 1.80 to 2.00 GeV CosTheta = -0.70 to -0.60
Entries 7
Ey = 1.80 to 2.00 GeV CosTheta = -0.60 to -0.50
Entries 35
Ey = 1.80 to 2.00 GeV CosTheta = -0.50 to -0.40
Entries 119
Ey = 1.80 to 2.00 GeV CosTheta = -0.40 to -0.30
Entries 213
Ey = 1.80 to 2.00 GeV CosTheta = -0.30 to -0.20
Entries 375
Ey = 1.80 to 2.00 GeV CosTheta = -0.20 to -0.10
Entries 562
Ey = 1.80 to 2.00 GeV CosTheta = -0.10 to 0.00
Entries 787
Ey = 1.80 to 2.00 GeV CosTheta = 0.00 to 0.10
Entries 1057
Ey = 1.80 to 2.00 GeV CosTheta = 0.10 to 0.20
Entries 1459
Ey = 1.80 to 2.00 GeV CosTheta = 0.20 to 0.30
Entries 1813
Ey = 1.80 to 2.00 GeV CosTheta = 0.30 to 0.40
Entries 2028
Ey = 1.80 to 2.00 GeV CosTheta = 0.40 to 0.50
Entries 2136
Ey = 1.80 to 2.00 GeV CosTheta = 0.50 to 0.60
Entries 2412
Ey = 1.80 to 2.00 GeV CosTheta = 0.60 to 0.70
Entries 2178
Ey = 1.80 to 2.00 GeV CosTheta = 0.70 to 0.80
Entries 2006
Ey = 1.80 to 2.00 GeV CosTheta = 0.80 to 0.90
Entries 2356
Ey = 1.80 to 2.00 GeV CosTheta = 0.90 to 1.00
Entries 855
Events
MM(K_s,Λ) (GeV)

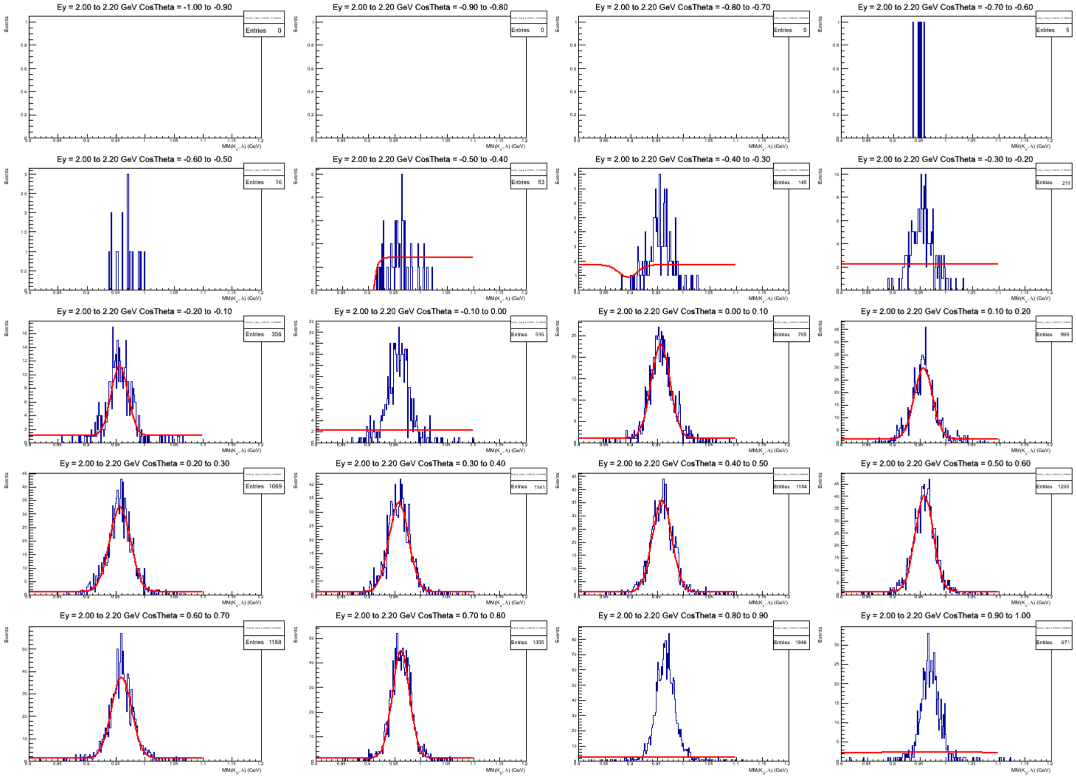
Ey = 2.00 to 2.20 GeV CosTheta = -1.00 to -0.90
Entries 0
Ey = 2.00 to 2.20 GeV CosTheta = -0.90 to -0.80
Entries 0
Ey = 2.00 to 2.20 GeV CosTheta = -0.80 to -0.70
Entries 0
Ey = 2.00 to 2.20 GeV CosTheta = -0.70 to -0.60
Entries 5
Ey = 2.00 to 2.20 GeV CosTheta = -0.60 to -0.50
Entries 16
Ey = 2.00 to 2.20 GeV CosTheta = -0.50 to -0.40
Entries 53
Ey = 2.00 to 2.20 GeV CosTheta = -0.40 to -0.30
Entries 145
Ey = 2.00 to 2.20 GeV CosTheta = -0.30 to -0.20
Entries 211
Ey = 2.00 to 2.20 GeV CosTheta = -0.20 to -0.10
Entries 356
Ey = 2.00 to 2.20 GeV CosTheta = -0.10 to 0.00
Entries 516
Ey = 2.00 to 2.20 GeV CosTheta = 0.00 to 0.10
Entries 765
Ey = 2.00 to 2.20 GeV CosTheta = 0.10 to 0.20
Entries 993
Ey = 2.00 to 2.20 GeV CosTheta = 0.20 to 0.30
Entries 1069
Ey = 2.00 to 2.20 GeV CosTheta = 0.30 to 0.40
Entries 1141
Ey = 2.00 to 2.20 GeV CosTheta = 0.40 to 0.50
Entries 1184
Ey = 2.00 to 2.20 GeV CosTheta = 0.50 to 0.60
Entries 1260
Ey = 2.00 to 2.20 GeV CosTheta = 0.60 to 0.70
Entries 1188
Ey = 2.00 to 2.20 GeV CosTheta = 0.70 to 0.80
Entries 1305
Ey = 2.00 to 2.20 GeV CosTheta = 0.80 to 0.90
Entries 1946
Ey = 2.00 to 2.20 GeV CosTheta = 0.90 to 1.00
Entries 671
Events
MM(K_s,Λ) (GeV)

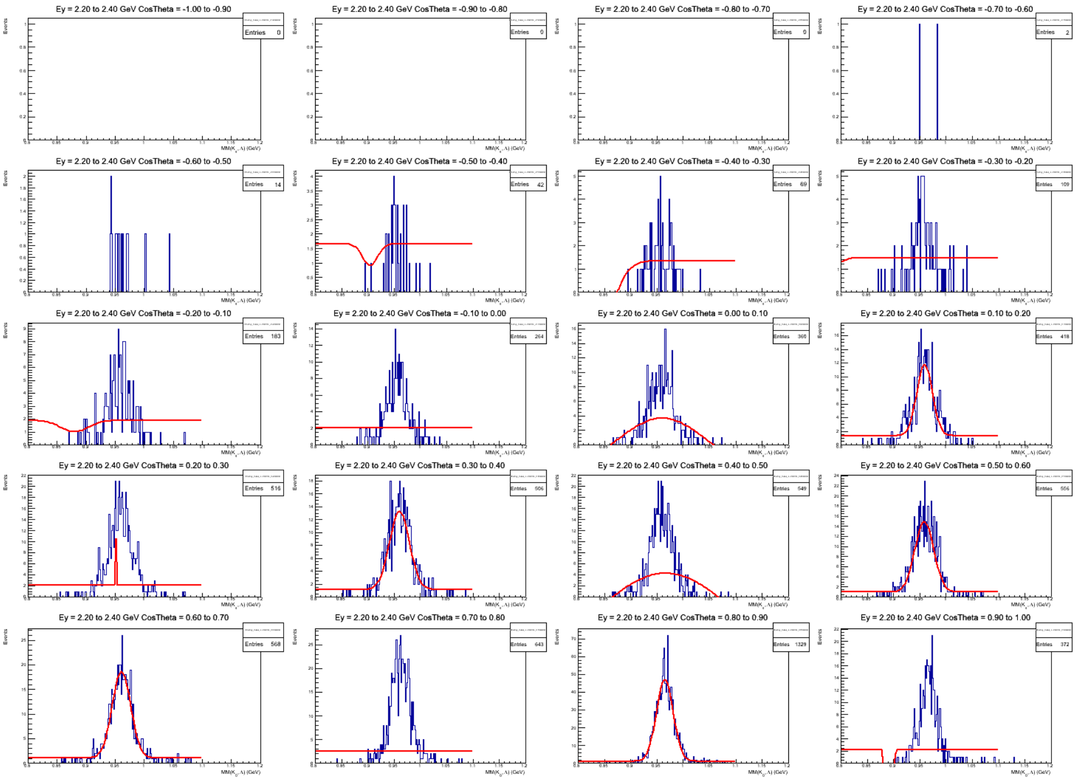
Ey = 2.20 to 2.40 GeV CosTheta = -1.00 to -0.90
Entries 0
Ey = 2.20 to 2.40 GeV CosTheta = -0.90 to -0.80
Entries 0
Ey = 2.20 to 2.40 GeV CosTheta = -0.80 to -0.70
Entries 0
Ey = 2.20 to 2.40 GeV CosTheta = -0.70 to -0.60
Entries 2
Ey = 2.20 to 2.40 GeV CosTheta = -0.60 to -0.50
Entries 14
Ey = 2.20 to 2.40 GeV CosTheta = -0.50 to -0.40
Entries 42
Ey = 2.20 to 2.40 GeV CosTheta = -0.40 to -0.30
Entries 69
Ey = 2.20 to 2.40 GeV CosTheta = -0.30 to -0.20
Entries 109
Ey = 2.20 to 2.40 GeV CosTheta = -0.20 to -0.10
Entries 183
Ey = 2.20 to 2.40 GeV CosTheta = -0.10 to 0.00
Entries 264
Ey = 2.20 to 2.40 GeV CosTheta = 0.00 to 0.10
Entries 360
Ey = 2.20 to 2.40 GeV CosTheta = 0.10 to 0.20
Entries 418
Ey = 2.20 to 2.40 GeV CosTheta = 0.20 to 0.30
Entries 516
Ey = 2.20 to 2.40 GeV CosTheta = 0.30 to 0.40
Entries 506
Ey = 2.20 to 2.40 GeV CosTheta = 0.40 to 0.50
Entries 549
Ey = 2.20 to 2.40 GeV CosTheta = 0.50 to 0.60
Entries 556
Ey = 2.20 to 2.40 GeV CosTheta = 0.60 to 0.70
Entries 568
Ey = 2.20 to 2.40 GeV CosTheta = 0.70 to 0.80
Entries 643
Ey = 2.20 to 2.40 GeV CosTheta = 0.80 to 0.90
Entries 1329
Ey = 2.20 to 2.40 GeV CosTheta = 0.90 to 1.00
Entries 372
Events
MM(K_s, Λ) (GeV)

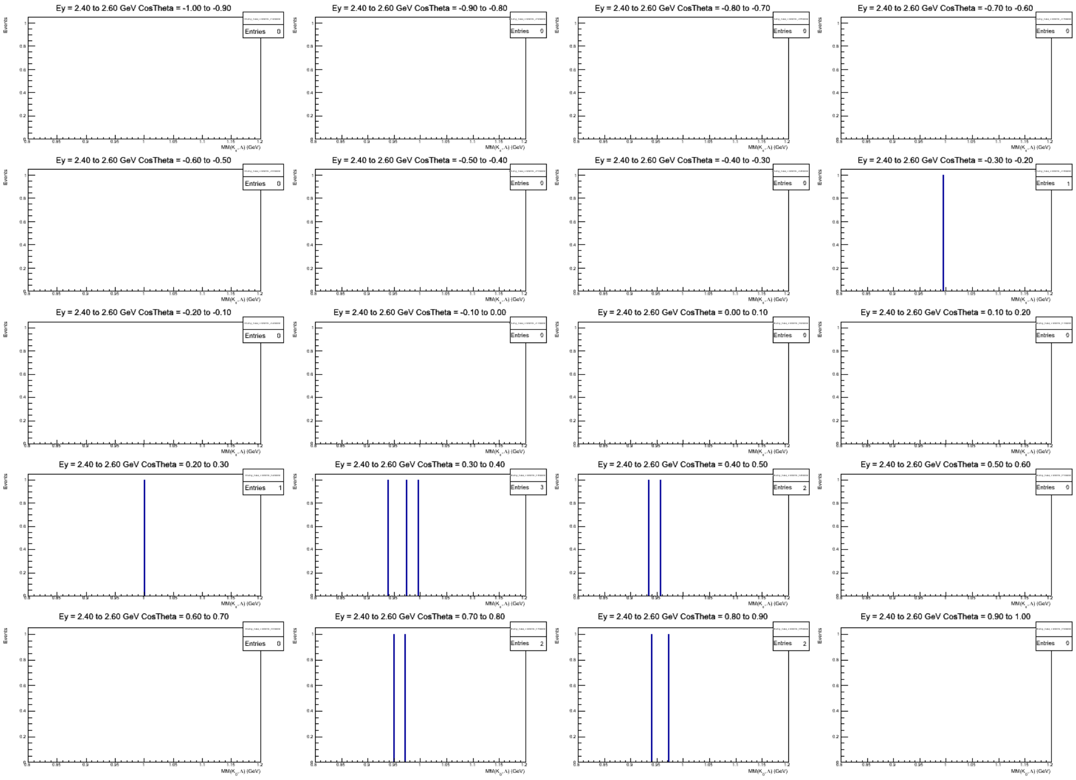
Ey = 2.40 to 2.60 GeV CosTheta = -1.00 to -0.90
Entries 0
Ey = 2.40 to 2.60 GeV CosTheta = -0.90 to -0.80
Entries 0
Ey = 2.40 to 2.60 GeV CosTheta = -0.80 to -0.70
Entries 0
Ey = 2.40 to 2.60 GeV CosTheta = -0.70 to -0.60
Entries 0
Ey = 2.40 to 2.60 GeV CosTheta = -0.60 to -0.50
Entries 0
Ey = 2.40 to 2.60 GeV CosTheta = -0.50 to -0.40
Entries 0
Ey = 2.40 to 2.60 GeV CosTheta = -0.40 to -0.30
Entries 0
Ey = 2.40 to 2.60 GeV CosTheta = -0.30 to -0.20
Entries 1
Ey = 2.40 to 2.60 GeV CosTheta = -0.20 to -0.10
Entries 0
Ey = 2.40 to 2.60 GeV CosTheta = -0.10 to 0.00
Entries 0
Ey = 2.40 to 2.60 GeV CosTheta = 0.00 to 0.10
Entries 0
Ey = 2.40 to 2.60 GeV CosTheta = 0.10 to 0.20
Entries 0
Ey = 2.40 to 2.60 GeV CosTheta = 0.20 to 0.30
Entries 1
Ey = 2.40 to 2.60 GeV CosTheta = 0.30 to 0.40
Entries 3
Ey = 2.40 to 2.60 GeV CosTheta = 0.40 to 0.50
Entries 2
Ey = 2.40 to 2.60 GeV CosTheta = 0.50 to 0.60
Entries 0
Ey = 2.40 to 2.60 GeV CosTheta = 0.60 to 0.70
Entries 0
Ey = 2.40 to 2.60 GeV CosTheta = 0.70 to 0.80
Entries 2
Ey = 2.40 to 2.60 GeV CosTheta = 0.80 to 0.90
Entries 2
Ey = 2.40 to 2.60 GeV CosTheta = 0.90 to 1.00
Entries 0
Events
MM(K_s, Λ) (GeV)

Appendix C

Analysis Code

The data analysis was performed with two different sets of code: a "skimming" code and "plotter" code. The skimmer code is a standalone binary. It was designed to read the data from the BOS files and sort them into data trees for event selection. Once the events were selected, they were then converted into hbook and root trees for the plotter routines. The plotter code were run as macros within a root interpreter. The plotter macros made some of the later data cuts and fit the peaks for phase space ratios and the final yields.

C.1 The Skimmer: Photonuclear Reaction Assembler

The pnr_assembler was designed to perform the initial sorting through events for a specified reaction. The resultant root trees must be further analyzed for overlapping resonances and competing channels. The code was adapted for potentially more general use by other grad students. It drops all hbook usage for root libraries and promotes more modern coding practice. The new code incorporates several methods developed by Paul Mattione[32]. All methods, objects and variables are pulled into classes to reduces potential memory leak issues. Root objects are the primary exception to this, since the pointer locations are not well preserved within another class.

Table C.1 Current input format

```
Usage: pnr_assembler [options] text.cfg [file1] file2 etc...
  Options:
    -a          analyze MC only
    -d          data directory
    -g          tagger correction file
    -h          print this message
    -i          interactive mode
    -m          Monte Carlo input
    -n#         write only # events
    -o<outfile> root file name
```

C.2 The Code Architecture

While retaining the sequential structure used by most analytic binaries, the new code format follows more current coding practices. Almost all the methods and structures have been pulled into classes. This encapsulation of data and logic significantly reduces the chances of lost (overwritten) data, and greatly improves the code's readability. This code uses Hungarian notation, which is commonly used in Java coding and occasionally in C++.

Figure one presents a flowchart of the current structure of the pnr_assembler code. The main method passes the input arguments to argumentParser.Parser() to sort the arguments and create a return object for the rest of the code to utilize. Next root object tree is created. Main then instantiates and calls even.Fill(), which handles the rest of the work. It then finishes by writing the root structures to file and closes them.

The event.Fill() method calls all the necessary routines for the processing of data. It also calls decayUtil methods written by Paul Mattione[32]. These decay utilities will soon be pulled into a single class as well.

pnrMain.cpp: Shell console app
ctrlCHandle –
main – Entry point for analysis: Calls PhotoEvent::Fill

argParser.cpp: Argument Parser
InitializeParsed – Set initial values
Parser – Store the values
PrintUsage – Displays console help text

pnrEvent.cpp: Main source for defining methods to use
PhotoEvent – Instantiate the PhotoEvent Class
Fill – Process the data and fill them into the class trees: Calls the other methods

pnrBooking.cpp: Book keeping
Booking – Tracking of lost events

pnrBOS.cpp: Copy Data
FillBOSData – Get event information from database
FillMCBanks – Get simulated event information from database

pnrPartID.cpp: Identify particles in an event
isProton – Check if proton
isPiMinus – Check if Pi minus
isPiPlus – Check if Pi Plus
isKMinus – Check if negative Kaon
isKPlus – Check if positive Kaon
isNegative – Check is particle is negative
isNeutral – Check if particle is neutral
isPositive – Check if particle is positive
isProtonNew – Check if proton and within time and beta cuts
isPiMinusNew – Check if pi minus and within time and beta cuts
isPiPlusNew – Check if pi plus and within time and beta cuts
VertexTime – Calculate a rough vertex time
sortEVNT – Sort events into matrix of like particles
ParticalID – Process all the events with the above methods

pnrPartRecon.cpp: Reconstruct originated particles from final state
SetupVectors – build the 4-momentum vectors
FillEvntData – fill in specific reconstructed event information
FillinEvntExtra – boost vectors into the CM frame
ParticalRecon – Process all the events with the above methods

pnrVertRecon.cpp: Reconstruct originated particles from final state
doca_work – Call doca routines to calculate doca for the secondary decays
baryon_doca_work – Calculate the original decay vertex
baryon_doca_back_calc – Calculate forward to check decay vertices

pnrPhoton.cpp: Choose the photon for the event
FillTagger – Get tagger info form the database
InitTaggerCorrections – Initiate the tagger corrections
PhotonSelection – Compare the photon chosen from the bank w/calculated

pnrMissingMass.cpp: Reconstruct the missing mass of the proton
baryonRecon – Using the photon energy, conserve 4-momentum

Doca.cpp: Distance of Closest Approach
Doca –Mathematical method for orthogonal relationships
Distance – Closest distance between the two tracks
Point – The point between the two tracks used for the vertex
Z – The positions along the beam line

ExitChannel.cpp: Method for reading FORTRAN BOS files
ExitChannel – Structure for storing BOS data
Init – Init BOS banks
Photon – Select original photon
NextPhoton – Check the next photons
closePhoton – Check for closest photons in alternate method

DecayFiducialCuts.cpp: Mattioni's Decay fiducial cuts
Get_dfcNegativeTrackDirectionCutArray –
Get_dfcNegativeTrackMomentumShiftFunc –
Get_dfcPositiveTrackDirectionCutArray –
Get_dfcPositiveTrackMomentumShiftFunc –
Get_dfcTrackDirection –
Get_dfcTrackDirectionCut –

DecayTrackCorrections.cpp: Mattioni's Beam, momentum and energy corrections
Create_dtcCorrectionFunctions –
Correct_dtcPhotonEnergy –
Correct_dtcPhotonEnergy_TaggerCalib –
Correct_dtcTrackAngles –
Correct_dtcTrackLocation –
Correct_dtcTrackMomentum –

DecayTrackFunctions.cpp: Mattioni's correction Code
Calc_dtfAlpha –
Calc_dtfDOCA –
Calc_dtfInterDOCA –
Calc_dtfSector –
Calc_dtfSectorNormLabPhi –
Convert_dtfBogdantoLabCoords –
Convert_dtfLabtoBogdanCoords –
Convert_dtfLabtoSectorCoords –
Convert_dtfSectortoLabCoords –
Construct_dtfCovMatrix –
Dismantle_dtfCovMatrix –

C.3 Classes

There are four main class structures: argumentParse, eventStructure, decayUtilities (written by Paul Mattoine) and EventChannel.

```
argumentParse:

   InitializeParsed()

   PrintUsage()
```

```
eventStructure:

   Init()

   Open()

   Fill()

   Booking()

   // Data structure filling

   FillTagger()

   FillBOSdata()

   FillEvntData()

   FillinEvntExtra()

   FillMCBanks()

   // Particle Identifica`tion

   sortEVNT()

   ParticleID()

   isPhoton()

   isProton()
```

```
    isPiMinus()

    isPiPlus()

    isKminus()

    isKplus()

    isPositive()

    isNegative()

    isNeutral()

    // New Particle Identification (using new cuts from the delta
beta

        vs momentum plots

    isProtonNew()

    isPiMinusNew()

    isPiPlusNew()

    // Time tests- This method sets the vertex time into the array
and

        incriments the number of particles in the event

    vertexTime()

        // Photon work

    InitTaggerCorrections()

    PhotonSelection()


    // Particle track work

    SetupVectors()

    ParticleRecon()

    VertexRecon()

    BaryonRecon()

    // Vertex reconstruction
```

```
   doca_work()

   baryon_doca_work()
```

```
   baryon_doca_back_calc()
```

```
decayUtilities:

   Get_dfcPositiveTrackDirectionCutArray()

   Get_dfcNegativeTrackDirectionCutArray()

   Get_dfcPositiveTrackMomentumShiftFunc()

   Get_dfcNegativeTrackMomentumShiftFunc()

   Set_dfcTrackDirectionCuts()

   Cut_dfcTrackDirection()

   Create_dtcCorrectionFunctions();

   Correct_dtcTrackMomentum();

   Correct_dtcTrackMomentum();

   Correct_dtcTrackAngles();

   Correct_dtcTrackLocation();

   Correct_dtcPhotonEnergy();

   Correct_dtcPhotonEnergy_TaggerCalib()
```

```
Exitchannel:

   Init()

   Photon()

   NextPhoton()
```

```
    closePhoton()
```

The root objects cannot be contained within structures without their pointers being broken. Until I figure this out, they will be left in the main routine.